

Investigation of solid solution effects on texture and dislocation activity in wrought lean-alloyed ternary Mg-Al-Ca alloys

Von der Fakultät für Georessourcen und Materialtechnik der
Rheinisch-Westfälischen Technischen Hochschule Aachen

zur Erlangung des akademischen Grades eines

Doktors der Ingenieurwissenschaften

genehmigte Dissertation

vorgelegt von

Wassilios Johannes Delis, M. Sc.

aus Aachen

Berichtende: Univ.-Prof. Dr. Sandra Korte-Kerzel
Univ.-Prof. Dr.-Ing. Hauke Springer

Tag der mündlichen Prüfung: 28.03.2024

Diese Dissertation ist auf den Internetseiten der Universitätsbibliothek online verfügbar.

Declaration on publications

This thesis includes the following articles, of which Publication 1, 2 and 3 have been published in international peer-reviewed journals:

Publication 1:

W. J. Delis, P. C. Huckfeldt, B. Hallstedt, P.-L. Sun, D. Raabe, S. Korte-Kerzel, S. Sandlöbes-Haut, 2024, Influence of Al and Ca on the ductility of Mg-Al-Ca alloys, *Advanced Engineering Materials*, 26: 202301071, DOI: 10.1002/adem.202301071

Publication 2:

W. J. Delis, L. Berners, S. Korte-Kerzel, S. Sandlöbes-Haut, 2023, Effect of lean alloyed Al and Ca on the texture development of cold rolled Mg-sheets, *Metals* 13(4), 712, DOI: 10.3390/met13040712

Publication 3:

D. Andre, M. Freund, U. Rehmann, **W. J. Delis**, M. Felten, J. Nowak, C. Tian, M. Zubair, L. Tanure, L. Abdellaoui, H. J. Springer, J. P. Best, D. B. Zander, G. Dehm, S. Sandlöbes-Haut, S. Korte-Kerzel, 2022, Metallographic preparation methods for the Mg based system Mg-Al-Ca and its Laves phases, *Materials characterization* Volume 192, DOI: 10.1016/j.matchar.2022.112187

Publication 4:

W. Luo, L. Tanure, M. Felten, J. Nowak, **W. J. Delis**, M. Freund, N. Ayeb, D. B. Zander, C. Thomas, M. Feuerbacher, S. Sandlöbes-Haut, S. Korte-Kerzel, H. Springer, 2023, Metallurgical synthesis methods for Mg-Al-Ca scientific model materials

D 82 (Diss. RWTH Aachen University, 2024)

Acknowledgments

Während meiner Promotionszeit konnte ich mich auf eine breite Unterstützung in allen Bereichen verlassen, die diese Promotionsarbeit bereichert und letztlich erst ermöglicht hat. Dafür möchte ich mich bei allen Beteiligten herzlich bedanken.

Dies gilt insbesondere für meine beiden Betreuerinnen Prof. Dr. Sandra Korte-Kerzel und Dr.-Ing. Stefanie Sandlöbes-Haut, die mir die Möglichkeit zur Mitarbeit im SFB 1394 gegeben haben und die damit verbundene Erstellung dieser Dissertation ermöglicht haben. Des Weiteren für die Unterstützung bei der fachlichen Bearbeitung, bei der Überwindung der mit der Promotion verbundenen Hürden und für eure unzähligen Beiträge mit Kommentaren und Diskussionen zu Tagungsbeiträgen und Publikationen. Für die Möglichkeit des bereichernden Forschungsaufenthaltes und des kulturellen Austausches mit den Kollegen an der University of British Columbia möchte ich euch und Prof. Dr. Benjamin Berkels für die Finanzierung durch das MGK des SFB nochmals herzlich danken. Many thanks to Dr Ben Britton and the team at UBC for welcoming me and supporting my research. Für die Übernahme der Zweitkorrektur möchte ich Prof. Dr.-Ing. Hauke Springer herzlich danken.

Darüber hinaus möchte ich mich bei allen Co-Autoren der bisher aus der wissenschaftlichen Arbeit entstandenen Publikationen bedanken, durch deren Beiträge, Unterstützung bei der Erstellung und dem Einreichungsprozess diese Publikationen erst möglich wurden. Neben meinen Betreuerinnen gilt besonderer Dank meiner Abschlussarbeiterin Pia Huckfeldt und meinem Abschlussarbeiter Lukas Berners sowie Dr. Pei-Ling Sun, Dr. Bengt Hallstedt und natürlich meinem Co-Betreuer im SFB Prof. Dr.-Ing. habil. Dierk Raabe.

Bei allen Mitarbeitern des IMMs möchte ich mich für die angenehme Arbeitsatmosphäre bedanken. Für die Bearbeitung der unzähligen Versuche danke ich dem gesamten Team der mechanischen Werkstatt unter der Leitung von Detlef Fuchs, insbesondere Gerd Schütz und André Schmitz für die Probenherstellung sowie Nico Poschmann für die Herstellung des Walzmaterials und die Unterstützung bei sonstigen Hürden. David Beckers danke ich für seine Expertise und Unterstützung bei der materialographischen Probenbearbeitung in allen Belangen. Thomas Burlet danke ich für seine Hilfe und Unterstützung bei der Durchführung der Versuche an den mechanischen Prüfständen und Mikroskopen. Nicht zuletzt möchte ich mich bei Arndt Ziemons für die Unterstützung bei der Materialsynthese und den allgemeinen Support sowie bei Matthias Loeck und Sergej Laiko für den IT-Support bedanken.

Für den enormen Anteil an fachlicher, emotionaler und mentaler Unterstützung, gerade in schwierigen Zeiten, möchte ich mich von ganzem Herzen bei meinen Kollegen und Mitdoktoranden bedanken. Insbesondere ohne Dich, Nina, wäre es nicht möglich gewesen. Ob beruflich an den Geräten und bei Tagungen oder privat bei einer Kaffeerunde oder im Urlaub, ich bin dankbar, dich nicht nur als unersetzliche Kollegin, sondern auch als Freundin gewonnen zu haben. Ebenso

möchte ich mich bei Max, Mattis und natürlich Kevin als Bürokollegen für die guten persönlichen und fachlichen Gespräche und natürlich die sommerlichen Volleyballspiele bedanken.

Dankbar bin ich auch für die gute Zusammenarbeit und den kollegialen Austausch im Rahmen des SFBs, der durch die Mitarbeit in diesem möglich wurde. Insbesondere Dir, Jakub, möchte ich für die vielen konstruktiven und persönlichen Gespräche und Telefonate danken, die nicht nur die fachliche Arbeit enorm bereichert haben, sondern auch eine Freundschaft entstehen ließen.

Der im Rahmen dieser Arbeit notwendige Umfang an Experimenten und Auswertungen wäre ohne die umfangreiche Unterstützung meiner Hilfswissenschaftler/-innen nicht so schnell und erfolgreich möglich gewesen. Insbesondere danken möchte ich Pia, die mir über weite Strecken der Promotionszeit als rechte Hand zur Seite stand, sowie Luiz, Nazli und Malik. In gleichem Maße zu danken ist meinen Abschlussarbeiter/-innen Clara, Pia und Lukas. Wobei den beiden Letztgenannten, wie eingangs erwähnt, durch ihre direkten Beiträge zu den Publikationen besonders zu danken ist.

Zu guter Letzt gilt mein besonderer Dank meiner Familie, meinen Freunden und natürlich Dir, Janik. Meiner Familie möchte ich vor allem für die stetige finanzielle, emotionale und mentale Unterstützung während des Studiums und der Promotion hinweg danken. Vielen Dank, dass ihr immer an meiner Seite seid! Der gleiche Dank gilt meinen Freunden, die immer für mich da sind mit motivierenden Worten, Unterstützung, Abwechslung vom Alltag, auch wenn ich mal nicht so gut drauf bin. Lieber Janik, auch Dir möchte ich ganz besonders für die Unterstützung im Alltag und den Ausgleich und die positive Energie neben der Promotion ganz herzlich danken.

Abstract

The development of high strength and ductile Mg alloys is a major focus due to Mg's lightweight properties, which make it valuable in industries such as automotive and aerospace, as well as its potential to reduce greenhouse gas emissions. However, Mg alloys face challenges in terms of room temperature formability. Research has explored various parameters, including texture modification and alloying with elements like Y and rare-earth elements to improve ductility. Recent studies suggest that the addition of Y and rare-earth elements activates non-basal slip systems, thereby improving formability. A joint computational and experimental study found the Mg-Al-Ca system to be promising, offering similar properties with low cost elements.

This work aims at a deeper understanding of the Mg-Al-Ca system by investigating the elemental effects on mechanical properties, texture and slip system activity. Different alloying compositions were synthesised and analysed while maintaining the same processing parameters. It was shown that the addition of Al and Ca significantly increases the strength and ductility of Mg, but only the combination of both Al and Ca gives to the highest values of both. Ca has an intrinsic grain refinement effect on the alloy, pinning the grain boundaries and therefore leading to weaker basal textures. Also, the amount of Ca is important as Al reduces the solubility of Ca in Mg. Adjusting the alloying contents of Ca and Al not only allows weak as-recrystallised textures but also allows weak textures to be maintained during further cold rolling. In general, the effect of Ca on both grain refinement and texture can be seen at very low Ca additions (0.005 wt.-%). However, the co-dependence of Al and Ca significantly increases the complexity of the alloy system. Al shows not only an effect on solid solution strengthening, but also increases the presence of $\langle c + a \rangle$ dislocations. APT at a 2nd order pyramidal slip line also shows Al segregation at the dislocation. Access to the CRSSs of non-basal slip systems with MP compression was not successful, because basal slip was ubiquitous even at very low Schmid factors. Consecutive TEM shows that non-basal slip was active but mainly stored in the matrix. It was also found, that $\langle c + a \rangle$ dislocations were more abundant near boundaries such as grain or twin boundaries, suggesting that these defects have favourable strain fields allowing easier activation of $\langle c + a \rangle$ slip there than in the matrix. Further investigations using HR-STEM are underway to investigate the effect of Al on the activation of the slip system.

In summary, this work provides a fundamental understanding of the Mg-Al-Ca alloy system, but its practical application depends on optimising the alloy content and further research to improve ductility. This includes, in particular, exploring the effect of the Al:Ca ratio in order to maximise the beneficial Ca effect while maintaining the Al effect, and also to gain a better understanding of the mechanisms behind the activation of $\langle c + a \rangle$ dislocations.

Zusammenfassung

Die Entwicklung von hochfesten und duktilen Mg-Legierungen ist aufgrund der Leichtbaueigenschaften von Mg, die es in Branchen wie der Automobil- und Luftfahrtindustrie wertvoll machen, sowie aufgrund seines Potenzials zur Verringerung der Treibhausgasemissionen ein wichtiger Schwerpunkt. Allerdings stehen Mg-Legierungen vor der Herausforderung, bei Raumtemperatur verformbar zu sein. In der Forschung wurden verschiedene Parameter untersucht, darunter die Veränderung der Textur und die Legierung mit Elementen wie Y und seltenen Erden zur Verbesserung der Duktilität. Jüngste Studien deuten darauf hin, dass der Zusatz von Y und Seltenen Erden nicht-basale Gleitsysteme aktiviert und dadurch die Umformbarkeit verbessert. Eine gemeinsame simulative und experimentelle Studie ergab, dass das Mg-Al-Ca-System vielversprechend ist und ähnliche Eigenschaften mit kostengünstigen Elementen bietet.

Daher zielt diese Arbeit auf ein tieferes Verständnis des Mg-Al-Ca-Systems ab, indem die Auswirkungen der Elemente auf die mechanischen Eigenschaften, die Textur und die Aktivität der Gleitsysteme untersucht werden. Es wurden verschiedene Legierungen mit identischen Verarbeitungsparametern hergestellt und analysiert. Es zeigt sich, dass die Zugabe von Al und Ca die Festigkeit und Duktilität von Mg deutlich erhöht, wobei jedoch nur die Kombination von Al und Ca zu den höchsten Werten führt. Ca führt intrinsisch zu einer Kornfeinung der Legierung, indem es die Korngrenzen fixiert und so zu weicheren basalen Textur führt. Auch die Menge an Ca ist wichtig, da Al die Löslichkeit von Ca in Mg verringert. Die Einstellung von Ca und Al ermöglicht nicht nur weiche Texturen im rekristallisierten Zustand, sondern auch die Beibehaltung weicher Texturen beim weiteren Kaltwalzen. Im Allgemeinen ist der Einfluss von Ca auf die Kornfeinung und die Textur bei sehr geringen Ca-Zugaben (0,005 Gew.-%) zu erkennen. Allerdings erhöht die Abhängigkeit von Al und Ca die Komplexität des Legierungssystems erheblich. Al wirkt sich nicht nur auf die Mischkristallverfestigung aus, sondern erhöht auch die Präsenz von $\langle c+a \rangle$ -Versetzungen. APT an einer pyramidalen Gleitlinie 2. Ordnung zeigt auch eine Al-Segregation an der Versetzung. Die Messung von kritischen Schubspannungen nicht-basaler Gleitsysteme mit MP-Kompression war nicht erfolgreich, da basales Gleiten selbst bei sehr niedrigen Schmid-Faktoren aktiv war. TEM-Untersuchungen zeigen, dass nicht-basale Gleitsysteme zwar aktiv waren, aber hauptsächlich in der Matrix gespeichert wurden. Es wurde auch festgestellt, dass $\langle c+a \rangle$ -Versetzungen in der Nähe von Grenzflächen wie Korn- oder Zwillingsgrenzen häufiger vorkamen, was darauf hindeutet, dass diese Defekte günstige Dehnungsfelder aufweisen, die dort eine leichtere Aktivierung von $\langle c+a \rangle$ -Versetzungen ermöglichen als in der Matrix. Weitere Untersuchungen mit HR-STEM sind im Gange, um den Einfluss von Al auf die Aktivierung des Gleitsystems zu untersuchen.

Zusammenfassend vermittelt diese Arbeit ein grundlegendes Verständnis des Legierungssystems Mg-Al-Ca, wobei seine praktische Anwendung jedoch von der Optimierung des Legierungsgehalts und weiteren Forschungen zur Verbesserung der Duktilität abhängt. Dazu gehört insbesondere die Untersuchung der Auswirkungen des Al:Ca-Verhältnisses, um den vorteilhaften Ca-Effekt zu maximieren und gleichzeitig den Al-Effekt beizubehalten, sowie ein besseres Verständnis der Mechanismen hinter der Aktivierung von $\langle c+a \rangle$ -Versetzungen.

Contents

Declaration on publications	II
Acknowledgments	III
Abstract	V
Zusammenfassung	VI
List of Abbreviations	VIII
1 Motivation	1
2 Basics of deformation and hardening mechanisms	4
2.1 Mechanisms of plastic deformation	5
2.1.1 Dislocation slip	5
2.1.2 Deformation twinning	6
2.1.3 Plastic deformation of magnesium	7
2.2 Stacking faults	9
2.2.1 Stacking faults in magnesium	10
2.3 Textures and polycrystalline deformation	11
2.3.1 Textures of magnesium	11
3 Status of research on Mg-Al-Ca alloys	13
4 Research findings of this study	17
4.1 Published results of peer-reviewed research and pre-print papers	17
4.2 Research results from ongoing investigations	22
5 Conclusions and Outlook	26
Influence of Al and Ca on the ductility of Mg-Al-Ca alloys	28
Effect of lean alloyed Al and Ca on the texture development of cold rolled Mg-sheets	42
Metallographic preparation methods for the Mg based system Mg-Al-Ca and its Laves phases	58
Metallurgical synthesis methods for Mg-Al-Ca scientific model materials	69
References	86
List of Figures List of Tables	108

List of Abbreviations

APT	atom probe tomography
BPI	basal peak intensity
CRSS	critical resolved shear stress
EBSD	electron backscatter diffraction
fcc	face centered cubic
GB	grain boundary
hcp	hexagonal closed packed
m.r.d.	multiples of random distribution
MP	micropillar
ODF	orientation distribution function
RE	rare-earth element
RX	recrystallization
RT	room temperature
m_s	Schmid factor
SE	secondary electron
SIS	slip system
SF	stacking fault
SFE	stacking fault energy
I1 SFE	I1 intrinsic stacking fault energy
SFI1	I1 intrinsic stacking fault
TB	twin boundary
TEM	transmission electron microscopy
HR-STEM	high-resolution scanning transmission electron microscopy
UTS	ultimate tensile strength
wt.-%	weight percentage
XRD	x-ray diffractometry
YS	yield strength

1 Motivation

Much effort has been devoted to the development of Mg alloys with both, high strength and good room temperature (RT) ductility [1–4]. As Mg and Mg alloys are the lightest structural metals available, they are of great interest for many applications where reducing the mass of structural parts leads to high cost reduction and/or increased efficiency e.g. in the automotive and aerospace industries [5, 6]. In addition, the ever-increasing pace of climate change has significantly increased the demand and public interest in reducing greenhouse gases, to which the lightweight design of Mg alloys can contribute [7, 8]. Furthermore, in terms of properties, Mg alloys exhibit good castability and recyclability [5].

Unfortunately, Mg has only limited formability at room temperature because it deforms mainly by tensile twinning or basal slip which has only two independent deformation modes available [9–11]. To satisfy the von Mises’ criterion at least five independent deformation modes are required for an arbitrary change in shape [12]. In order to develop alloys with improved RT formability, many parameters have been investigated and simulative and experimental studies have been carried out. Not only the weakening of the sharp basal texture [13–18] that develops after rolling has been found to have a major influence on the ductility properties, but also the activation of non-basal slip systems (SISs) [19, 20] and the manipulation of the grain size [21–24]. The strong interconnectivity between these parameters makes it difficult to separate their explicit effects.

Most research has been carried out to manipulate the properties through processing [1]. Both, grain size [25, 26] and texture [27] can be significantly altered by different processing routes and with thermal treatments [23, 28]. Often the changes in texture and grain size also lead to the activation of non-basal SISs, improving the overall performance of the alloys [29–32]. Similar changes can be achieved by the addition of alloying elements such as Y [33–37] and rare-earth elements (REs) [35, 38–41], which have been extensively studied. More recently, the effects of cheaper and more environmentally friendly alloying elements such as Al [42–46], Zn [36, 38, 47], Mn [48, 49], and Ca [24, 46, 50–55] have also been investigated and may also induce similar improvements. The formation of precipitates (e.g. Laves phases) in alloys beyond the solubility limits has also been investigated [56–60]. The increased strength of these alloys is attractive for creep and elevated temperature applications [60, 61]. However, the predominantly brittle precipitates generally also lead to a reduction in ductility [46].

In previous studies, Mg alloys with Y and RE additions have shown increased RT ductility which could be related to an increased activation of non-basal slip [33, 62–68]. The observed $\langle c + a \rangle$ dislocation slip is usually not a predominant SIS in Mg and its alloys [9]. It has been suggested that Y and RE reduce the I1 intrinsic stacking fault energy (I1 SFE), leading to the formation of I1 intrinsic stacking fault (SFI1) associated with the activation of shear modes out of the basal plane [63, 64]. Here, a sessile SFI1 bound with pyramidal partial dislocations is assumed to act as a Frank-Read-like [69] source of $\langle c + a \rangle$ dislocations resulting in an increased

formability through more available deformation modes [70, 71]. Using the I1 SFE as a leading parameter, a systematic joint computational and experimental study by Sandlöbes et al. found the Mg-Al-Ca system to have similar properties with inexpensive and widely available elements [46, 72].

All too often, studies change a combination of parameters. As a result, it is difficult to extract the effect on properties of changing individual parameters. Therefore, the aim of this thesis is to provide a systematic analysis of the ductility mechanisms of the previously introduced Mg-Al-Ca alloy system. Two binary, one Mg-Al and one Mg-Ca alloy, and seven ternary Mg-Al-Ca alloys with lean alloying contents ensuring a solid solution or near solid solution state have been identically synthesised and investigated. In conclusion, the following research questions should be answered:

- ① How does the lean addition of the elements Al and Ca affect the mechanical properties of Mg?
- ② How does the lean addition of the elements Al and Ca influence the texture of Mg and the texture evolution under cold rolling conditions?
- ③ How does the lean addition of the elements Al and Ca affect the activity of the slip systems, in particular non-basal slip systems, in Mg?

To achieve this, mechanical properties were first measured to investigate property changes between the alloys. Textures and texture evolution under further deformation were measured by x-ray diffractometry (XRD). The activation of SIs was analysed by statistical evaluation of slip traces on deformed surfaces with a correlative secondary electron (SE)/ electron backscatter diffraction (EBSD) examination. Consequently, critical resolved shear stresses (CRSSs) of the SIs were measured with micropillar (MP) compression and further investigated with transmission electron microscopy (TEM). Finally, local chemical and structural changes of dislocations and boundary configurations have been studied by atom probe tomography (APT) and will be correlated with forthcoming high-resolution scanning transmission electron microscopy (HR-STEM) results. An overview of the workflow and the results related to the published work is given in 1.1.

After motivating the topic of this cumulative thesis, an overview of the basic theory is given. An attempt is also made to provide a literature review of the broad field of alloying effects in Mg-Al-Ca alloys. Emphasis is placed on unraveling the relationship between strength and ductility and influencing parameters such as grain size and texture. The results of the peer-reviewed publications are summarised and contributions from collaborative work associated with the scope of these investigations are presented. This work concludes with a conclusion and outlook followed by the publications.

Improvement of the synthesis route of Mg-Al-Ca alloys for homogenisation and reduction of oxide inclusions

Improvement of the preparation of Mg-Al-Ca alloys. Reduction of the surface roughness and increase of the pattern detection.

Effect of Al and Ca on the mechanical properties, texture and slip system activation in Mg (Paper 1)

Effect of Al and Ca on the texture evolution under cold rolling conditions in Mg (Paper 2)

Mechanisms of $\langle c+a \rangle$ slip system activation (ongoing)

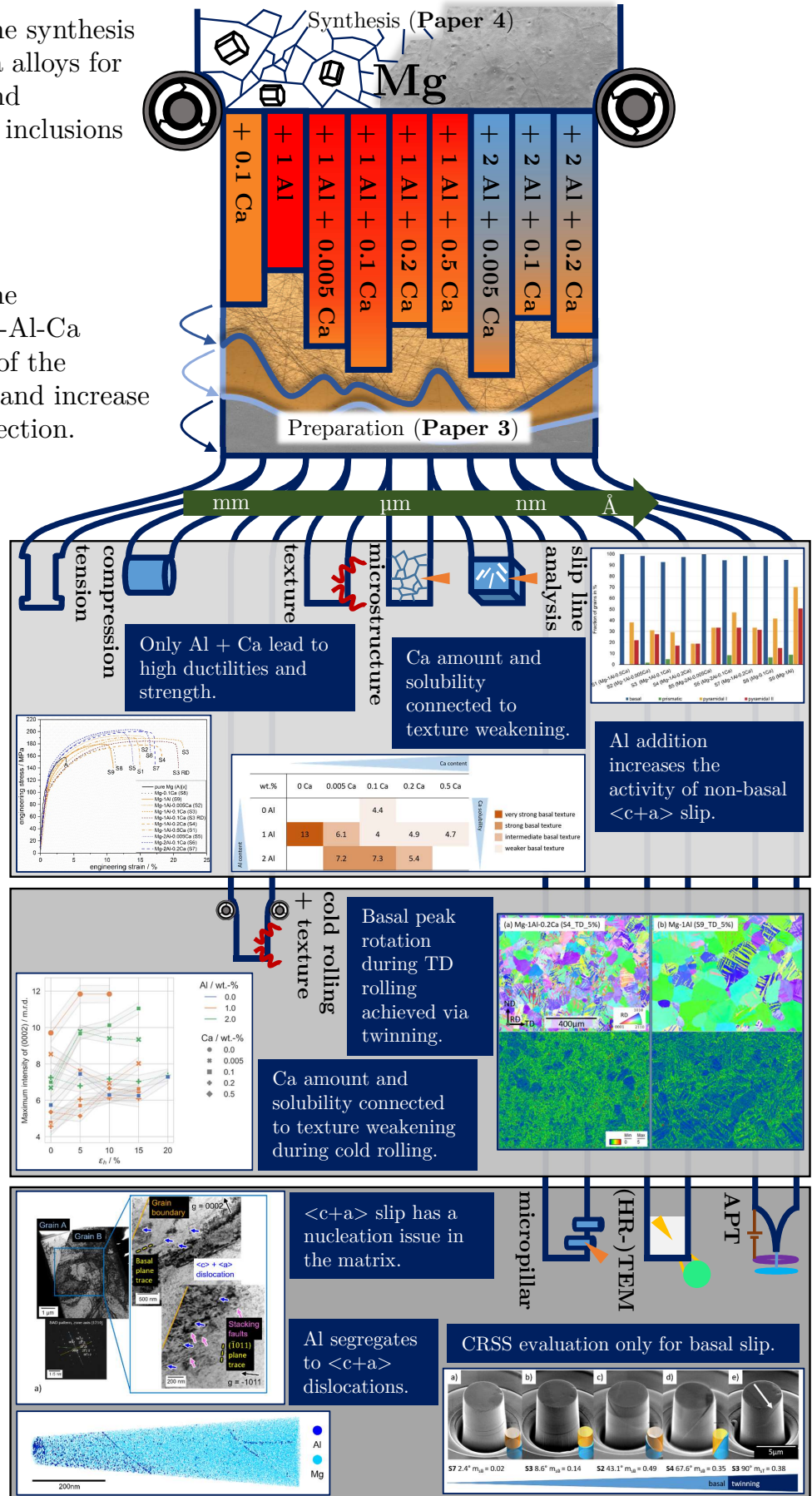


Figure 1.1: Workflow and structure of this thesis including the resulting publications. All alloy compositions stated in weight percentage (wt.-%).

2 Basics of deformation and hardening mechanisms

The plasticity of materials is mainly controlled by dislocation motion [73]. For materials with limited SLSs available for dislocation movement, or during deformation at low temperatures, deformation twinning also becomes a relevant deformation mechanism [74–76]. In general, dislocation slip is thermally activated and each SLS has a characteristic CRSS that depends on strain and strain rate in addition to temperature, whereas deformation twinning is less sensitive to temperature and strain rate [77, 78]. In particular, inhibition of dislocation movement by crystallographic defects dramatically increases the strength of the material and is one of the main strategies for tailoring materials properties for applications [74].

Hardening mechanisms can be summarised as different approaches to tailoring the mechanical properties of a material. Crystallographic defects that are associated with the hardening of a material are substitutional or interstitial foreign atoms, dislocations, grain and phase boundaries, and precipitates or particles. Major hardening mechanisms observed in Mg alloys are Peierls stress, grain refinement, forest hardening, solid solution strengthening and precipitation hardening [1, 44, 74, 79, 80]. The sum of all hardening mechanisms gives the total strength of a material and is usually inversely correlated with its ductility [81, 82]. The Peierls stress [83, 84] describes the stress required for a dislocation to slip through a perfect crystal, the so-called lattice friction. As it usually makes a rather small contribution to the overall strength of hexagonal metals, it is often neglected. A larger contribution to strength comes from grain refinement. According to Hall [85] and Petch [86] there is a relationship between the grain size and the stress required for dislocations in one grain to activate SLSs in neighbouring grains. Since in smaller grains only small amounts of dislocations can accumulate at the grain boundary (GB), less internal stress is built up and larger external stresses are required to activate dislocation slip, or deformation twinning, in the adjacent grain. The interaction between the dislocations themselves also leads to hardening of the material. Forest hardening results from the additional stresses required for cutting or passing of dislocations [87]. Therefore, forest hardening is strongly correlated with the dislocation density of the material. Furthermore, solute atoms can contribute to the strength [74, 88, 89]. There are three hardening effects resulting from solid solution strengthening by these foreign atoms. Firstly, the par elastic interaction between the different atom sizes of the matrix and the foreign atoms leads to a distortion of the crystal lattice. Therefore, dislocations require higher stresses for slip motion. Secondly, the dielastic interaction of different shear moduli of matrix and foreign atom leads to altered bonding situations which then attract or repel dislocations. Higher stresses are required to overcome these regions. Thirdly, the chemical interaction resulting from the altered chemical composition affects the stacking fault energy (SFE) and represents locally different circumstances for dislocations. In these regions different energetically favourable dislocation configurations are dominant and further dislocation slip may require higher stresses. Finally, precipitation hardening can contribute to the overall hardness as precipitates are difficult for dislocations to pass through. Either cutting or bypassing by the Orowan mechanism [90] is necessary and requires higher stresses.

2.1 Mechanisms of plastic deformation

2.1.1 Dislocation slip

Dislocation slip allows plastic deformation by crystallographic sliding of atomic layers in a material [91, 92]. As one-dimensional defects, dislocations are defined by their line vector \vec{l} and Burgers vector \vec{b} [93]. Two types of dislocation can be distinguished. Firstly, edge dislocations with $\vec{l} \perp \vec{b}$ and secondly, screw dislocations with $\vec{l} \parallel \vec{b}$ [93]. Usually, only mixed dislocation types are observed in real materials, with the screw dislocation fraction dominating in a dislocation loop because its line energy is lower than that of the edge dislocations [94]. Depending on the SFE, dislocations tend to dissociate into partial dislocations further minimising their energy and therefore are unable to cross slip [73, 94]. Screw dislocations also have the ability to cross slip and change their slip plane since their slip plane is not defined [95]. In any case, dislocation configurations always have a complex configuration and lead to complex interaction and deformation behaviour [96, 97].

The CRSS can be used to evaluate which SIS becomes active under a given stress condition. According to Schmid's law [98, 99], the SIS with the highest shear stress applied to the sliding plane and direction is activated first after a critical value is exceeded. The predominantly activated SISs are usually those with the highest Schmid factor (m_s) [100, 101]. Eq. 1 gives the relationship between the resolved shear stress τ and the external stress σ associated with the m_s represented by the product of the cosines of the angles between both the external stress and the slip direction λ and the plane normal φ .

$$\tau = \sigma \cos(\varphi) \cos(\lambda) \quad (1)$$

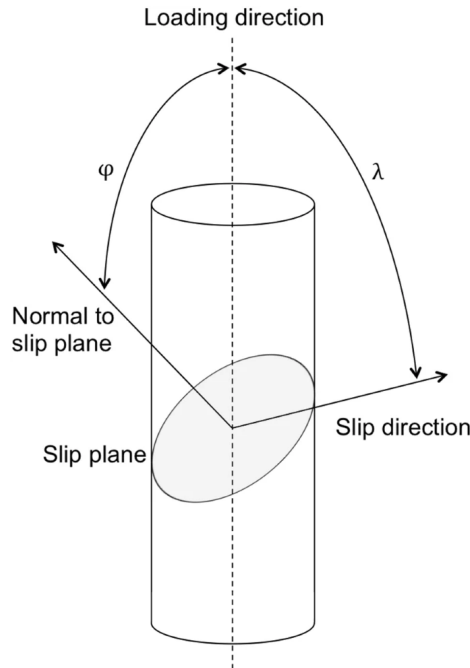


Figure 2.1: Determination of the Schmid factor (published under a Creative Commons CC BY 4.0 license [102]).

A graphical overview of the determination of the m_s based on Eq. 1 is given in Fig. 2.1. To a certain extent, this concept can also be applied to the activation of twin systems [74].

2.1.2 Deformation twinning

Predominantly, deformation twins are observed in poorly deformable materials with high stacking faults (SFs) and limited or during low temperature deformation [76, 103]. The nucleation point for the deformation twin is mainly at a GB [104, 105] or at a twin boundary (TB) itself [106] and therefore the activation of twinning is microstructure dependent. It has also been reported that the grain size affects twinning and it is proposed that this effect is even greater than for slip [107, 108]. In addition, a link between twinning and the SFE has been found [109], and solutes introduced by alloying have a positive effect on the twinning probability with reduced dislocation mobility [110].

The formation of deformation twins induces a shear at a defined twinning plane leading to a domain with the same crystal structure as the matrix but with a mirror symmetry [111]. Fig. 2.2 a) shows the transformation of the matrix under stress exposition leading to twin formation [112]. Here P is the plane of shear with s defining the twinning shear. K_1 and η_1 are the twinning plane and the shear direction, while K_2 and η_2 describe their conjugates. In Fig. 2.2 b) an example for the formation of an extension twin is given, where the angle ω is also given, which gives the rotation of the basal plane during twinning [112].

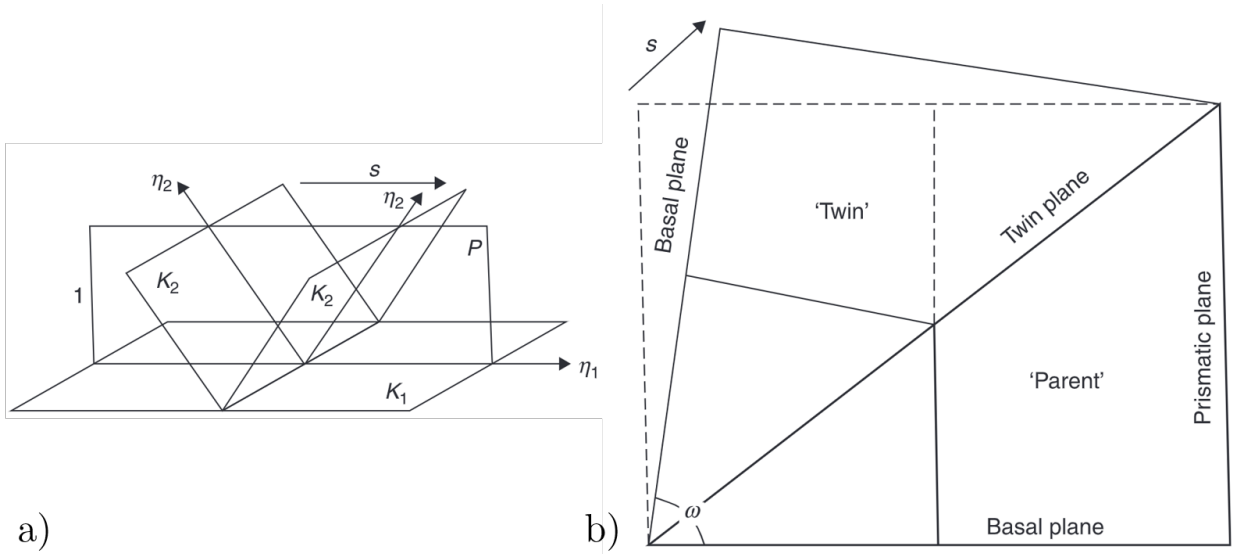


Figure 2.2: Mechanism of deformation twinning. a) Twinning elements b) Example: Schematic for an extension twin in Mg (adapted from [112]).

While the total deformation is related to the fraction of twinned volume, the induced shear is fixed [76]. Twinning systems are only activated in certain directions for a given stress state, making deformation twinning a polar deformation mechanism [113]. Nevertheless, deformation twinning often supports the activation of other deformation mechanisms. As the twin leads to a reorientation of the crystal, the activation of other SLSs becomes attractive after twinning, allowing for higher overall degrees of deformation [114].

2.1.3 Plastic deformation of magnesium

Mg has a hexagonal crystal structure [11]. For hexagonal closed packed (hcp) structures the ideal c/a ratio is 1.633 [11]. This value is close to that of Mg with a c/a ratio of 1.623 [11]. The hexagonal structure allows for different SLSs, divided into basal, prismatic and pyramidal SLSs [10, 114]. The major planes in Mg are shown in Fig. 2.3 and the corresponding predominant SLSs are summarised in Tab. 2.1.

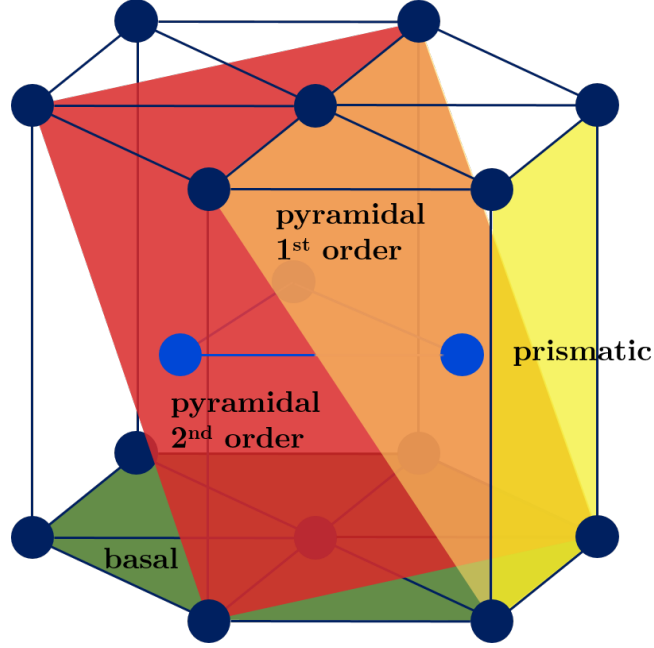


Figure 2.3: Schematic hexagonal lattice structure with the important slip planes.

Table 2.1: Predominant slip systems in hexagonal Mg [10, 11, 115].

Slip system	Burgers vector type	Slip direction	Slip plane	No. of slip systems		d/b	w/b (edge)
				Total	Independent		
basal	$\langle a \rangle$	$\langle 11\bar{2}0 \rangle$	(0002)	3	2	0.81	0.61
prismatic	$\langle a \rangle$	$\langle 11\bar{2}0 \rangle$	$\{10\bar{1}0\}$	3	2	0.87	0.62
pyramidal 1 st order	$\langle a \rangle$	$\langle 11\bar{2}0 \rangle$	$\{10\bar{1}1\}$	6	4	0.76	0.56
pyramidal 1 st order	$\langle c + a \rangle$	$\langle 11\bar{2}3 \rangle$	$\{10\bar{1}1\}$	6	5	-	-
pyramidal 2 nd order	$\langle c + a \rangle$	$\langle 11\bar{2}3 \rangle$	$\{11\bar{2}2\}$	6	5	0.22	0.17

As seen in Tab. 2.1, the Burgers vectors in Mg are of type $\langle a \rangle$ or $\langle c + a \rangle$. The active SLS in metals occurs in most cases on the plane with the highest atomic density and the largest interplanar spacing in the direction of the highest packing density [115]. Two parameters are defined that

indicate the possibility of an active SIS. The first describes the relationship between the Burgers vector and the dislocation crystallographic plane spacing (d/b) and the second sets the Burgers vector in relation to the dislocation width (w/b) [115]. For Mg, both parameters are in favour of prismatic slip (compare Tab. 2.1). However, for reasons that are not yet fully understood, Mg is mainly observed to have basal slip in experiments, leading to a more complex behaviour for Mg [10].

Basal $\langle a \rangle$ slip usually has a very low CRSS and is therefore easy to activate [114]. Other $\langle a \rangle$ -type SISs can also be observed at RT, but basal slip remains the main active SIS [114]. Although SISs show thermal activation behaviour leading to reduced CRSSs with increasing temperature, basal slip can be observed to be almost athermal [114, 116, 117]. As $\langle c + a \rangle$ slip has increased Burgers vectors, it is naturally more difficult to activate [118]. Here, the activation is indeed temperature dependent [119, 120].

Cubic metals have 12 independent SISs fulfilling the von Mises criterion and allowing arbitrary shape changes, whereas hexagonal materials usually suffer from limitations for plastic deformation [71, 121, 122]. Here, the predominantly observed basal slip has only two independent SISs, as shown in Tab. 2.1 and does not allow deformation along the $\langle c \rangle$ axis. $\langle c + a \rangle$ dislocation SISs allow strain along the $\langle c \rangle$ axis [123], which makes their activation inevitable for higher degrees of deformation [114]. However, the CRSS of non-basal SISs is more than 2.5 times higher than that of basal slip and the resulting high CRSS anisotropy prevents the activation of more SISs [62, 124]. This results in limited formability of Mg, especially at RT.

Consequently, the activation of non-basal SISs accommodating strains along the $\langle c \rangle$ axis is necessary for an arbitrary shape change and has been extensively investigated [125–129]. Alloying with REs has been found to lead to enhanced $\langle c + a \rangle$ slip activity [19, 33, 34, 130–135] and recently also non-RE alloying elements have been shown to allow similar improvements [46, 136–139]. The main underlying mechanism is proposed to be the reduction of the CRSS anisotropy [140–143] and improvement the cross-slip probability [137, 144–147] by manipulation of the c/a ratio [148], SFEs [67, 149–151] and/or Peierls stress [152, 153].

To a lesser extent, deformation twinning also leads to deformation along the $\langle c \rangle$ axis and has been observed and studied to a greater extent in Mg alloys [154]. On the one hand, deformation twinning is an important mechanism in strain accommodation due to the general lack of deformation modes with dislocation slip [155–160]. On the other hand, deformation twinning has been reported to induce strain localisation and shear banding leading to early failure [161, 162]. The most important and observed twinning systems are summarised in Tab. 2.2 [74, 112].

Table 2.2: Predominant twinning systems in Mg [74, 112].

Twin system	K_1	η_1	ω
extension twin	$\{10\bar{1}2\}$	$\langle 10\bar{1}1 \rangle$	86.3°
compression twin	$\{10\bar{1}1\}$	$\langle 11\bar{1}2 \rangle$	56°
double twin	$(10\bar{1}1)$	$[\bar{1}012]$	37.5°

In particular, extension twins are easily activated due to the low CRSSs reported in the literature and therefore the main twin system [163]. This leads to higher twin activation during compression testing than tensile testing, resulting in an asymmetry in yield stress between the two test modes [164–169]. More important than the $\langle c \rangle$ axis strain is the crystal lattice reorientation induced by twinning, as it allows basal slip in grains, that were previously not preferentially oriented for basal slip [170, 171]. Double twinning can further improve the orientation of grains for basal slip due to its double shear plus rotation mechanism [75, 172, 173]. Deformation twins further influence textures during cold rolling, refining microstructures and are thought to be responsible for work hardening/softening effects [112]. As the activation of deformation twins is also dependent on the grain size [174–176], texture [177–179] and chemical composition [180–182], the likelihood of twin nucleation is also influenced by synthesis and processing history [112]. TBs have been reported to promote the nucleation of slip and may be important in increasing overall formability [183–190].

2.2 Stacking faults

Planar defects resulting from a shift of lattice planes out of their regular crystallographic stacking lead to a SF [191]. As described in Ch. 2.1.1, dislocations usually occur as partial dislocations to minimise their line energy. The displacement with a Burgers vector of these partial dislocations does not correspond to a full displacement of the crystal lattice leading to a SF. Consequently, the SF has the energy required to form the defect. As the partial dislocation has both edge and screw character, the edge and screw parts have repulsive forces between each other [74]. The dissociation width of the partial dislocations is therefore characterised as the point where the energy minimisation and the repulsion forces are in equilibrium. In particular, this equilibrium is related to the SFE (Γ) which can be described by Eq. 2 where E_{SF} is the energy and L is the length of the SF and x is the distance between the partial dislocations [74].

$$\Gamma = \frac{E_{SF}}{Lx} \quad (2)$$

The dissociation width is higher when the SFE is lower and vice versa. For recovery and recrystallization (RX) processes, the SFE is of great importance as a low SFE leads to a suppression of recovery and promotion of RX due to the high energy required for recombination of the partial dislocations required for recovery [74]. Furthermore, the SFE is also relevant for the dislocation cross-slip probability, since at high SFEs the dislocation core is compact [192]. On the other hand, at lower SFEs the dissociated core increases the twinning probability [193–195].

The evaluation of the SFE can be done experimentally with a direct TEM examination of the dissociation width of partial dislocations or the radii of the dislocation nuclei [196], and also with indirect measurement methods by examining the shear-stress τ_{III} at the beginning of stage 3 of the single crystal stress-strain curve [197], or by peak shifts during XRD investigation [198]. Thermodynamic approaches can also be used e.g. the Olson-Cohen approach [199]. Density functional theory has been also used to evaluate SFE [200].

2.2.1 Stacking faults in magnesium

While SFs are more straightforward for face centered cubic (fcc) structures, the situation is more complex for hexagonal crystal structures. In Mg four different types of basal SFs are known, but the complex behaviour of non-basal SFs and their dissociation reaction has only been confirmed by molecular dynamics [201–207]. Due to the low basal SFE of $<50 \frac{mJ}{m^2}$ [194, 207, 208] compared to non-basal SFE, SFs are most likely to be observed on the basal plane and have been confirmed by TEM analysis [209]. Non-basal SFs have not been observed in TEM experiments [118], although there are indications [210]. Fig. 2.4 shows the crystal plane ordering of the four basal SFs.

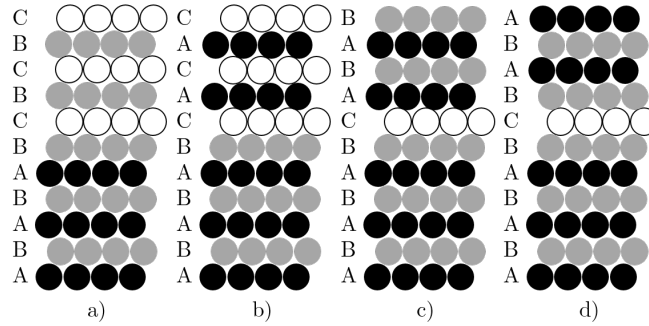


Figure 2.4: Basal stacking faults in Mg. a) I1 intrinsic stacking fault, b) I2 intrinsic stacking fault, extrinsic stacking fault and d) twin-like stacking fault.

The most important is the SFI1 (compare Fig. 2.4 a)). Here, an A-layer above the B-layer is removed and the remaining layers are sheared by $\frac{1}{3}[\bar{1}\bar{1}00]$, resulting in a Shockley-type basal $\langle a \rangle$ and a Frank-type $\frac{1}{2}\langle c+a \rangle$ partial. Next, the I2 intrinsic stacking fault results from a direct shearing of an A-layer and above by $\frac{1}{3}[\bar{1}\bar{1}00]$, inducing a fcc-like intrinsic SF with two Shockley basal partials $\frac{1}{3}[01\bar{1}0] + \frac{1}{3}[\bar{1}\bar{1}00]$ (Fig. 2.4 b)). The extrinsic stacking fault is formed by an additional C-layer introduced into the hcp layer, which is not energetically favourable (Fig. 2.4 c)) [207, 208, 211]. Of less importance is also the twin-like SF with a mirror symmetry on one side of the faulted layer, which has not been reported to occur in pure Mg (Fig. 2.4 d)) [207, 211].

In studies, the I2 intrinsic stacking fault has been associated with the likelihood of cross-slip events [63, 212, 213]. On the other hand, SFI1 have been proposed as a source of non-basal $\langle c+a \rangle$ slip [46, 63, 70, 214, 215]. Subsequently, the manipulation of the SFE with alloying approaches and thereby increasing the non-basal $\langle c+a \rangle$ slip activity has been intensively investigated [20, 216–219].

2.3 Textures and polycrystalline deformation

Textures are of particular importance in the study of wrought material [2, 220]. A texture is defined as the distribution of crystallographic planes in a polycrystalline sample [221, 222]. These orientations may be random or may form preferred orientations of varying intensity [221]. As many material properties are affected by texture (e.g. Young's modulus and the general stress-strain behaviour, but also electromagnetic and corrosive properties), the knowledge of their state and evolution during deformation history is of great interest [220, 223]. A random distribution of orientations generally leads to isotropic properties while strong textures usually lead to anisotropic behaviour [224].

Textures can be represented either by two-dimensional pole figures or in the three-dimensional Euler space [222]. Pole figures show all measured orientations for a given family of crystallographic planes, calculated with a normalisation factor that expresses the higher frequency of a particular orientation with respect to all orientations called multiples of random distribution (m.r.d.) [221]. In contrast, the Euler space provides a complete description of all orientations (described by the orientation distribution function (ODF) as the intensity distribution over all orientations) in a space constructed by three Euler angles resulting from the mathematical transformation of the crystallographic axes into the sample coordinate system [222].

In polycrystalline deformation, the activation of the deformation mechanisms for each grain is mainly controlled by the m_s which is more complicated to approach in the polycrystalline state than for single crystals (see Ch. 2.1.1). The GB acts as an obstacle and interaction point for dislocations and twins, and stress concentrations at the boundary, e.g. due to dislocation pile-up, can lead to activation of dislocation slip or twinning in neighbouring grains [225, 226]. The activity of both dislocation slip and twinning induces a shear deformation and hence rotation of all grains, leading to the development of deformation textures [227]. Consequently, the intensity and type of active SLSs and twinning modes are strongly related to texture formation.

2.3.1 Textures of magnesium

The previously described limitation of deformation modes for Mg alloys leads to the observation of rather strong basal textures (see Fig. 2.5) [1, 27, 62, 228–231]. The absence of $\langle c \rangle$ axis deformation during the predominant basal slip activity causes a strong basal-type texture to develop during rolling [221, 232, 233]. Furthermore, the highly anisotropic orientation of the grains themselves prevents further deformation due to the lack of deformation modes with a $\langle c \rangle$ axis component. Therefore, early fracture is observed, especially during cold rolling of pure Mg [46].

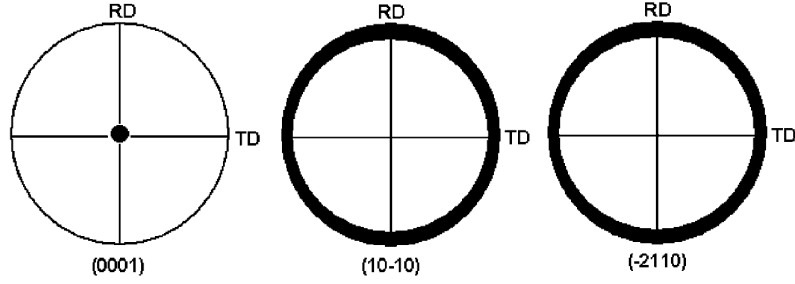


Figure 2.5: Ideal pole figures for the $\{0001\}$ basal texture (adapted from [221]).

Manipulations to overcome this disadvantage have been successfully implemented. The application of temperature during the rolling process allows the activation of more SLSs leading to higher degrees of deformation. The use of heat treatments as post-treatment [234, 235] is also well established. Also, the use of complex process routes involving extrusion [18, 24, 35], asymmetric [27, 228, 236, 237] or cross rolling [238, 239] as well as severe plastic deformation [9] and grain refinement approaches [25, 240–242] have been used to optimise the microstructure and texture. In addition, the effect of alloying elements on the texture formation has been investigated and shows the potential for texture improvements. In particular, REs [13, 35, 243–246] have been shown to be effective in weakening basal textures, namely Y [35, 62, 247], Gd [35, 248–250], Nd [244, 251] and Ce [35, 252, 253], but also non-REs such as Al [46, 254, 255], Zn [256–259] and Ca [249, 256–258, 260] can weaken the basal texture peak.

3 Status of research on Mg-Al-Ca alloys

Mg-Al-Ca alloys have received increased attention in the last 10 years [1, 46, 51]. Most of the research has focused either on the binary systems Mg-Al [26, 42, 51, 261–264] and Mg-Ca [24, 54, 240, 241, 260, 261, 263, 265–267] or higher order alloys containing four or more elements [43, 49, 51, 53, 260, 268–270], while for the ternary Mg-Al-Ca system only a few papers have been published [43, 46, 51, 260, 271, 272] prior to this work and only three of these studies focused on pure solid solution alloys [46, 51, 260].

For this reason, a broad analysis of the alloys that have been studied in the literature so far and their properties is carried out. The aim is to gain a more fundamental understanding of the influence of the available parameters on the properties. It should be noted that due to the limited data available on pure rolling, the processing itself has not been considered, but only the resulting grain sizes. The precipitation behaviour is also of great interest for achieving high strength while maintaining considerable ductility for forming of sheet material [58, 59]. Here, the most important phases are Laves phases of the C14, C15 and C36 type, but will not be explicitly discussed further [45, 60, 273–276]. The formation of these phases is closely related to the solubility limit which is a maximum of 10.5 wt.-% Al in Mg [277] and 0.3 wt.-% Ca in Mg [278] and the Ca/Al ratio [279–286]. However, the solubility of Ca also continues to decrease with increasing Al [254]. In order to reduce the complexity of this study, the precipitates are only indirectly evaluated with the resulting strengths and ductilities. These limits lead to a higher scatter but still allow the analysis of trends in this alloy system.

Fig. 3.1 shows that all values considered for yield strengths (YSs) and ultimate tensile strengths (UTSs) of relevant Mg-Al, Mg-Ca, Mg-Al-Ca and higher order alloys have an almost linear trend between strength and ductility indicating a decrease in ductility with increasing strength. This classical relationship between strength and ductility is based on the fact that most strengthening mechanisms are accompanied by embrittlement on the other hand [81, 82]. For example, the formation of hard but brittle precipitates increases strength at the expense of ductility [58]. For Mg-Al-Ca based alloys, this tendency is more pronounced for alloys with two and more alloying elements but less pronounced for binary alloys. This observation is thought to be a result of the increased occurrence of precipitations for higher alloy compositions leading to a more brittle behaviour in conjunction with higher measured absolute YSs.

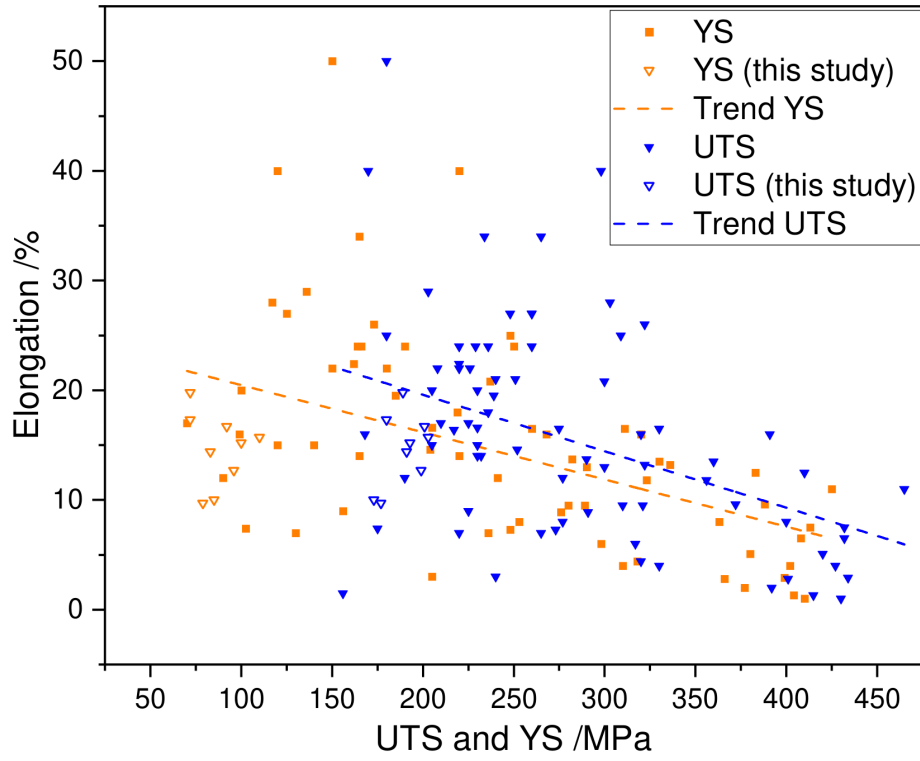


Figure 3.1: Correlation of the elongation with YS and UTS [24, 26, 42, 43, 46, 49, 51, 53, 54, 240, 241, 260–272], including the results of this study [287].

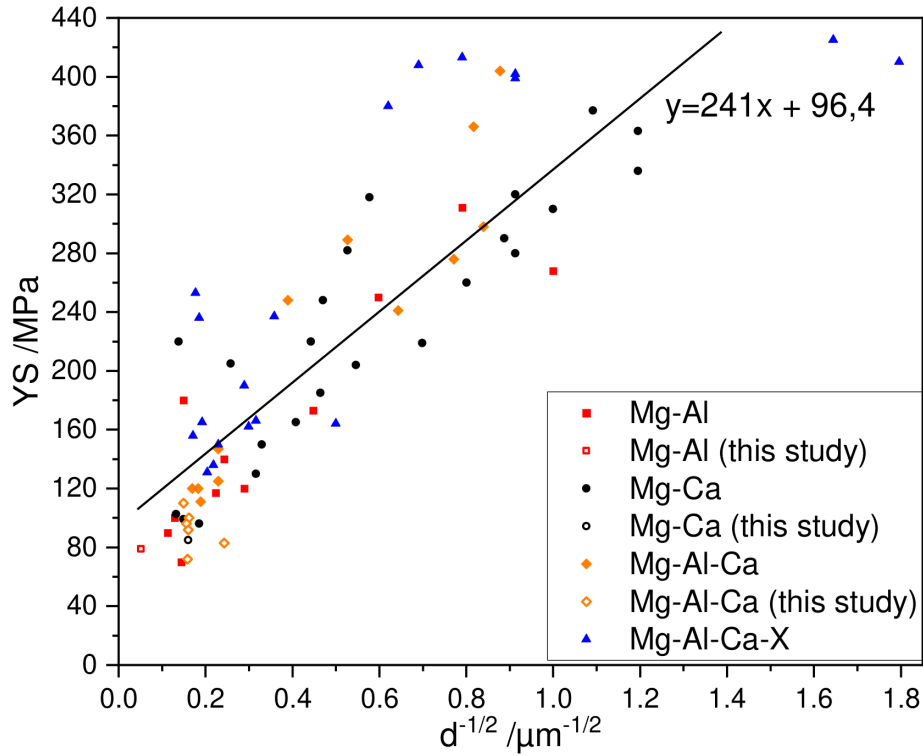


Figure 3.2: Determination of the Hall-Petch constant by linear correlation of the YS and grain size $d^{-1/2}$ for all considered Mg-Al-Ca-X alloys [24, 26, 42, 43, 46, 49, 51, 53, 54, 240, 241, 260–272], including the results of this study [287].

To investigate the influence of the grain size on the YS, all alloys considered and the results of this study were plotted on to a Hall-Petch plot (compare Fig. 3.2). The averaged Hall-Petch constant for all alloys considered, including the results of this study, is $241 \text{ MPa } \mu\text{m}^{1/2}$. Separation of the alloys gives a Hall-Petch constant of $237 \text{ MPa } \mu\text{m}^{1/2}$ for the Mg-Al alloys and $215 \text{ MPa } \mu\text{m}^{1/2}$ for the Mg-Ca alloys. The ternary Mg-Al-Ca alloys have a slightly higher Hall-Petch constant of $332 \text{ MPa } \mu\text{m}^{1/2}$ and the higher order Mg-Al-Ca-X alloys have a slightly lower Hall-Petch constant of $194 \text{ MPa } \mu\text{m}^{1/2}$. Comparable AZ31 alloys processed by rolling with grain sizes between $2\text{-}55 \mu\text{m}$ and $26\text{-}78 \mu\text{m}$ are reported to have Hall-Petch constants of 209 [288] and $228 \text{ MPa } \mu\text{m}^{1/2}$ [289] respectively. Pure Mg processed by extrusion with grain sizes of $4\text{-}63 \mu\text{m}$ has a Hall-Petch constant of $157 \text{ MPa } \mu\text{m}^{1/2}$ [290]. Values for Hall-Petch constants up to $472 \text{ MPa } \mu\text{m}^{1/2}$ have been reported [22, 291]. Grain size can therefore be considered as a strong parameter for adjusting the strength of Mg alloys [289, 292].

The mechanical behaviour of the alloys considered can also be related to the alloy composition. As shown in Fig. 3.3, binary Mg-Al alloys show a tendency for UTS and elongation values to be correlated with composition. In contrast, binary Mg-Ca alloys do not show this behaviour.

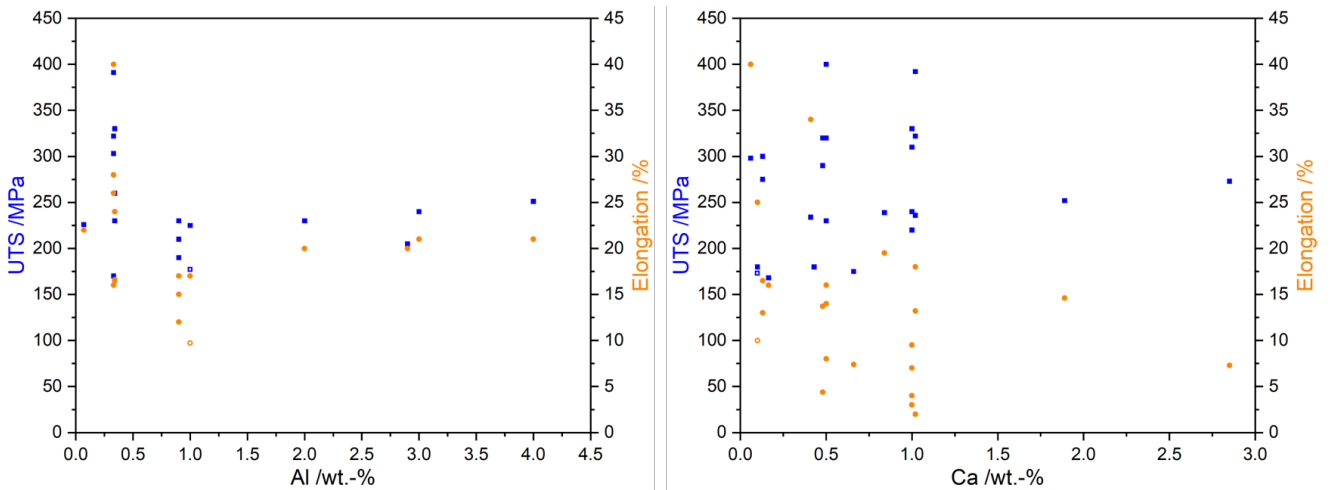


Figure 3.3: Correlation of the UTS and tensile elongation with the alloying content of Al to Mg (left) (filled icons from literature [26, 42, 51, 261–264] and open icons from this study [287]) and Ca to Mg (right) (filled icons from literature [24, 54, 240, 241, 260, 261, 263, 265–267] and open icons from this study [287]).

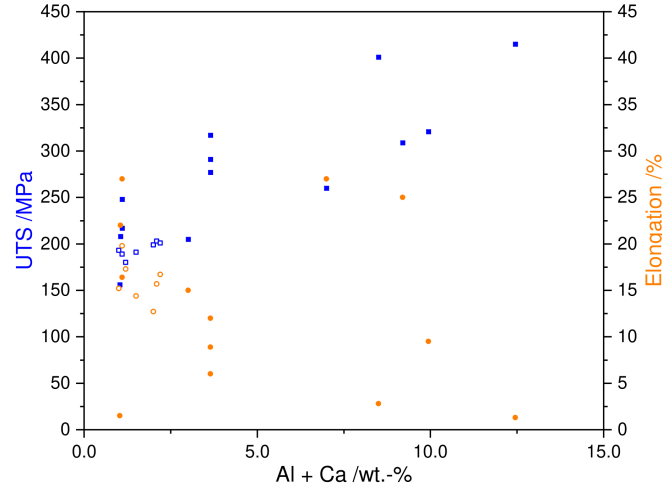


Figure 3.4: Correlation of the UTS and tensile elongation with the alloying content of Mg-Al-Ca alloys (filled icons from literature [43, 46, 51, 260, 271, 272] and open icons from this study [287]).

Fig. 3.4 shows the values of UTS and tensile elongation as a function of the amount of solutes for Mg-Al-Ca alloys showing a difference between low alloyed and high alloy compositions. Specifically, for low alloy compositions the values between UTS and elongation are more correlated than for high alloy compositions. It is suggested that the high YSs and low tensile elongation values are related to the influence of precipitates in high alloy compositions. For low alloy compositions, mainly solid solution strengthening is predominant, resulting in lower strength but also maintaining intermediate tensile elongation values (compare Fig. 3.4).

Texture has also been reported to have a strong influence on the strength and ductility of Mg and Mg alloys [293, 294]. As the texture is mainly developed during processing, a comparison of the resulting texture is not useful. In particular, the lack of publications on solid solution alloys emphasises the need for further investigation. Two main types of texture have been reported: basal type textures, also with peak splitting, and extrusion type textures with $\{10\bar{1}1\}$ parallel to the extrusion direction. Further differentiation with respect to grain size and precipitates would be necessary, but was not pursued due to the limited amount of data. Nevertheless, the wide range of strengths and ductilities can be achieved with both texture types and supports the importance of texture adjustments in alloy development for the Mg alloys investigated.

Much less work has been done on the SIS activity of Mg-Al-Ca alloys. The most fundamental work has been published by Sandlöbes et al. [46], who propose the similarity of the joint alloying of Al and Ca to the sole alloying of Y, thus also allowing higher degrees of non-basal $\langle c + a \rangle$ (see Ch. 1). It is also reported that all types of foreign atoms can increase the probability of non-basal slip due to the change in CRSS anisotropy resulting from the change in dislocation binding energy [295]. The atomic size mismatch could be critical here and an increased activity of non-basal $\langle a \rangle$ and $\langle c + a \rangle$ is also observed for Mg-Zn-Ca in this context with MP compression [296], where Zn has a comparable atomic size to Al and might be transferable to Mg-Al-Ca alloys with respect to the Hume-Rothery rules [297].

4 Research findings of this study

This section presents the research results obtained in this thesis. Particular attention will be paid to the links between these publications and the main conclusions drawn from them.

4.1 Published results of peer-reviewed research and pre-print papers

Based on preliminary results on RE-free Mg-Al-Ca alloys carried out by Sandl bes et al. [46], this thesis aims to continue the investigation of the effects of Al and Ca on the ductility of the wrought material resulting from texture and SFS activity. Starting with seven ternary Mg-Al-Ca alloys, one binary Mg-Al and one binary Mg-Ca all with alloying contents between 0-2 Al and 0-0.5 Ca (see Tab. 4.1, a systematic study was carried out.

Table 4.1: Alloys studied with nominal compositions and chemical analysis (ICP-OES) in wt.-%.

Alloy	Nominal composition	Mg	Al	Ca	Cu	Ni
S1	1Al-0.5Ca	Bal.	1.040	0.524	<0.002	<0.002
S2	1Al-0.005Ca	Bal.	1.080	0.006	0.004	<0.002
S3	1Al-0.1Ca	Bal.	1.040	0.103	<0.002	<0.002
S4	1Al-0.2Ca	Bal.	1.100	0.232	0.002	<0.002
S5	2Al-0.005Ca	Bal.	2.110	0.007	<0.002	<0.002
S6	2Al-0.1Ca	Bal.	2.140	0.113	<0.002	<0.002
S7	2Al-0.2Ca	Bal.	2.120	0.217	0.002	<0.002
S8	0.1Ca	Bal.	0.044	0.108	<0.002	<0.002
S9	1Al	Bal.	1.000	<0.001	<0.001	<0.001

Mainly, in the first publication **”Influence of Al and Ca on the ductility of Mg-Al-Ca alloys”** [287], a comprehensive study of the mechanical properties was presented. Both, tensile and compressive tests were carried out to elucidate the changes in properties due to the chemical difference while maintaining identical processing. The results of the tensile tests are shown in Fig. 4.1. All alloys show improved stress-strain behaviour compared to pure Mg, with the ternary alloys in particular achieving the highest UTSs and elongations. The microstructure was analysed by SE and EBSD to determine grain sizes and precipitation behaviour. The precipitates found in the high Ca sample Mg-1Al-0.5Ca are C36 Laves phases and did not lead to premature failure as previously found to occur with C14 Laves phase precipitates. Grain sizes for all Ca-containing samples were comparable, with only the binary Mg-1Al sample showing larger grains by one order of magnitude.

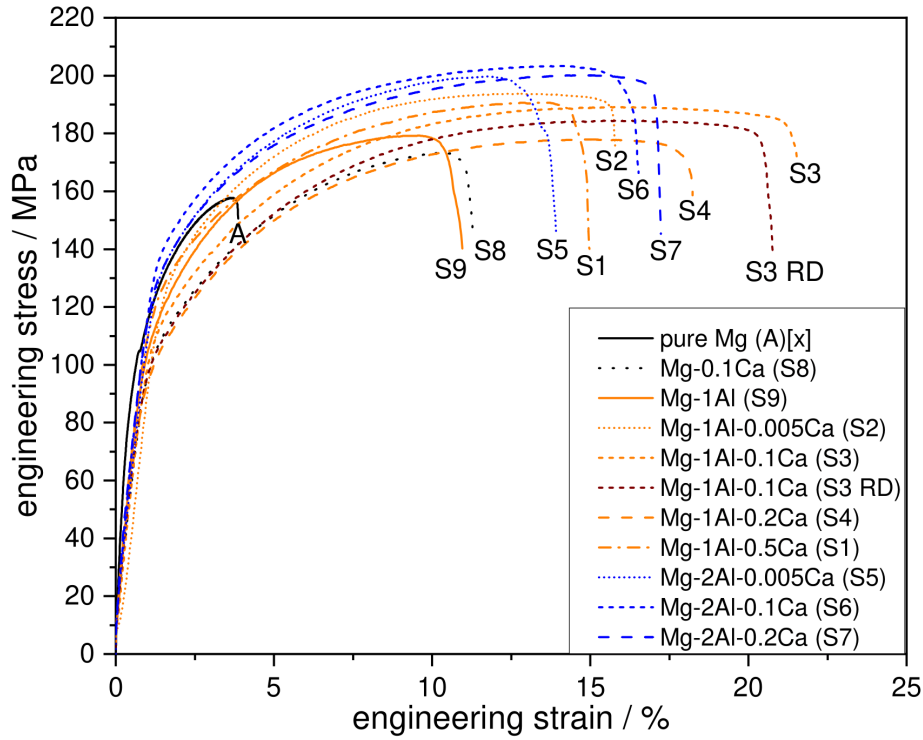


Figure 4.1: Mechanical properties obtained from tensile tests of all investigated compositions [287].

In addition, both active SLSs and texture were examined as important mechanisms for improving ductility. The evaluation of the texture shows a close relationship between the alloying element Ca and the texture formation between the investigated alloys as shown in Fig. 4.2.

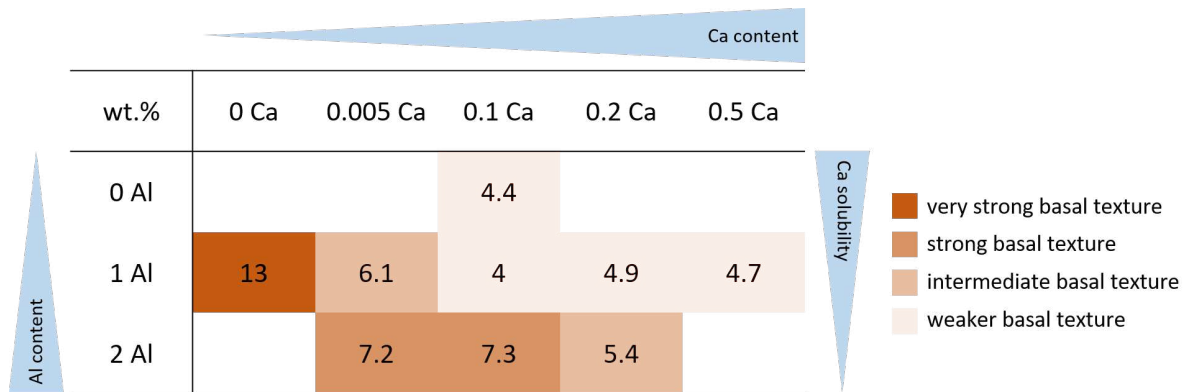


Figure 4.2: Intensities of the (0002)-peak in dependence of the Ca content and its solubility [287].

It is proposed, that the grain pinning effect of Ca found by Nandy et al. [260] not only leads to the intrinsically smaller grain sizes but also prevents the formation of strong basal textures usually observed for Mg sheets. The evaluation of the slip system activity after deformation is done by the examination of the four major slip systems activity per grain and is shown in Fig. 4.3. It can be seen, that an increased activity of non-basal $\langle c + a \rangle$ -slip with an increasing Al content.

As the Al content influences the Ca solubility, a fine tuning of both alloying elements is necessary to benefit from both effects.

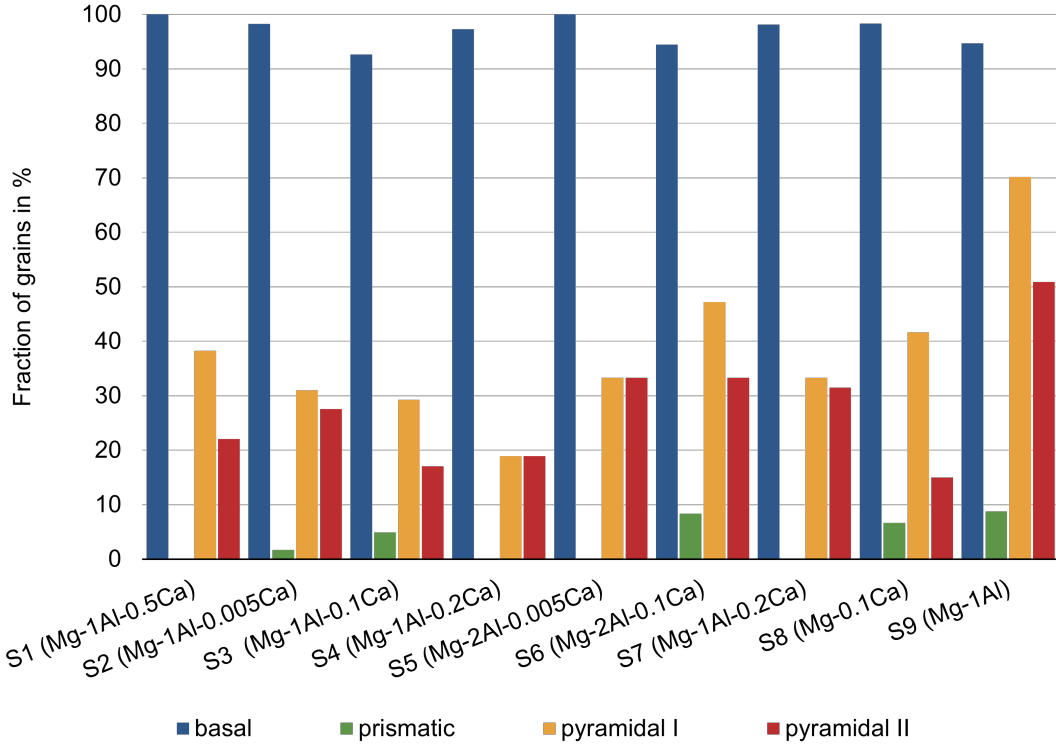


Figure 4.3: Statistic analysis of the activated slip system in each composition [287].

Following from the results of the first publication on the texture-weakening effect of Ca on the basal peak intensity (BPI) of as-RX textures in the ternary Mg-Al-Ca alloys, a more intensive study of texture formation was carried out. Usually Mg alloys show a sharpening of the basal peak during cold rolling, which motivates a deeper analysis. The second publication **”Effect of lean alloyed Al and Ca on the texture development of cold rolled Mg-sheets”** [298] presents the results of the continued systematic investigation of the previously introduced alloys with respect to texture development during cold rolling experiments. Samples were examined both with the normal direction upwards and with the transverse direction facing upwards from the initial rolling direction. The results from the BPI of the samples with the normal direction facing upwards shown in Fig. 4.4 indicate that not only the as-RX textures are influenced by Ca and its solubility, but also the texture development. It has been shown that reduced Ca solubility due to higher Al contents, and hence sharpening of the BPI, can be overcome by increasing Ca content, which is proposed to result from the introduction of larger agglomerations of segregated Ca as obstacles, pinning the GBs observed by Nandy et al. [260].

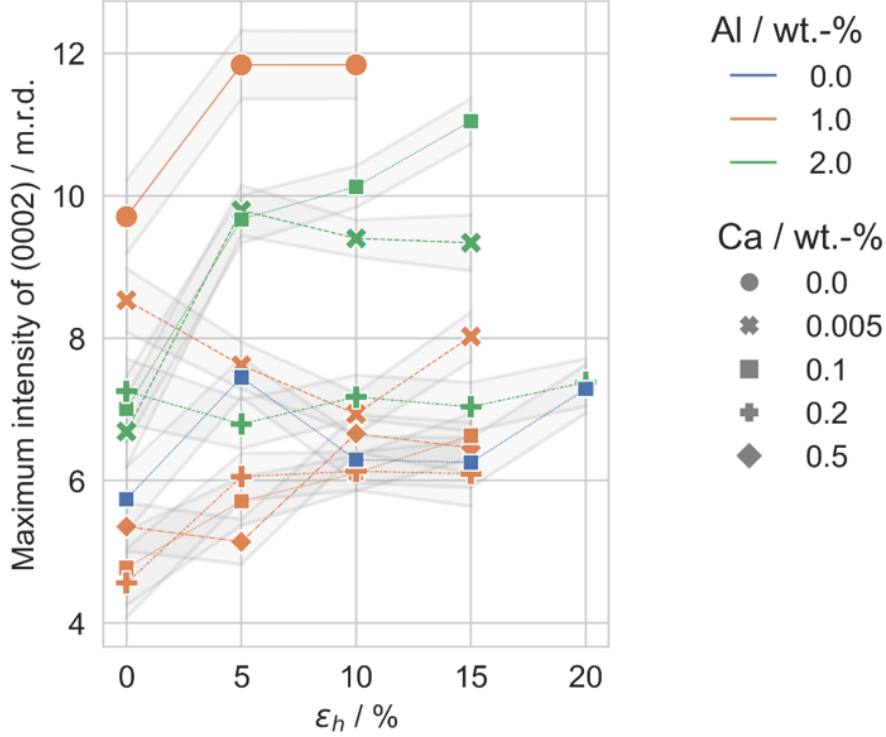


Figure 4.4: Maximum intensities of the basal (0002) peak for samples with basal normal direction related to the relative height reduction (ϵ_h) during cold rolling, including the absolute mean error (published under a Creative Commons CC BY 4.0 license [298]).

It can be seen that by adjusting the Al and Ca content, not only weak as-RX textures but also constant textures can be maintained and thus higher degrees of deformation can be achieved. This is especially true for the samples with basal normal direction. The samples with the off-basal transverse direction show a reorientation of the previously off-basal laying grains to the expected basal orientation.

EBSD measurements in Fig. 4.5 show that this occurs with extensive twinning. The slightly higher degrees of deformation achieved during cold rolling of these samples is proposed to be due to the refinement of the microstructure with smaller grains after twinning, leading to overall weaker textures and allowing more grains to participate in the deformation process with easily activated basal slip. For example the larger grains in the S9 alloy show lower kernel average misorientation values during rolling in with the transverse direction facing upwards (see Fig. 4.5 b)) leading to more inhomogenous strain accommodation and early failure.

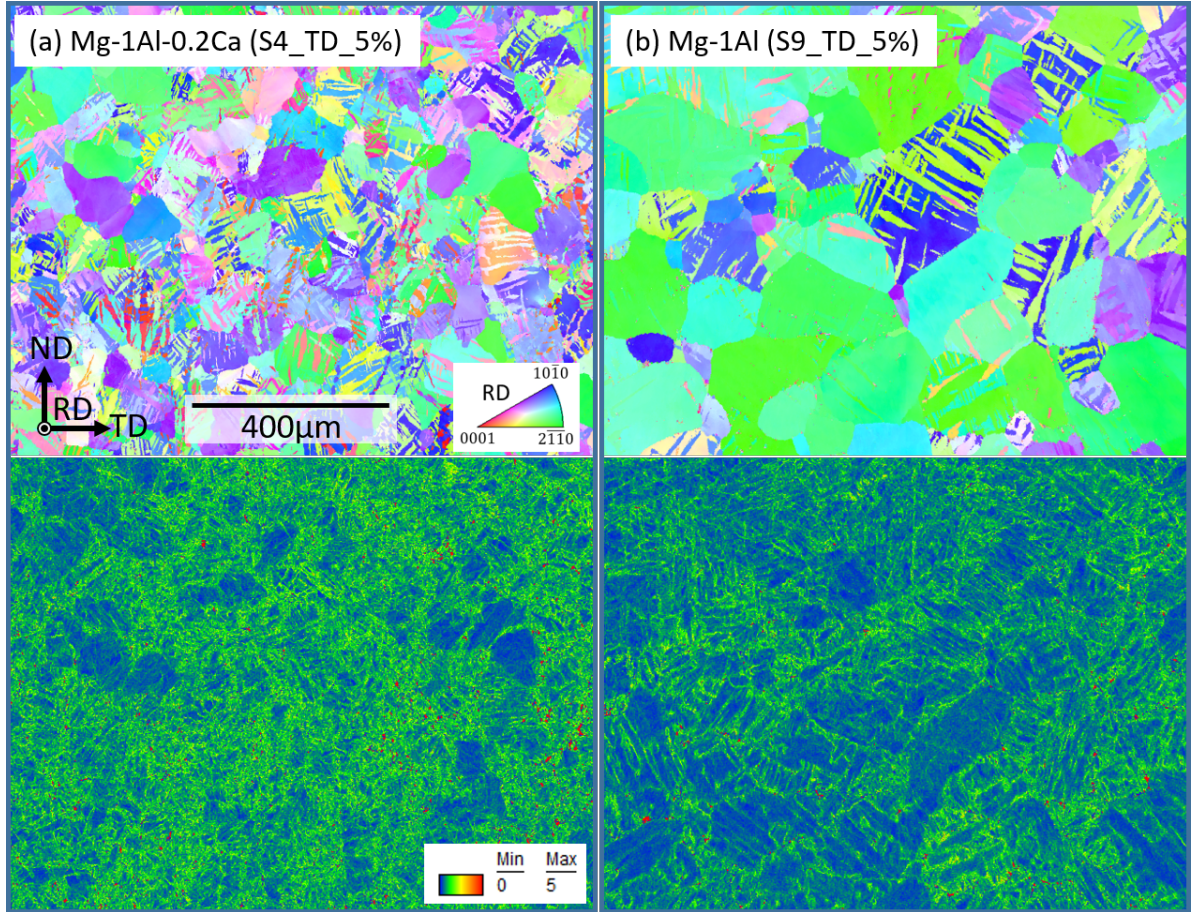


Figure 4.5: (a) S4 alloy with the transverse direction facing upwards cold rolled to 5% height reduction: Top: Inverse pole figure map. Bottom: Kernel average misorientation map. (b) S9 alloy with the transverse direction facing upwards cold rolled to 5% height reduction: Top: Inverse pole figure map. Bottom: Kernel average misorientation map (published under a Creative Commons CC BY 4.0 license [298]).

At the start of the main investigation, a thorough study of the synthesis of the material and the metallographic preparation was necessary. For the synthesis, casting under pressure was found to be essential to avoid casting defects, and longer homogenisation times have effectively minimised elemental homogeneities. The results were combined with results from the same alloying system focusing on the Laves phases and composites containing both Laves phases and solid solution matrix and published as a pre-print in the joint paper **Metallurgical synthesis methods for Mg-Al-Ca scientific model materials** [299]. In the same way, combining metallographic achievements, the publication **Metallographic preparation methods for the Mg based system Mg-Al-Ca and its Laves phases** [300] shows the results of the diverse and complex approaches in the preparation of the material systems, providing an overview of the preparation routes for multiple investigation methods. The solid solution alloy preparation approach stands out, allowing EBSD analysis with good indexing up to months after final preparation, when stored in a desiccator.

4.2 Research results from ongoing investigations

To further investigate the active SIs, MPs were prepared on four alloys with different Al:Ca ratios to calculate the CRSSs for the active SIs. A special effort was made to identify grains with the highest m_s for non-basal SIs [301]. MPs were then cut into differently oriented grains in an attempt to activate these SIs.

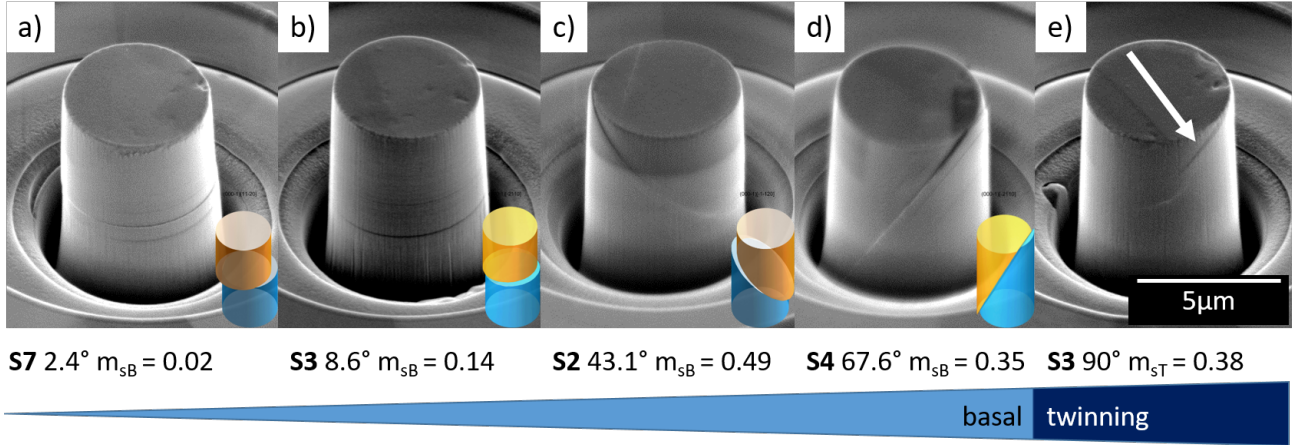


Figure 4.6: Examples of compressed MPs with different off-basal tilt. a) - d) showing basal slip and e) shows twinning indicated with the arrow.

Basal slip was active in all MPs, although basal slip was not expected in MPs with near zero m_s . As a result, for 0-85°tilted grain orientations, only basal slip traces were found on the outside of the MPs, allowing only the basal CRSS to be evaluated (see. Fig. 4.6 a)-d)). A dependence on the Al:Ca ratio was found, resulting in a lower CRSS value for basal slip with a ratio of 10:1 than for 167:1 and 5:1 respectively (compare Tab. 4.2).

Table 4.2: Average CRSSs for basal slip in dependency of the composition and the corresponding Al:Ca ratio.

Al:Ca ratio	1:167	1:10	1:5
	S2: 26.4 ± 1.5 MPa	S3: 7 ± 2.8 MPa	S4: 13.3 ± 3.3 MPa
	S7: 5.8 ± 1.5 MPa		

Further molecular dynamic simulations will be carried out to evaluate this phenomenon and to assess the effect of altered bonding situations due to the alloying elements. For MPs cut in grains with 85-90°off-basal orientation, twinning was found to occur, which is proposed to be caused by a low m_s for twinning (see. Fig. 4.6 e)). A subsequent TEM study of lamellae taken from the MPs showed that non-basal slip was indeed active in all the MPs studied, although it was not visible on the surface of the MPs. This is supported by the fact that $\langle c + a \rangle$ dislocations are found to be mainly stored in the crystal. Exemplary two TEM lamellae taken from of MP with a GB (Fig. 4.7) and a TEM lamella taken from of MP with a TB (Fig. 4.8) are shown.

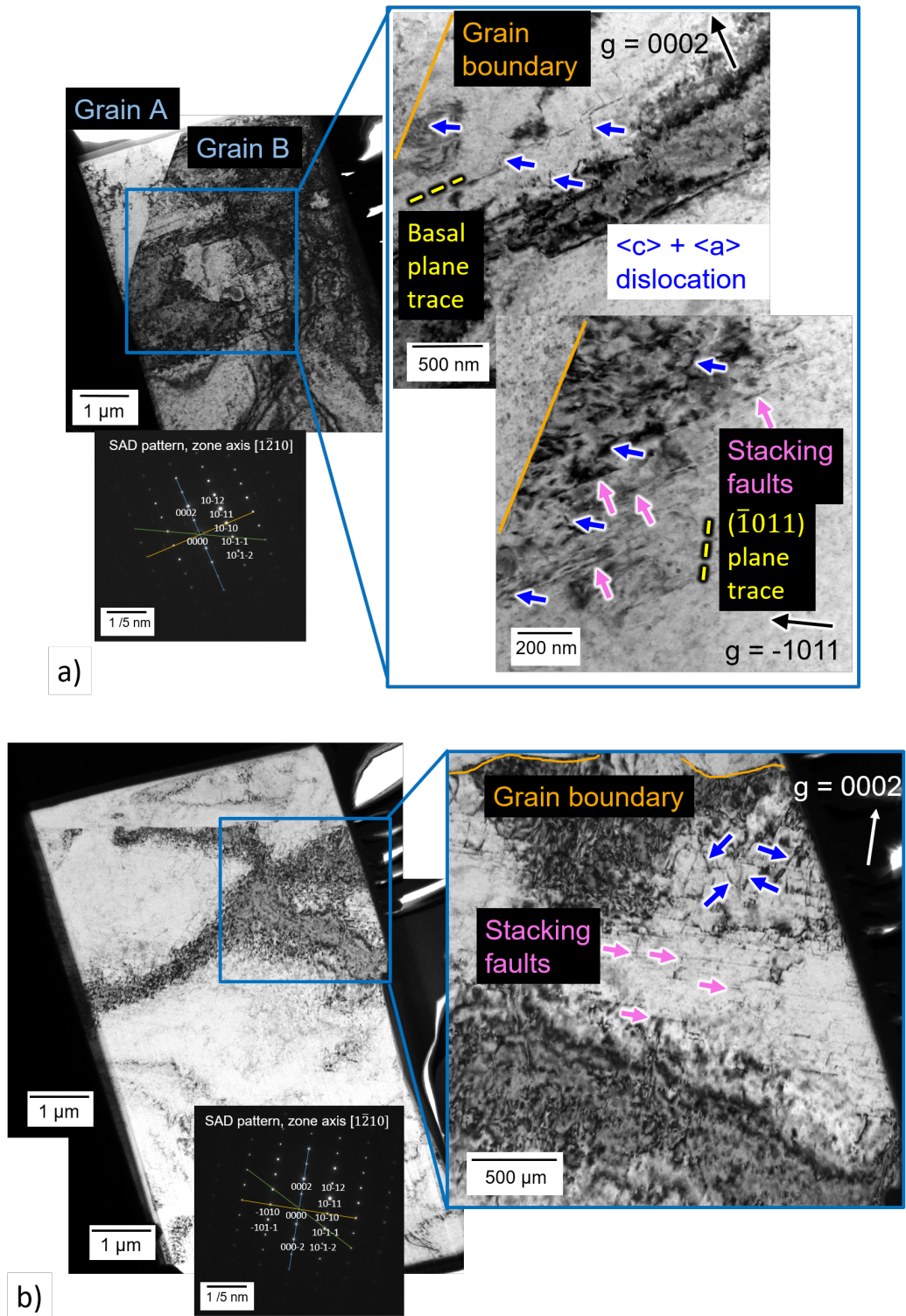


Figure 4.7: Two examples of TEM lamellae taken from MPs exhibiting GBs. a) S4 alloy with 15.1° off c-axis tilt and b) S2 alloy with 77.7° off c-axis tilt. Blue arrows indicate $\langle c + a \rangle$ slip and pink arrows indicating SFs.

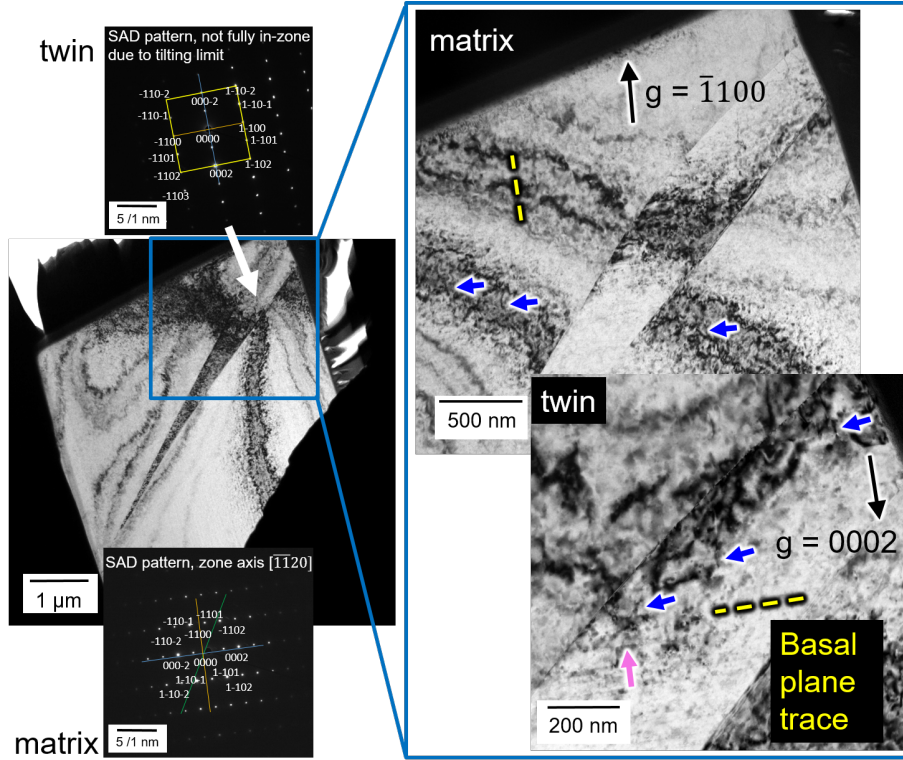


Figure 4.8: Example of a TEM lamella taken from a MP (S3 alloy with 88.6° off c-axis tilt) deformed with twin formation. Blue arrows indicate $\langle c + a \rangle$ slip and pink arrows indicating SFs

It is apparent that although non-basal slip traces are found in all parts of the MPs, a preferential concentration of $\langle c + a \rangle$ slip is found in the vicinity of both GBs and TBs. This suggests a nucleation problem in the matrix. The local inhomogeneous stress and strain fields around the defect may be favourable for the nucleation of $\langle c + a \rangle$ dislocations. A possible interaction between dislocations and both GBs and TBs was also investigated as a support for $\langle c + a \rangle$ dislocation nucleation in the neighbouring grain [187, 215].

To evaluate the activity of $\langle c + a \rangle$ slip and relate it to the nucleation situation APT tips are taken from a selected $\langle c + a \rangle$ slip trace and chemically examined as shown in Fig. 4.9.

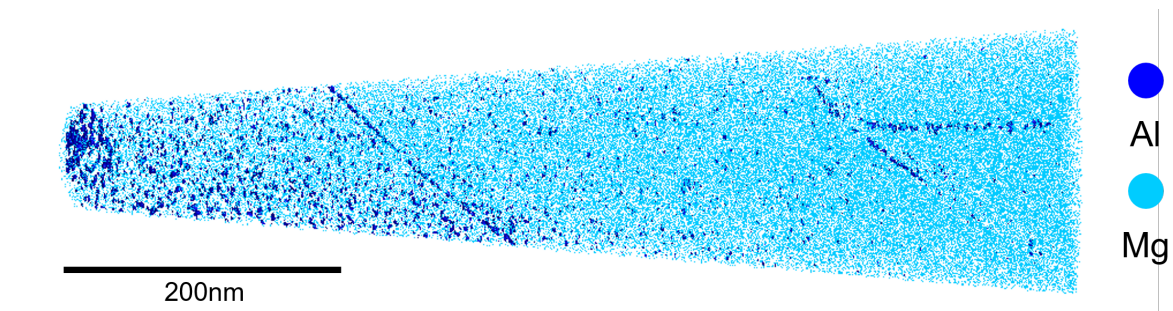


Figure 4.9: Reconstructed APT specimen taken from a 2nd order pyramidal slip line detected during the slip line analysis of the S5 alloy showing the distribution of Al and Mg. Courtesy of Deborah Neuss, Materials Chemistry, RWTH Aachen University.

According to APT, Al is segregated to the slip trace which is supporting the previous finding of a relation of Al to the activity of 2nd order pyramidal slip from the slip line analysis. A consecutive, correlative HR-STEM investigation will soon to be carried out to gain a deeper understanding of the dislocation core of this dislocation type and examine the atoms in the dislocation core. It is assumed that $\langle a \rangle$ dislocations might cross-slip slip planes containing $\langle c + a \rangle$ Burgers vectors when interacting with the distributed Al atoms in the matrix. Also Al segregated to the $\langle c + a \rangle$ dislocation might lead to more stable configuration preventing their dissociation.

5 Conclusions and Outlook

A systematic analysis of wrought lean alloyed binary and ternary Mg-Al-Ca alloys has been carried out. The aim was to investigate the alloying effects of both Al and Ca concerning the mechanical properties and, especially, the RT ductility. Particular attention was paid to dislocation activity and texture formation, along with their associated effects.

The following conclusions can be drawn:

- With identical processing, Ca leads to intrinsic grain refinement through GB pinning.
- The intrinsic grain refinement leads to a weaker basal type texture.
- Cold formability is dependent on the amount and the solubility of Ca in the Mg matrix, which in ternary alloys leads to a co-dependence with Al, as Al reduces the solubility of Ca.
- Very small amounts of Ca (0.005 wt.-%) are sufficient to introduce these effects.
- Al improves the strength of the alloy through solid solution strengthening.
- The presence of Al increases the activity of $\langle c + a \rangle$ dislocations.
- Al shows a preference to segregate to $\langle c + a \rangle$ dislocations probably increasing the stability and hindering the dissociation.
- The CRSS of basal slip in the deformed MPs shows a dependence on the Al:Ca ratio and reaches a minimum at a 10:1 ratio (alloys Mg-1Al-0.1Ca and Mg-2Al-0.2Ca).

The present study shows that Mg-Al-Ca alloys have improved mechanical properties after rolling, especially cold rolling, compared to pure Mg by lean alloying only. It is evident that the influence of Al and Ca on the main ductilisation mechanisms: activation of non-basal $\langle c + a \rangle$ slip and weakening of the basal texture, is complex. The first important contributions that this study adds to the understanding of the Mg-Al-Ca alloy system are the association of Ca with texture formation through grain refinement and weakening of the basal texture (hereafter referred to as the "Ca effect") and the association of Al with the activation of 2nd order pyramidal slip and solid solution strengthening (hereafter referred to as the "Al effect"). Although both elements contribute to the overall performance of the alloy, the dependence of Ca solubility on Al content limits the exploitation of the beneficial aspects of Ca. As the applicability of Mg as a sheet material for light weight applications is particularly limited due to its poor formability at RT, the exceptional improvement in ductility and rollability resulting from the Ca effect is very critical to the overall performance of the alloy. The Al effect then helps to refine the properties. Subsequently, careful tuning of the Al:Ca ratio should be of great interest in order to maximise the Ca effect while maintaining the Al effect. With regard to the effect of Ca on the stability of the microstructure, a lower limit should be set for the required Ca content. Here the dependence on the Al content has to be taken into account and comparisons with binary Mg-Ca with as low Ca contents as for the ternary alloys have to be made. In general, it may be interesting to explore the gap between 0.005 and 0.1 wt.-% Ca for the ternary alloys in this context. Furthermore, it may be beneficial to include a Mg-2Al alloy in future studies, both to further analyse the effect of Al on

the activity of non-basal slip, and to draw further conclusions on the co-dependency of Al and Ca on texture development. The influence and effect of lean alloying elements and the purity of the raw material should be carefully considered and evaluated when reviewing the literature and in future experiments.

In this study it remained unclear how Al supports the activation of 2nd order pyramidal slip, which is necessary to understand and improve of the alloy system. Therefore, further HR-STEM investigations are required to understand the local chemistry and structure of the Al segregations found at $\langle c + a \rangle$ dislocations. In particular, a detailed understanding of the $\langle c + a \rangle$ dislocation core is necessary to learn more about the stability of this slip system, which is required to assess the effect of Al addition. This will also be of great interest for simulations, which are essential for further improvements of the ductility and investigations with regard to the inclusion of other alloying elements.

During the study of the MPs it became clear that the GBs, as defect structures, are important as possible nucleation sites for SFs and consequently for $\langle c + a \rangle$ slip, since in their vicinity the concentration of $\langle c + a \rangle$ slip is much higher than in the matrix. The strain fields around them have not been much studied, but their contribution to the nucleation mechanism has been clearly proposed [187, 215], which can be supported by the results of this study. Understanding the local strain field at the GBs and the support of the alloying elements segregated there is also of great interest, especially to assess the influence of $\langle c + a \rangle$ slip nucleation at the GB or in the matrix. Simulations and high-resolution methods such as high-resolution transmission kikuchi diffraction or high-resolution EBSD may be useful here. During the cold rolling of transverse direction facing upwards samples, it was evident that the rotation of the texture to basal-type occurs with twinning. The clarification of the importance of the nucleation site could clarify here how much the weakened texture and the activated basal slip and how much the increased number of GBs with increased $\langle c + a \rangle$ slip nucleation sites contribute to the achieved higher degrees of height reduction. This may lead to new design approaches in the field of Mg-based alloys.

The access to CRSSs for slip systems other than basal during the MP study was not successful in this work and only provided indications leading to the assumption of a reduced CRSS anisotropy. This method is therefore not ideal and advanced simulations are likely to be more reliable. Nevertheless, it is clear from the sequential TEM analysis that many $\langle c + a \rangle$ dislocations are stored in the material throughout the deformed region. It may be interesting to further investigate the effect of the number of the $\langle c + a \rangle$ dislocations in the volume on the ductility of the material. This may also identify further areas for improvement of the ductility.

This work provides a fundamental understanding of the Mg-Al-Ca alloy system and fills gaps in the understanding of the underlying mechanisms resulting from the two alloying elements Al and Ca in Mg. However, the promotion of its applicability as a light weight sheet material with promising mechanical properties depends on the design of the optimum alloying contents of Al and Ca and the understanding of the mechanisms behind the $\langle c + a \rangle$ dislocation activation for further alloy development.

Publication 1

Influence of Al and Ca on the ductility of Mg-Al-Ca alloys

W. J. Delis, P. C. Huckfeldt, B. Hallstedt, P.-L. Sun, D. Raabe,
S. Korte-Kerzel, S. Sandlöbes-Haut

2024, Advanced Engineering Materials

<https://doi.org/10.1002/adem.202301071>

For this publication, the candidate (in collaboration with Pia Huckfeldt as part of her bachelor's thesis supervised by the candidate) performed all the experiments except the thermodynamic calculation and TEM analysis, and evaluated and analysed the results. In collaboration with the co-authors, the candidate wrote the original manuscript as well as the final reviewed version.

RESEARCH ARTICLE

Influence of Al and Ca on the Ductility of Mg–Al–Ca Alloys

Wassilios J. Delis,* Pia C. Huckfeldt, Bengt Hallstedt, Pei-Ling Sun, Dierk Raabe, Sandra Korte-Kerzel, and Stefanie Sandlöbes-Haut

Magnesium and its alloys offer huge potential for lightweight applications. However, many Mg alloys suffer from limited room-temperature formability. It has previously been shown that the addition of aluminium and calcium to Mg can improve ductility. Therefore, in the present work, it is aimed to systematically vary the alloying content of Al and Ca and to study their effects on the slip system activity and crystallographic texture after rolling and recrystallization. In the results, it is shown that all investigated ternary alloys in the range of 1–2 wt% Al and 0.005–0.5 wt% Ca have an increased ductility (in the range of 10–17% increase compared to pure Mg), whereas the binary Mg–Al and Mg–Ca alloys suffer from limited ductility (10% tensile elongation) and strength (175 MPa ultimate tensile strength). Non-basal and especially $\langle c + a \rangle$ -slip is active in all compositions (in 15–33% of the grains examined). Basal-type textures are observed for all compositions, but with significantly weaker basal peak intensities for Ca-containing samples when compared to pure Mg. The combination of activation of the $\langle c + a \rangle$ slip system and texture weakening is discussed as being responsible for the improved ductility of the ternary Mg–Al–Ca alloys.

1. Introduction

Magnesium (Mg) and its alloys are the lightest structural materials. The use of Mg sheet material is limited due to its low room-temperature ductility, whereas cast alloys are widely used.^[1] The demand for lighter materials in the automotive and

aerospace industries has generated considerable interest in the development of Mg-wrought alloys, particularly in view of the dramatic increase in the weight of electric vehicles.^[2] Considering that a sport utility vehicle now weighs around 3 tonnes, lightweight materials are needed in addition to lightweight design. In particular, due to the limited room-temperature ductility of pure Mg of only 3% tensile elongation,^[3] forming and machining of wrought Mg alloys is still a barrier for most applications.^[4,5] The deformation of Mg and its alloys is mainly realized by basal $\langle a \rangle$ slip and tensile twinning as the critical resolved shear stress (CRSS) of the other slip and twinning systems is significantly higher (up to 100 times).^[6] This predominant activation of basal slip in conjunction with extension twinning results in the formation of basal textures during rolling.^[7] Activation of non-basal slip systems, in particular $\langle c +$


$a \rangle$ slip, can improve the room-temperature ductility by allowing strain accommodation along the crystal c -axis, that is not possible when only $\langle a \rangle$ dislocations are active. Over the last decades, several approaches such as microstructure optimization (grain refinement^[8,9] and second-phase precipitates^[10]) and advanced processing (extrusion^[11,12] and asymmetric forming^[13]) have been pursued to improve the ductility of Mg. Further research has focused on improving the intrinsic ductility with the aim of increasing the room-temperature formability of Mg alloys. Two main strategies for increasing room-temperature ductility have been identified.^[4,7,14–17] First, activation of non-basal slip systems to satisfy the von Mises criterion (i.e., activation of five independent slip systems in the single-crystal yield surface) and allow arbitrary shape changes that are not possible by basal slip alone.^[4,14] Second, softening of the strong basal-type texture allows basal slip in more grains and also allows the activation of non-basal slip systems due to their higher resolved shear stresses, both of which contribute to improved formability.^[7,15–17]

Previous research has shown that alloying of Mg up to a few wt% with rare-earth (RE) elements,^[18–21] lithium (Li),^[22–24] and yttrium (Y)^[25,26] can significantly improve the intrinsic ductility. In these papers, the authors reported increased activity of non-basal slip.^[18–26] However, the RE elements, Li and Y, are costly, require complex processing, and have a poor recyclability, making such alloy variants unsustainable and commercially unviable. Therefore, research on other possible alloy compositions has been investigated. Ternary alloys with Mg–Zn–Ca^[27–30] have been reported to exhibit improved ductility, as have Mg–Al–Ca

W. J. Delis, P. C. Huckfeldt, P.-L. Sun, S. Korte-Kerzel, S. Sandlöbes-Haut
Institute for Physical Metallurgy and Materials Physics
RWTH Aachen University
52074 Aachen, Germany
E-mail: delis@imm.rwth-aachen.de

B. Hallstedt
Institute for Materials Applications in Mechanical Engineering
RWTH Aachen University
52062 Aachen, Germany

D. Raabe
Department of Microstructure Physics and Alloy Design
Max-Planck Institut für Eisenforschung
40237 Düsseldorf, Germany

 The ORCID identification number(s) for the author(s) of this article can be found under <https://doi.org/10.1002/adem.202301071>.

© 2023 The Authors. Advanced Engineering Materials published by Wiley-VCH GmbH. This is an open access article under the terms of the Creative Commons Attribution-NonCommercial-NoDerivs License, which permits use and distribution in any medium, provided the original work is properly cited, the use is non-commercial and no modifications or adaptations are made.

DOI: 10.1002/adem.202301071

alloys.^[3,29,31] Solid solution Mg–Al–Ca ternary alloys have been found to give similar properties to Mg–RE, Mg–Li, and Mg–Y alloys, but the underlying dislocation slip mechanisms are still unclear.^[3]

Therefore, in the present study, we investigated the activation of slip systems in binary and ternary Mg–Al–Ca with varying amounts of Al and Ca to contribute to a better understanding of the influence of Al and Ca on the texture and slip system activation. Tensile and compression testing, X-ray diffraction (XRD), electron backscatter diffraction (EBSD), and EBSD-assisted slip line analysis were used.

2. Experimental Section

All alloys were cast and then hot-rolled to a total thickness reduction of 50%. Casting was performed in an induction furnace under Ar atmosphere and pressure with elemental Mg, Al, and Ca (all >99.98% purity). Hot-rolling was carried out in steps of 10% thickness reduction at 430 °C with 10 min reheating in between followed by a recrystallization treatment at an annealing temperature of 450 °C for 15 min and water quenching.

An overview of the alloys studied in this work is given in **Table 1**. All compositions are in wt%, unless otherwise stated.

Thermodynamic calculations of the Mg–Al–Ca system were carried out using Thermo–Calc software^[32] and the database of Janz et al.^[33] This was done to investigate the solubility ranges of the alloying elements and to observe the precipitation behavior in the Mg-rich corner of the ternary-phase diagram.

Samples for mechanical testing were cut from the sheets (initial thickness between 11.9 and 13.4 mm) by electrical discharge machining. Tensile tests were performed in the transverse direction (TD) direction using flat specimens with a gauge length of 10 mm and a constant cross section of 1.88×1.50 mm (width \times thickness). Tensile tests were performed under strain control on an electromechanical testing machine (DZM) at an initial strain rate of 10^{-3} s^{-1} . Compression test specimen had a cylindrical geometry with a height of 9 mm and a cross section of 6 mm, i.e., an aspect ratio of 1.5. Compression tests were also performed in TD using a ZWICK 1484 universal testing machine with an initial strain rate of 10^{-3} s^{-1} . A minimum of three specimens per composition and test mode were tested.

Table 1. Nominal compositions and chemical analysis measured by inductively coupled plasma optical emission spectrometry (ICP-OES) with impurities of the investigated compositions. All compositions are in wt%.

Sample	Nominal composition	Mg	Al	Ca	Cu	Ni
S1	1Al–0.5Ca	Bal.	1.040	0.524	<0.002	<0.002
S2	1Al–0.005Ca	Bal.	1.080	0.006	0.004	<0.002
S3	1Al–0.1Ca	Bal.	1.040	0.103	<0.002	<0.002
S4	1Al–0.2Ca	Bal.	1.100	0.232	0.002	<0.002
S5	2Al–0.005Ca	Bal.	2.110	0.007	<0.002	<0.002
S6	2Al–0.1Ca	Bal.	2.140	0.113	<0.002	<0.002
S7	2Al–0.2Ca	Bal.	2.120	0.217	0.002	<0.002
S8	0.1Ca	Bal.	0.044	0.108	<0.002	<0.002
S9	1Al	Bal.	1.000	<0.001	<0.001	<0.001

Samples for scanning electron microscopy (SEM) were first mechanically ground, then polished to 0.25 μm with diamond paste and finally electropolished using Struers AC2 electrolyte. An SEM (Zeiss LEO1530) equipped with an EBSD detector (Oxford Instruments plc/HKL) was used for grain size measurement.

Pole figures were collected with a Bruker D8 Advanced X-ray goniometer using a $\text{FeK}\alpha$ target. The XRD samples were mechanically ground and then polished to 3 μm with diamond paste. Measurements were made in the normal direction (ND)–TD–plane on an area of $6 \times 6 \mu\text{m}^2$ (S1–S8) and $10 \times 10 \mu\text{m}^2$ (S9). For the calculation of the orientation distribution function, a value of 3.5° was used for both for half-width and resolution. The pole figures were then rotated to the rolling direction (RD)–TD–plane to examine the (0002)-peak intensities.

Slip line analysis was performed in the ND–TD–plane on compressed cuboidal specimens ($1 \times 1 \text{ cm} \times$ sheet thickness), which have a flat surface parallel to the direction of loading and allow metallographic preparation for suitable slip line investigation. The preparation surface to be analyzed was identical to that used for SEM specimens. Compression was applied normal to RD until a total plastic deformation of $\approx 3\%$ was achieved. The process was strain controlled using an initial strain rate of 10^{-3} s^{-1} on a ZWICK 1484 universal testing machine. Secondary electron (SE) images and EBSD maps for slip line analysis were obtained using a dual-beam SEM-focused ion beam (FIB) (Helios Nanolab 600i, FEI, Eindhoven, NL). For better contrast, both, the SE images and EBSD maps, were acquired under at angle of 70° . Tilt correction was used to transform the images and maps to 0° (unprojected) dimensions. The SE images were acquired at 15 kV acceleration voltage, 1.4 nA current and $1000\times$ (S1–S8) and $500\times$ (S9) magnification. Due to distortions, the EBSD maps were taken at $800\times$ (S1–S8) and $420\times$ (S9) magnification at 20 kV acceleration voltage, 5.5 nA current, and using a step size of 0.7 μm (S1–S8) and 1 μm (S9). The reason for using different parameters for alloy S9 is the significantly larger grain size in S9. For each alloy, three areas of the surface were analyzed and visible slip lines were correlated to the corresponding slip system.

Precipitates that formed in alloy S1 were characterized by transmission electron microscopy (TEM) on samples that were prepared site-specifically using FIB. Measurements were made using a Jeol JEM-F200 operated at 200 kV.

Data post-processing was performed using the MTEX package for MatLab,^[34] and OIM Analysis 8 from EDAX and ATEX.^[35]

3. Results

3.1. Thermodynamic Modeling

Prior to the experiments, Thermo–Calc was used with the database from Janz et al.^[33] to calculate the solubility limits of Ca in Mg in the presence of Al. This database is widely used for Mg alloys alloyed with Al and Ca and has been shown to have a high accuracy for Mg-rich alloys, including the solubility limits of the Mg matrix. In the Mg–Al–Ca system, intermetallic Laves phases can form, of which the cubic C15 CaAl_2 , the hexagonal C14 CaMg_2 , and the hexagonal C36 $\text{Ca}(\text{Mg},\text{Al})_2$ phases have been mainly studied and can form in the Mg-rich corner.^[36–40]

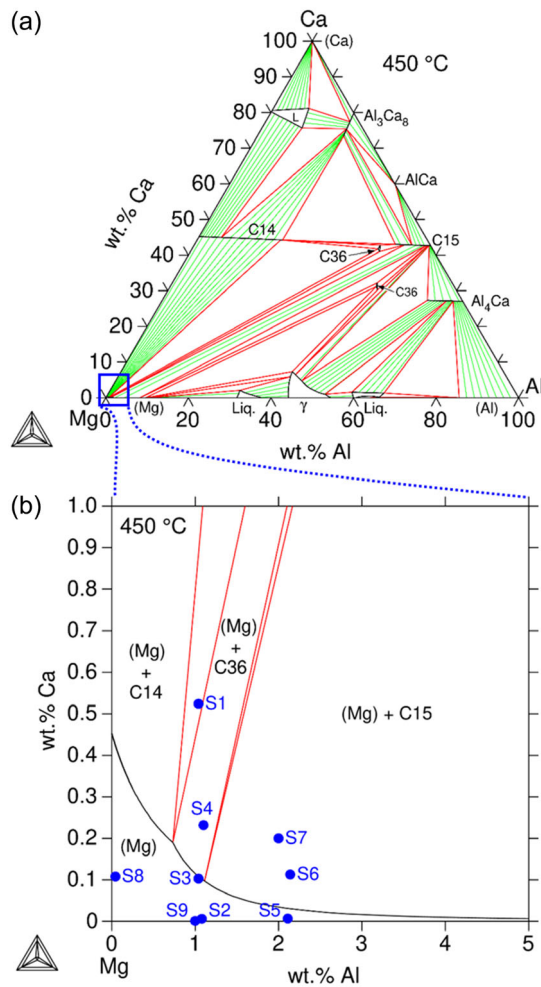


Figure 1. a) Calculated isothermal section of the Mg–Al–Ca system at 450 °C using Thermo–Calc and the data from Janz et al.^[33] and b) the Mg-rich corner of the 450 °C isothermal section showing the compositions of the investigated alloys. S1–S9: selected alloy compositions for this study (see details in Table 1, Figure 2 and 3).

However, the stability range of the C36 phase in Mg-rich alloys is still unclear. **Figure 1** shows a) the calculated isothermal section at 450 °C and b) the Mg-rich corner including the compositions of the investigated alloys.

As can be seen in Figure 1b, the solubility of Ca decreases with increasing amount of Al. This has already been observed by Jo et al.^[41] Considering the compositions studied, S2 (Mg–1Al–0.005Ca), S5 (Mg–2Al–0.005Ca), S8 (Mg–0.1Ca), and S9 (Mg–1Al) are expected to be single phase (Mg) solid solution alloys. S3 (Mg–1Al–0.1Ca) is very close to the solubility limit. S6 (Mg–2Al–0.1Ca) and S7 (Mg–2Al–0.2Ca) are above the solubility limit and could contain C15 precipitates, while S4 (Mg–1Al–0.2Ca) may contain C36 precipitates and S1 (Mg–1Al–0.5Ca) may contain both C14 and C36 precipitates. However, it should be noted that all compositions are very close to the solubility limit and, except in alloy S1 (Mg–1Al–0.5Ca), we have not observed precipitates using SEM and TEM. Alloys S4, S6, and S7 should form very few precipitates as shown in Figure 1. Ca has a strong tendency

to segregate to grain boundaries and dislocations, so that the apparent Ca solubility may be higher than the true equilibrium solubility, particularly if the grains are fine, or the dislocation density is high. It is possible that these alloys are close enough to the solubility limit not to form precipitates within the time available during annealing at 450 °C.

3.2. Mechanical Testing

Mechanical characterization of the alloys was carried out using tensile (**Figure 2**) and compression (**Figure 3**) tests. For clarity, only one representative tensile and compression test curve per alloy is shown in Figure 2 and 3, respectively. However, at least

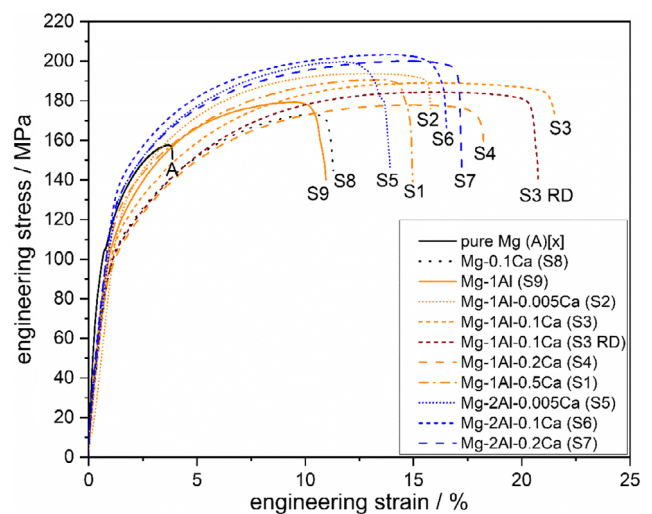


Figure 2. Mechanical properties obtained from tensile tests of all investigated compositions including pure Mg as reference material indicated with [X] taken from ref. [3].

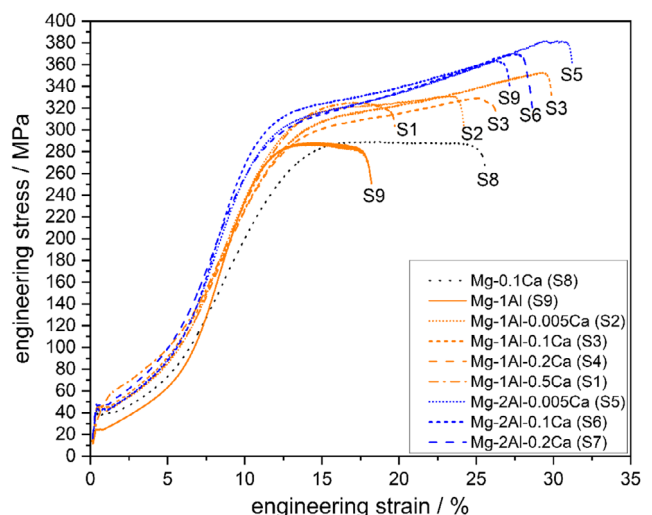


Figure 3. Mechanical properties obtained from compression tests of all investigated compositions.

three specimens per alloy have been tested in both tension and in compression and all show similar results. Also included is the stress–strain curve of pure Mg taken from a previous study,^[3] showing very low ductility.

All the samples examined in this study, including those alloys that may contain precipitates, experience higher ductile deformation than pure Mg with tensile elongations not less than 10%. However, when comparing the binary and the ternary alloys, it is evident that the ternary alloys show significantly higher elongations than the binary alloys. Composition S3 (Mg–1Al–0.1Ca) showed the highest tensile elongations of more than 20%. The ultimate tensile strength (UTS) ranges from 172 MPa for S8 (Mg–0.1Ca) to 203 MPa for S6 (Mg–2Al–0.1Ca). As the amount of Al increases, so does the UTS. The yield strength of all alloys is approximately 87 MPa. Uniform strain and true fracture strain are close to each other for all alloys investigated. The amount of necking observed is small, resulting in a rapid loss of work hardening near the fracture point. No significant differences in the stress–strain behavior were found between RD and TD tensile specimens (evaluated as an example for S3 [Mg–1Al–0.1Ca]) (see Figure 2). Similar mechanical properties have previously been reported for a Mg–1Al–0.1Ca alloy.^[3]

In addition to tensile tests, compression tests were also carried out, particularly to avoid early failure due to a relatively high level

of oxide inclusions resulting from the laboratory-scale synthesis of the alloys. The results are shown in Figure 3.

All ternary samples show an ultimate compressive strength (UCS) above 300 MPa. S5 (Mg–2Al–0.005Ca) has the highest UCS at nearly 400 MPa reaches the highest UCS. The binary compositions S8 (Mg–0.1Ca) and S9 (Mg–1Al) both have a UCS of 287 MPa, which is slightly lower than that of the ternary alloys. Furthermore, the compressive strain ranges between 15% and 28%. Binary S9 (Mg–1Al) has the lowest compressive strain. The yield strength is ≈ 42 MPa for S1–S8 and 22 MPa for S9. All the compression test curves have the characteristic hump leading to an s-shaped curve, which has been reported previously in the literature.^[42,43]

3.3. Microstructure Analysis

To study only compositional effects, synthesis and processing parameters (casting conditions, rolling degree, recrystallization temperatures, and times) were kept identical for all samples. The microstructure of all samples shows no porosity and a small ($<0.5\%$ by volume), homogeneously distributed number of oxide inclusions (see Figure 4).

The grain sizes calculated from EBSD for the samples S2–S8 are $40\ \mu\text{m} \pm 5\ \mu\text{m}$ and are therefore also comparable with a

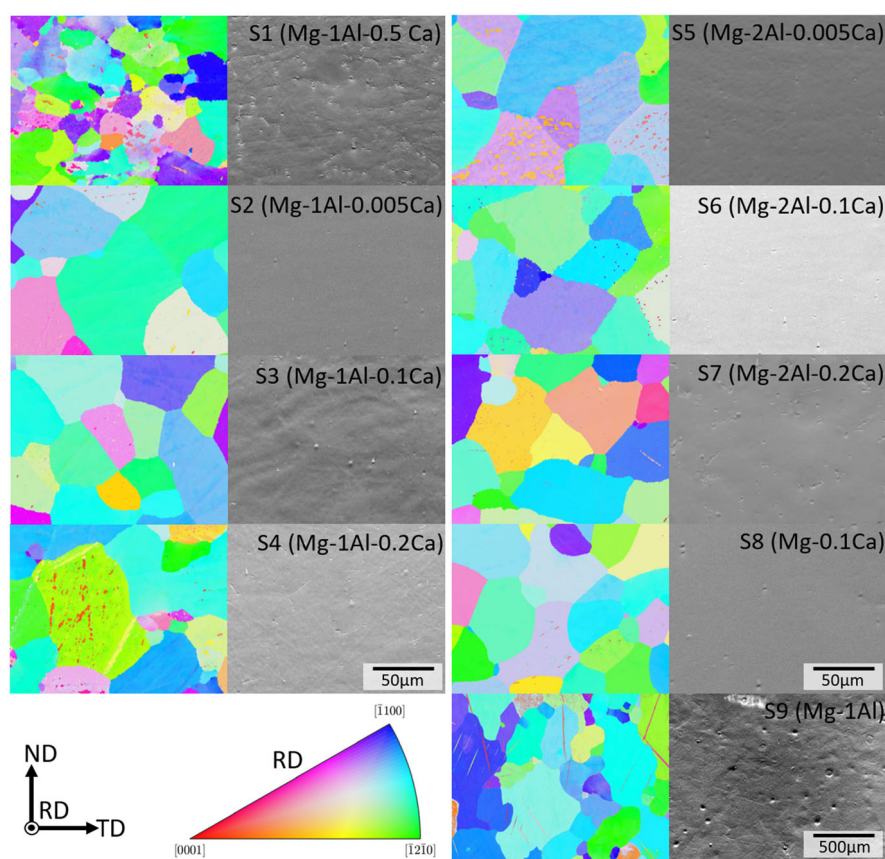


Figure 4. Representative electron backscatter diffraction (EBSD) map (left) and secondary electron (SE) image (right) of the normal direction–transverse direction–plane for each alloy with the corresponding inverse pole figure (IPF) color legend. The scale is identical for alloys S1–S8, but different for alloy S9 due to larger the grain size.

previous study on Mg–Al–Ca.^[3] Exceptions are on the one side composition S1 (Mg–1Al–0.5Ca) with the highest Ca content, which shows reduced grain sizes of about $17\ \mu\text{m} \pm 14\ \mu\text{m}$, and on the other side S9 (Mg–1Al) without Ca, which shows significantly coarser grain sizes of about $381 \pm 222\ \mu\text{m}$. Taking this into account, we have increased the areas examined for the S9 (Mg–1Al) composition to maintain comparability in terms of the number of grains further characterized.

While alloys S2–S9 are at or very close to the solubility limit, alloy S1 contains a higher amount of Ca (0.5 wt%) and is likely to form Laves phase precipitates. Therefore, SEM,

energy-dispersive X-ray spectroscopy (EDS) and TEM were used to investigate the presence and nature of precipitates in S1 (Mg–1Al–0.5Ca). A TEM lamella was taken from the area marked by the rectangle in Figure 5a and subjected to EDS analysis (Figure 5b) and TEM diffraction (Figure 5c). Both methods show the presence of fine C36 Laves phase precipitates.

3.4. As-Recrystallized Textures

During rolling and subsequent recrystallization, Mg and most Mg alloys develop a basal texture^[44,45] which affects the

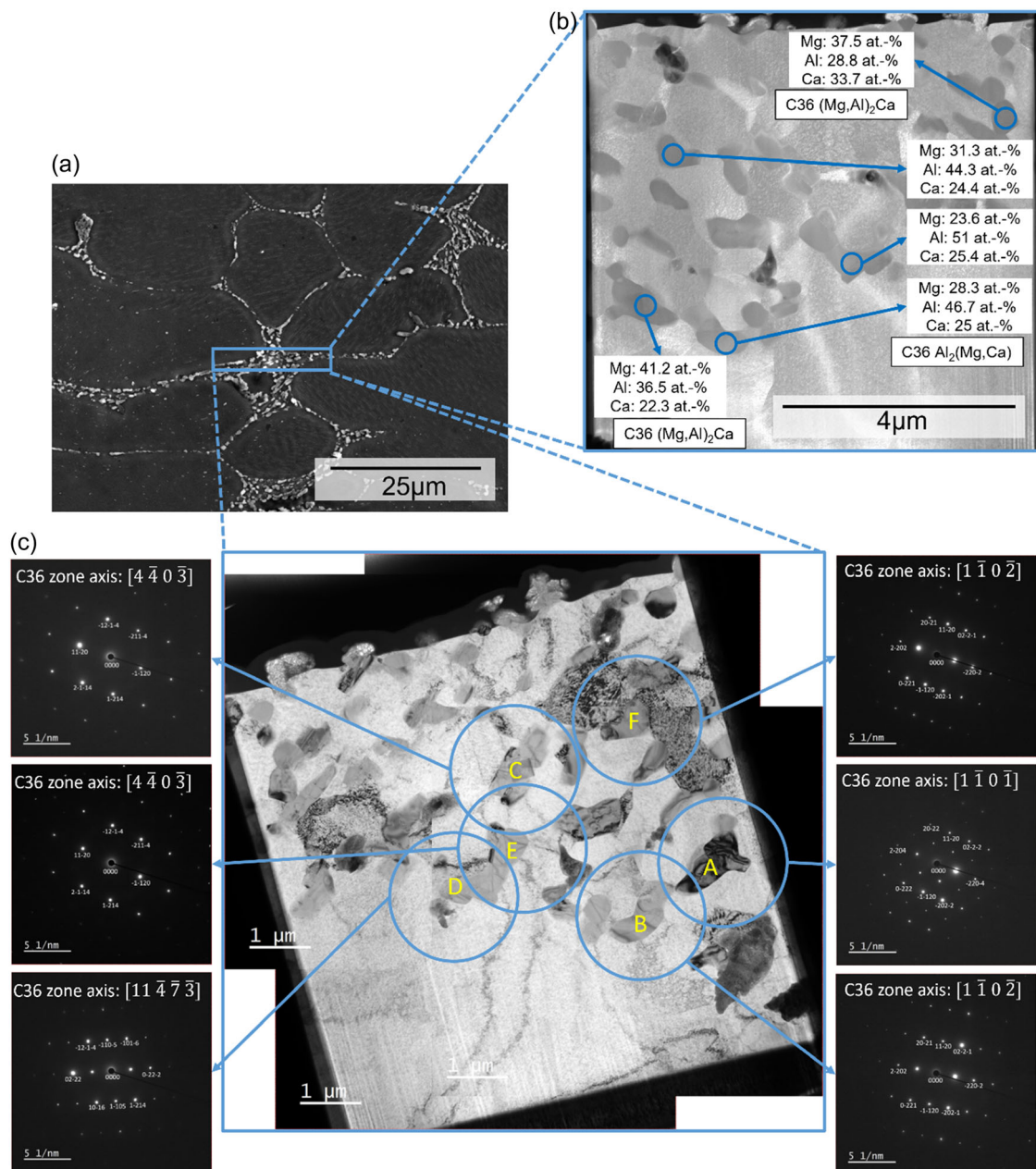


Figure 5. a) SE image of the S1 composition taken at 10 kV and 4.0 mm working distance (WD). Marked area for transmission electron microscopy (TEM) lamella extraction, b) scanning transmission electron microscope image taken at 30 kV and 6.0 mm WD, including energy-dispersive X-ray spectroscopy point measurements of different precipitates, and c) TEM image with diffraction patterns of selected precipitates (A–F) and zone axis showing the presence of the C36 phase.

subsequent forming processes. To investigate the relationship between texture-activated deformation mechanisms and the mechanical properties, texture measurements were carried out. **Figure 6** shows the (0002) and $\{10\bar{1}0\}$ pole figures of the hot-rolled and recrystallized samples.

The basal texture intensities of alloys S1–S8 range from four multiples of a random distribution (m.r.d) for alloy S3 to 7.3 m.r.d for alloy S6 (Mg–2Al–0.1Ca). In contrast, alloy S9 (Mg–1Al) shows a significantly higher basal peak intensity

of 13 m.r.d. In addition, a tendency toward a TD splitting is observed.

3.5. Slip Line Analysis

The activation of the deformation mechanisms in alloys S1–S9 was analyzed using slip line analysis. For this purpose, several grains per alloy were examined and per grain 3–10 slip lines were analyzed. **Table 2** shows the number of grains.

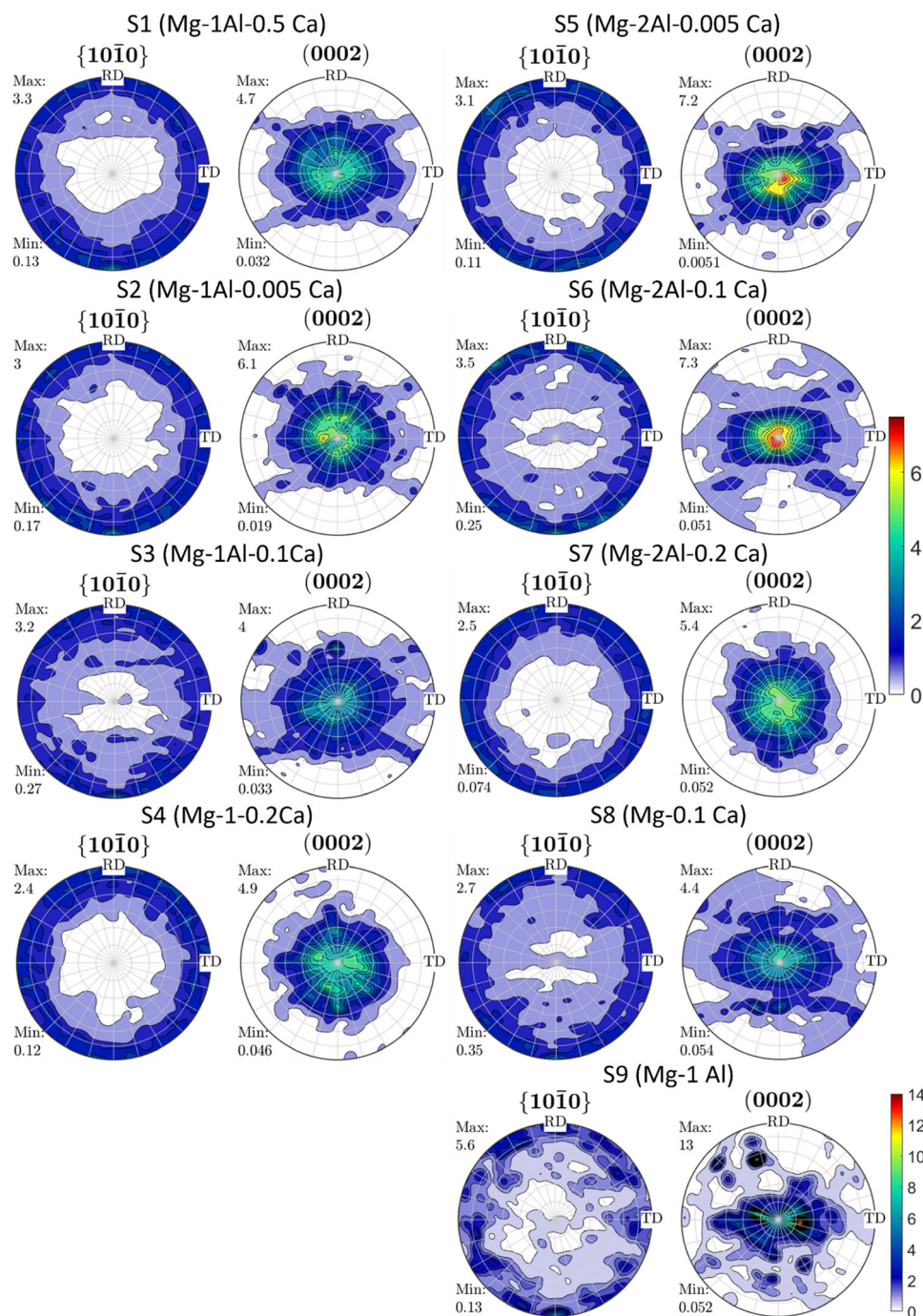


Figure 6. (0002) and $\{10\bar{1}0\}$ pole figures of compositions S1–S9.

Table 2. Number of grains as statistical basis for the slip trace analysis.

Alloy	S1	S2	S3	S4	S5	S6	S7	S8	S9
Number of grains	68	58	41	37	51	36	54	60	57

As not all images can be shown here, we have selected a few representative images that show the observed trends of activated slip systems (Figure 7).

By correlating surface steps formed during dislocation slip on the surface with potential slip plane traces observed using EBSD, the different activated slip planes were identified (Figure 7a)). It should be noted here that $\langle a \rangle$ dislocations can glide on basal, prismatic and first-order pyramidal planes, while $\langle c + a \rangle$ dislocations can glide on first- and second-order pyramidal planes. Consequently, we interpret slip events on basal and prismatic planes to stem from $\langle a \rangle$ dislocations and slip events on second-order pyramidal planes to arise due to $\langle c + a \rangle$ dislocations (Figure 7b). For slip events on first-order pyramidal planes, $\langle a \rangle$ and $\langle c + a \rangle$ dislocations cannot be distinguished based on the slip plane alone. Cross-slip events between the first- and second-order planes (compare Figure 7c) can only be formed by $\langle c + a \rangle$ dislocations.

To compare the activation of different slip planes in the alloys and to draw more general conclusions from this analysis, the relative proportion of grains showing slip on a particular slip plane is used. An overview of this analysis is given in Figure 8.

For all alloys, basal slip is the predominant active slip system that was observed in over 90% of the grains. In addition, all alloys exhibit $\langle c + a \rangle$ second-order pyramidal slip. The binary alloy S8 (Mg–0.1Ca) has the lowest activation frequency of second-order pyramidal slip, being observed in only 15% of the grains, while the other binary alloy S9 (Mg–1Al) has the highest amount of second-order pyramidal slip, being observed in 50% of the grains. The ternary alloys fall between these values. First-order pyramidal slip is also present in all compositions. Activation frequencies range from 18.9% to 70.2% of the grains. As mentioned earlier, both, $\langle a \rangle$ and $\langle c + a \rangle$ Burgers vectors, are able to slip on first-order pyramidal planes. Prismatic slip is only observed in a few grains and only in five compositions (S2 [Mg–1Al–0.005Ca], S3 [Mg–1Al–0.1Ca], S6 [Mg–2Al–0.1Ca], S8 [Mg–0.1Ca], and S9 [Mg–1Al]). Interestingly, all three alloys containing 0.1 wt% Ca show prismatic slip. It should also be noted that a high number of tensile twins were observed for all alloys but were not further analyzed in this study, as no

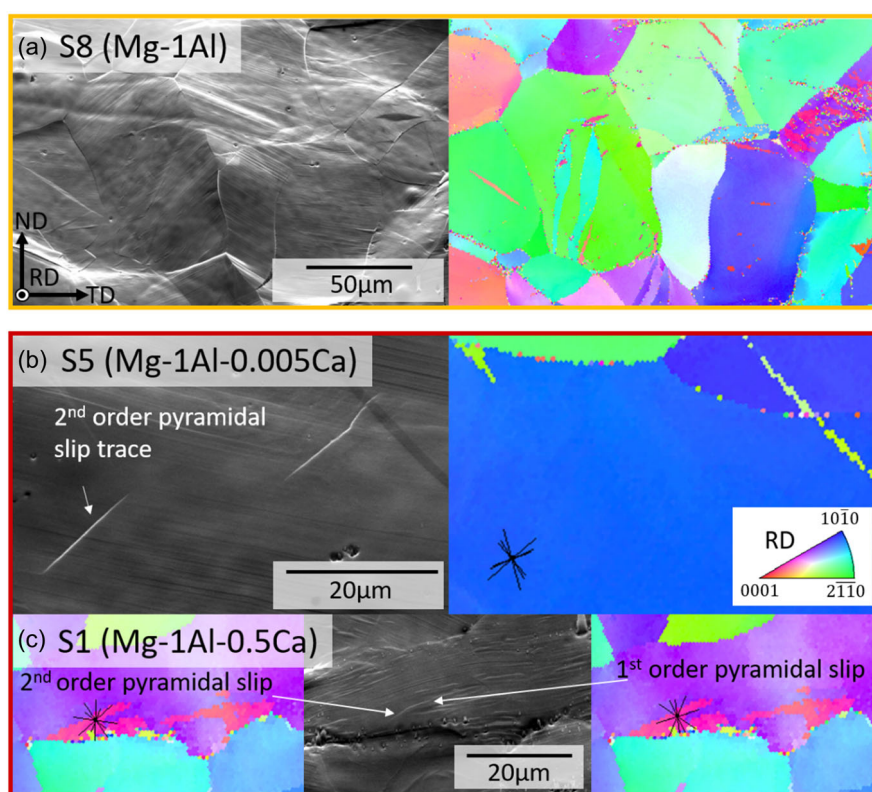


Figure 7. Orange box: a) example area of the correlative SE-EBSD slip line analysis of composition S8. SE image (left) and corresponding EBSD image (right) of the deformed sample. Red box: example slip lines. b) Composition S5: SE image with a second-order pyramidal slip line (left) and corresponding EBSD image with possible second-order pyramidal slip lines for the measured grain orientation (right) of the deformed sample and c) composition S1: SE image with a cross slip event between first- and second-order pyramidal slip line (center) and corresponding EBSD image with possible second-order pyramidal slip traces (left) and first-order pyramidal slip trace (right) for the measured grain orientation of the deformed sample. The sample orientation of all images and the IPF color map for EBSD images are identical for all images as indicated in (a) and (b), respectively. The total plastic deformation is $\approx 3\%$.

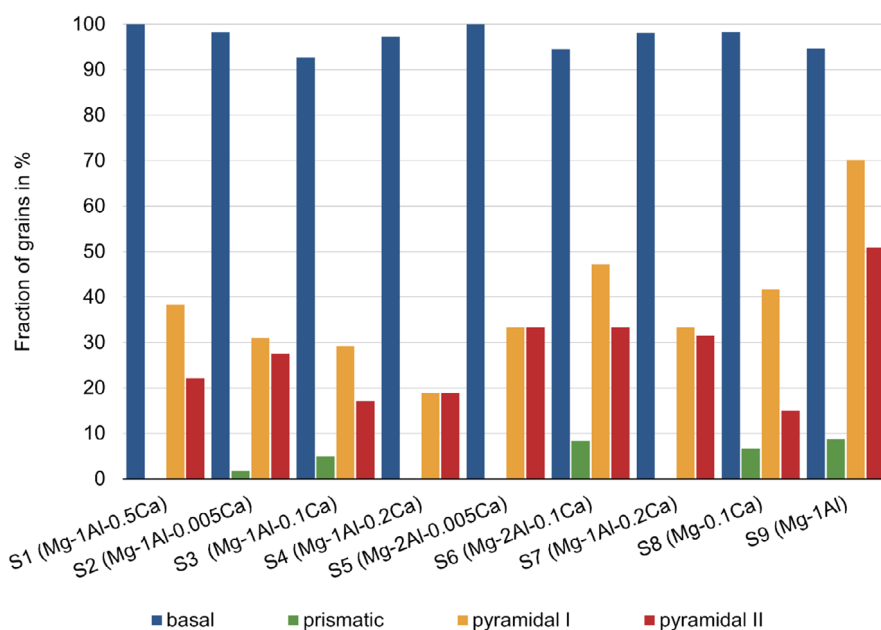


Figure 8. Statistical analysis of the activated slip system in each composition after a total plastic deformation of approximately 3%.

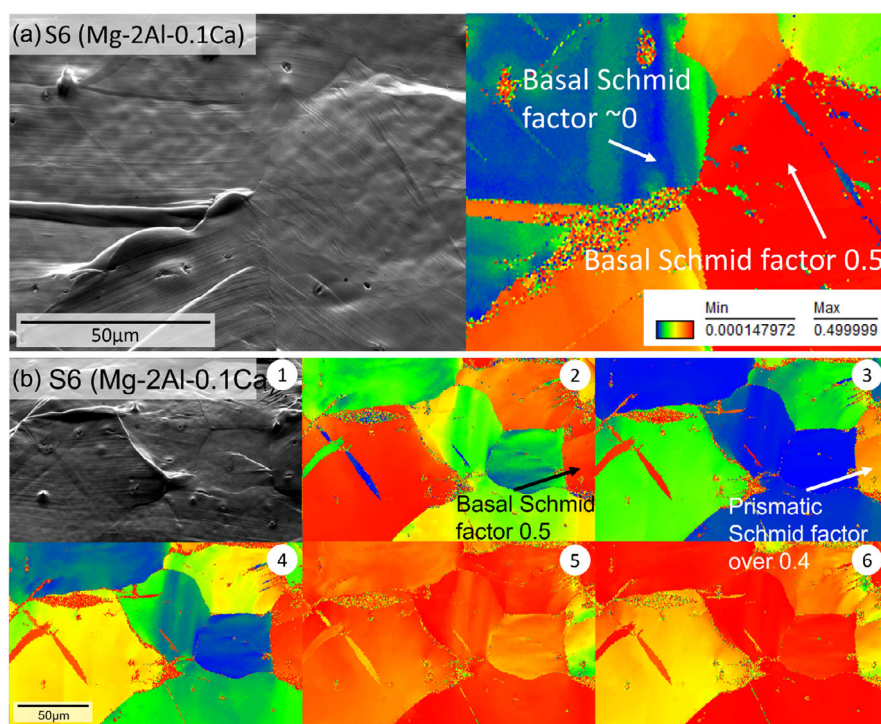


Figure 9. Sample S6: a) SE image with basal slip lines (left) and corresponding calculated m_s values for basal slip (right). b) 1) Overview SE image and 2) corresponding calculated m_s values for basal slip, 3) prismatic slip, 4) first-order $\langle a \rangle$ and 5) $\langle c + a \rangle$, and 6) second-order pyramidal slip.

differences in the activation of tensile twinning were observed for the different alloys.

Figure 9 shows some representative images showing the correlation between the Schmid factors and the activation of slip systems. From this analysis, it is evident that the Schmid factor for

basal slip is high in most grains due to the basal-type textures. Furthermore, as can be seen in Figure 9b (3), the Schmid factor for prismatic slip is low in most grains, presumably due to the basal-type textures. Most of the grains also have Schmid factors of ≥ 0.4 for first-order $\langle c + a \rangle$ and second-order pyramidal slip

(compare Figure 9b (5) and (6)). In terms of Schmid factors for first-order pyramidal slip, $\langle c + a \rangle$ slip has higher Schmid factors than $\langle a \rangle$ slip (Figure 9b (4)), which is due to the more preferential geometric orientation of $\langle c + a \rangle$ slip under compression for basal-textured Mg.^[46] In most grains, the slip system with the highest Schmid factor was activated. An exception is shown in Figure 9b), where the grain was deformed by prismatic slip although the Schmid factor of prismatic slip was <0.4 , which is lower than the Schmid factor for basal and first-order $\langle a \rangle$ pyramidal slip. It should be noted that all grains with non-basal slip traces also have additional basal slip traces. If the Schmid factor for any type of pyramidal plane is less than 0.4, no slip traces belonging to that slip plane were observed.

4. Discussion

4.1. Grain Sizes

Alloys S2–S8 all show similar grain sizes of about 40 μm . In the case of S1 (Mg–1Al–0.5Ca), the Laves phase precipitates at the grain boundaries may have resulted in reduced grain growth during recrystallization due to Zener pinning.^[47] A similar effect in binary Mg–Ca alloys was recently observed by Chaudry et al.^[48] Although the alloys S4 (Mg–1Al–0.2Ca), S6 (Mg–2Al–0.1Ca), and S7 (Mg–2Al–0.2Ca) have a solubility slightly above the solubility limit of Ca in a defect-free crystal, we did not observe any precipitates and expect no or only very few precipitates, which apparently do not affect the recrystallization and grain growth of the alloys. In contrast, alloy S9 (Mg–1Al), although being processed in the same way, shows much larger grains, probably due to rapid grain growth. We suggest that this is due to the absence of Ca, as it has been reported that Ca in Mg segregates to grain boundaries, improving grain-boundary strength and reducing their mobility.^[49,50]

4.2. Mechanical Testing

As has been shown previously,^[31–33] Mg–Al–Ca alloys do indeed exhibit increased intrinsic ductility relative to pure Mg and tensile elongations more than 20%. Although the alloys studied have only small variations in composition, clear differences in the deformation behavior were observed. A very small amount of Ca (0.005 wt%) already increases the ductility by $\geq 5\%$ compared to the binary Mg–1Al sample without Ca.

In the group of alloys containing 1 wt% Al, the highest ductility under tensile loading conditions of 20.5% was obtained for the alloy containing 0.1 wt% Ca and in the group of alloys containing 2 wt% Al, the highest ductility of 17% was observed for the alloy containing 0.2 wt% Ca. This indicates that the observed ductility of ternary Mg–Al–Ca alloys may not only be an effect of the joint addition of these alloying elements, but may also be influenced by the Ca:Al ratio. Looking at the alloys investigated in the present study, the best properties are found at a Ca:Al ratio of 1:10. Previously, Sanyal et al.,^[51] Li et al.,^[52] and Elamami et al.^[53] investigated the effects of the Ca:Al ratio of Mg–Al–Ca–Mn alloys on the solubility limits, textures, and preferred precipitate compositions and indeed showed an effect of the Ca:Al ratio on the microstructure and mechanical properties.

A similar effect was also observed by Zhang et al.^[54] for ternary Mg–Al–Ca. More recently, metastable, ordered defect phases^[55] have been found in Mg alloyed with Al and Ca,^[56,57] and their occurrence and competition may be related to the Ca:Al ratio. The detailed characterization of these atomically ordered defects, including the deformation mechanisms and mechanical properties they give rise to, necessarily involves a large number of experiments at atomic resolution and is the subject of ongoing research.

Although the binary Mg–Ca alloy S8 (Mg–0.1Ca) has a lower ductility than the ternary alloys, the tensile and compression test results indicate that the alloying of Mg with Ca already increases the ductility when compared to pure Mg. Similar results have been reported previously by refs. [29,30]. Similarly, the binary Mg–Al alloy shows lower room-temperature ductility than the ternary alloys and the binary Mg–Ca alloy, but increased ductility compared to pure Mg. It is important to note that the compression test results consistently show higher compressive fracture strains for the binary Mg–Ca alloy than for the binary Mg–Al alloy. This may be since the compression test is less sensitive to oxide inclusions that may be present in the samples as they are produced on a laboratory scale. The increased ductility of the binary Mg–Al alloy over pure Mg is thought to be due to the lower basal texture intensity in Mg–Al than in pure Mg.

The addition of either Al (S9) or Ca (S8) results in an increase in UTS compared to pure Mg, but the ternary alloys exhibit even higher UTS values than the binary alloys. Al has been proposed to have a high-solid-solution-strengthening effect in Mg,^[58,59] which agrees with our observation that increasing the Al content increases the UTS. The UTS values of alloys containing 1 and 2 wt% Al measured in the present study are comparable to those reported by Caceres et al.^[58] Chino et al.^[60] investigated the effects of Al and Ca on the mechanical properties of Mg and suggested that Ca has a solid-solution-softening effect in contrast to Al. Chino et al.^[60] proposed that Ca causes an increased formation of double kinks for basal and prismatic slip and therefore does not act as an obstacle to dislocation movement, whereas Al acts as an obstacle for dislocation movement. The stress–strain curve of alloy S3 is in good agreement with another Mg–1Al–0.1Ca composition reported previously.^[3] They^[3] found that in a Mg–1Al–0.3Ca sample above the solubility limit of Ca, large and brittle C14 Mg₂Ca precipitates at the grain boundaries lead to premature failure. Interestingly, the limitation of the ductility effect observed in this study does not apply to alloy S1 (Mg–1Al–0.5Ca). It is suggested, that the smaller ternary C36 precipitates observed in this study do not affect the mechanical properties as much as the large C14 precipitates. The SEM and TEM results show that these precipitates have a small platelet-shaped morphology and do not form a closed skeleton at the grain boundaries. We therefore suggest that they are less likely to initiate early cracking, as observed in the case of an interconnected C14 skeleton in a cast Mg–Al–Ca alloy.^[61] The influence of the morphology of the Laves phases on the deformation behavior has also been observed by Liu et al.^[62] for the interaction of deformation twinning and precipitates with different morphologies. According to the thermodynamic calculation, the observation of C36 instead of C14 is not unexpected. The observed C36 precipitates show a higher deviation from the ideal stoichiometry, including near (Mg,Al)₂Ca and near Al₂(Mg,Ca)

compositions, than expected from the literature. Near $(\text{Mg,Al})_2\text{Ca}$ compositions have been measured previously by Zubair et al.,^[61,63] while $\text{Al}_2(\text{Mg,Ca})$ compositions have been reported by Zhong et al.^[64] We suggest that this may be due to limited diffusion resulting in a large variation in precipitation for compositions that have not (yet) reached thermodynamic equilibrium. The actual composition and the Laves phase precipitated in Mg–Al–Ca alloys therefore depend sensitively on the processing conditions (time-temperature history).^[63]

Comparing the tensile tests with the compression tests, both the UCSs and compressive strains are higher than the UTSs and the tensile elongations. In contrast, the yield strengths are lower in the compression test than in tensile test. A similar tension–compression asymmetry has been observed previously and has been related with an increased activity of extension twinning due to the more favorable orientation in the compression test.^[42,65–68] The asymmetry has been suggested to be 0.4–0.6, which is in good agreement with our results showing an asymmetry of about 0.5.^[69] Smaller strains to failure in tension tests than in compression tests have previously been observed by other researchers.^[42,66] As the difference in the strains to failure between tensile tests and compression tests for the present study is higher than expected, we assume that the higher strains achieved in compression tests are caused by oxide inclusions that cause earlier failure in tensile tests. Therefore, we assume that the tensile elongation in particular could be even higher if oxide inclusions were reduced.

Notwithstanding the higher stresses and strains observed in compression tests, the trends in alloy specific stress–strain behavior, i.e., ultimate strength, work hardening, and strain to failure, were comparable in the tension and compression tests. Minor deviations from this observation are mainly due to the scatter coming from the aforementioned oxide inclusions, because of the small laboratory scale of this study.

By separating the compressive stress–strain curves into two stages, three types of stress–strain behavior can be extracted as shown in **Figure 10**.

All alloys show a similar behavior in regime 1: a high strain hardening which occurs probably due to deformation twinning during compression.^[60,64,65] In regime 2, the different alloy types show different behavior. Alloy S1 (Mg–1Al–0.5Ca) shows almost no regime 2 hardening and fails shortly after reaching the regime 2 strain hardening. The ternary alloys show steady-state strain hardening in regime 2. Similar steady-state strain hardening during compression has recently been reported in low alloy Mg–Gd alloys and the authors have proposed that this is due to the balance between strain localization and self-hardening of shear bands.^[70] In addition, we assume that this is due to the interaction of different slip systems causing forest hardening and also the interaction of dislocations with twins. Deformation twinning is assumed to be less active in regime 2 strain hardening since deformation twinning in the grains, which are preferentially oriented for deformation twinning, has already twinned during regime 1 strain hardening. Finally, strain softening was observed for the binary solid solution alloys. Strain softening is usually reported for dynamic recrystallization processes at elevated temperatures^[71,72] and has also been associated with the formation of double twins resulting in grains oriented more favorable for basal slip.^[73,74] Indeed, we observed double twins in the

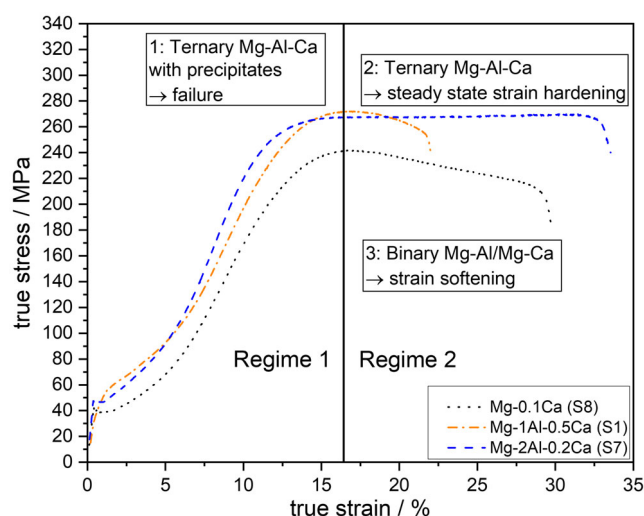


Figure 10. Different compressive behavior of the alloys studied represented by regime 1 and regime 2 strain hardening, exemplary for the different alloy types (ternary solid solution (S2–S7), ternary solid solution + precipitates (S1), binary solid solutions (S8 + S9)), one representative curve per group is shown.

ternary alloys at higher strains using EBSD, while no evidence of dynamic recrystallization was found. We therefore propose that the formation of double twins in the present study caused the observed strain softening.

4.3. Mechanisms to Improve Ductility

4.3.1. Effect of Slip System Activation

One of the possible reasons for the observed increased room-temperature ductility is the activation of not only the basal but also the non-basal slip systems. Here, the activation of $\langle c + a \rangle$ slip is the critical mechanism to satisfy the von Mises criterion and to allow the accommodation of strain along the crystal c -axis. It has been suggested that lean alloying of Al and Ca leads to enhanced activation of non-basal $\langle c + a \rangle$ slip.^[3,27,50] In general, basal slip is the dominant slip system due to the very low CRSS compared to other slip systems,^[6,75] but the additional activation of $\langle c + a \rangle$ slip can lead to increased ductility.^[3,27,50] As basal dislocations produce higher surface steps and occur as parallel lines, they are easy to detect. In contrast, non-basal slip systems are less straight and form lower surface steps, making their identification more difficult.^[25] Although we carefully examined the slip traces, the detection was performed manually, and errors may occur in the correlation between the observed slip lines and the measured EBSD maps occur. Due to the distortion of the EBSD map, misalignments are possible. In case of ambiguity regarding the matching slip system, the affected slip lines were taken into account.

The slip line analysis carried out in this study showed that non-basal $\langle c + a \rangle$ second-order pyramidal slip was indeed activated in all the compositions investigated. It should be noted that only 0.005 wt% Ca alloyed with Al is sufficient for activation. Furthermore, slip on the first-order pyramidal plane is also active

in all alloys. For most alloys, it is the predominant non-basal slip system, which has been also seen for pure Mg by Xie et al.^[76] in c-axis-compressed single crystals. As both, $\langle a \rangle$ and $\langle c + a \rangle$ Burgers vectors can slip on the first-order pyramidal plane, we cannot conclude which of these slip systems ($\langle a \rangle$ or $\langle c + a \rangle$ first-order pyramidal slip) is activated without further analysis using micropillar compression and/or TEM analysis. Cross slip between the first-order pyramidal plane and the second-order pyramidal plane was observed in one grain (see Figure 7c), which has previously been discussed as a possible mechanism for $\langle c + a \rangle$ slip.^[77–79] Slip on prismatic planes has only been observed in a few compositions. Zhu et al.^[80] and Chaudry et al.^[81] reported that the increased ductility of Mg–Ca alloys could be based on the activation of prismatic slip, but in the present study, in addition to basal slip, slip on the pyramidal planes was mainly observed. It should also be noted that Zhu et al.^[80] worked with extruded alloys, which due to the different texture, may indeed contain grains with a preferential orientation for prismatic slip. In the present study, we have investigated rolled Mg samples, which result in a basal-type texture with grain orientations that make prismatic slip difficult.

One mechanism proposed by Jang et al.^[27] and Kim et al.^[82] is to reduce of the CRSS anisotropy by changing the dislocation binding energy. It has been shown^[27] that the ductility can be improved by adjusting the amount of Zn and Ca in Mg–Zn–Ca alloys. It has been pointed out^[82] that especially the atomic size mismatch to Mg is a critical parameter for the dislocation binding energy. Considering that the atomic size of Zn is comparable to that of Al,^[83] this model may also be applicable to the Mg–Al–Ca alloys studied in this work. Indeed, an increased activity of non-basal $\langle a \rangle$ and also $\langle c + a \rangle$ slips is observed in this study and the reduction of their CRSS and/or an increased CRSS for basal slips is a promising explanation. The interpretation of the activation of slip systems requires consideration of the resolved shear stresses on the different slip systems in a crystal. As we do not have information on the actual 3D microstructure and therefore the local stress states, we have used the Schmid factors (m_s) as a simple approximation. It should be noted that the Schmid factors give only an approximation of the actual resolved shear stresses, as the shear induced by the neighboring grains is not included (see Figure 9). However, here we consider slip traces across many grains and will only give a relative interpretation of the slip activity on the different slip systems with different alloy contents. The increased activity of $\langle c + a \rangle$ pyramidal slip in particular indicates that the CRSS is most likely

lower than that for pure Mg, but still significantly higher than that for basal slip. Therefore, the activation of pyramidal slip is only observed in grains with a Schmid factor m_s greater than 0.4. This result is in good agreement with calculations made by Nandy et al.^[50] on similar Mg–Al–Ca alloys, showing in particular a reduction in the CRSS of non-basal slip systems; a similar effect may apply to the alloys investigated in this study.

4.3.2. Effect of Texture Weakening

Weakening of the basal-type texture is a second important mechanism for the ductility of Mg and Mg alloys. Rolled Mg and Mg alloys typically develop a sharp basal-type texture which limits further deformation due to the unfavorable orientation for further deformation.^[44,45,84] In weaker textures, both, basal slip and non-basal slip, can be more easily activated because the Schmid factors m_s are higher in off-basal orientations. Consequently, more grains can contribute to plastic deformation.

All the Ca-containing alloys investigated here show significantly weaker basal-type textures than pure Mg,^[75,85] suggesting that i) the higher activation of non-basal slip systems results in weaker basal textures and that ii) the weaker textures may also have contributed to the increased room ductility of the alloys. Furthermore, the texture intensities show a dependence on the amount of Ca in the sample and the solubility of Ca in the alloy. **Figure 11** shows the observed influence of the Ca content and Ca solubility on the basal peak intensities.

Chapuis et al.^[86] analyzed the different crystal axis rotations during deformation depending on the active slip system and the resulting lattice rotation as the sum of the rotations of all contributing slip systems, resulting in a weaker basal-type texture when non-basal slip systems are activated. A weakening of the basal texture by the addition of Ca has been reported in several studies, suggesting that the increased activation of non-basal slip may have weakened the development of a basal texture during rolling.^[29,87–90] Another reason for the weakening of the basal-type texture could be a change in the recrystallization and grain growth kinetics induced by the presence of Ca atoms as proposed by Jo et al.^[41] Similarly, Zeng et al.^[49] suggested that the segregation of Ca at grain boundaries could influence the recrystallization behavior. The texture intensities measured in this work are in good agreement with what was suggested by Jo et al.^[41] We therefore suggest that a change in recrystallization and grain growth kinetics due to the presence of Ca atoms at the grain

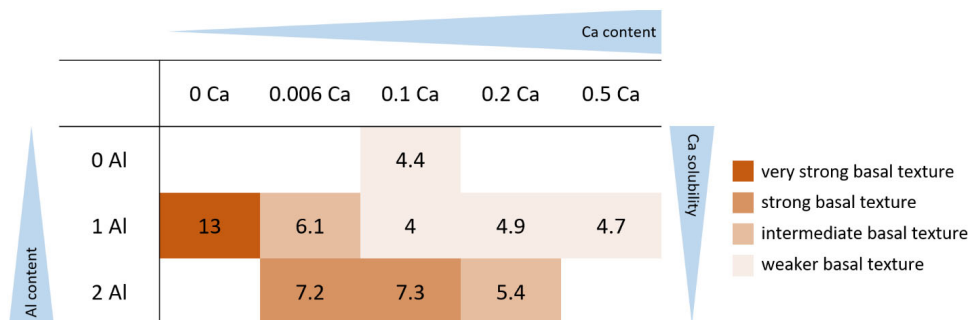


Figure 11. Intensities of the (0002)-peak in dependence of the Ca content and its solubility.

boundaries and the activation of non-basal slip systems causes the observed weakening of the basal texture component. This weaker basal texture then allows easier activation of both basal and non-basal dislocation slip, contributing to the observed good room-temperature ductility. It should also be noted that even 0.005 wt% Ca results in a decrease of the basal peak intensity from 13 (S9 [Mg–1Al]) to 6.1 (S2 [Mg–1Al–0.005Ca]) m.r.d., indicating that even very small amounts of Ca can affect the recrystallization and also the deformation behavior. A more comprehensive analysis of the texture-related features of this alloy system is presented in ref. [91].

5. Conclusions

In this study, we investigated the mechanical properties and activation of slip systems in nine Mg alloys: one binary Mg–Ca alloy, one binary Mg–Al alloy, one ternary Mg–Al–Ca alloy containing C36 precipitates, and six ternary solid solution Mg–Al–Ca alloys. It was shown that both, the activation of non-basal deformation systems and the weakened basal-type textures, lead to increased room-temperature ductility. Interestingly, only the co-addition of Ca and Al causes the observed high increase in ductility, even when the amount of Ca is very low. Although the binary alloys also show some increase in ductility, the ternary alloys show a much greater increase in ductility. The following conclusions can be drawn from the present study: 1) the co-addition of 0.005–0.5 wt% Ca and 1–2 wt% Al to Mg results in a greater increase in room-temperature ductility (10%–17%) than the addition of either Ca or Al alone (6% each). 2) The addition of Ca leads to a weakening of the basal-type texture intensity by ≥ 6.7 m.r.d. compared to Mg–1Al. This is thought to be due to a change in recrystallization and grain growth kinetics through the presence of Ca atoms at the grain boundaries and the activation of non-basal slip systems. Interestingly, this effect is observed even at very low levels of Ca (0.005 wt%). 3) In addition to basal slip as the dominant slip system, non-basal slip systems including $\langle c + a \rangle$ slip were observed in 15%–33% of the grains examined for all compositions. 4) Slip on first-order and second-order pyramidal planes was observed in all compositions, while prismatic slip was preferred in compositions containing 0.1 wt% Ca. 5) Slip on pyramidal planes was only observed when the Schmid factor was greater than 0.4, indicating that the difference between the CRSS for basal slip and that for slip on pyramidal planes is still large. 6) In addition to the activation of non-basal slip systems, the weakened basal-type textures contribute to the observed ductility of the Mg–Al–Ca alloys.

Acknowledgements

The authors gratefully acknowledge funding by the Deutsche Forschungsgemeinschaft (DFG, German Research Foundation) of SFB 1394 (CRC 1394), Project-ID 409476157, subprojects A01 und C06. The authors also thank Hauke Springer for sample synthesis, Luiz R. Guimarães for his support during samples preparation, Risheng Pei for his support during texture measurements, David Beckers for his assistance during metallographic preparation, and Gerd Schütz for sample cutting.

Open Access funding enabled and organized by Projekt DEAL.

Conflict of Interest

The authors declare no conflict of interest.

Data Availability Statement

The data that support the findings of this study are available from the corresponding author upon reasonable request.

Keywords

electron microscopy, mechanical properties, Mg–Al–Ca alloys, microstructures, solid solutions

Received: July 14, 2023

Revised: September 11, 2023

Published online: October 15, 2023

- [1] J. F. Nie, K. S. Shin, Z. R. Zeng, *Metall. Mater. Trans. A* **2020**, 51, 6045.
- [2] C. Romanowski, in *Magnesium Technology 2019* (Eds: V. V. Joshi, J. B. Jordon, D. Orlov, N. R. Neelameggham), Springer International Publishing, Cham **2019**, pp. 3–12.
- [3] S. Sandlöbes, M. Friák, S. Korte-Kerzel, Z. Pei, J. Neugebauer, D. Raabe, *Sci. Rep.* **2017**, 7, 10458.
- [4] M. H. Yoo, *Metall. Mater. Trans. A* **1981**, 12, 409.
- [5] J. Bohlen, D. Letzig, K. U. Kainer, *Mater. Sci. Forum* **2007**, 546–549, 1.
- [6] J. Koike, T. Kobayashi, T. Mukai, H. Watanabe, M. Suzuki, K. Maruyama, K. Higashi, *Acta Mater.* **2003**, 51, 2055.
- [7] T. Al-Samman, X. Li, *Metall. Mater. Trans. A* **2011**, 528, 3809.
- [8] S. R. Agnew, J. A. Horton, T. M. Lillo, D. W. Brown, *Scr. Mater.* **2004**, 50, 377.
- [9] A. Yamashita, Z. Horita, T. G. Langdon, *Metall. Mater. Trans. A* **2001**, 300, 142.
- [10] J.-F. Nie, *Metall. Mater. Trans. A* **2012**, 43, 3891.
- [11] T. Nakata, T. Mezaki, C. Xu, K. Oh-ishi, K. Shimizu, S. Hanaki, S. Kamado, *J. Alloys Compd.* **2015**, 648, 428.
- [12] H. Wang, *Int. J. Plast.* **2016**, 84, 255.
- [13] B. Beausir, S. Biswas, D. Ik Kim, L. S. Tóth, S. Suwas, *Acta Mater.* **2009**, 57, 5061.
- [14] R. V. Mises, *Appl. Math. Mech.* **1928**, 8, 161.
- [15] J. Bohlen, M. R. Nürnberg, J. W. Senn, D. Letzig, S. R. Agnew, *Acta Mater.* **2007**, 55, 2101.
- [16] N. Stanford, M. Barnett, *Scr. Mater.* **2008**, 58, 179.
- [17] L. Wang, Y. Li, H. Zhang, Z. Zhang, Q. Yang, Q. Zhang, H. Wang, W. Cheng, K. S. Shin, M. Vedani, *J. Mater. Res. Technol.* **2020**, 9, 12604.
- [18] N. Stanford, *Metall. Mater. Trans. A* **2010**, 527, 2669.
- [19] Y. Chino, M. Kado, M. Mabuchi, *Metall. Mater. Trans. A* **2008**, 494, 343.
- [20] F. Wang, S. Sandlöbes, M. Diehl, L. Sharma, F. Roters, D. Raabe, *Acta Mater.* **2014**, 80, 77.
- [21] A. Imandoust, C. D. Barrett, T. Al-Samman, K. A. Inal, H. El Kadiri, *J. Mater. Sci.* **2016**, 52, 1.
- [22] H. Miyano, K. Takemoto, M. Tsushida, H. Kitahara, S. Ando, *Mater. Trans.* **2021**, 62, 1097.
- [23] S. R. Agnew, J. A. Horton, M. H. Yoo, *Metall. Mater. Trans. A* **2002**, 33, 851.
- [24] S. R. Agnew, M. H. Yoo, C. N. Tomé, *Acta Mater.* **2001**, 49, 4277.
- [25] S. Sandlöbes, M. Friák, J. Neugebauer, D. Raabe, *Metall. Mater. Trans. A* **2013**, 576, 61.

- [26] K. X. Sun, Y. Zeng, D. D. Yin, F. Gao, L. J. Long, X. Y. Qian, Y. J. Wan, G. F. Quan, B. Jiang, *Metall. Mater. Trans. A* **2020**, 792, 139801.
- [27] H.-S. Jang, D. Seol, B.-J. Lee, *J. Magnes. Alloy* **2021**, 9, 317.
- [28] Y. Chino, X. Huang, K. Suzuki, M. Mabuchi, *Mater. Trans.* **2010**, 51, 821.
- [29] Y. Chino, T. Ueda, Y. Otomatsu, K. Sassa, X. Huang, K. Suzuki, M. Mabuchi, *Mater. Trans.* **2011**, 52, 1477.
- [30] Z. R. Zeng, M. Z. Bian, S. W. Xu, C. H. J. Davies, N. Birbilis, J. F. Nie, *Metall. Mater. Trans. A* **2016**, 674, 459.
- [31] Q. Huang, Y. Liu, M. Tong, H. Pan, C. Yang, T. Luo, Y. Yang, *Vacuum* **2020**, 177, 109356.
- [32] J. O. Andersson, T. Helander, L. Höglund, P. Shi, B. Sundman, *Calphad* **2002**, 26, 273.
- [33] A. Janz, J. Gröbner, H. Cao, J. Zhu, Y. A. Chang, R. Schmid-Fetzer, *Acta Mater.* **2009**, 57, 682.
- [34] R. Hielscher, H. Schaeben, *J. Appl. Cryst.* **2008**, 41, 1024.
- [35] B. Beausir, J.-J. Fundenberger, ATEX - software, Université de Lorraine – Metz, **2017**, www.atex-software.eu.
- [36] A. Suzuki, N. D. Saddock, J. W. Jones, T. M. Pollock, *Acta Mater.* **2005**, 53, 2823.
- [37] M. Freund, D. Andre, C. Zehnder, H. Rempel, D. Gerber, M. Zubair, S. Sandlöbes-Haut, J. S. K.-L. Gibson, S. Korte-Kerzel, *Materialia* **2021**, 20, 101237.
- [38] H. Cao, C. Zhang, J. Zhu, G. Cao, S. Kou, R. Schmid-Fetzer, Y. A. Chang, *Acta Mater.* **2008**, 56, 5245.
- [39] W.-Y. Yu, N. Wang, X.-B. Xiao, B.-Y. Tang, L.-M. Peng, W.-J. Ding, *Solid State Sci.* **2009**, 11, 1400.
- [40] D. Kevorkov, M. Medraj, J. Li, E. Essadiqi, P. Chartrand, *Intermetallics* **2010**, 18, 1498.
- [41] S. Jo, D. Letzig, S. Yi, *Metals* **2021**, 11, 468.
- [42] X. Y. Lou, M. Li, R. K. Boger, S. R. Agnew, R. H. Wagoner, *Int. J. Plast.* **2007**, 23, 44.
- [43] E. Kelley, W. Hosford, *Trans. Met. Soc. AIME* **1968**, 242, 5.
- [44] J. Wu, L. Jin, J. Dong, F. Wang, S. Dong, *J. Mater. Sci. Technol.* **2020**, 42, 175.
- [45] Y. N. Wang, J. C. Huang, *Mater. Chem. Phys.* **2003**, 81, 11.
- [46] X.-L. Nan, H.-Y. Wang, L. Zhang, J.-B. Li, Q.-C. Jiang, *Scr. Mater.* **2012**, 67, 443.
- [47] C. S. Smith, *Trans. Metall. Soc. AIME* **1948**, 175, 15.
- [48] U. M. Chaudry, G. Han, Y. Noh, T.-S. Jun, *J. Alloys Compd.* **2023**, 950, 169828.
- [49] Z. R. Zeng, Y. M. Zhu, S. W. Xu, M. Z. Bian, C. H. J. Davies, N. Birbilis, J. F. Nie, *Acta Mater.* **2016**, 105, 479.
- [50] S. Nandy, S.-P. Tsai, L. Stephenson, D. Raabe, S. Zaefferer, *J. Magnes. Alloy* **2021**, 9, 1521.
- [51] S. Sanyal, M. Paliwal, T. K. Bandyopadhyay, S. Mandal, *Metall. Mater. Trans. A* **2021**, 800, 140322.
- [52] Z. T. Li, X. G. Qiao, C. Xu, X. Q. Liu, S. Kamado, M. Y. Zheng, *Metall. Mater. Trans. A* **2017**, 682, 423.
- [53] H. A. Elamami, A. Incesu, K. Korgiopoulos, M. Pekgulerlyuz, A. Gungor, *J. Alloys Compd.* **2018**, 764, 216.
- [54] L. Zhang, K.-K. Deng, K.-B. Nie, F.-J. Xu, K. Su, W. Liang, *Metall. Mater. Trans. A* **2015**, 636, 279.
- [55] S. Korte-Kerzel, T. Hickel, L. Huber, D. Raabe, S. Sandlöbes-Haut, M. Todorova, J. Neugebauer, *Int. Mater. Rev.* **2021**, 67, 89.
- [56] A. Tehranchi, M. Lipinska-Chwalek, J. Mayer, J. Neugebauer, T. Hickel, *arXiv*, **2023**.
- [57] A. Tehranchi, S. Zhang, A. Zendegani, C. Scheu, T. Hickel, J. Neugebauer, *arXiv*, **2023**.
- [58] C. H. Cáceres, D. M. Rovera, *J. Light Met.* **2001**, 1, 151.
- [59] H. Somekawa, A. Singh, T. Mukai, T. Inoue, *Philos. Mag.* **2016**, 96, 2671.
- [60] Y. Chino, T. Ueda, M. Kado, M. Mabuchi, *Mater. Trans.* **2011**, 52, 1840.
- [61] M. Zubair, S. Sandlöbes, M. A. Wollenweber, C. F. Kusche, W. Hildebrandt, C. Broeckmann, S. Korte-Kerzel, *Metall. Mater. Trans. A* **2019**, 756, 272.
- [62] B.-Y. Liu, N. Yang, J. Wang, M. Barnett, Y.-C. Xin, D. Wu, R.-L. Xin, B. Li, R. L. Narayan, J.-F. Nie, J. Li, E. Ma, Z.-W. Shan, *J. Mater. Sci. Technol.* **2018**, 34, 1061.
- [63] M. Zubair, M. Felten, B. Hallstedt, M. V. Paredes, L. Abdellaoui, R. B. Villoro, M. Lipinska-Chwalek, N. Ayeb, H. Springer, J. Mayer, B. Berkels, D. Zander, S. Korte-Kerzel, C. Scheu, S. Zhang, *Mater. Des.* **2023**, 225, 111470.
- [64] Y. Zhong, J. Liu, R. A. Witt, Y.-h. Sohn, Z.-K. Liu, *Scr. Mater.* **2006**, 55, 573.
- [65] E. A. Ball, P. B. Prangnell, *Scr. Mater.* **1994**, 31, 111.
- [66] P. Zhou, E. Beeh, H. E. Friedrich, *J. Mater. Eng. Perform.* **2016**, 25, 853.
- [67] J. P. Nobre, U. Noster, M. Kornmeier, A. M. Dias, B. Scholtes, *Key Eng. Mater.* **2002**, 230–232, 267.
- [68] P. Klimanek, A. Pötzsch, *Metall. Mater. Trans. A* **2002**, 324, 145.
- [69] Y. Xin, X. Zhou, Q. Liu, *Metall. Mater. Trans. A* **2013**, 567, 9.
- [70] A. Kula, T. Tokarski, M. Niewczas, *Metall. Mater. Trans. A* **2020**, 51, 3742.
- [71] S. E. Ion, F. J. Humphreys, S. H. White, *Acta Metallurgica* **1982**, 30, 1909.
- [72] S. H. Choi, D. H. Kim, B. S. Seong, *Met. Mater. Int.* **2009**, 15, 239.
- [73] M. R. Barnett, in *Advances in Wrought Magnesium Alloys* (Eds: C. Bettles, M. Barnett), Woodhead Publishing, Sawston, Cambridge **2012**, pp. 105–143.
- [74] L. Jiang, J. J. Jonas, A. A. Luo, A. K. Sachdev, S. Godet, *Scr. Mater.* **2006**, 54, 771.
- [75] S. Sandlöbes, S. Zaefferer, I. Schestakow, S. Yi, R. Gonzalez-Martinez, *Acta Mater.* **2011**, 59, 429.
- [76] K. Y. Xie, Z. Alam, A. Caffee, K. J. Hemker, *Scr. Mater.* **2016**, 112, 75.
- [77] R. Ahmad, Z. Wu, W. A. Curtin, *Acta Mater.* **2020**, 183, 228.
- [78] Z. Wu, W. A. Curtin, *Proc. Natl. Acad. Sci. U S A* **2016**, 113, 11137.
- [79] Z. Wu, R. Ahmad, B. Yin, S. Sandlöbes, W. A. Curtin, *Science* **2018**, 359, 447.
- [80] G. Zhu, L. Wang, H. Zhou, J. Wang, Y. Shen, P. Tu, H. Zhu, W. Liu, P. Jin, X. Zeng, *Int. J. Plast.* **2019**, 120, 164.
- [81] U. M. Chaudry, T. H. Kim, S. D. Park, Y. S. Kim, K. Hamad, J.-G. Kim, *Metall. Mater. Trans. A* **2019**, 739, 289.
- [82] K.-H. Kim, J. H. Hwang, H.-S. Jang, J. B. Jeon, N. J. Kim, B.-J. Lee, *Metall. Mater. Trans. A* **2018**, 715, 266.
- [83] W. Hume-Rothery, G. W. Mabbott, K. M. C. Evans, *Philos. Trans. Royal Soc. A* **1934**, 233, 1.
- [84] W. Gambin, *Textures and Plasticity*, Springer Science & Business Media, Berlin **2001**.
- [85] I. Basu, T. Al-Samman, *Metall. Mater. Trans. A* **2017**, 707, 232.
- [86] A. Chapuis, Q. Liu, *Comput. Mater. Sci.* **2015**, 97, 121.
- [87] C. Ha, J. Bohlen, S. Yi, X. Zhou, H.-G. Brokmeier, N. Schell, D. Letzig, K. U. Kainer, *Metall. Mater. Trans. A* **2019**, 761, 138053.
- [88] C. Ha, J. Bohlen, X. Zhou, H. G. Brokmeier, K. U. Kainer, N. Schell, D. Letzig, S. Yi, *Mater. Charact.* **2021**, 175, 111044.
- [89] D. Guan, X. Liu, J. Gao, L. Ma, B. P. Wynne, W. M. Rainforth, *Sci. Rep.* **2019**, 9, 7152.
- [90] J.-Y. Lee, Y.-S. Yun, W.-T. Kim, D.-H. Kim, *Met. Mater. Int.* **2014**, 20, 885.
- [91] W. J. Delis, L. Berners, S. Korte-Kerzel, S. Sandlöbes-Haut, *Metals* **2023**, 13, 712.

Publication 2

Effect of lean alloyed Al and Ca on the texture development of cold rolled Mg-sheets

W. J. Delis, L. Berners, S. Korte-Kerzel, S. Sandlöbes-Haut

2023, Metals 13(4), 712

<https://doi.org/10.3390/met13040712>

For this publication, the candidate (in collaboration with Lukas Berners as part of his master's thesis supervised by the candidate) performed all the experiments and evaluated and analysed the results. In collaboration with the co-authors, the candidate wrote the original manuscript as well as the final reviewed version.

Article

Effect of Lean Alloyed Al and Ca on the Texture Development of Cold Rolled Mg Sheets

Wassilios J. Delis , Lukas Berners, Sandra Korte-Kerzel  and Stefanie Sandlöbes-Haut

Institute for Physical Metallurgy and Materials Physics, RWTH Aachen University, 52074 Aachen, Germany

* Correspondence: delis@imm.rwth-aachen.de

Abstract: Lean alloyed Mg-Al-Ca alloys reveal weakened basal-type texture intensities and increased room-temperature ductility when compared to pure Mg. Since the combined effects of the alloying elements Al and Ca on texture evolution are not yet fully understood, in this study, two binary and seven ternary Mg-Al-Ca alloys (ranging between 0–2 wt.-% Al and 0–0.5 wt.-% Ca) were subjected to cold rolling with texture measurement after each rolling step. These measurements showed that the basal-type texture of Mg is weakened by the addition of Ca, while the addition of Al leads to stronger basal-type textures compared to the samples containing Ca. The joint effect of Al and Ca can, for specific alloy compositions, lead to a steady-state basal texture intensity, which does not become stronger with further rolling. We expect that the solubility limit of Ca in Mg affects this behaviour. For comparison, mechanical properties were obtained by compression testing, showing high degrees of deformation, of 15–25%.

Keywords: Mg-Al-Ca alloys; solid solution; cold rolling; mechanical properties; scanning electron microscopy



Citation: Delis, W.J.; Berners, L.; Korte-Kerzel, S.; Sandlöbes-Haut, S. Effect of Lean Alloyed Al and Ca on the Texture Development of Cold Rolled Mg Sheets. *Metals* **2023**, *13*, 712. <https://doi.org/10.3390/met13040712>

Academic Editor: Zbigniew Pater

Received: 10 March 2023

Revised: 24 March 2023

Accepted: 25 March 2023

Published: 5 April 2023



Copyright: © 2023 by the authors. Licensee MDPI, Basel, Switzerland. This article is an open access article distributed under the terms and conditions of the Creative Commons Attribution (CC BY) license (<https://creativecommons.org/licenses/by/4.0/>).

1. Introduction

Magnesium and Mg alloys combine low density with moderate strengths, delivering a promising lightweight structural metal to replace common Al alloys and modern steels and further increase the efficiency of industrial applications [1]. However, their poor room-temperature ductility, which is mainly caused by their hexagonal structure, prevents wrought Mg alloys from entering commercial processing [2,3]. The activation of mainly basal slip and tension twinning limits the overall formability and leads to sharp basal-type textures during cold rolling [4,5].

Therefore, further cold rolling leads to premature failure and complex processing routes need to be applied. Extrusion [6,7], asymmetric/cross rolling [8–10], and microstructure optimisation with grain refinement [11–13] have been successfully used in previous research to modify the texture. Intrinsic alloy development approaches with the addition of alloying elements have also been established. In particular, the addition of rare earth (RE) elements [14–17], especially Y [18,19], Gd [18], Nd [15,20], and Ce [18,21], has been shown to lead to texture improvement.

To overcome the use of these costly and rare elements, Pei et al. [22] and Sandlöbes et al. [23] identified Mg-Al-Ca as a suitable alloy system with similar texture weakening behaviour. Even small amounts of the alloying elements showed a significant impact on the texture formation compared to pure Mg. Here, a higher level of non-basal slip activity was observed. Non-basal slip is known to contribute to texture weakening and to increase formability [14,24]. Recently, Jo et al. [25] investigated the impact of the Al content in Mg-Al-Ca alloys, confirming texture weakening and the improvement of the formability with decreasing amounts of Al. Further, Nandy et al. [26] indicated that the addition of Ca weakens the basal texture and decreases the critical resolved shear stress (CRSS) anisotropy, leading to enhanced ductility, while Al helps to increase strength. In our

previous study [27], texture measurements of as-recrystallized (as-RX) samples with the same compositions as those investigated in this work also showed weaker basal textures and revealed that the alloy system is very sensitive towards compositional changes.

It has been shown that the initial texture is an important parameter influencing the formability during cold rolling. For an AZ31 alloy, Atik et al. [28] measured higher strains during cold rolling with off-basal textures and less strain localisation than with the initial basal-type texture. In addition, high amounts of tension twins were observed. Further, in the same alloy system, shear bands were observed after a height reduction of 10% during the cold rolling of a sample with a basal-type texture and no shear bands for an off-basal texture [29]. The lack of shear bands was attributed to the activation of both prismatic $\langle a \rangle$ slip and tension twinning. Recently, Lee et al. [30] showed large shear bands for AZ31, which they attributed to double twins occurring during cold rolling of a sample with a basal-type texture, whereas, in a sample of the same alloy with an off-basal texture, it was mainly the tension twins that were active, leading to very fine micro-shear bands and, therefore, a finer microstructure.

The influence of both the initial textures and the two alloying elements, Al and Ca, on the texture in Mg during cold rolling remains to be unraveled. This study aims to systematically determine the effect of the Al and Ca contents on the texture by varying their amounts and investigating the influence of different cold-rolling degrees, considering samples with basal normal direction (ND) as well as off-basal transverse direction (TD) orientations. To achieve this aim, we deformed two binary and seven ternary Mg-Al-Ca alloys by step-wise cold rolling, and analysed their texture and microstructure after each rolling step using x-ray diffraction (XRD) and electron backscatter diffraction (EBSD).

2. Experimental Methods

Sample synthesis was performed by casting and subsequent hot rolling to an overall thickness reduction of 50%. Elemental Mg, Al, and Ca with purities higher than 99.98% were used as starting materials. The casting procedure was conducted in an induction furnace under pressure and Ar atmosphere. The subsequent hot rolling was achieved in thickness-reduction steps of 10% at 430 °C, with intermediate reheating of 10 min. Next, at an annealing temperature of 450 °C, a recrystallization treatment with subsequent water quenching was carried out. Table 1 shows the investigated sample compositions in wt.-%, which is used throughout this study unless otherwise stated.

Table 1. Investigated compositions in wt.-% with their nominal and measured chemical compositions (with ICP-OES), respectively.

Sample	Nominal Composition	Mg	Al	Ca	Cu	Ni
S1	1Al-0.5Ca	Bal.	1.040	0.524	<0.002	<0.002
S2	1Al-0.005Ca	Bal.	1.080	0.006	0.004	<0.002
S3	1Al-0.1Ca	Bal.	1.040	0.103	<0.002	<0.002
S4	1Al-0.2Ca	Bal.	1.100	0.232	0.002	<0.002
S5	2Al-0.005Ca	Bal.	2.110	0.007	<0.002	<0.002
S6	2Al-0.1Ca	Bal.	2.140	0.113	<0.002	<0.002
S7	2Al-0.2Ca	Bal.	2.120	0.214	0.002	<0.002
S8	0.1Ca	Bal.	0.044	0.108	<0.002	<0.002
S9	1Al	Bal.	1.000	<0.001	<0.001	<0.001

Samples for texture measurement were cut out of the sheets with electrical discharge machining (EDM). The ND samples had a fixed length of 3 cm and width of 1.5 cm, while the TD samples were 3 cm long and 1 cm high. The variable dimension was the initial sheet thickness, which varied between 11.9 and 13.4 mm. A rolling mill from Carl Wezel

Mühlacker was used to perform cold rolling. The roll diameter was 250 mm and the rotation velocity was 15.7 m/min. The target height reduction (ϵ_h) per pass was 5%. Between the rolling steps, a slice of 4–5 mm was cut by EDM for texture investigation. This procedure was identical for both investigated rolling directions with ND and TD facing upwards, respectively. Throughout this paper, the sample nomenclature is “S_x_ND/TD_ε%”, with x indicating the sample composition and ε% denoting the height reduction. The mechanical properties were measured with compression tests in the same loading direction as during cold rolling with the TD orientation facing upwards. The cylindrical compression samples had a diameter of 6 mm and were 9 mm high. A ZWICK 1484 universal testing machine (ZwickRoell AG, Ulm, Germany) was used for testing, with an initial strain rate of 10^{-3} s^{-1} .

Texture measurements were conducted with a D8 Advance X-ray texture diffractometer (Bruker, Karlsruhe, Germany) with a FeK α target. All specimens were mechanically ground and polished with diamond paste down to 1 μm . A total of six pole figures were measured per sample. Parameters used for the orientation distribution function (ODF) calculation were 3.5° for half width and resolution, respectively. For both ND- and TD-oriented samples, the rotation of the ODF from the ND–TD-plane to the RD–TD-plane was necessary to visualise basal (0002)-peak intensities.

For EBSD, the samples were further polished with diamond paste to 0.25 μm and finished with an electropolishing step using AC2 by Struers (30 V, 30 s, -20 – -30°C) (Struers GmbH, Willich, Germany). A Helios Nanolab 600i (FEL, Eindhoven, The Netherlands) was used for imaging using a current of 5.5 nA and acceleration voltage of 20 kV, with a 70° tilted sample setup. Further analysis of the texture components was performed with the MTEX package for MATLAB (2020a, MathWorks, Inc., MA, USA) [31] and Python (3.8, Python Software Foundation, DE, USA).

In addition to the representation of the texture in (0002) pole figures, two distinct features of the textures were analysed: the spread ratio of the basal peak towards TD and RD directions and the prevalence of a component in the pole figures. For the spread-ratio parameter, the basal peak was averaged in a range of 10° around TD and RD, respectively. The spread of the basal peak towards TD or RD is represented by the integral half width of both averaged peaks, which was calculated using Simpson’s rule. The ratio of TD over RD represents a prevalence of TD spread when the parameter was larger than one. With respect to the prevalent component, only the rim of the $\{10\bar{1}0\}$ pole figure was plotted to obtain a one-dimensional representation, which is more intuitive to analyse.

3. Results

3.1. Mechanical Properties and Cold Rolling

The screening of the mechanical properties was performed through compression testing of the as-recrystallized material. Compression testing was selected, as the stress state during compression testing is more similar to the stress state during rolling than tensile testing. However, tensile tests on the same alloys were reported in [27]. The results of the compression tests are shown in Figure 1.

All the alloys showed clear ductile behaviour, with at least 15% compressive strain for alloy S9 (Mg-1Al) and up to 25% for alloy S7 (Mg-2Al-0.2Ca). While the yield stresses for all the alloys were similar, at around 45 MPa (except alloy S9 (Mg-1Al), with 22 MPa), the ultimate compressive strength (UCS) showed differences between the alloys. The binary alloys S8 and S9 delivered the lowest UCS values, at 286 MPa and 280 MPa, respectively. The highest UCS in the group of alloys containing 1 wt.-% Al was 338 MPa (S3 (Mg-1Al-0.1Ca)), while the highest UCS in the group of alloys with 2 wt.-% Al was 366 MPa (S6 (Mg-2Al-0.1Ca)).

A relative height reduction of up to 25% was reached for all the samples during cold rolling. Among the S_ND samples, S9_ND (Mg-1Al) reached the lowest height reduction, with 15%, S7_ND (Mg-2Al-0.2Ca), and S8_ND (Mg-0.1Ca) reached 25%; all the other alloys deformed to 20%. Among the S_TD samples, S9_TD (Mg-1Al) reached a height reduction

of only 15%, S6_TD (Mg-2Al-0.1Ca) and S7_TD (Mg-2Al-0.2Ca) deformed to 20%, and all the other alloys reached 25%.

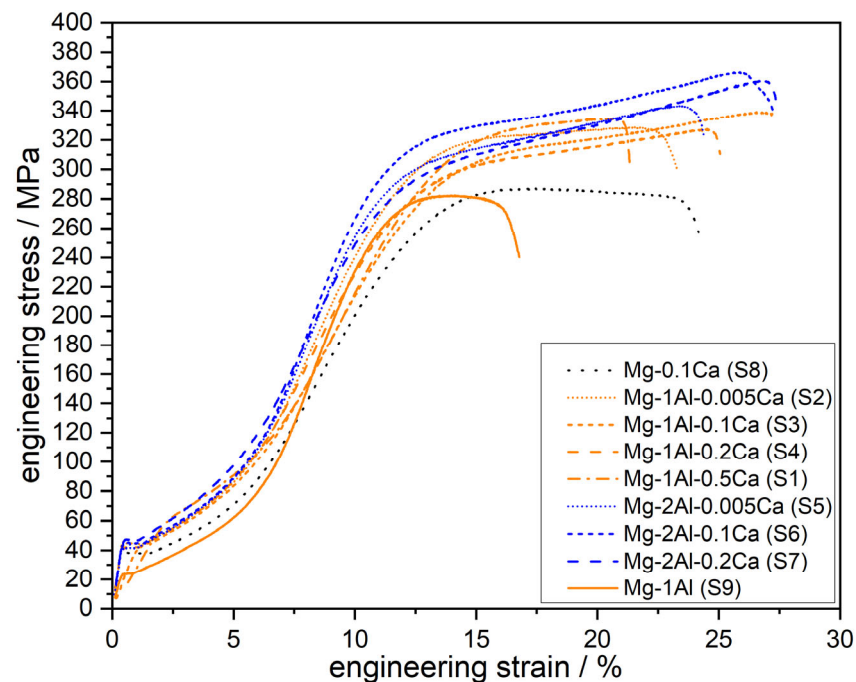


Figure 1. Stress–strain behaviour of the investigated Mg–Al–Ca alloys under compression loading in TD direction.

3.2. Texture Development—Pole Figure Types

To describe the texture evolution during cold rolling, a total of 64 pole figures were measured and evaluated. Five different types of pole figure shape were distinguished for both the S_ND and S_TD samples, as follows: ‘Smooth’ pole figures, with clear peaks; ‘scattered’ pole figures, with more than one peak in an undefined manner; and ‘split’ pole figures, with two peaks split in a defined direction. For the ‘unclear’ pole figures, it was difficult to categorise the peaks between the first three types and they did not show systematic connections among themselves (denoted by the question mark in Figure 2). The ‘intermediate’ pole figures showed peaks both at the rim and in the centre of the pole figure, indicating a peak rotation. An example of each type is depicted in Figure 2.

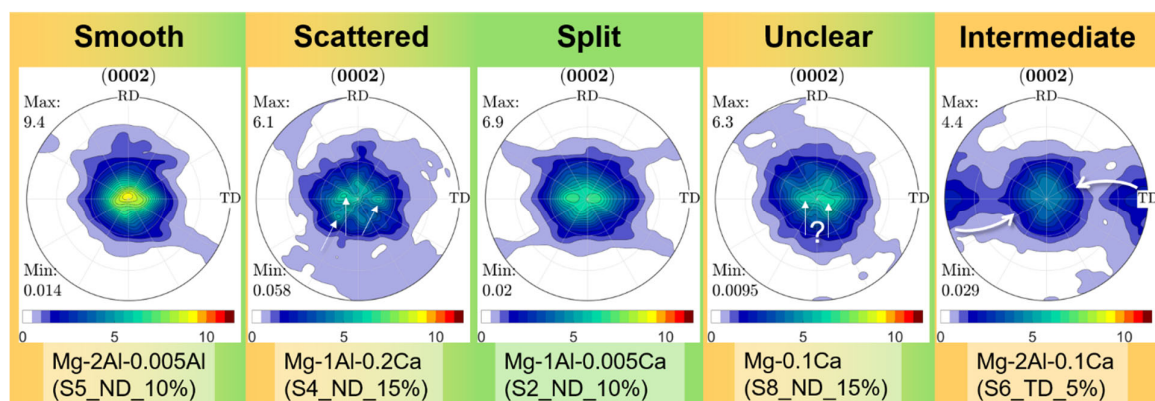


Figure 2. Observed types of pole figure for samples with different compositions and rolling reductions (in %) deformed in normal direction (ND) and transverse direction (TD). Yellow and green background colours indicate whether the type was observed for ND (green), TD (yellow), or both directions.

While the ‘smooth’, ‘scattered’, and ‘unclear’ types occur in both the S_ND sample and the S_TD sample, the TD split is only observed for two of the S_ND samples, namely the S1_ND_5% (Mg-1Al-0.5Ca) and S2_ND_10% (Mg-1Al-0.005Ca) samples. The ‘intermediate’ type only occurs during the investigation of the S_TD samples. ‘Smooth’ pole figure types can be predominantly seen in the pole figures with higher maximum basal intensities (>6 multiples of a random distribution (m.r.d.)) and increasing degrees of cold rolling (10–25%). In contrast, the ‘scattered’ types are more frequently observed for the pole figures with lower maximum basal intensities (≤ 6 m.r.d.) and rolling degrees between 0 and 5%. ‘Unclear’ types can not be attributed to distinct samples or rolling degrees. The ‘intermediate’ type is found for the S_TD_5% samples, indicating the rotation of the grains after the change in the rolling orientation before rotating back into the basal orientation. An overview of the association of the measured pole figures with the types, depending on both the height reduction and the chemical composition, can be seen in Figure 3.

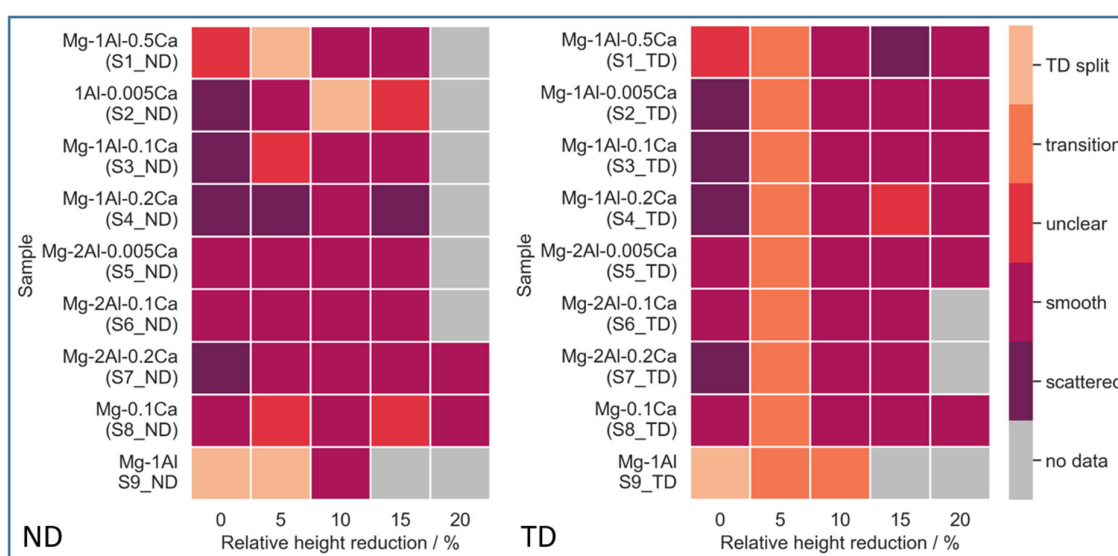


Figure 3. Overview of the pole-figure types for the investigated alloys. Left, S_ND samples, and Right, S_TD samples.

3.3. Texture Development—ND Samples

3.3.1. Development of the Basal Peak Intensity

For the ND samples, the development of the basal peak intensities for the different alloys is depicted in Figure 4.

The S9_ND (Mg-1Al) has the highest initial as-RX intensity, followed by the alloys with 2 wt.-% Al at around 7 m.r.d. All the other alloys with 1 wt.-% Al have lower initial intensities around 5 m.r.d. An exception is S2_ND (Mg-1Al-0.005Ca), which has an initial intensity of 8.5 m.r.d. The binary S8 lays in between, with an initial basal intensity of almost 6 m.r.d.

The different alloys show varying evolution in their basal peak intensity during the ongoing deformation. Regarding the alloys containing 2 wt.-% Al, the samples S5_ND (Mg-2Al-0.005Ca) and S6_ND (Mg-2Al-0.1Ca) show a sharp increase in basal texture intensity after the first rolling step, stable intensities in the case of the S5_ND (Mg-2Al-0.005Ca), and further slight increases in the case of the S6_ND (Mg-2Al-0.1Ca) sample during further rolling. The S9_ND (Mg-1Al) behaves similarly to the S5_ND (Mg-2Al-0.005Ca). In contrast, the S7_ND (Mg-2Al-0.2Ca) sample exhibits constant basal intensities throughout the rolling process. For the alloys containing 1 wt.-% Al, the alloys with low initial basal-texture intensities (S1_ND (Mg-1Al-0.5Ca), S3_ND (Mg-1Al-0.1Ca), and S4_ND (Mg-1Al-0.2Ca)) experience a slight increase, from around 5 m.r.d to around 6 m.r.d, during the rolling process. The S2_ND (Mg-1Al-0.005Ca) sample, on the other hand, shows a decrease in

intensity until a height reduction of 10% was reached, while at 15%, an increase to similar basal intensities to the initial value is detected. For the S8_ND (Mg-0.1Ca) sample, a first increase is followed by a decrease to almost the initial intensity. In the last rolling step, another increase leads to a final basal peak intensity of 7.3 m.r.d.

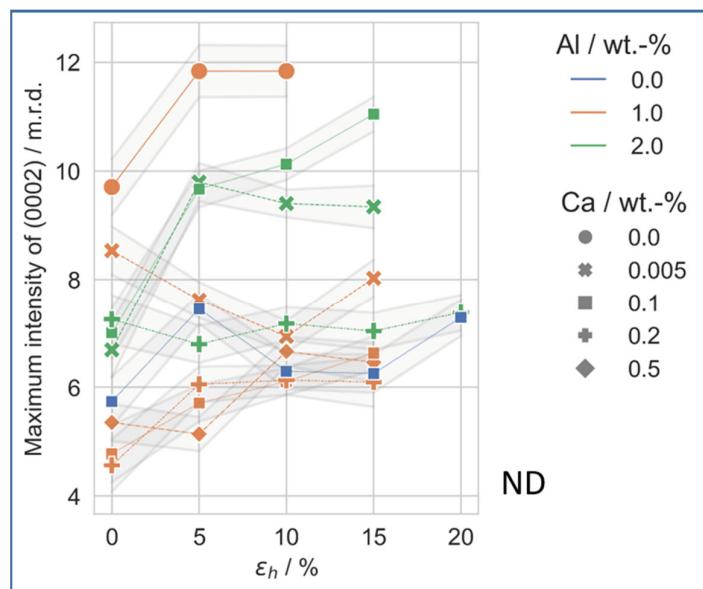


Figure 4. Maximum intensities of the basal (0002) peak for S_ND samples related to the relative height reduction (ϵ_h) during cold rolling, including the absolute mean error resulting from the recalculation.

3.3.2. Development of the Peak Shape

In addition to the maximum basal pole-figure intensity, the peak shape was investigated to illustrate the spread of the peak towards TD or RD, as explained in the section on the experimental methods. As shown in Figure 5, most of the samples exhibit a spread ratio of over 1, which indicates a spread towards TD.

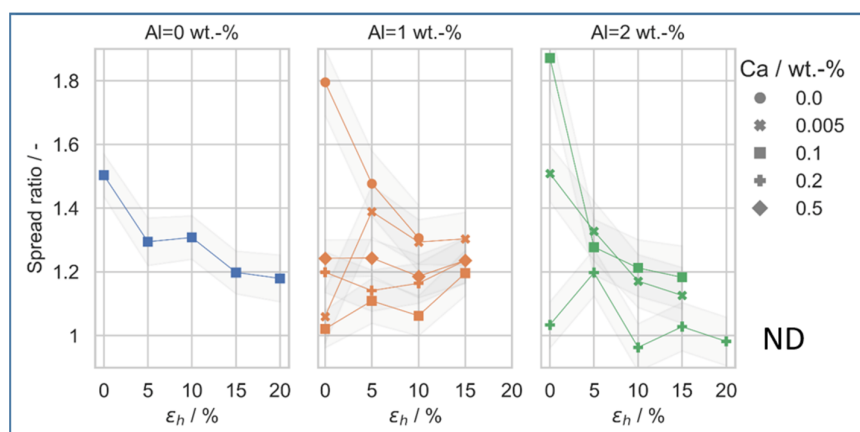


Figure 5. Spread ratio of the peak shape related to the relative height reduction (ϵ_h) towards rolling direction (RD)/TD of the pole figures for S_ND samples, including the error in the spread towards RD and TD estimated at 1.75° (half of the resolution).

While the samples containing 0 wt.-% Al and 2 wt.-% Al show a decrease in TD spread towards higher rolling degrees, for the 1 wt.-% Al samples, a more stable spread ratio, of approximately 1.2, is measured. In case of the S6_ND (Mg-2Al-0.1Ca) sample, the initial pole figure has the highest spread ratio, at over 1.8. The sample S7_ND (Mg-2Al-0.2Ca) has the least overall spread.

3.3.3. Development of the Prevalent Components

The measured intensities of the $\{10\bar{1}0\}$ -pole figures were analysed to identify prevalent components of the different alloys. Therefore, the rims of these pole figures were investigated. The calculated intensities can be seen in Figure 6.

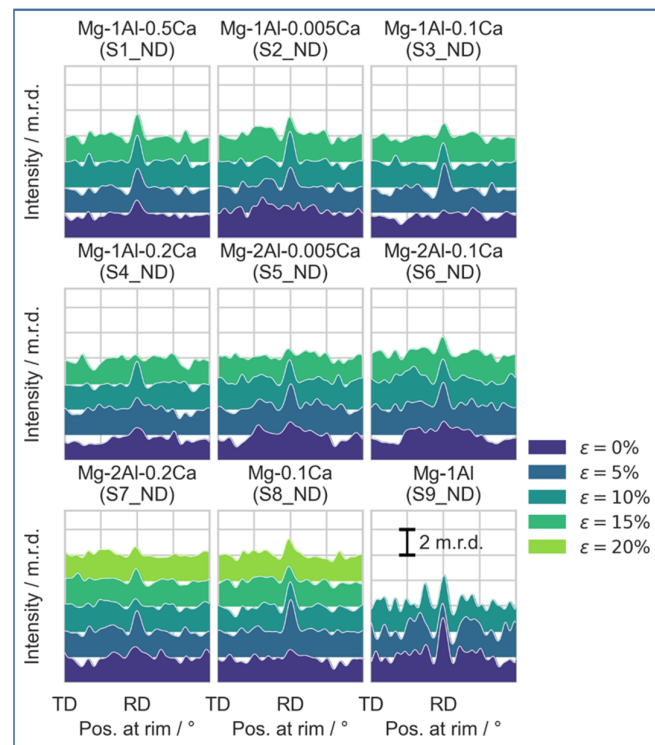


Figure 6. Preferred components for S_ND samples as variation along the rim of the $\{10\bar{1}0\}$ -pole figures. Distance between TD and RD is 90° .

Mainly, there is a slight prevalence of the $\{10\bar{1}0\}$ poles lying parallel to the RD. For the as-RX conditions, only S1_ND (Mg-1Al-0.5Ca) shows this prevalence, while the other alloys have a more random variation in intensity. With increasing degrees of deformation, this prevalence tends to intensify. An exception to this rule is visible only for the S4_ND_5% (Mg-1Al-0.2Ca), S4_ND_15% (Mg-1Al-0.2Ca), S5_ND_15% (Mg-2Al-0.005Ca), and S7_ND_20% (Mg-2Al-0.2Ca).

3.4. Texture Development—TD Samples

3.4.1. Development of the Basal Peak Intensity

As with the S_ND samples, the basal peak intensities of the S_TD samples were investigated. The resulting basal peak intensities are shown in Figure 7.

In the S_TD samples, the values for the initial textures are the same as those in Figure 4. From that point, a significant drop in basal intensity with initial straining is observed for all the alloys. However, at a height reduction of 10%, the basal peak intensities increase to almost the initial values (except S2_TD (Mg-1Al-0.005Ca)). Further deformation leads to almost constant basal peak intensities until failure. Contrary to this observation, the S9_TD (Mg-1Al) does not exhibit this texture reorientation during the investigated range of height reductions, and only a decreasing trend in the basal peak intensity is visible. Overall, the alloys containing 2 wt.-% Al show higher basal peak intensities after the peak rotation, in comparison to the alloys containing 1 wt.-% Al. The binary S8_TD (Mg-0.1Ca) has basal peak intensities in the same range as the alloys containing 1 wt.-% Al.

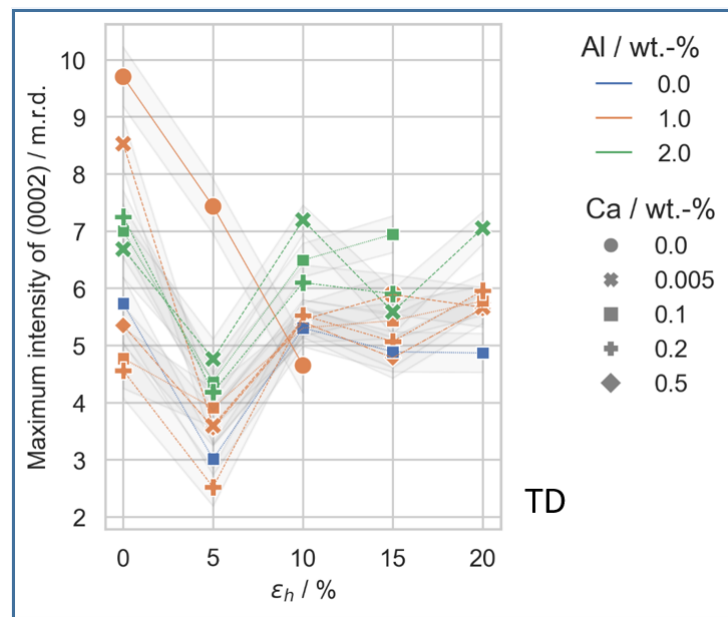


Figure 7. Maximum intensities of the basal (0002) peak for S_TD samples related to the relative height reduction (ϵ_h) during cold rolling, including the absolute mean error resulting from the recalculation.

3.4.2. Development of the Peak Shape

As with the S_ND samples, the S_TD samples' spread ratio was evaluated. The measured spread ratio can be seen in Figure 8.

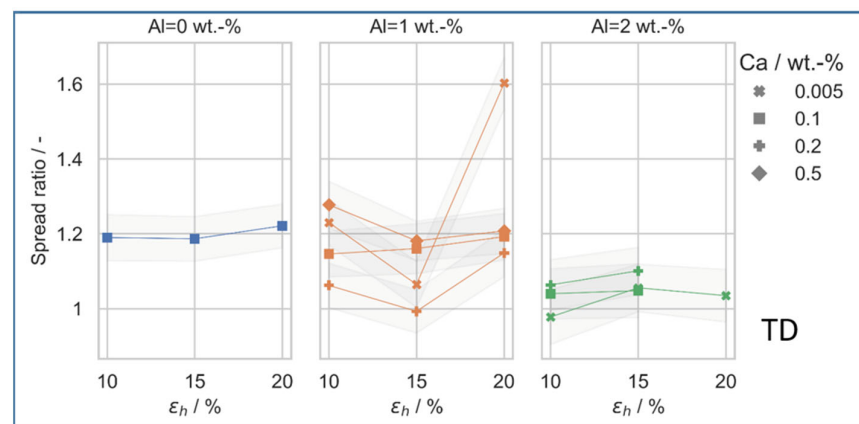


Figure 8. Spread ratio of the peak shape related to the error relative height reduction (ϵ_h) towards RD/TD of the pole figures for S_TD samples, including the error in the spread towards RD and TD estimated at 1.75° (half of the resolution).

Here, the spread ratio is shown after the peak reoriented at a height reduction of 10%. In contrast to the S_ND samples, the spread ratio remains more stable. Only sample S1_TD_20% (Mg-1Al-0.5Ca) exhibits a sharp increase in spread ratio. A visible trend is that with the increasing Al content, the spread ratio tends to decrease. For the alloy containing 0 wt.-% Al, the spread ratio is 1.2, and for the alloys containing 2 wt.-% Al, it is around 1. The alloys containing 1 wt.-% Al alloys lay in between those containing 0 and 2 wt.-% Al.

3.4.3. Development of the Prevalent Components

The prevalent components were also studied for the S_TD samples. The results can be seen in Figure 9.

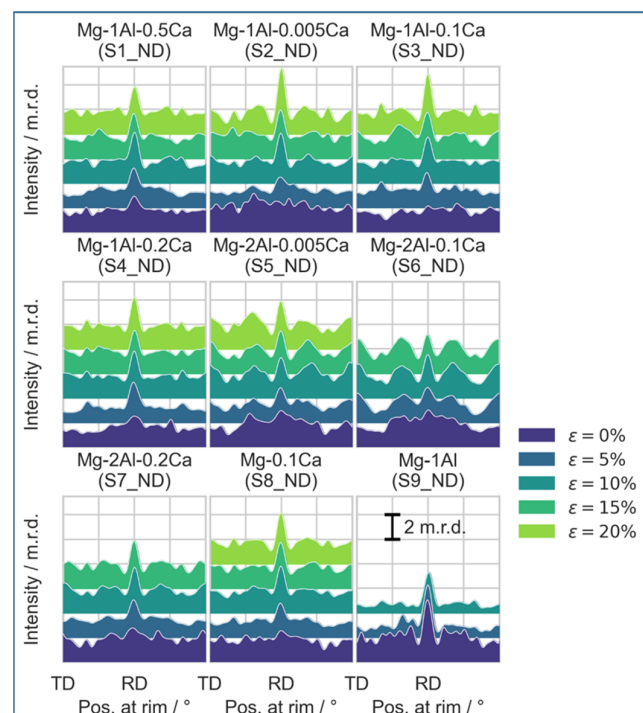


Figure 9. Preferred components for S_TD samples as variation along the rim of the $\{10\bar{1}0\}$ -pole figures. Distance between TD and RD is 90° .

As with the S_ND samples, for the S_TD samples, a prevalence of $\{10\bar{1}0\}$ poles lying parallel to RD is visible. Among the S_TD samples, all the deformed samples show this prevalence, which tends to intensify with increasing degrees of deformation. A slight peak inclined by 30° towards the TD can be seen for most of the samples. The S2_TD (Mg-1Al-0.005Ca), S5_TD (Mg-2Al-0.005Ca), and S6_TD (Mg-2Al-0.1Ca) have the strongest magnitude of these peaks. It should be noted that the S_TD samples show prevalent components with a more pronounced and less scattered appearance.

4. Discussion

4.1. Mechanical Properties and Deformation under Cold Rolling Conditions

In our previous work [27], we investigated the mechanical properties of the same alloys using tensile and compression testing, revealing that, especially for ductile Mg alloys, casting defects and other impurities can lead to an underestimation of the formability. The maximum deformation of 15–25% during the compression testing is of the same order of magnitude as that achieved during cold rolling. For cold rolled pure Mg, maximum deformations of only 10% have been observed [23]. It should be noted that for the S_ND samples, more samples failed during the 20% rolling step, while among the S_TD samples, most failed during the 25% rolling step. This might indicate that the 90° tilt of the texture allows slightly higher deformation.

4.2. Sources of Error

Different error sources that affect the texture measurement have to be considered. A negligible influence is attributed to the sample preparation. Fan et al. [32] reported that only in materials with a high atomic number and, thus a low penetration depth for X-ray, sample preparation might induce errors in XRD measurements. This is not the case for Mg alloys. In addition, no differences were observed between unprepared samples and samples polished up to $1\ \mu\text{m}$ by Jäger et al. [33]. Intensity variations in the X-ray source can occur; however, these are also negligible because intensities are normalised and the background of the measurement is known. Also, aberrations due to X-ray optics and absorption should not have a strong effect, as the measured data are automatically corrected for potential

errors. The strongest influence on the resulting pole figures is considered to be caused by the determination of the ODFs. The chosen parameters for half width and the resolution of the grid during the calculation of the ODFs affect the basal peak intensities and pole figure shapes. In particular, when comparing texture-related parameters to values from the literature, the selection of the parameters for pole figure calculation has to be taken into account carefully. We therefore suggest the inclusion of these parameters into publications on texture.

Throughout this study, all the parameters were kept in line with the values given in the section on the experimental methods to ensure the comparability of the pole figures.

4.3. Texture Development—ND Samples

All the investigated samples showed rather weak basal textures in the as-RX condition, which were much lower than those observed for pure Mg [19,34]. This was also observed in our previous study [27]. It has to be considered that the grain size of the S1_ND is slightly lower than that of the other alloys [27]. Generally, with further deformation, an increase in the basal peak intensity is expected, and has been seen in pure Mg [35], AZ31 [30], and other Mg-alloys [35–37]. For most of the alloys in this study, this texture evolution was also observed. The predominant activation of the basal $\langle a \rangle$ slip in Mg alloys is the main cause of the formation of basal-type textures, as reported by Chapuis et al. [38]. Basal slip leads to a reorientation of the basal slip planes perpendicular to the rolling force. This leads to a near-zero Schmid factor for basal slip and sharp basal textures [39]. Both the increasing basal peak intensity and the decreasing peak spread ratio indicate this reorientation through basal $\langle a \rangle$ slip.

A significant impact on both the as-RX texture and the texture evolution is attributed to the alloying elements. Here, Ca has a rather activating effect because very low amounts of Ca lead to texture weakening [40,41]. In contrast, the addition of Al has a more significant influence on the basal peak intensity. Generally, an increased activation of $\langle c + a \rangle$ slip can lead to a weaker basal texture in Mg-Al-Ca alloys [23,27]. Wu et al. [42] investigated the influence of the combined addition of Al and Ca to Mg with DFT calculations in the solid solution composition range, indicating a lower cross slip energy for the $\langle c + a \rangle$ -dislocations in comparison to the sole Al alloying or conventional AZ31. In our previous work, we proposed a strong connection between the Al content and both the solubility limit of Ca and the amount of Ca in the alloy [27]. The results of the present study confirm that this correlation appears to occur not only for the as-RX textures, but also for deformation textures. Increasing Al amounts lead to decreases in Ca solubility [25].

Three different effects can be distinguished. First, for low amounts of Al and Ca solved in the matrix, non-basal slip systems were activated. In cases such as this, remarkably low amounts of Ca (0.005 wt.-%) were sufficient to enable non-basal slip. Second, when the Al amount increased, less Ca was solved in the matrix and under ongoing deformation, basal slip was predominant. This led to increasing basal textures, especially for the S5_ND (Mg-2Al-0.005Ca) and S6_ND (Mg-2Al-0.1Ca) samples (compare Figure 4). Third, further increases in Ca induced a new additional mechanism that suppressed the strengthening of the basal-type texture. For this mechanism, we propose that the increasing influence of Ca segregation at grain boundaries observed by Nandy et al. [26] hinders grain rotations and supports weaker textures.

The peak spread analysis revealed a slight tendency towards a TD spread of the basal texture peak for most of the alloys and deformation degrees. In the literature, RD splitting is attributed to the activity of the $\langle c + a \rangle$ slip, while a TD split is formed by the activation of prismatic and/or pyramidal $\langle a \rangle$ slip [43,44]. For pure Mg [35], AZ31 [43], and Mg-Y alloys [19], often, RD splitting is observed. A similar TD spread was observed for Mg-RE alloys [14–16,45,46] and Ca-containing alloys [47,48]. Since our previous study [27] indicated significant activity of the pyramidal $\langle a \rangle$ slip, which increases with increasing Al, we assume that the high Al content caused the observed higher TD spread. Kim et al. [48] also noted that $\langle c + a \rangle$ slip was still possible, although a slight TD split was visible. As

more non-basal slip systems are active, an overlap between different slip systems is the most likely outcome [27].

Steiner et al. [49] found for an AZ31 alloy that the $\{0001\} \langle 10\bar{1}0 \rangle$ texture component, which was also found in the present study, evolves during cold rolling. The authors assumed that joint basal and prismatic slip is necessary to form this component. Interestingly, the S7_ND (Mg-2Al-0.2Ca) sample, which shows stable basal peak intensities, shows only a very weak presence of the $\{0001\} \langle 10\bar{1}0 \rangle$ texture component. According to Steiner et al. [49], the absence of prismatic slip could be concluded. A similar observation, with a more scattered texture, can be drawn for the S4_ND (Mg-1Al-0.2Ca) sample. To the authors' best knowledge, prismatic slip was not detected in Mg-Al-Ca-alloys with Ca contents above 0.2 wt.-% Ca [27]. We suggest, at least for alloys containing Al and 0.2 wt.-% Ca, that the activation of prismatic slip is hindered by either an increased CRSS for prismatic slip or, more likely, the easier activation of other slip systems. Furthermore, the increased ductility due to texture weakening with Ca-segregation, as observed by Nandy et al. [26], could lead to an increased activity of basal slip accommodating deformation in the $\langle a \rangle$ -direction, making the further activation of prismatic slip difficult.

An overview of the intensities of the basal peak in the as-RX condition and their evolution during cold rolling is given in Figure 10. As indicated, some of the alloys corresponded to two-phase fields, which led to precipitates in the case of S1 (Mg-1Al-0.5Ca), as previously shown in [27], while the other alloys very close to the solubility limit did not show precipitation behaviour. The influence of the precipitates can be considered negligible in the context of texture formation [27].

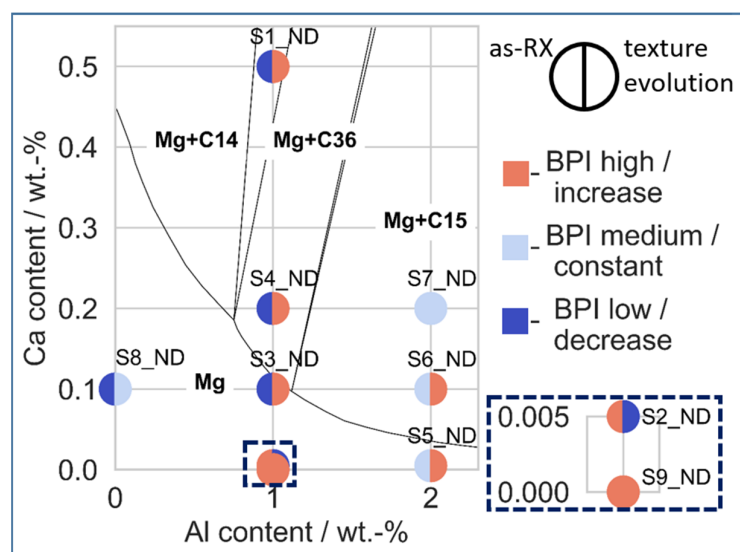


Figure 10. Overview of the as-RX basal peak intensities (BPI) and their evolution during cold rolling for the S_ND samples depicted in the Mg-rich corner of the Mg-Al-Ca phase diagram adapted from [27].

4.4. Texture Development—TD-Samples

The main difference between the S_ND and S_TD samples is the observed rotation of the basal peak parallel to the loading force. This rotation can be related to the ‘intermediate’ texture type presented previously. To investigate how this rotation was achieved, we additionally performed EBSD on two selected samples, the ternary TD_S4_5% (Mg-1Al-0.2Ca), which experienced rotation, and the binary TD_S9_5% (Mg-1Al), which did not experience rotation. Figure 11 shows representative inverse pole figure (IPF) and kernel average misorientation (KAM) maps of both samples.

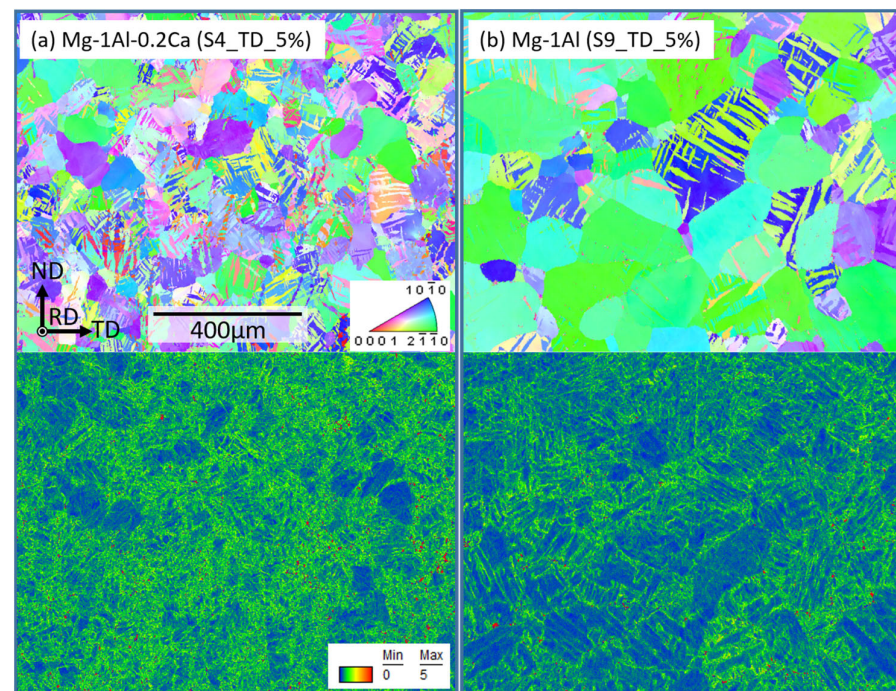


Figure 11. (a) S4_TD_5%: Top: IPF map. Bottom: KAM map. (b) S9_TD_5%: Top: IPF map. Bottom: KAM map.

Deformation twinning is active in both conditions, indicating that the reorientation was induced by deformation twinning, as was also reported by [50,51]. The tensile twins led to a re-orientation of the c-axis by about 86° , resulting in the observed basal-type texture after further rolling. Interestingly, the binary alloy did not show this reorientation. We consider two possible reasons for this observation. First, for the reorientation of the intrinsically larger grain sizes by deformation twinning, higher deformation degrees could be needed, as the nucleation of deformation twins mostly occurs at grain boundaries [52], resulting in premature failure before the reorientation has finished. Second, in addition to the large grain size, a pronounced basal-type texture is present. Therefore, fewer grains were preferably oriented for twinning and basal slip when compared to the other alloys investigated in this study, hindering homogenous strain accommodation. In comparison, the KAM maps in Figure 10 show that the alloy S4 (Mg-1Al-0.2Ca) contains both higher and more homogeneously distributed strain in its microstructure than alloy S9 (Mg-1Al). In addition to the previously proposed higher activation of $\langle c + a \rangle$ slip in most of the ternary alloys, we also attribute the increased formability to the small grain sizes in the alloys containing Ca, combined with weaker basal textures. The increased number of grains contributing to the deformation with generally easily activated deformation twinning and basal $\langle a \rangle$ slip was not compensable with non-basal slip and, hence, not negligible.

We observed for the S_ND samples that the as-RX basal peak strength also influenced the peak strength after the deformation. Here, a stronger as-RX basal peak intensity also led to a higher basal peak intensity after the cold rolling. Although the basal peak intensities after the reorientation increased to approximately the as-RX values, no further increase was seen during the ND cold rolling. The refinement of the microstructure during twinning probably allows more uniform deformation with further rolling, and the basal-type texture intensity does not increase further [30].

For the S_TD rolling orientation, the TD spread is smaller than that of the S_ND samples. In addition, the spread ratio remains constant until failure. This could indicate a uniform deformation, in which the activated slip systems contribute with similar fractions to the deformation. Different Schmid factors are also likely to have affected the TD spread, especially for the as-RX conditions.

5. Conclusions

In this study, seven Mg-Ca-Al alloys, one Mg-Ca alloy, and one Mg-Al alloy with systematically varied alloying contents were investigated to unravel the alloying-related effects on the texture development during cold rolling. The following conclusions can be drawn:

- All the investigated alloys showed a high degree of deformation compared to pure Mg during compression testing and cold rolling.
- The initial as-RX textures were weak for all the alloys compared to pure Mg.
- The cold rolling of the basal oriented samples (with the initial sheet in the normal direction) led to a gradual increase in the basal peak intensity, except for the Mg-1Al-0.005Ca, which showed a slight decrease until a height reduction of 10% was reached, followed by an increase.
- For the off-basal oriented samples (with the initial sheet in the transverse direction) the cold rolling resulted in a reorientation of the basal peak accompanied by a drop in basal peak intensity at a height reduction of 5%. At a height reduction of 10%, the reorientation was complete, and the basal peak intensity had similar levels to the initial texture strength. No further increase in the basal peak intensity was observed. The Mg-1Al did not show this reorientation, probably due to premature failure. Overall, the TD samples exhibited weaker basal peaks than the ND samples.
- The basal peak intensities of the initial and the cold rolling textures were dependent on both the Ca and the Al content. While increasing amounts of Al led to stronger basal peak intensities, the addition of Ca weakened the basal texture's intensity. It is proposed that the solubility of Ca is closely related to the texture formation. An increasing amount of Al lowers the solubility of Ca, which leads to an increase in basal peak intensity. Higher Ca addition again leads to weaker basal peak intensity, and might be used to overcome of this effect.

Author Contributions: Conceptualization, L.B., S.S.-H. and W.J.D.; methodology, W.J.D. and S.S.-H.; formal analysis, W.J.D. and L.B.; investigation, W.J.D. and L.B.; writing—original draft preparation, W.J.D. and L.B.; writing—review and editing, L.B., S.S.-H. and S.K.-K.; supervision, S.S.-H.; project administration, S.K.-K. and S.S.-H.; funding acquisition, S.K.-K. All authors have read and agreed to the published version of the manuscript.

Funding: We gratefully acknowledge funding by the Deutsche Forschungsgemeinschaft (DFG, German Research Foundation), SFB 1394(CRC 1394), Project-ID 409476157, subprojects A01, C02 and S.

Data Availability Statement: The data presented in this study are available on request from the corresponding author.

Acknowledgments: Many thanks to Hauke Springer for sample synthesis and to Luiz R. Guimarães for his support during sample preparation. Further, we would like to thank Risheng Pei for his support during texture measurements. In addition, David Beckers is acknowledged for his assistance during metallographic preparation and Gerd Schütz and Nico Poschmann for their support during sample rolling and processing. For his support during the interpretation and discussion of the results, we also want to thank Dierk Raabe.

Conflicts of Interest: The authors declare no conflict of interest.

References

1. Nie, J.F.; Shin, K.S.; Zeng, Z.R. Microstructure, Deformation, and Property of Wrought Magnesium Alloys. *Metall. Mater. Trans. A* **2020**, *51*, 6045–6109. [\[CrossRef\]](#)
2. Partridge, P.G. The crystallography and deformation modes of hexagonal close-packed metals. *Metall. Rev.* **1967**, *12*, 169–194. [\[CrossRef\]](#)
3. Yoo, M.H.; Wei, C.T. Slip Modes of Hexagonal-Close-Packed Metals. *J. Appl. Phys.* **1967**, *38*, 4317–4322. [\[CrossRef\]](#)
4. Agnew, S.R.; Duygulu, Ö. Plastic anisotropy and the role of non-basal slip in magnesium alloy AZ31B. *Int. J. Plast.* **2005**, *21*, 1161–1193. [\[CrossRef\]](#)

5. Hirsch, J.; Al-Samman, T. Superior light metals by texture engineering: Optimized aluminum and magnesium alloys for automotive applications. *Acta Mater.* **2013**, *61*, 818–843. [CrossRef]
6. Cheng, R.; Li, M.; Du, S.; Pan, H.; Liu, Y.; Gao, M.; Zhang, X.; Huang, Q.; Yang, C.; Ma, L.; et al. Effects of single-pass large-strain rolling on microstructure and mechanical properties of Mg–Al–Ca alloy sheet. *Mater. Sci. Eng. A* **2020**, *786*, 139332. [CrossRef]
7. Pan, H.; Yang, C.; Yang, Y.; Dai, Y.; Zhou, D.; Chai, L.; Huang, Q.; Yang, Q.; Liu, S.; Ren, Y.; et al. Ultra-fine grain size and exceptionally high strength in dilute Mg–Ca alloys achieved by conventional one-step extrusion. *Mater. Lett.* **2019**, *237*, 65–68. [CrossRef]
8. Biswas, S.; Kim, D.-I.; Suwas, S. Asymmetric and symmetric rolling of magnesium: Evolution of microstructure, texture and mechanical properties. *Mater. Sci. Eng. A* **2012**, *550*, 19–30. [CrossRef]
9. Chen, T.; Chen, Z.; Yi, L.; Xiong, J.; Liu, C. Effects of texture on anisotropy of mechanical properties in annealed Mg–0.6%Zr–1.0%Cd sheets by unidirectional and cross rolling. *Mater. Sci. Eng. A* **2014**, *615*, 324–330. [CrossRef]
10. Chino, Y.; Sassa, K.; Kamiya, A.; Mabuchi, M. Enhanced formability at elevated temperature of a cross-rolled magnesium alloy sheet. *Mater. Sci. Eng. A* **2006**, *441*, 349–356. [CrossRef]
11. Agnew, S.R.; Horton, J.A.; Lillo, T.M.; Brown, D.W. Enhanced ductility in strongly textured magnesium produced by equal channel angular processing. *Scr. Mater.* **2004**, *50*, 377–381. [CrossRef]
12. Jeong, Y.S.; Kim, W.J. Enhancement of mechanical properties and corrosion resistance of Mg–Ca alloys through microstructural refinement by indirect extrusion. *Corros. Sci.* **2014**, *82*, 392–403. [CrossRef]
13. Motoyama, T.; Watanabe, H.; Ikeo, N.; Mukai, T. Mechanical and damping properties of equal channel angular extrusion-processed Mg–Ca alloys. *Mater. Lett.* **2017**, *201*, 144–147. [CrossRef]
14. Imandoust, A.; Barrett, C.D.; Al-Samman, T.; Inal, K.A.; El Kadiri, H. A review on the effect of rare-earth elements on texture evolution during processing of magnesium alloys. *J. Mater. Sci.* **2016**, *52*, 1–29. [CrossRef]
15. Al-Samman, T.; Li, X. Sheet texture modification in magnesium-based alloys by selective rare earth alloying. *Mater. Sci. Eng. A* **2011**, *528*, 3809–3822. [CrossRef]
16. Bohlen, J.; Nürnberg, M.R.; Senn, J.W.; Letzig, D.; Agnew, S.R. The texture and anisotropy of magnesium–zinc–rare earth alloy sheets. *Acta Mater.* **2007**, *55*, 2101–2112. [CrossRef]
17. Stanford, N.; Barnett, M. Effect of composition on the texture and deformation behaviour of wrought Mg alloys. *Scr. Mater.* **2008**, *58*, 179–182. [CrossRef]
18. Stanford, N. Micro-alloying Mg with Y, Ce, Gd and La for texture modification—A comparative study. *Mater. Sci. Eng. A* **2010**, *527*, 2669–2677. [CrossRef]
19. Sandlöbes, S.; Zaefferer, S.; Schestakow, I.; Yi, S.; Gonzalez-Martinez, R. On the role of non-basal deformation mechanisms for the ductility of Mg and Mg–Y alloys. *Acta Mater.* **2011**, *59*, 429–439. [CrossRef]
20. Ha, C.W.; Bohlen, J.; Zhou, X.H.; Brokmeier, H.G.; Kainer, K.U.; Schell, N.; Letzig, D.; Yi, S.B. Texture development and dislocation activities in Mg–Nd and Mg–Ca alloy sheets. *Mater. Charact.* **2021**, *175*, 111044. [CrossRef]
21. Hadorn, J.P.; Mulay, R.P.; Hantzsche, K.; Yi, S.; Bohlen, J.; Letzig, D.; Agnew, S.R. Texture Weakening Effects in Ce-Containing Mg Alloys. *Metall. Mater. Trans. A* **2013**, *44*, 1566–1576. [CrossRef]
22. Pei, Z.; Friák, M.; Sandlöbes, S.; Nazarov, R.; Svendsen, B.; Raabe, D.; Neugebauer, J. Rapid theory-guided prototyping of ductile Mg alloys: From binary to multi-component materials. *New J. Phys.* **2015**, *17*, 093009. [CrossRef]
23. Sandlöbes, S.; Friák, M.; Korte-Kerzel, S.; Pei, Z.; Neugebauer, J.; Raabe, D. A rare-earth free magnesium alloy with improved intrinsic ductility. *Sci. Rep.* **2017**, *7*, 10458. [CrossRef] [PubMed]
24. Griffiths, D. Explaining texture weakening and improved formability in magnesium rare earth alloys. *Mater. Sci. Technol.* **2015**, *31*, 10–24. [CrossRef]
25. Jo, S.; Letzig, D.; Yi, S. Effect of Al Content on Texture Evolution and Recrystallization Behavior of Non-Flammable Magnesium Sheet Alloys. *Metals* **2021**, *11*, 468. [CrossRef]
26. Nandy, S.; Tsai, S.P.; Stephenson, L.; Raabe, D.; Zaefferer, S. The role of Ca, Al and Zn on room temperature ductility and grain boundary cohesion of magnesium. *J. Magnes. Alloys* **2021**, *9*, 1521–1536. [CrossRef]
27. Delis, W.J.; Huckfeldt, P.C.; Hallstedt, B.; Sun, P.L.; Raabe, D.; Korte-Kerzel, S.; Sandlöbes-Haut, S. Understanding the Role of Al and Ca on the Ductility of Mg–Al–Ca Alloys. 2023. Available online: https://papers.ssrn.com/sol3/papers.cfm?abstract_id=4358733 (accessed on 9 March 2023).
28. Atik, K.; Efe, M. Twinning-induced shear banding and its control in rolling of magnesium. *Mater. Sci. Eng. A* **2018**, *725*, 267–273. [CrossRef]
29. Chun, Y.B.; Davies, C.H.J. Texture effects on development of shear bands in rolled AZ31 alloy. *Mater. Sci. Eng. A* **2012**, *556*, 253–259. [CrossRef]
30. Lee, S.W.; Han, G.; Jun, T.S.; Park, S.H. Effects of initial texture on deformation behavior during cold rolling and static recrystallization during subsequent annealing of AZ31 alloy. *J. Mater. Sci. Technol.* **2021**, *66*, 139–149. [CrossRef]
31. Hielscher, R.; Schaeben, H. A novel pole figure inversion method: Specification of the MTEX algorithm. *J. Appl. Crystallogr.* **2008**, *41*, 1024–1037. [CrossRef]
32. Fan, H.Y.; Liu, S.F.; Guo, Y.; Deng, C.; Liu, Q. Quantifying the effects of surface quality on texture measurements of tantalum. *Appl. Surf. Sci.* **2015**, *339*, 15–21. [CrossRef]

33. Jäger, A.; Lukáč, P.; Gärtnerová, V.; Haloda, J.; Dopita, M. Influence of annealing on the microstructure of commercial Mg alloy AZ31 after mechanical forming. *Mater. Sci. Eng. A* **2006**, *432*, 20–25. [\[CrossRef\]](#)
34. Basu, I.; Al-Samman, T. Competitive twinning behavior in magnesium and its impact on recrystallization and texture formation. *Mater. Sci. Eng. A* **2017**, *707*, 232–244. [\[CrossRef\]](#)
35. Barnett, M.R.; Nave, M.D.; Bettles, C.J. Deformation microstructures and textures of some cold rolled Mg alloys. *Mater. Sci. Eng. A* **2004**, *386*, 205–211. [\[CrossRef\]](#)
36. Zeng, Z.R.; Bian, M.Z.; Xu, S.W.; Davies, C.H.J.; Birbilis, N.; Nie, J.F. Texture evolution during cold rolling of dilute Mg alloys. *Scr. Mater.* **2015**, *108*, 6–10. [\[CrossRef\]](#)
37. Wu, D.; Tang, W.N.; Chen, R.S.; Han, E.H. Strength enhancement of Mg–3Gd–1Zn alloy by cold rolling. *Trans. Nonferrous Met. Soc. China* **2013**, *23*, 301–306. [\[CrossRef\]](#)
38. Chapuis, A.; Liu, Q. Simulations of texture evolution for HCP metals: Influence of the main slip systems. *Comput. Mater. Sci.* **2015**, *97*, 121–126. [\[CrossRef\]](#)
39. Al-Samman, T.; Gottstein, G. Room temperature formability of a magnesium AZ31 alloy: Examining the role of texture on the deformation mechanisms. *Mater. Sci. Eng. A* **2008**, *488*, 406–414. [\[CrossRef\]](#)
40. Jiang, H.; Zhang, Y.; Kang, Q.; Xu, Z.; Dong, P.; Li, H. The influence of Ca and Gd microalloying on microstructure and mechanical property of hot-rolled Mg–3Al alloy. *Procedia Eng.* **2017**, *207*, 932–937. [\[CrossRef\]](#)
41. Zeng, Z.R.; Bian, M.Z.; Xu, S.W.; Davies, C.H.J.; Birbilis, N.; Nie, J.F. Effects of dilute additions of Zn and Ca on ductility of magnesium alloy sheet. *Mater. Sci. Eng. A* **2016**, *674*, 459–471. [\[CrossRef\]](#)
42. Wu, Z.; Ahmad, R.; Yin, B.; Sandlöbes, S.; Curtin, W.A. Mechanistic origin and prediction of enhanced ductility in magnesium alloys. *Science* **2018**, *359*, 447–452. [\[CrossRef\]](#) [\[PubMed\]](#)
43. Styczynski, A.; Hartig, C.; Bohlen, J.; Letzig, D. Cold rolling textures in AZ31 wrought magnesium alloy. *Scr. Mater.* **2004**, *50*, 943–947. [\[CrossRef\]](#)
44. Wang, Y.N.; Huang, J.C. Texture analysis in hexagonal materials. *Mater. Chem. Phys.* **2003**, *81*, 11–26. [\[CrossRef\]](#)
45. Chino, Y.; Sassa, K.; Mabuchi, M. Texture and Stretch Formability of Mg–1.5 mass%Zn–0.2 mass%Ce Alloy Rolled at Different Rolling Temperatures. *Mater. Trans.* **2008**, *49*, 2916–2918. [\[CrossRef\]](#)
46. Mackenzie, L.W.F.; Pekguleryuz, M.O. The recrystallization and texture of magnesium–zinc–cerium alloys. *Scr. Mater.* **2008**, *59*, 665–668. [\[CrossRef\]](#)
47. Chino, Y.; Huang, X.; Suzuki, K.; Mabuchi, M. Enhancement of Stretch Formability at Room Temperature by Addition of Ca in Mg–Zn Alloy. *Mater. Trans.* **2010**, *51*, 818–821. [\[CrossRef\]](#)
48. Kim, D.W.; Suh, B.C.; Shim, M.S.; Bae, J.H.; Kim, D.H.; Kim, N.J. Texture Evolution in Mg–Zn–Ca Alloy Sheets. *Metall. Mater. Trans. A* **2013**, *44*, 2950–2961. [\[CrossRef\]](#)
49. Steiner, M.A.; Bhattacharyya, J.J.; Agnew, S.R. The origin and enhancement of {0001} $\langle 112^-0 \rangle$ texture during heat treatment of rolled AZ31B magnesium alloys. *Acta Mater.* **2015**, *95*, 443–455. [\[CrossRef\]](#)
50. Al-Samman, T.; Gottstein, G. Influence of Starting Textures on the Development of Texture and Microstructure during Large Strain Hot Rolling of Pure Magnesium. *Solid State Phenom.* **2005**, *105*, 201–206. [\[CrossRef\]](#)
51. Yang, P.; Yu, Y.; Chen, L.; Mao, W. Experimental determination and theoretical prediction of twin orientations in magnesium alloy AZ31. *Scr. Mater.* **2004**, *50*, 1163–1168. [\[CrossRef\]](#)
52. Beyerlein, I.J.; Capolungo, L.; Marshall, P.E.; McCabe, R.J.; Tomé, C. Statistical analyses of deformation twinning in magnesium. *Philos. Mag.* **2010**, *90*, 2161–2190. [\[CrossRef\]](#)

Disclaimer/Publisher’s Note: The statements, opinions and data contained in all publications are solely those of the individual author(s) and contributor(s) and not of MDPI and/or the editor(s). MDPI and/or the editor(s) disclaim responsibility for any injury to people or property resulting from any ideas, methods, instructions or products referred to in the content.

Publication 3

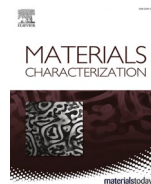
Metallographic preparation methods for the Mg based system Mg-Al-Ca and its Laves phases

D. Andre, M. Freund, U. Rehmann, W. J. Delis, M. Felten, J. Nowak, C. Tian,
M. Zubair, L. Tanure, L. Abdellaoui,
H. J. Springer, J. P. Best, D. B. Zander, G. Dehm,
S. Sandlöbes-Haut, S.Korte-Kerzel

2022, Materials Characterization, 192

<https://doi.org/10.1016/j.matchar.2022.112187>

For this publication, the candidate carried out the experiments to optimise of the metallographic preparation procedure for EBSD measurements of solid solution Mg-Al-Ca alloys and carried out the SEM observations and their evaluation for this part. The candidate wrote the relevant sections in the Experimental and Results and Discussion sections of the original manuscript and the final published version in collaboration with the co-authors.



Metallographic preparation methods for the Mg based system Mg-Al-Ca and its Laves phases

D. Andre^{a,*}, M. Freund^a, U. Rehman^b, W. Delis^a, M. Felten^c, J. Nowak^c, C. Tian^{b,1},
M. Zubair^{a,d}, L. Tanure^{b,e}, L. Abdellaoui^b, H. Springer^{b,e}, J.P. Best^b, D. Zander^c, G. Dehm^b,
S. Sandlöbes-Haut^a, S. Korte-Kerzel^a

^a Institute for Physical Metallurgy and Materials Physics, RWTH Aachen University, Aachen, Germany

^b Max-Planck-Institut für Eisenforschung GmbH, Max-Planck-Strasse 1, Düsseldorf, Germany

^c Chair of Corrosion and Corrosion Protection, RWTH Aachen University, Aachen, Germany

^d Department of Metallurgical and Materials Engineering, UET, Lahore, Pakistan

^e Institute of Metal Forming, RWTH Aachen University, Aachen, Germany

ARTICLE INFO

Keywords:

Mg-Al-Ca alloys
Solid solution Mg-Al-Ca
Laves phases
Metallography
EBSD
Micromechanical testing
Corrosion testing

ABSTRACT

The Mg-Al-Ca system has been shown to be a promising alloy system since it combines the low density of Mg with a high creep resistance at high alloying contents and a high ductility for dilute alloys, while simultaneously avoiding the requirement of alloying with costly rare earth elements. Nevertheless, the adequate preparation of the alloy system for subsequent microstructural, mechanical, electrochemical and defect analysis is challenging. Therefore, within this publication, we present and apply methods for the structural, mechanical, electrochemical and defect analysis with a focus on the corresponding required metallographic preparation methods in order to support research on the alloy system.

1. Introduction

The increasing requirement to improve fuel efficiency in automotive and aerospace applications leads to a shift in used materials towards light-weight alloys. A suitable candidate for light-weight applications is Mg, which is frequently alloyed with Al. However, there are several shortcomings of these alloys: the wrought alloys with low alloying content suffer from low formability due to the prevalence of basal slip and many successful alloying concepts are still based on additional rare earth elements; the cast alloys, which may contain higher alloying contents to include reinforcing intermetallic phases are still limited in their application at higher temperatures as their strength and creep resistance are reduced at elevated temperatures ($T > 150\text{ °C}$) due to the instability of the commonly precipitated $\text{Mg}_{17}\text{Al}_{12}$ phase [1,2].

A recent approach in both types of alloys to overcome these difficulties is the addition of small amounts of Ca to the Mg-Al alloys. This leads to an increase in ductility in the solid solution Mg-Al-Ca alloys and the formation of an intermetallic skeleton within the Mg matrix of alloys

with Al and Ca above the solubility limit. Such in-situ composites of metallic matrix and intermetallic reinforcement are reported to possess improved creep properties [1,3–5].

If the Mg-matrix is alloyed with only small amounts of Ca and Al (e.g. 1 wt.-% Al and 0.1 wt.-% Ca), the strength and formability of the Mg-solid solution is increased. These improved mechanical properties are reported to stem from the activation of $\langle c + a \rangle$ slip compared to the basal slip and tensile deformation twinning as activated in pure Mg [6]. According to a correlative transmission electron microscopy and atom probe tomography study by Bian et al. [7], the Al and Ca atoms were found to segregate to basal $\langle a \rangle$ dislocations and were consequently hindering them in their free motion. Also, in a study by Cihova et al. [8], clusters of Al and Ca atoms have been observed in Mg-Al-Ca-Mn alloys by APT (atom probe tomography) analysis. However, the authors could not assign these clusters to certain defects. Despite recent efforts to gain a deeper understanding of the mechanisms enhancing plasticity in the Mg-Ca-Al and Mg-Ca-Zn solid solutions, much remains unknown such as the effects of solutes on the nucleation of defects, the competition

* Corresponding author.

E-mail address: andre@imm.rwth-aachen.de (D. Andre).

¹ Current address: Laboratory for Mechanics of Materials and Nanostructures, EMPA – Swiss Federal Institute for Materials Science and Technology, 3603, Thun, Switzerland.

between the different slip systems and twinning and the underlying interactions of the solutes with partial dislocations and the enclosed stacking faults or the effect of the solutes on the cross-slip behaviour from the basal plane as well as the mobility of grain boundaries during recrystallization and grain growth [9–11].

Higher alloying contents lead to the precipitation of an intermetallic skeleton consisting of different Laves phases, namely the C14 CaMg_2 , C15 CaAl_2 and C36 $\text{Ca}(\text{Mg},\text{Al})_2$, which can be adjusted in their volume fraction, morphology and type by an adjustment of the Ca/Al ratio and the solidification rate [12–16]. In principle, a continuous intermetallic skeleton improves creep resistance but limits ductility. In tensile and creep tests at 170 °C, several co-deformation and damage mechanisms have been observed, including cracking of the Laves phases, local plastic co-deformation via dislocation slip and interfacial sliding [17]. Although recent work proposes a possible mechanism of co-deformation between the α -Mg matrix and the $\text{Ca}(\text{Mg},\text{Al})_2$ Laves phase in Mg-Al-Ca alloys [18], there are still further open questions, such as the effect of different orientation relationships, type of Laves phases and temperature on the mechanisms of co-deformation. Recently, Guénolé et al. [17] showed by means of atomistic simulations that the orientation relationship and temperature significantly influences the transfer of plasticity across α -Mg/ CaMg_2 Laves phases. However, so far, these results remain only partially experimentally validated [18]. Furthermore, Mg-Al-Ca alloys have already been studied extensively regarding improved corrosion properties. Especially, secondary phases lead to micro galvanic coupling and the formation of an interconnected network at high alloy content [19–23]. However, there is still a lack in understanding the influence of small alloying contents such as in solid solutions and the interdependency of additional alloying elements with respect to the corrosion mechanism [24]. Due to their two-phase structure with intrinsically different mechanical and corrosion properties, the metallographic preparation of these alloys often proves challenging, but is a necessary pre-requisite for studying deformation and also corrosion mechanisms in these two-phase alloys. Here, we therefore describe successful preparation methods in detail.

In addition to the deformation and corrosion behaviour of the above-mentioned Mg-Al-Ca solid solutions and composites, the mechanisms of plasticity and selective dealloying during corrosion [25] of the Laves phases themselves also remain to be unravelled. These phases form a class of intermetallic compounds combining an AB_2 stoichiometry with a topologically close-packed structure. They exist in different structural types, namely, the hexagonal C14 type, which is represented by e.g. the above-mentioned CaMg_2 , the cubic C15 structure in e.g. CaAl_2 and the hexagonal $\text{Ca}(\text{Mg},\text{Al})_2$ C36 structure [26]. Since Laves phases generally combine a high hardness with a high brittleness, the metallographic preparation of these phases differs from that of the much softer alloys and comes with its own challenges. Therefore, a further focus of this study lies on the metallographic preparation of the Laves phases.

In summary, the ternary system Mg-Al-Ca is of high relevance for future applications as the basis of promising alloy systems. However, research on the resulting alloys is often impeded by the need to prepare the materials for detailed characterisation, which is not always straightforward and varies depending on the intended analysis to be performed. The successful preparation of Mg-based alloys remains challenging not only due to its high softness and quick oxidation, but also, in case of the composites due to the mechanical contrast and different response to electrolytes of the constituent phases.

Here, we therefore present different metallographic preparation methods which can be used across the ternary system from solid solution Mg-Al-Ca alloys over metallic-intermetallic composites to bulk intermetallic Laves phases $\text{Ca}(\text{Mg},\text{Al})_2$.

There are three main purposes for which we compare and apply these methods, namely (1) structural analysis including phase imaging and electron backscatter diffraction (EBSD), which requires a particularly high surface quality, (2) mechanical testing with often similar target surfaces as EBSD but the need for a flat surface, and (3) electrochemical

investigations to assess corrosion mechanisms including their relation to specific microstructural elements, such as precipitates, grain or phase boundaries. We hope that the methods and discussions of pitfalls and achievable results will support research efforts in other groups starting out on these materials or transitioning to different methods of their analysis.

2. Experimental

The materials metallographically prepared and investigated are all from the Mg-Al-Ca system, namely a solid solution Mg-Al-Ca alloy, a Mg composite consisting of a Mg matrix and an intra- and intergranular eutectic intermetallic skeleton and the CaMg_2 and CaAl_2 - CaAl_4 intermetallic phases. The following sections are subdivided into these different material groups in order to describe their preparation routines in detail and discuss potential experimental applications. The solid solution, as well as the composite Mg-Al-Ca alloys were synthesised by induction melting charges of about 800 g of raw elements in a steel crucible under an Argon atmosphere of 10 bar in order to limit oxidation and evaporation. The alloys were cast into rectangular copper moulds with an internal cross section of $30 \times 60 \text{ mm}^2$. The composite material was investigated in the as-cast state [12] whereas the solid solution material was heated to 450 °C for 30 min and subsequently hot rolled to about 50% reduction in thickness (reduction per pass about 10%, reheating between each pass, reheating and water quenching after the final pass). The rolling temperature for the solid solution alloys was chosen due to preliminary work, where the temperature was found to result in superior mechanical properties as well as a homogeneous microstructure [6].

Synthesis of the intermetallic phases is detailed elsewhere [27,28], only the CaAl_2 material was additionally annealed at 600 °C for 24 h under Argon atmosphere to improve chemical homogeneity and reduce residual stresses (cooled within the furnace to room temperature).

2.1. Solid solution Mg-Al-Ca alloys

In the following, two preparation methods for solid solution Mg-Al-Ca specimens will be described and applied to a Mg-1Al-0.1Ca alloy. Both methods allow successful preparation of the soft specimens which are prone to scratches while simultaneously avoiding the formation of twins. However, in order to avoid any chemical modification of the specimen surface, no electropolishing step was performed if the specimens were analysed for corrosion properties.

In method I, which is particularly suitable for subsequent EBSD measurements and slip trace analyses (Fig. 1), the specimen was manually ground and polished. Grinding was performed using SiC abrasive paper with a grit size of #2000 and #4000 in conjunction with ethanol as a lubricant in order to reduce surface oxidation. The corresponding grinding times are given in Fig. 1. The polishing procedure of method I was further performed with 6 μm diamond paste on MD-DAC cloth by Struers GmbH for 20 min, while rotating the sample concentrically against the rotation direction of the cloth. The subsequent 3 μm , 1 μm and 0.25 μm steps were performed on MD-DUR cloth by Struers GmbH in the same manner as on MD-DAC, again for approximately 20 min. The lubricant for all polishing steps consisted of a mixture of 94% isopropanol and 6% polyethylene glycol in order to minimize oxidation. Furthermore, ultrasonic cleaning in ethanol was repeated after each polishing step.

In a last step, the electrolyte AC2 by Struers GmbH was cooled down to -20 to -30 °C. As the electrolyte decomposes quickly, first a beaker with ethanol was cooled down with dry ice to -30 °C. Then the beaker with freshly mixed AC2 was placed in the ethanol to be cooled down quickly. For the electropolishing procedure, the specimen was placed in the AC2 solution and the electropolishing was started immediately for 30 s. After the process, the sample was removed from the electrolyte and cleaned with ethanol. Insufficiently slow handling of the sample might

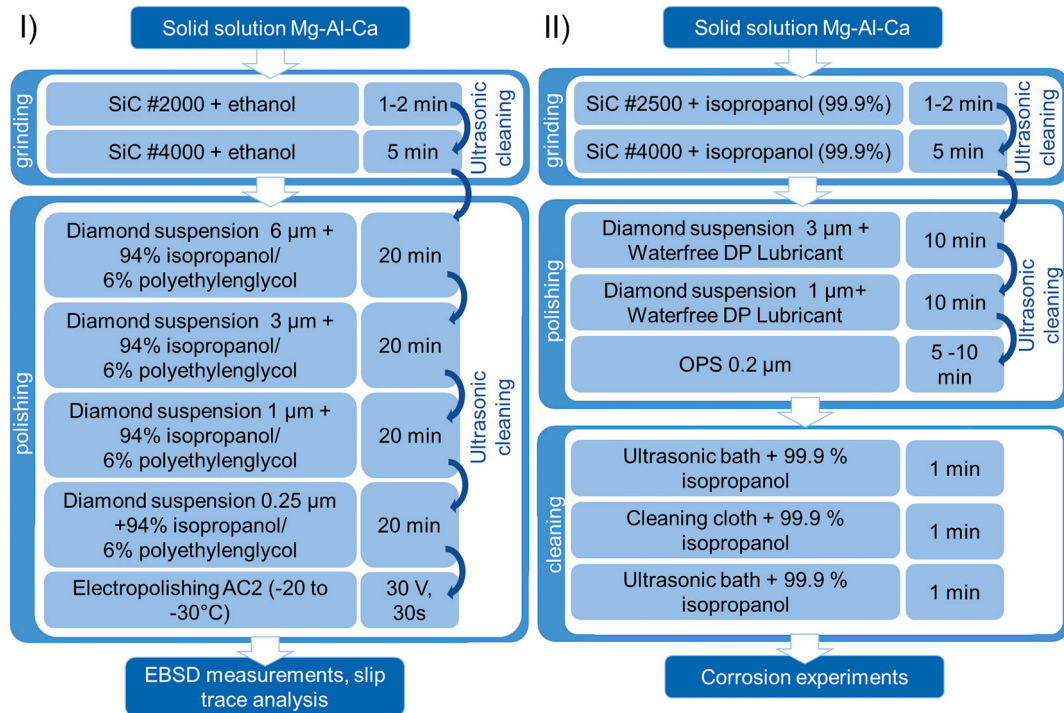


Fig. 1. Metallographic preparation procedure for the solid solution Mg-Al-Ca alloys: I) EBSD measurements and slip trace analysis, II) corrosion experiments.

result in an inhomogeneous surface quality of the sample or the start of etching, which can negatively affect further analyses. The electropolishing parameters fitting for the Mg-Al-Ca alloy was found to be 30 V for 30 s. Thereafter, the specimen surface was almost scratch free and planar.

The usage of electropolishing in method I has the advantage of a better indexing rate for EBSD measurements also post deformation. However, if the specimen will be subjected to corrosion experiments, electropolishing is not the method of choice since it might lead to potential chemical modifications of the surface. Therefore, for corrosion experiments, preparation procedure II was applied.

In preparation procedure II (Fig. 1), a steel sample holder was used to ensure plane parallelism without embedding of the sample (Fig. 2). The holder applied a constant load of 0.015 MPa on the sample. During the grinding processes, SiC abrasive paper with a grit size of #2500 and

#4000 was used together with isopropanol (99.9%) as a lubricant. The corresponding grinding times are again given in Fig. 1. Between all grinding steps, the specimen was cleaned in an ultrasonic bath in 99.9% isopropanol for approximately one minute.

After the last grinding step, the sample was directly polished with 3 μm and 1 μm diamond slurry on MD-DUR cloths rotating the sample concentrically against the rotation direction of the cloth. Additionally, the waterfree DP Lubricant Blue by Struers GmbH was used as a coolant. The final polishing step used water free 0.2 μm fused silica suspension on MD-CHEM cloth by Struers GmbH. For this, approximately 5 mL of the OP-S suspension was spread on the polishing plate and distributed on the cloth with the holder. The specimen was then rotated concentrically against the rotation direction of the cloth for two minutes. Immediately after polishing, the specimen was cleaned with isopropanol and a further cleaning step in ultrasonic bath in isopropanol for one minute was performed. The last cleaning step consisted of polishing the specimen on a MD-CHEM cloth wetted with isopropanol suspension followed by an ultrasonic bath in isopropanol for one minute.

2.2. Mg-Al-Ca composites

The specimen preparation methods given below are suitable for nearly all different compositions of Mg-Al-Ca alloys at least till the point where the total alloying elements (Al + Ca wt.-%) content stays below 8 wt.-%. The preparation might also work for higher alloying contents, but has not been evaluated by the authors yet. Here, a Mg-Al-Ca-alloy in the as-cast condition with the nominal chemical composition listed in Table 1 was selected in order to exemplify a suitable preparation routine for Mg-composite alloys.

Table 1
Chemical composition of the investigated magnesium composite.

Al [wt.-%]	Ca [wt.-%]	Ca/Al	Mg [wt.-%]	Sec. Phases
5.5	1.7	0.3	92.8	Ca(Mg,Al) ₂

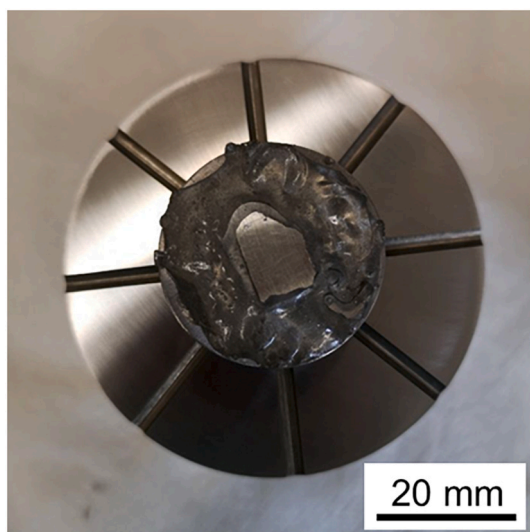


Fig. 2. Specimen attached to a steel sample holder using Crystalbond adhesive.

For the metallographic preparation of this alloy, a square shaped sample with a surface area of approximately 1 cm^2 was wet cut using a corundum blade. In the following, two metallographic preparation methods will be introduced (Fig. 3). Method III is well suited for EBSD measurements and is therefore suited for a surface/slip line analysis after macro- and micromechanical testing whereas method IV allows to perform corrosion experiments (e.g. potentiodynamic polarization, linear polarization and electrochemical impedance spectroscopy). Similar to the preparation of the solid solution Mg-Al-Ca sample, electropolishing should be avoided for the magnesium composites if corrosion experiments were to be conducted after preparation due to potential chemical modifications induced in the specimen.

For method III, the grinding process involved manual grinding on SiC abrasive paper with a grit size #2000 and #4000 using ethanol as a lubricant. The following polishing procedure was performed using a diamond suspension of $3 \mu\text{m}$ and $1 \mu\text{m}$ together with 99% ethanol and 1% PEG 400 for ten minutes each. In order to further improve the surface quality, electropolishing with AC2 at $\sim -20^\circ\text{C}$ was performed at 15 V for 60 s followed by polishing using an OP-U suspension by Struers GmbH (colloidal suspension of SiO_2 of $0.04 \mu\text{m}$) for one minute. Afterwards, the specimen was cleaned on a polishing cloth with isopropanol for three minutes and a last cleaning step in isopropanol in an ultrasonic bath for two minutes.

For method IV, the specimen was hand ground using a SiC abrasive paper with a grit size of #500 and #1000 and water as a lubricant for 1–2 min. During the next grinding step at a grit size of #4000, the lubricant was changed to 99.9% isopropanol. In a further step, the specimen was hand-polished with waterfree diamond suspension of $3 \mu\text{m}$ and $1 \mu\text{m}$ using a waterfree DP Lubricant Blue by Struers GmbH on a MD-Dur cloth. The final polishing step was conducted using a waterfree fumed silica suspension of $0.2 \mu\text{m}$ on a MD-Chem cloth by Struers GmbH. Each polishing step was carried out for approximately five minutes. The specimen was further subjected to a cleaning process with 99.9% isopropanol in an ultrasonic bath for two minutes after each polishing step. The specimen was then cleaned for approximately four minutes on the rotating and cleaned polishing cloth combined with a frequent wetting using isopropanol which was followed by two minutes

in isopropanol in an ultrasonic bath.

2.3. Laves phases of Mg-Al-Ca alloys

Specimens of the intermetallic C14-CaMg_2 and the C15-CaAl_2 Laves phase were analysed in the as-cast condition. Both samples were cut into small pieces using electric discharge machining and attached to a sample holder using CrystalbondTM adhesive, as it was also performed for the solid solution Mg-Al-Ca alloys (Fig. 2). Mechanical grinding for both specimens was performed using a grid size of #800, #1000, #2400 and #4000 on a SiC abrasive paper with water as a lubricant. Each grinding step was finished once the grinding grooves of the former grinding step disappeared. The approximate grinding times are given in Fig. 4. For the polishing procedure, $3 \mu\text{m}$ diamond DP-Suspension, $1 \mu\text{m}$ diamond DP-Suspension and $0.25 \mu\text{m}$ DP-Suspension by Struers GmbH were used with ethanol as lubricant agent for the CaMg_2 phase, whereas for the CaAl_2 phase, the above-mentioned suspensions were used alongside the diamond solution as a lubricating agent. Similar results could be obtained by using another solution containing 96% ethanol and 4% polyethylene glycol. A further deviation in the polishing procedure occurred for the CaMg_2 phase, which was electropolished. Electropolishing was avoided for the CaAl_2 phase due to an undesired resulting topography but could be successfully applied to the CaMg_2 phase. Here, electropolishing was performed using AC2 for 20 s at 5 V followed by a cleaning step of 5 s, whereas the CaAl_2 specimen was polished using an OP-U $0.04 \mu\text{m}$ colloidal silica suspension. This last polishing step was subdivided in a 20 s polishing step with OP-U suspension on a DUR cloth and an immediately following polishing step with water and dish-washing liquid.

The entire metallographic preparation procedure pursued for the intermetallics is given in Fig. 4. The specimens were afterwards suitable for EBSD measurements as well as for micromechanical testing and electron channelling contrast imaging (ECCI) measurements.

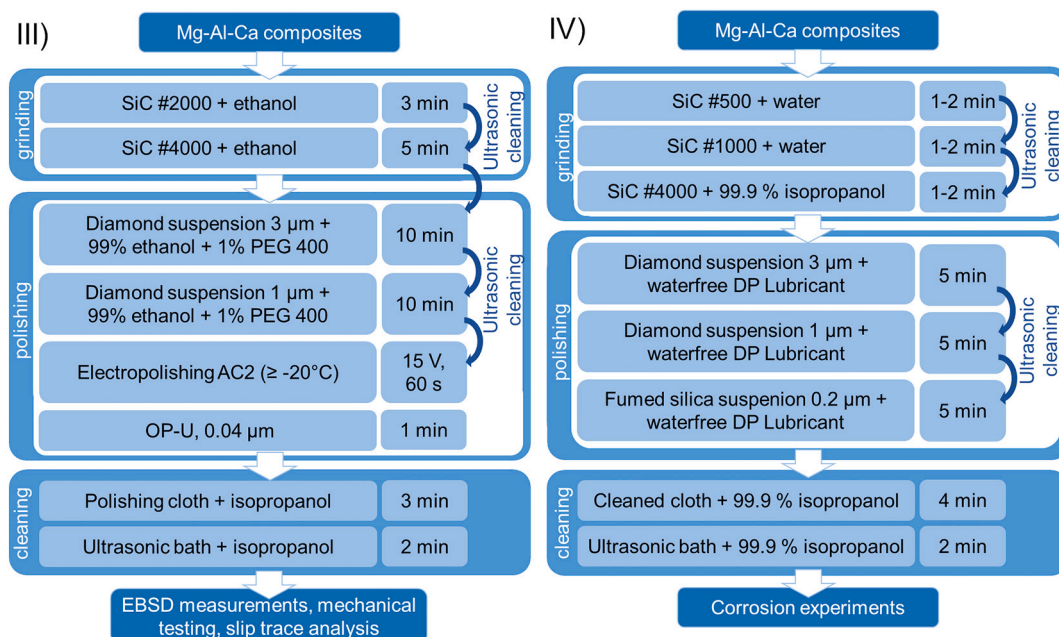


Fig. 3. Metallographic preparation procedure for the Mg-Al-Ca composites: III) this method is well suited for EBSD measurements, macro- and micromechanical testing and slip trace analysis, whereas method IV) is well suited for corrosion experiments.

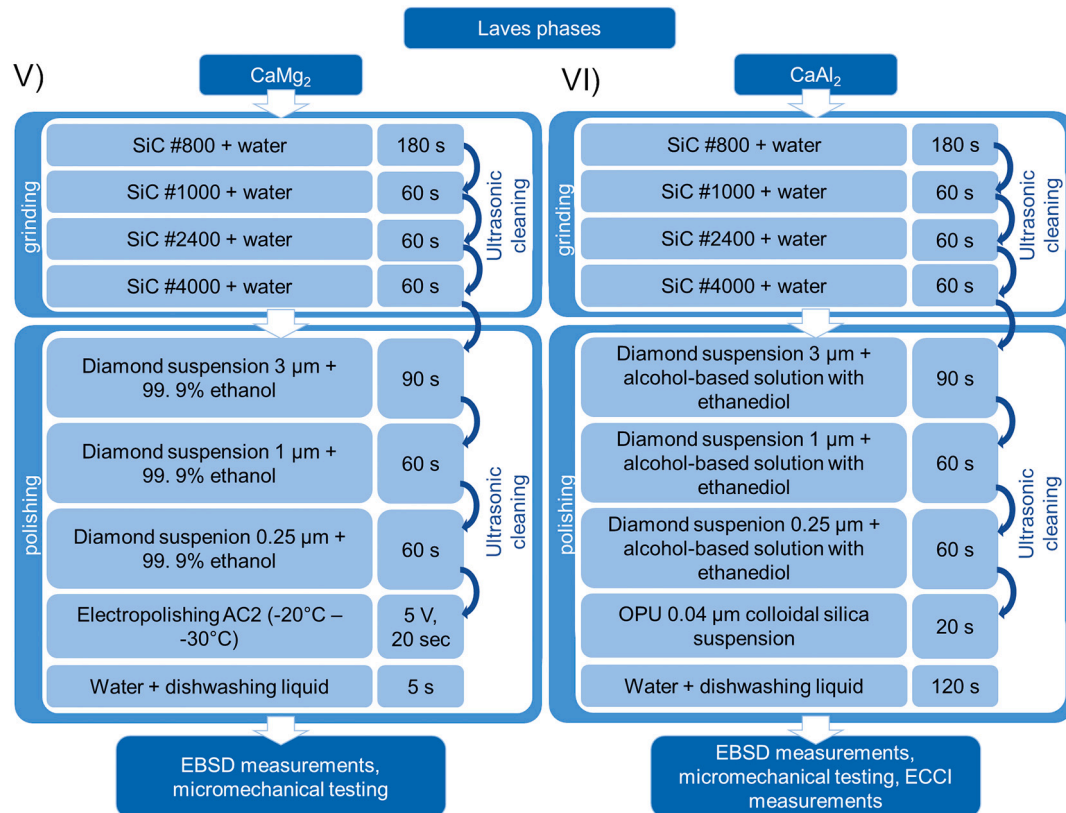


Fig. 4. Metallographic preparation procedure for Laves phases: V: the CaMg_2 phase and VI: the CaAl_2 intermetallics.

3. Results and discussion

3.1. Solid solution Mg-Al-Ca alloys

The first preparation method described for the solid solution Mg-Al-Ca alloys, which underwent a rolling procedure after casting to break the cast structure and reach a homogeneous microstructure, is well suited for EBSD measurements and following surface analysis such as slip traces after plastic deformation and leads to a high indexing rate which can still be achieved after several months when stored in vacuum, whereas the second method is well suited for corrosion experiments due to the missing electropolishing step preventing from strong surface-near dealloying effects.

The image quality (IQ) map (Fig. 5 a)), which provides a measure of the pattern quality and, thus, can be used to qualitatively estimate the strain distribution within the material gives further insights on the preparation quality. As evident from Fig. 5 a), the IQ map of the Mg-1Al-

0.1Ca alloy prepared using method I reveals a homogenous contrast for all grains, representing a homogeneous pattern quality and therefore also a homogeneous strain distribution and topography within the grains [29]. The dark spots in Fig. 5 a) correspond to oxides. The corresponding confidence index (CI) map reveals an average indexing rate above 0.1 (Fig. 5 b)). The high indexing rate corresponds to a correct indexing of 95% of the Kikuchi pattern [30], which is also due to the high signal-to-noise ratio within the measured Kikuchi patterns (Fig. 5 c)). The high indexing rate did not significantly deteriorate approximately half a year after the preparation if stored in a desiccator under vacuum. These factors all indicate the suitability of the performed preparation routine for the given alloy system. All given EBSD maps within this publication correspond to raw data and did not undergo any clean-up procedure.

The specimen was further subjected to macroscopic compression tests (Zwick testing machine) at a strain rate of 10^{-3} s^{-1} until a maximum strain of $\sim 3\%$ at ambient temperature and afterwards imaged

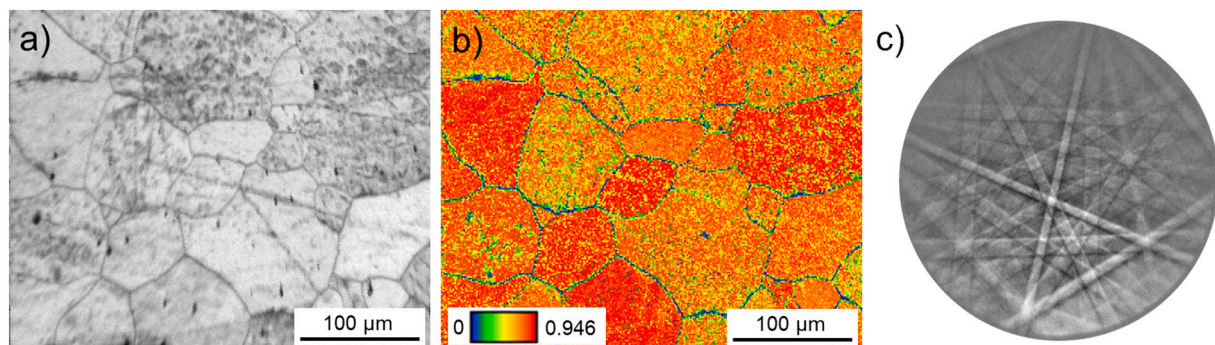


Fig. 5. a) IQ map of the as-cast Mg-1Al-0.1Ca solid solution sample, b) the CI map generated from EBSD data on the same microstructural region and c) representative Kikuchi pattern. (For interpretation of the references to colour in this figure legend, the reader is referred to the web version of this article.)

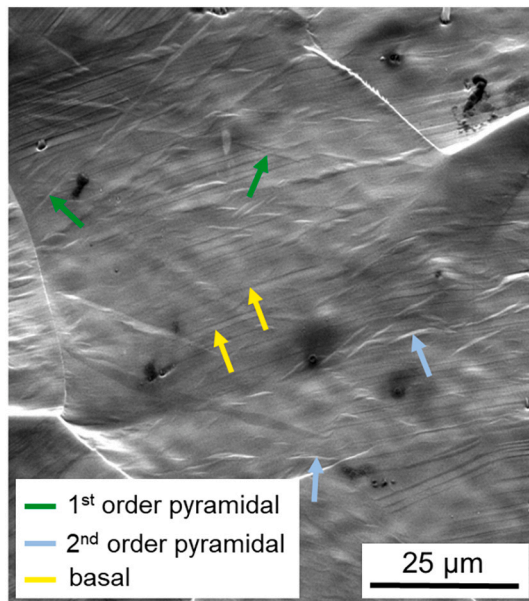


Fig. 6. SE-image of the compressed Mg-1Al-0.1Ca alloy revealing distinct slip traces on the specimen surface. (For interpretation of the references to colour in this figure legend, the reader is referred to the web version of this article.)

in a scanning electron microscope (SEM) (Helios Nanolab 600i, FEI) using an acceleration voltage of 15 kV. The subsequent surface analysis allowed a correlation between the visible slip traces on the specimen surface and possible slip planes using EBSD orientation data. In the image given in Fig. 6, the slip traces marked in yellow correspond to basal traces and can be distinguished from 1st order pyramidal (marked in green) and 2nd order pyramidal slip planes (marked in blue).

Secondary electron (SE) images taken at an acceleration voltage of 10 kV using a Supra 55VP, Carl Zeiss AG of the specimen surface of the Mg-1Al-0.1 alloy after metallographic preparation according to method II and subsequent surface corrosion in pH = 8.0 \pm 0.1 for 30 min are given in Fig. 7 a-b). An increase in OPS polishing time from a) 3 min to b) 5–10 min reduced the density of residual artefacts and led to a more uniform dissolution but did not affect the appearance of corrosion

groves. These (Fig. 7 a-b)) are not related to polishing artefacts but rather correlate to material inherent defects, such as grain boundaries.

The above-described preparation methods are suitable for the investigated material system since slip traces on the specimen surface are successfully identified and the applied preparation method exhibits straightforward results on studying the influence of corrosion on, e.g. selective dissolution at grain boundaries.

3.2. Mg-Al-Ca composites

The Mg-4.55Al-2.91Ca alloy, which was metallographically prepared according to preparation routine III underwent an EBSD measurement (FEI Helios Nanolab 600i) at an accelerating voltage of 15 kV and a step size of 0.2 μm. The resulting inverse pole figure (IPF) map, Kikuchi patterns, IQ map and CI map are given in Fig. 8. The IPF map (Fig. 8 a)) visualises the crystallographic orientation of the α-Mg matrix. However, care should be taken in determining the orientation relationship existing between the α-Mg matrix and the C36-Ca(Mg,Al)₂ Laves phase. A sufficiently good Kikuchi pattern for the C36-Ca(Mg,Al)₂ Laves phase (Fig. 8 b)) is observable only from a small fraction of the total intermetallic phases. The IQ map has a homogeneous grayscale distribution within each α-Mg grain indicating a good pattern quality, while a darker colour along the phase boundaries indicates a rather poor pattern quality of the C36-Ca(Mg,Al)₂ Laves phase. This observation is based on the low indexed C36-Ca(Mg,Al)₂ Laves phase struts in the Mg-Al-Ca ternary alloys due to their small sizes ($\sim \leq 1 \mu\text{m}$). The C36 Laves phase patterns overlap with the pattern from the α-Mg matrix, thus leading to a significant difficulty in their indexing. This is further evident from the CI map (Fig. 8 d)), where the intermetallic skeleton reaches a small confidence index and is thus represented by blue. All other microstructural regions exhibit a CI of above 0.1, which represents the threshold of a 95% correct indexing of the Kikuchi bands [30]. Nevertheless, one single intra- or intermetallic C36-Ca(Mg,Al)₂ Laves phase strut appears to be one grain of the C36-Ca(Mg,Al)₂ Laves phase, as indicated by the white arrows in Fig. 8 a). Therefore, the used preparation routine is suitable for obtaining good quality diffraction patterns for this material system.

The SE-images of an indent made in a Mg-3.7Al-3.8Ca alloy up to a load of 500 mN at ambient temperature highlight the advantages of the metallography scheme III with regard to the visibility of surface features, see Fig. 9 a-b). These images were taken at an accelerating voltage of 10 kV using a Zeiss LEO1530 SEM. As can be seen in Fig. 9, the

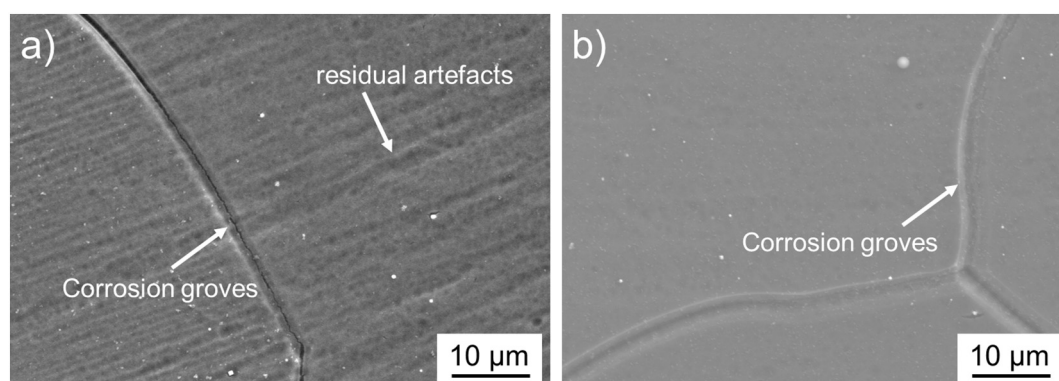


Fig. 7. SE-images of the Mg-1Al-0.1 alloy after metallographic preparation according to method II reveal varying amounts of selective dissolution (residual artefacts) depending on the applied OPS polishing time: a) 3 min and b) 5–10 min. The corrosion groves are independent of the preparation.

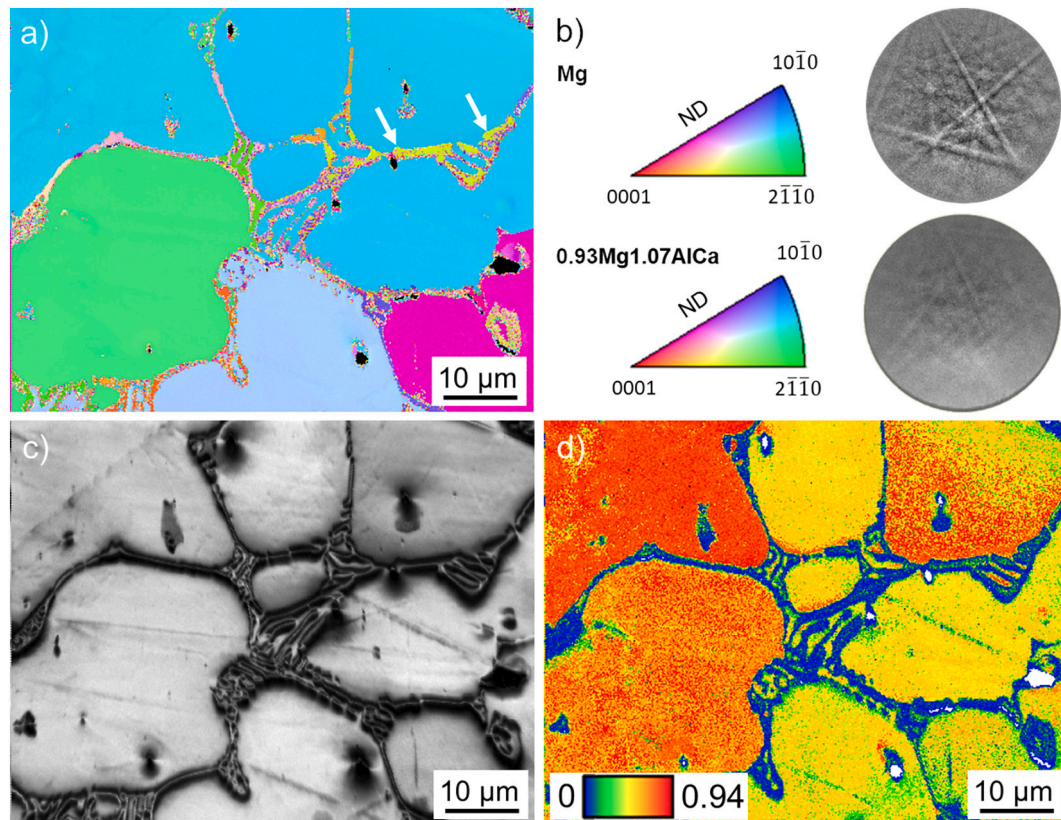


Fig. 8. a) IPF map of the α -Mg and C36 (0.93Mg1.07AlCa) Laves phase in an as-cast Mg-4.55Al-2.91Ca alloy, with struts of the C36 phase having the same orientation, as indicated by white arrows, b) IPF legends and Kikuchi patterns for α -Mg and C36 Laves phase, c) IQ map of the same region and d) CI map generated from EBSD data on the same microstructural region. (For interpretation of the references to colour in this figure legend, the reader is referred to the web version of this article.)

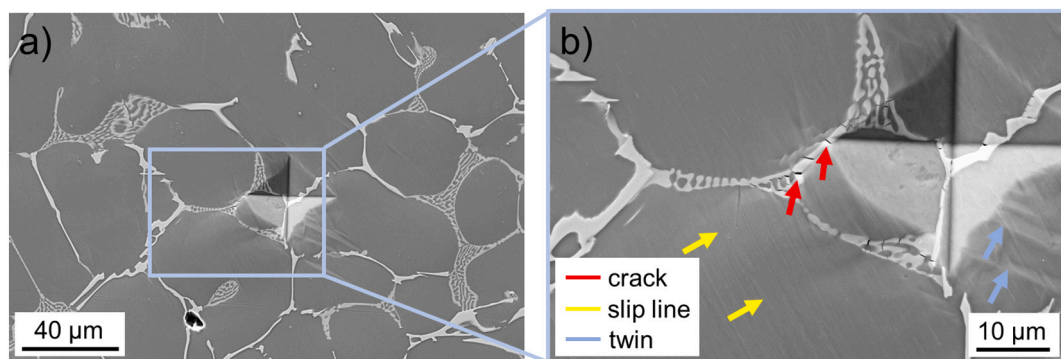


Fig. 9. a) SE-image of the indent performed at room temperature on as-cast Mg-3.7Al-3.8Ca alloy and b) magnified image of the region bounded by blue rectangle in (a). (For interpretation of the references to colour in this figure legend, the reader is referred to the web version of this article.)

deformed area around the indent reveals deformation features in the vicinity of the indent. In this case, the deformation features represent cracks in the Laves phase (highlighted in red) as well as basal slip traces (highlighted in yellow) and twins in the Mg phase (highlighted in blue). Therefore, this polishing scheme is also suitable to analyse deformation mechanisms on the specimen surface.

After preparation procedure IV, the Mg composite specimen was free from scratches and exhibited no corrosive pre-damage, as evident from the SE-image in Fig. 10 a). The specimen topography was further analysed using atomic force microscopy (AFM) (Dimension Icon XR, Bruker Corporation, Massachusetts, USA) in the tapping mode equipped with a PFQNE-silicon nitride tip (Bruker Corporation, Massachusetts, USA). The resulting topography scan in Fig. 10 b) reveals, that the

comparatively softer Mg matrix was subjected to higher material removal during the preparation routine compared to the hard Laves phase. The height difference was <50 nm, but it might be relevant for any subsequent material analysis and evaluation methods.

The specimen further underwent an electrochemical measurement on the free corrosion potential for an immersion time of 30 min in a sodium borate buffer (pH = 8 \pm 0.1). The corresponding back-scattered electron (BSE) image of the specimen surface after the electrochemical measurement is given in Fig. 11.

The Mg-matrix, at a distance of 1–2 μ m from the interface to the secondary phases, exhibits homogeneously distributed corrosion, which is assumed to arise as a consequence of a uniform corrosion process of the Mg-matrix under the immersion conditions. Therefore, the local

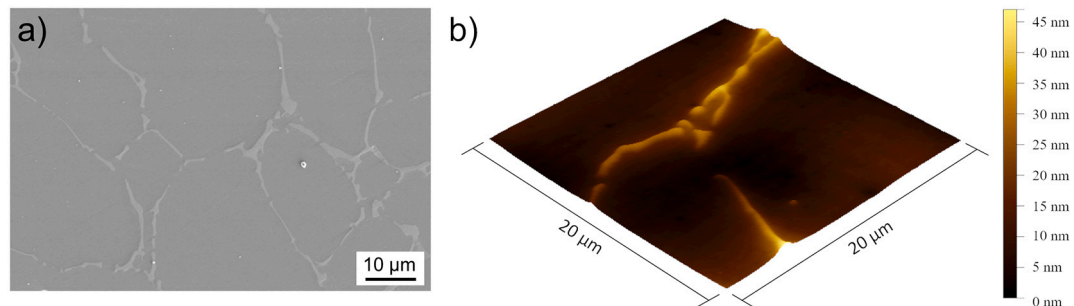


Fig. 10. a) SE-image of the metallographically prepared specimen surface of the Mg-composite at an acceleration voltage of 3 kV and b) AFM topography scan of the Mg-composite revealing a height difference of <50 nm between the intermetallic skeleton. (For interpretation of the references to colour in this figure legend, the reader is referred to the web version of this article.)

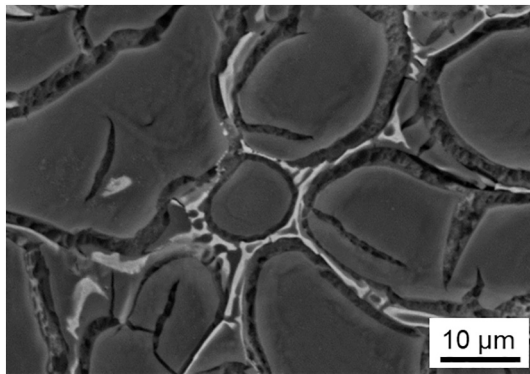


Fig. 11. BSE-image at an acceleration voltage of 10 kV of the Mg-composite specimen surface after electrochemical measurement at the free corrosion potential for 30 minutes in a borate buffer electrolyte.

corrosion reactions seem to be unaffected by preparation-related artefacts and represents the material's inherent electrochemical corrosion properties. The different morphology of the corrosion products near the interface between the Mg-matrix and the secondary phases, might arise due to the formation of microgalvanic elements.

3.3. Laves phases of Mg-Al-Ca alloys

The C14-CaMg₂ Laves phase studied consists of 68.7 ± 0.5 at.-% Mg, corresponding to a deviation of 2 at.-% from the ideal stoichiometric composition according to energy dispersive X-Ray (EDX) analysis. Nanomechanical testing could be conducted on the metallographically prepared specimen surface (method V) and allowed to perform

micropillar compression experiments [28]. The example shown in Fig. 12 a) corresponds to an SE-image taken at an acceleration voltage of 10 kV.

Nanomechanical tests could also be conducted after the metallographic preparation of the C15-CaAl₂ phase according to method VI. These allowed to identify e.g. slip traces in the vicinity of the indent (Fig. 12 b)), which are taken at an acceleration voltage of 5 kV.

The C15-CaAl₂ phase was analysed for its chemical composition using electron probe microanalysis (EPMA) and EDX measurements on the metallographically prepared specimen. The EPMA analysis was performed at an acceleration voltage of 10 kV and the resulting chemical composition was averaged over 12 areas of interest per phase. The analysis reveals the existence of the CaAl₂ phase as well as the CaAl₄ phase in the microstructure (Table 2).

The subsequent EDX analysis, which was performed at an acceleration voltage of 10 kV, revealed a dual-phase structure consisting of a CaAl₂ matrix and a CaAl₄ skeleton, Fig. 13.

The phase distribution is also evident from the BSE-image in Fig. 14, taken at 5 kV. Here, the heavier CaAl₂ matrix phase appears brighter, whereas the lighter CaAl₄ phase appears in darker grey in the grain boundary regions.

EBSD measurements were conducted in a Zeiss Auriga SEM at 20 kV and a step size of 0.3 μm and resulted in a scratch free surface with no

Table 2

EPMA analysis CaAl₂-CaAl₄ sample composition after annealing of the intermetallic.

Phases	Al [at.-%]	Ca [at.-%]
CaAl ₂	65.86 ± 0.15	34.14 ± 0.15
CaAl ₄	79.03 ± 0.35	20.97 ± 0.35

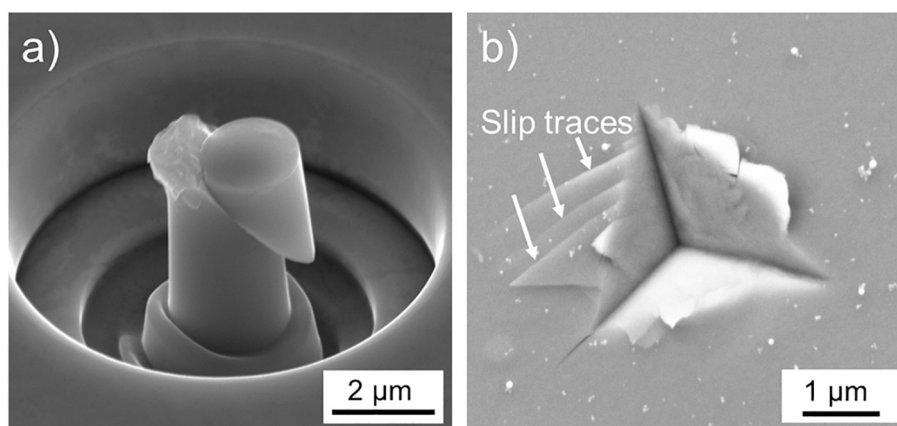


Fig. 12. SE-image of a) a plastically deformed micropillar of the CaMg₂ C14 phase and b) a nanoindent with slip traces in its vicinity of the CaAl₂ C15 phase.

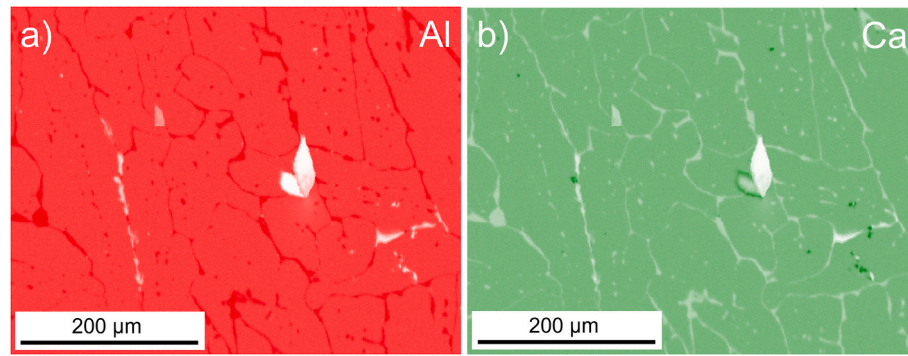


Fig. 13. SEM-EDX mapping of the intermetallic specimen with a) an elemental map of Al and b) an elemental map of Ca. Both maps reveal a skeleton structure consisting of CaAl_2 and a CaAl_4 skeleton.

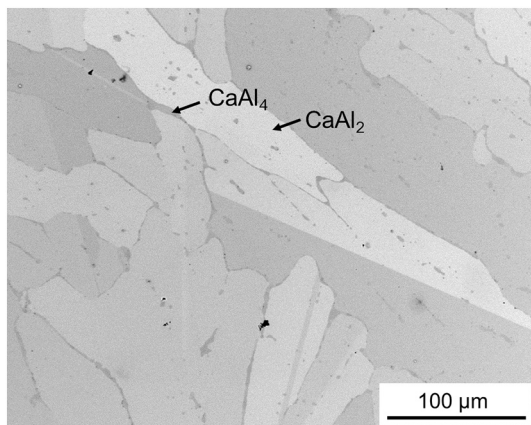


Fig. 14. BSE-image of the dual-phase CaAl_2 - CaAl_4 intermetallic specimen, with the darker phase being the CaAl_4 phase and the brighter phase being the CaAl_2 phase.

strain inhomogeneities, as evident from the IQ map in Fig. 15 a). The CI map (Fig. 15 b)) reveals a high CI of above 0.1 for the entire microstructural region, except for the intermetallic CaAl_4 phase, which is represented in blue. The high CI of the C15 CaAl_2 phase stems from the good recognition of the band structure in the Kikuchi pattern, as given in Fig. 15 c). Due to a small deviation of the crystal structure of the CaAl_4 phase from its ideal structure in conjunction with its small volume fraction, resulting in a pattern overlap, it was not possible to refine its crystal structure. Consequently, only low CI values were obtained for the CaAl_4 phase.

The high surface quality of the specimen using the described

preparation route VI, further allowed electron channelling contrast imaging (ECCI) measurements. Using ECCI, the underlying defects in the microstructure close to the surface of the bulk specimen could be investigated by a slight tilting of the specimen so that a specific grain fulfilled Bragg's Law. Since lattice defects such as dislocations disturb the electron channelling, a brighter contrast is obtained as in the image [31–33]. An example of the gained dislocation substructure close to a second phase particle is given in Fig. 16 and taken at 30 kV and a probe current of 2 nA.

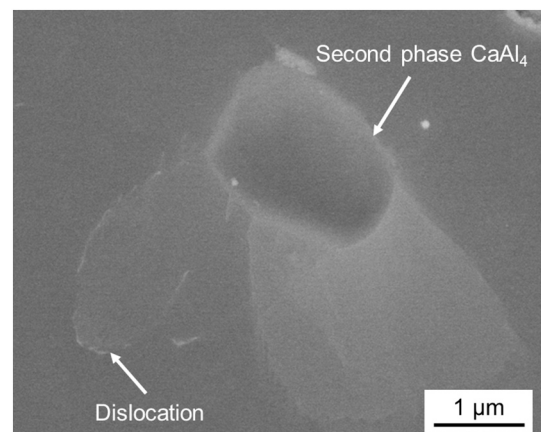


Fig. 16. ECCI image of the dislocations underneath the specimen surface close to the second phase in the C15- CaAl_2 phase.

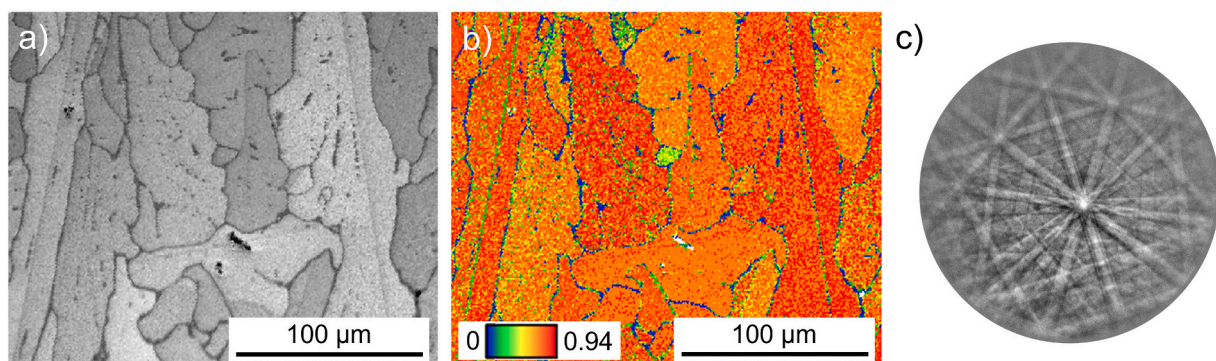


Fig. 15. a) IQ map of the as-cast CaAl_2 - CaAl_4 intermetallic, b) CI map of the same microstructural region, generated from EBSD data and c) Kikuchi pattern obtained from the CaAl_2 phase. (For interpretation of the references to colour in this figure legend, the reader is referred to the web version of this article.)

4. Conclusion

Several methods for the metallographic preparation of the Mg-Al-Ca alloy system have been presented and can be applied on solid solution Mg-Al-Ca alloys, Mg-Al-Ca composites and intermetallic Laves phases of the Mg-Al-Ca system. The described preparation procedures are suitable for the following characterisation methods: Corrosion experiments, EBSD measurements, macro- and micromechanical testing including a subsequent slip trace analysis and ECCI. For the solid solution Mg-Al-Ca alloy and the Mg-Al-Ca composites, the metallographic preparation included an electropolishing step if EBSD measurements, a slip trace analysis or micromechanical tests were performed afterwards since electropolishing did not only improve the indexing rate for EBSD measurements even after deformation, but also allowed EBSD measurements after longer storage times. However, if corrosion testing followed the preparation, no electropolishing was applied to avoid potential selective dealloying of the surface. In case of the intermetallic phases, the use of electropolishing has to be considered on an individual basis. While electropolishing was successfully applied for CaMg_2 for subsequent EBSD measurements and micromechanical testing, the same routine induced an undesired topography if applied to CaAl_2 .

Declaration of Competing Interest

The authors declare that they have no known competing financial interests or personal relationships that could have appeared to influence the work reported in this paper.

Data availability

Data will be made available on request.

Acknowledgement

The authors gratefully acknowledge the financial support of the Deutsche Forschungsgemeinschaft (DFG) within projects A01, A05, B01, B05, B06, C01, C02, C03 of the Collaborative Research Center (SFB) 1394 “Structural and Chemical Atomic Complexity - from defect phase diagrams to material properties” – project number 409476157 and INST 256/455-1 FUGG. We would like to further acknowledge Patrick Grünwald from the Department of Material Science and Technology at the Saarland University in Saarbrücken (Germany) for the technical support during the AFM measurements. H. Springer wishes to acknowledge financial support from the Heisenberg Program of the Deutsche Forschungsgemeinschaft (SP1666/1).

References

- [1] B. Kondori, R. Mahmudi, Effect of Ca additions on the microstructure and creep properties of a cast Mg–Al–Mn magnesium alloy, *Mater. Sci. Eng. A* 700 (2017) 438–447, <https://doi.org/10.1016/j.msea.2017.06.007>.
- [2] M.O. Pekguleryuz, A.A. Kaya, Creep resistant magnesium alloys for powertrain applications, *Adv. Eng. Mater.* 5 (12) (2003) 866–878, <https://doi.org/10.1002/adem.200300403>.
- [3] D. Amberger, P. Eisenlohr, M. Göken, Microstructural evolution during creep of Ca-containing AZ91, *Mater. Sci. Eng. A* 510 (2009) 398–402, <https://doi.org/10.1016/j.msea.2008.04.115>.
- [4] A.A. Luo, B.R. Powell, M.P. Balogh, Creep and microstructure of magnesium–aluminum–calcium based alloys, *Metall. Mater. Trans. A* 33 (3) (2002) 567–574, <https://doi.org/10.1007/s11661-002-0118-1>.
- [5] Y. Terada, et al., A thousandfold creep strengthening by Ca addition in die-cast AM50 magnesium alloy, *Metall. Mater. Trans. A* 35 (9) (2004) 3029–3032, <https://doi.org/10.1007/s11661-004-0046-3>.
- [6] S. Sandlöbes, et al., A rare-earth free magnesium alloy with improved intrinsic ductility, *Sci. Rep.* 7 (1) (2017) 1–8, <https://doi.org/10.1038/s41598-017-10384-0>.
- [7] M. Bian, et al., Bake-hardenable Mg–Al–Zn–Mn–Ca sheet alloy processed by twin-roll casting, *Acta Mater.* 158 (2018) 278–288, <https://doi.org/10.1016/j.actamat.2018.07.057>.
- [8] M. Cihova, et al., Rational design of a lean magnesium-based alloy with high age-hardening response, *Acta Mater.* 158 (2018) 214–229, <https://doi.org/10.1016/j.actamat.2018.07.054>.
- [9] I. Basu, et al., Stacking-fault mediated plasticity and strengthening in lean, rare-earth free magnesium alloys, *Acta Mater.* 211 (2021), 116877, <https://doi.org/10.1016/j.actamat.2021.116877>.
- [10] I. Basu, et al., Segregation-driven exceptional twin-boundary strengthening in lean Mg–Zn–Ca alloys, *Acta Mater.* (2022), 117746, <https://doi.org/10.1016/j.actamat.2022.117746>.
- [11] H.-S. Jang, D. Seol, B.-J. Lee, A comparative study on grain boundary segregation and solute clustering in Mg–Al–Zn and Mg–Zn–Ca alloys, *J. Alloys Compd.* 894 (2022), 162539, <https://doi.org/10.1016/j.jallcom.2021.162539>.
- [12] M. Zubair, et al., On the role of laves phases on the mechanical properties of Mg–Al–Ca alloys, *Mater. Sci. Eng. A* 756 (2019) 272–283, <https://doi.org/10.1016/j.msea.2019.04.048>.
- [13] M. Zubair, et al., Strain heterogeneity and micro-damage nucleation under tensile stresses in an Mg–5Al–3Ca alloy with an intermetallic skeleton, *Mater. Sci. Eng. A* 767 (2019), 138414, <https://doi.org/10.1016/j.msea.2019.138414>.
- [14] D. Amberger, P. Eisenlohr, M. Göken, On the importance of a connected hard-phase skeleton for the creep resistance of Mg alloys, *Acta Mater.* 60 (5) (2012) 2277–2289, <https://doi.org/10.1016/j.actamat.2012.01.017>.
- [15] Y. Chai, et al., Role of Al content on the microstructure, texture and mechanical properties of Mg–3.5 Ca based alloys, *Mater. Sci. Eng. A* 730 (2018) 303–316, <https://doi.org/10.1016/j.msea.2018.06.011>.
- [16] H.A. Elamami, et al., Phase selection and mechanical properties of permanent-mold cast Mg–Al–Ca–Mn alloys and the role of Ca/Al ratio, *J. Alloys Compd.* 764 (2018) 216–225, <https://doi.org/10.1016/j.jallcom.2018.05.309>.
- [17] J. Guénolé, et al., Exploring the transfer of plasticity across laves phase interfaces in a dual phase magnesium alloy, *Mater. Des.* 202 (2021), 109572, <https://doi.org/10.1016/j.matdes.2021.109572>.
- [18] M. Zubair, et al., Co-deformation between the metallic matrix and intermetallic phases in a creep-resistant Mg–3.68 Al–3.8 Ca alloy, *Mater. Des.* 210 (2021), 110113, <https://doi.org/10.1016/j.matdes.2021.110113>.
- [19] S. Manivannan, et al., Corrosion Analysis of AZ61 Alloy with Different Level of Ca Addition and Aging, in: *Applied Mechanics and Materials*, Trans tech Publ., 2014, <https://doi.org/10.4028/www.scientific.net/AMM.592-594.821>.
- [20] E. Dabab, et al., The influence of Ca on the corrosion behavior of new die cast Mg–Al-based alloys for elevated temperature applications, *J. Mater. Sci.* 45 (11) (2010) 3007–3015, <https://doi.org/10.1007/s10853-010-4302-1>.
- [21] J. Yang, et al., Effect of Ca addition on the corrosion behavior of Mg–Al–Mn alloy, *Appl. Surf. Sci.* 369 (2016) 92–100, <https://doi.org/10.1016/j.apsusc.2016.01.283>.
- [22] U.M. Chaudry, et al., Corrosion behavior of AZ31 magnesium alloy with calcium addition, *Corros. Sci.* (2022), 110205, <https://doi.org/10.1016/j.corsci.2022.110205>.
- [23] D. Zander, C. Schnatterer, C. Kuhnt, Influence of heat treatments and Ca additions on the passivation behaviour of high-pressure die cast AM50, *Mater. Corros.* 66 (12) (2015) 1519–1528, <https://doi.org/10.1002/maco.201508273>.
- [24] M. Deng, et al., Approaching “stainless magnesium” by Ca micro-alloying, *Materials Horizons* 8 (2) (2021) 589–596, <https://doi.org/10.1039/D0MH01380C>.
- [25] M. Cihova, et al., Biocorrosion zoomed in: Evidence for dealloying of nanometric intermetallic particles in magnesium alloys, *Adv. Mater.* 31 (42) (2019) 1903080, <https://doi.org/10.1002/adma.201903080>.
- [26] G.E. Schulze, Zur Kristallchemie der intermetallischen AB₂-Verbindungen (Laves-Phasen), *Z. Elektrochem. Angew. Phys. Chem.* 45 (12) (1939) 849–865, <https://doi.org/10.1002/bbpc.19390451202>.
- [27] C. Zehnder, et al., Plastic deformation of single crystalline C14 Mg₂Ca Laves phase at room temperature, *Mater. Sci. Eng. A* 759 (2019) 754–761, <https://doi.org/10.1016/j.msea.2019.05.092>.
- [28] M. Freund, et al., Plastic deformation of the CaMg₂ C14-Laves phase from 50–250° C, *Materialia* 20 (2021), 101237, <https://doi.org/10.1016/j.mtl.2021.101237>.
- [29] S.I. Wright, M.M. Nowell, EBSD image quality mapping, *Microsc. Microanal.* 12 (1) (2006) 72–84, <https://doi.org/10.1017/S1431927606060090>.
- [30] D.P. Field, Recent advances in the application of orientation imaging, *Ultramicroscopy* 67 (1–4) (1997) 1–9, [https://doi.org/10.1016/S0304-3991\(96\)00104-0](https://doi.org/10.1016/S0304-3991(96)00104-0).
- [31] I. Gutierrez-Urrutia, S. Zaefferer, D. Raabe, Coupling of electron channeling with EBSD: toward the quantitative characterization of deformation structures in the SEM, *Jom* 65 (9) (2013) 1229–1236, <https://doi.org/10.1007/s11837-013-0678-0>.
- [32] H. Kriaa, A. Guitton, N. Maloufi, Fundamental and experimental aspects of diffraction for characterizing dislocations by electron channeling contrast imaging in scanning electron microscope, *Sci. Rep.* 7 (1) (2017) 1–8, <https://doi.org/10.1038/s41598-017-09756-3>.
- [33] S. Zaefferer, N.-N. Elhami, Theory and application of electron channelling contrast imaging under controlled diffraction conditions, *Acta Mater.* 75 (2014) 20–50, <https://doi.org/10.1016/j.actamat.2014.04.018>.

Publication 4

Metallurgical synthesis methods for Mg-Al-Ca scientific model materials

W. Luo, L. Tanure, M. Felten, J. Nowak, W. J. Delis, M. Freund, N. Ayeb, D. B. Zander, C. Thomas, M. Feuerbacher, S. Sandlöbes-Haut, S. Korte-Kerzel, H. Springer

2023, arXiv

<https://doi.org/10.48550/arXiv.2303.08523>

For this pre-print paper, the candidate carried out the experimental evaluation with mechanical tests and SEM observations during the synthesis optimisation of solid solution Mg-Al-Ca alloys.

The candidate wrote the relevant sections in the Materials and Methods and Results and Discussion sections of the original manuscript in collaboration with the co-authors.

Metallurgical synthesis methods for Mg-Al-Ca scientific model materials

W. Luo^a, L. Tanure^a, M. Felten^b, J. Nowak^b, W. Delis^c, M. Freund^c, N. Ayeb^a, D. Zander^b, C. Thomas^d, M. Feuerbacher^d, S. Sandlöbes-Haut^c, S. Korte-Kerzel^c, H. Springer^{a,e,*}

^a RWTH Aachen University, Institute of Metal Forming, Intzestrasse 10, 52072 Aachen, Germany

^b RWTH Aachen University, Corrosion and Corrosion Protection, Intzestrasse 5, 52072 Aachen, Germany

^c RWTH Aachen University, Institute of Physical Metallurgy and Metal Physics, Kopernikusstrasse 14, 52074 Aachen, Germany

^d Forschungszentrum Jülich GmbH, ER-C-1, Wilhelm-Johnen-Straße, 52428 Jülich, Germany

^e Max-Planck-Institut für Eisenforschung GmbH, Max-Planck-Strasse 1, 40237 Düsseldorf, Germany

* Corresponding author

E-mail address: hauke.springer@ibf.rwth-aachen.de

Abstract

Mg-based alloys are industrially used for structural applications, both as solid solutions alloys and as composites containing intermetallic compounds. However, a further development in terms of mechanical properties requires the investigation of underlying causalities between synthesis, processing and microstructure to adjust the mechanical and the corrosion properties, ideally down to the near atomic scale. Such fundamental scientific investigations with high resolution characterisation techniques require model materials of exceptionally high purity and strictly controlled microstructure e.g. with respect to grain size, morphology, chemical homogeneity as well as content and size of oxide inclusions. In this context, the Mg-Al-Ca system appears exceptionally challenging from a metallurgical perspective due to the high reactivity and high vapor pressures, so that conventional industrial techniques cannot be successfully deployed. Here, we demonstrate the applicability of various scientific synthesis methods from arc melting over solution growth to diffusion couples, extending to effects and parameters for thermo-mechanical processing. Suitable pathways to overcome the specific challenges of the Mg-Al-Ca system are demonstrated, as well as the persistent limitations of the current state of the art laboratory metallurgy technology.

1 Introduction

The application of light-weight components in the aeronautics and automotive industry has both environmental and economic benefits [1]. Mg-based alloys are especially attractive due to their low density compared to steels, aluminium, and even some polymer-based materials. However, they typically suffer from a limited strength and especially low ductility [2]. Recent studies showed that Mg-based solid solution alloys with a small amount of Ca and Al (e.g. Mg-1Al-0.1Ca (wt.%)) exhibit improved formability and ductility due to the activation of $\langle c+a \rangle$ slip [3]. With increasing Al and Ca content, different types of intermetallic phases precipitate in the Mg-Al-Ca alloys and composites consisting of a Mg matrix and an intermetallic skeleton are obtained [4]. The precipitate changes from $\text{Mg}_{17}\text{Al}_{12}$ to the C15- CaAl_2 , C36- $\text{Ca}(\text{Mg},\text{Al})_2$ and C14- CaMg_2 Laves phases with increasing Ca/Al ratio [5,6]. The continuous Laves phase network can reinforce the soft Mg matrix and improve the creep resistance of the Mg-Al-Ca alloys [7-9]. However, the knowledge of the mechanical properties [10-12] and corrosion properties [13] of the Laves phase is still limited. A systematic investigation of the Mg-Al-Ca solid solutions, composites and intermetallic phases will therefore facilitate the development of advanced Mg alloys for structural applications.

The main challenges in the production and processing of Mg-Al-Ca alloys of solid solutions and composites are related to the high reactivity [14] and high vapor pressures [15,16] of Mg and Ca. Although the synthesis of Mg-Al-Ca alloys based on industrial standards is feasible [17,18], it is more challenging to prepare the Mg-Al-Ca alloys of solid solutions and composites for specific scientific purposes, i.e. achieving very high purity, precisely controlling the phases, grain sizes and microstructures. Induction melting under protective atmosphere with high pressure can reduce evaporation of Mg and Ca during melting. Since Mg and Ca do not dissolve Fe during melting, Mg-Ca alloys can be melted and held in a crucible made of steel. However, as Al has a very high affinity with Fe [19], the molten Mg-Al-Ca alloys may react with the ferrous crucible, leading to Fe contamination in the Mg-Al-Ca alloys. Furthermore, phenomena such as grain boundary precipitation and intergranular segregation in the as-cast Mg alloys need to be reduced by further thermal mechanical processing [20].

In addition to the solid solutions and composites of the Mg-Al-Ca system, we also consider the binary [21-23] and ternary [24] intermetallic phases of the Mg-Al-Ca system. While induction melting using a steel crucible under Ar atmosphere is applicable to the synthesis of C14- CaMg_2 Laves phase, it is not suitable for the synthesis of the C15- CaAl_2 Laves phase due to Fe contamination. Alternatively, as there is a lack of Mg, we might be able to prepare the C15- CaAl_2 Laves phase by arc melting without causing serious evaporation. Due to the distinct

brittleness of the Laves phase [25], the alloys of the C14-CaMg₂ and C15-CaAl₂ Laves phases might disintegrate during cooling. Casting into a pre-heated alumina crucible followed by slow cooling [26] was reported to reduce thermal stress during cooling. However, alumina crucibles cannot be used in the synthesis of the C14-CaMg₂ and C15-CaAl₂ Laves phases due to the high reactivity of Ca. It has been reported that Mg₁₇Al₁₂ intermetallic phase with a small amount of a second phase can be produced by using an electrical resistance melting furnace in a graphite crucible under protective Ar atmosphere [27]. Although homogenization heat treatment reduced the amount of the second phase, it leads to the formation of porosity in the alloys [27]. In order to obtain pure Mg₁₇Al₁₂ phase, we prepared a Mg-Al diffusion couple in the present work. It is even more challenging to synthesize the C36-Ca(Mg,Al)₂ Laves phase which has high Mg and Ca contents and narrow composition and temperature ranges [24,28]. The C36-Ca(Mg,Al)₂ Laves phase was only observed in Mg-Al-Ca alloys containing multiple phases [24,28]. To synthesize single-phase C36-Ca(Mg,Al)₂ Laves phase, we need to overcome not only the high vapor pressures and reactivity of Mg and Ca but also the difficulties in control of composition and temperature. Different methods such as the manual induction melting, diffusion couple technique, flux-growth method, and Bridgman method were utilized to synthesize the C36-Ca(Mg,Al)₂ Laves phase. In summary, the aim of the present work is to explore the challenges and pitfalls in the synthesis of the Mg-Al-Ca bulk materials of solid solution, composite and intermetallic phases, and to discuss solutions to the synthesis. An overview of metallographic preparation methods for the Mg-Al-Ca alloys has been published elsewhere [29]. We hope that these methods of synthesis and metallographic preparation could help other researchers working on the Mg-Al-Ca alloys.

2 Materials and methods

The Mg-Al-Ca alloys were prepared from pure Mg (99.95 wt.%), Ca (98.8 wt.%) and Al (99.999 wt.%). To overcome the challenges in synthesis, different methods including induction melting, arc-melting, diffusion couple technique, manual induction melting, flux-growth method and Bridgman method, were used to produce the Mg-Al-Ca alloys of solid solutions, composites and intermetallic phases (Table 1). The chemical analyses of the starting materials and the synthesized alloys were performed by inductively coupled plasma optical emission spectroscopy (ICP-OES). The metallographic preparation methods for the Mg-Al-Ca alloys are explained in details elsewhere [29]. The microstructures of the alloys were observed using scanning electron microscopy (SEM) (Helios Nanolab 600i, FEI Inc.). The compositions of the phases in the alloys were determined by energy dispersive X-ray spectroscopy (EDS) (EDAX

Inc.). Phase analyses were carried out by electron backscatter diffraction (EBSD) (Hikari, EDAX Inc.). Some samples were colour etched with a picric acid-based solution for optical microscopy (OM) (Leica DMR, Leica AG) observations.

Table 1 Summary of the metallurgical synthesis methods for the Mg-Al-Ca solid solutions, composites and intermetallics.

Materials	Composition (wt.%)	Phase	Method	Heat treatment/ thermal mechanical processing
Mg-Al-Ca solid solution	Mg-1Al-0.5Ca	Mg	Induction melting under Ar atmosphere at 10 bar using a steel crucible and casting under Ar atmosphere at 15 bar in a Cu mould	Hot-rolling at 450 °C in five passes with 10 % reduction in thickness per pass followed by annealing at 500 °C for 24 h
	Mg-1Al-0.05Ca			
	Mg-1Al-0.1Ca			
	Mg-1Al-0.2Ca			
	Mg-2Al-0.05Ca			
	Mg-2Al-0.1Ca			
Mg-Al-Ca composite	Mg-6Al-2Ca	Mg + Laves phase	Induction melting under Ar atmosphere at 0.8 bar using a steel crucible and casting under Ar atmosphere at 0.8 bar in a Cu mould	Annealed under Ar atmosphere at 500 °C for 48 h, followed by furnace cooling
	Mg-5Al-3Ca			
	Mg-4Al-4Ca			
Mg-Al-Ca intermetallic	Mg-45Ca	C14-CaMg ₂	Induction melting under Ar atmosphere at 0.8 bar using a steel crucible and casting under Ar atmosphere at 0.8 bar in a Cu mould	As-cast
	Al-42Ca	C15-CaAl ₂	Arc-melting on a water-cooled copper hearth under Ar atmosphere	Annealed in a glass tube furnace at 600 °C for 24 h under Ar atmosphere
	Mg-28Al-46Ca	C36-Ca(Mg,Al) ₂	Pure elements were placed in a cylindrical tantalum crucible sealed with 0.6 bar Ar, placed on a water-cooled cold finger in a Bridgman apparatus and then heated to 900 °C. The growth was carried out by lowering the crucible out of the hot zone at a velocity of 5 mm/h.	As-cast

3 Results and discussion

3.1 Mg-Al-Ca solid solutions

In the present work, the Mg-Al-Ca solid solutions were melted in a 60 kW induction furnace using a steel crucibles under Ar atmosphere with pressure of 10 bar. As the Al content is only 1-2 wt.% in the Mg-Al-Ca solid solutions, solid solution of Fe in the melt is considered to be negligible (0.0068 wt.% Fe measured by ICP-OES). During melting, the inductive field couples with the ferromagnetic crucible and stirs the melt in the steel crucible, which facilitates homogenization of the melt. In order to reduce the casting defects, the Mg-Al-Ca solid solutions were cast under Ar atmosphere with pressure of 15 bar. The melt was cast into a copper mould with an internal cross section $30 \times 150 \text{ mm}^2$ and an ingot of about 500 g was obtained. As shown in Fig. 1(a), the Mg-1Al-0.05Ca (wt.%) alloy cast under high pressure Ar exhibit only a small amount of pores. Tensile tests (Fig. 1(b)) further reveal that the Mg-1Al-0.05Ca (wt.%) alloy cast under Ar atmosphere with pressure of 15 bar exhibit higher tensile strength and ductility than those cast under Ar atmosphere with pressure of 0.8 bar, as a result of the reduced defect density.

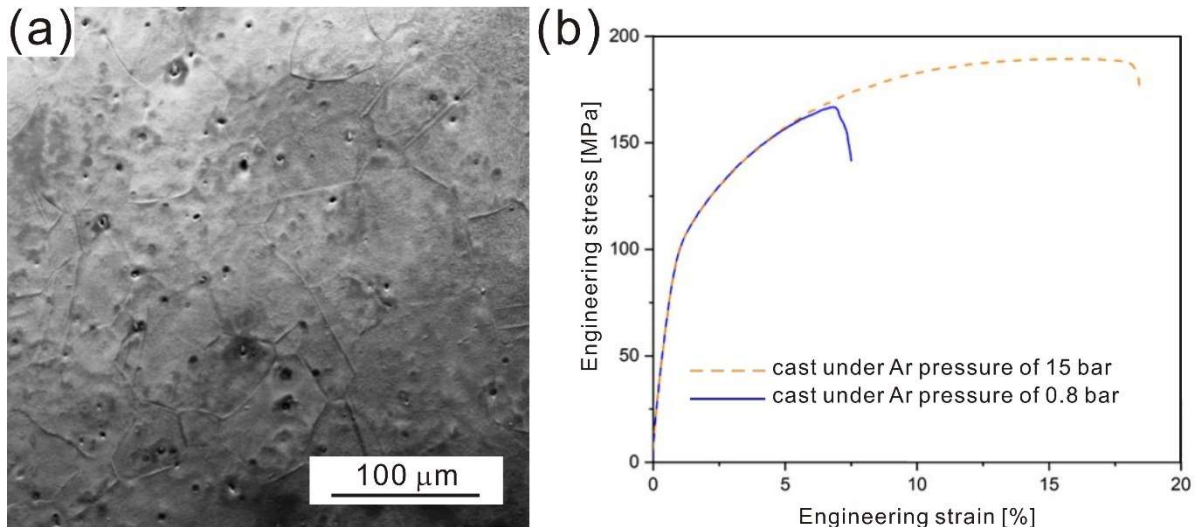


Fig. 1 (a) SEM image of the Mg-1Al-0.05Ca (wt.%) alloy cast under Ar atmosphere with pressure of 15 bar. (b) Engineering stress-strain curves of the tensile tests of the Mg-1Al-0.05Ca (wt.%) alloys cast under Ar atmosphere with pressure of 15 bar and 0.8 bar.

Furthermore, the as-cast Mg-Al-Ca solid-solution alloys were subjected to thermal mechanical processing by hot rolling followed by homogenization and recrystallization annealing to reduce the shrinkage cavities and porosity caused during solidification, and to homogenise the elements distribution. The temperatures of the thermal mechanical processing including the annealing temperature and rolling temperature have been selected based on the Mg-Al-Ca phase

diagram [24,28], to obtain homogeneous microstructures and to avoid the precipitation of further unwanted phases. The forming parameters including the rolling diameter, speed and reduction need to be well controlled to avoid fracture during processing. In the present work, two different thermal mechanical processes were performed to obtain optimal results. Fig. 3 shows the routes of the thermal mechanical processing and the corresponding microstructures of the Mg-2Al-0.2Ca (wt.%) alloy. As shown in Fig. 2(a), the as-cast Mg-2Al-0.2Ca (wt.%) alloy was hot-rolled at 450°C in five passes with 10 % reduction in thickness per pass. Between each pass, the alloy was re-heated at 450 °C for 10 minutes. After the final pass the alloy was annealed at 450 °C for 15 minutes followed by quenching in water. After hot rolling, a Mg-2Al-0.2Ca (wt.%) alloy (Fig. 2(b)) consisting of columnar grains with an average grain size of $74 \pm 6 \mu\text{m}$ was obtained. However, the EDS measurements (Fig. 2(c)) show that there are intragranular segregation and a small amount of precipitates along the grain boundaries. In order to homogenise the composition and dissolve the precipitates, the Mg-2Al-0.2Ca (wt.%) alloy was subjected to annealing at 500 °C for 24 h after hot-rolling (Fig. 2(d)). After annealing, the precipitates along the grain boundaries and the intragranular segregation are significantly reduced (Figs. 2(e) and 3(f)).

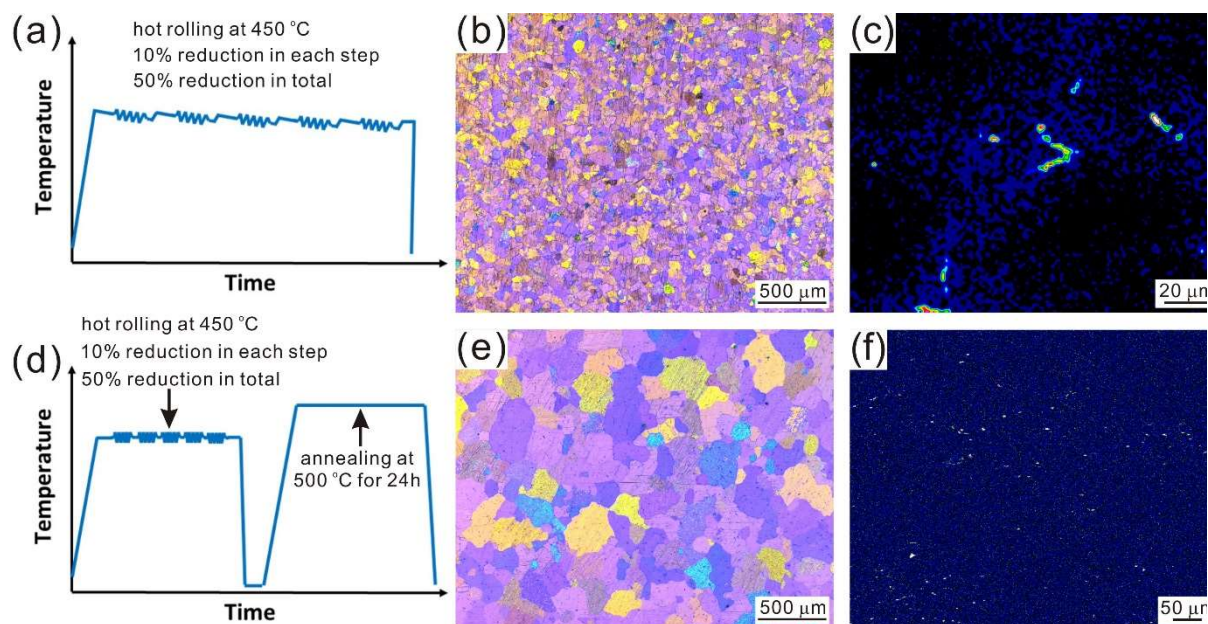


Fig. 2 (a) Route of thermal mechanical processing of a Mg-2Al-0.2Ca (wt.%) alloy: hot-rolling at 450 °C in five passes with 10 % reduction in thickness per pass followed by water quenching, and (b) the OM image and (c) EDS map of Al (the areas in red and yellow indicate high concentrations of Al) showing the resulting microstructures. (d) Route of thermal mechanical processing of a Mg-2Al-0.2Ca (wt.%) alloys: hot-rolling at 450 °C in five passes

with 10 % reduction in thickness per pass followed by annealing at 500 °C for 24 h, and (e) the OM image and (f) EDS map of Al showing the resulting microstructures.

3.2 Mg-Al-Ca composites

Mg-Al-Ca composites containing a Mg solid solution and a network of the Mg-based Laves phase could also be synthesized by induction melting using a steel crucible under protective Ar atmosphere. It is worth noting that it is inevitable to have Fe contamination in the Mg-Al-Ca alloys due to the solubility of Fe in Al. Since Fe-Al intermetallic layers [30], which hinder the diffusion of Fe into the melt, can be formed between the melt and the steel crucible, Fe contamination is negligible (0.002 – 0.018 wt.% Fe measured by ICP-OES) when the Al content is low (≤ 6 wt.%). The phases of the Mg-Al-Ca composites can be modified by adjusting the alloy composition [4-7,31]. With increasing Ca/Al ratio from 0 to 1, the type of secondary phases changes from $\text{Mg}_{17}\text{Al}_{12}$ to the C15-CaAl_2 , C36-Ca(Mg,Al)_2 and C14-CaMg_2 Laves phases [5,6]. Moreover, the precipitates become more interconnected and form a skeleton structure [6,7]. In the present work, Mg-Al-Ca composites were melted by induction melting using a steel crucible under Ar atmosphere at 0.8 bar and cast under Ar atmosphere at 0.8 bar in a Cu mould with 10 mm wall thickness and an internal cross section of $25 \times 65 \text{ mm}^2$. Representative images of the as-cast Mg-6Al-2Ca, Mg-5Al-3Ca and Mg-4Al-4Ca (wt.%) alloys of composites are shown in Figs. 3(a-c), respectively. The respective Ca/Al ratios of the Mg-6Al-2Ca, Mg-5Al-3Ca and Mg-4Al-4Ca (wt.%) alloys are 0.21, 0.41 and 0.65. It has been confirmed that their main types of intermetallic phases are C15-CaAl_2 , C36-Ca(Mg,Al)_2 and C14-CaMg_2 , respectively [32]. After heat treatment at 500 °C for 48 h, the interconnected skeletons of Laves phases in the as-cast Mg-Al-Ca composites become rounded and dispersed [32].

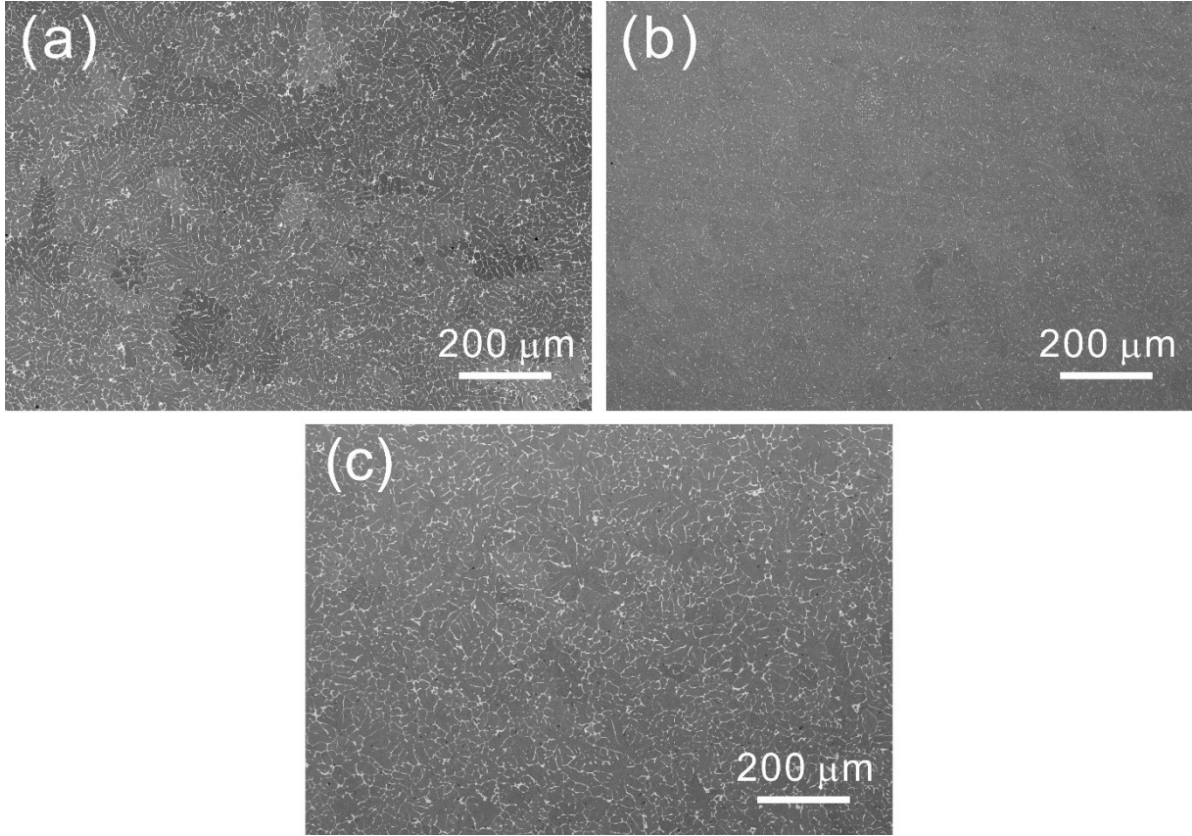


Fig. 3 Image of the as-cast (a) Mg-6Al-2Ca, (b) Mg-5Al-3Ca and (c) Mg-4Al-4Ca (wt.%) alloys synthesized by induction melting. The intermetallic precipitates in the Mg-6Al-2Ca, Mg-5Al-3Ca and Mg-4Al-4Ca (wt.%) alloys are C15-CaAl₂, C36-Ca(Mg,Al)₂ and C14-CaMg₂ Laves phases, respectively.

3.3 Mg-Al-Ca intermetallic phases

The phase diagrams of the Mg-Al-Ca ternary system and the Mg-Al, Mg-Ca and Al-Ca binary systems show various types of intermetallic phases. The ternary C36-Ca(Mg,Al)₂ Laves phase and the binary C14-CaMg₂, C15-CaAl₂ and Mg₁₇Al₁₂ intermetallic phases are the targeted intermetallic phases in the present work. In order to synthesize the C14-CaMg₂ Laves phase, the Mg-45Ca (wt.%) alloys were produced from pure Mg and pure Ca by induction melting using a steel crucible. Before melting, the vessel was evacuated and refilled with Ar for several times. In the last step the vessel was evacuated to at least 10⁻⁵ hPa and filled with Ar to 0.8 bar. During melting, the inductive field couples with the ferromagnetic crucible and stirs the melt. The melt was cast into a copper mould with an internal cross section of 30 × 60 mm² followed by furnace cooling. The Al-42Ca (wt.%) alloys were prepared from the pure Al and pure Ca by arc-melting on a water-cooled copper hearth in an Ar atmosphere to synthesize the C15-CaAl₂ Laves phase. After arc-melting, the Al-42Ca (wt.%) alloy was heat treated in a glass tube furnace at 600 °C for 24 h under Ar protection. A Mg-Al diffusion couple was prepared from

two blocks of pure Mg and Al to synthesize the $\text{Mg}_{17}\text{Al}_{12}$ intermetallic phase. The two blocks of pure Mg and Al were grinded up to 400 grit using SiC paper and polished up to 1 μm using diamond paste and ethanol lubricant. They were pressed together and annealed under Ar atmosphere at 400 °C for 1 week, followed by furnace cooling.

The microstructures of the C14- CaMg_2 and C15- CaAl_2 Laves phases are shown in Figs. 4(a) and 4(b), respectively. While a high density of pores is present in the C14- CaMg_2 Laves phase (Fig. 4(a)), the C15- CaAl_2 Laves phases (Fig. 4(b)) show homogeneous microstructures and a coarse grain size. The synthesis of $\text{Mg}_{17}\text{Al}_{12}$ intermetallic phase using the diffusion couple technique was not successful. As shown in Fig. 4(c), neither concentration gradient nor intermetallic phases were obtained in the Mg-Al diffusion couple. The reason for the failure of the Mg-Al diffusion couple might be oxidation of the contact surfaces. Even though the heat treatment was performed in a furnace filled with high purity Ar, oxidation is difficult to avoid during heat treatment in the furnace due to the high reactivity of Mg and Al. Encapsulation of the diffusion couple in a quartz tube might help to reduce oxidation, but to grow thick diffusion layers of the Mg-Al intermetallic phases with coarse grain sizes for dedicated scientific purposes remains challenging.

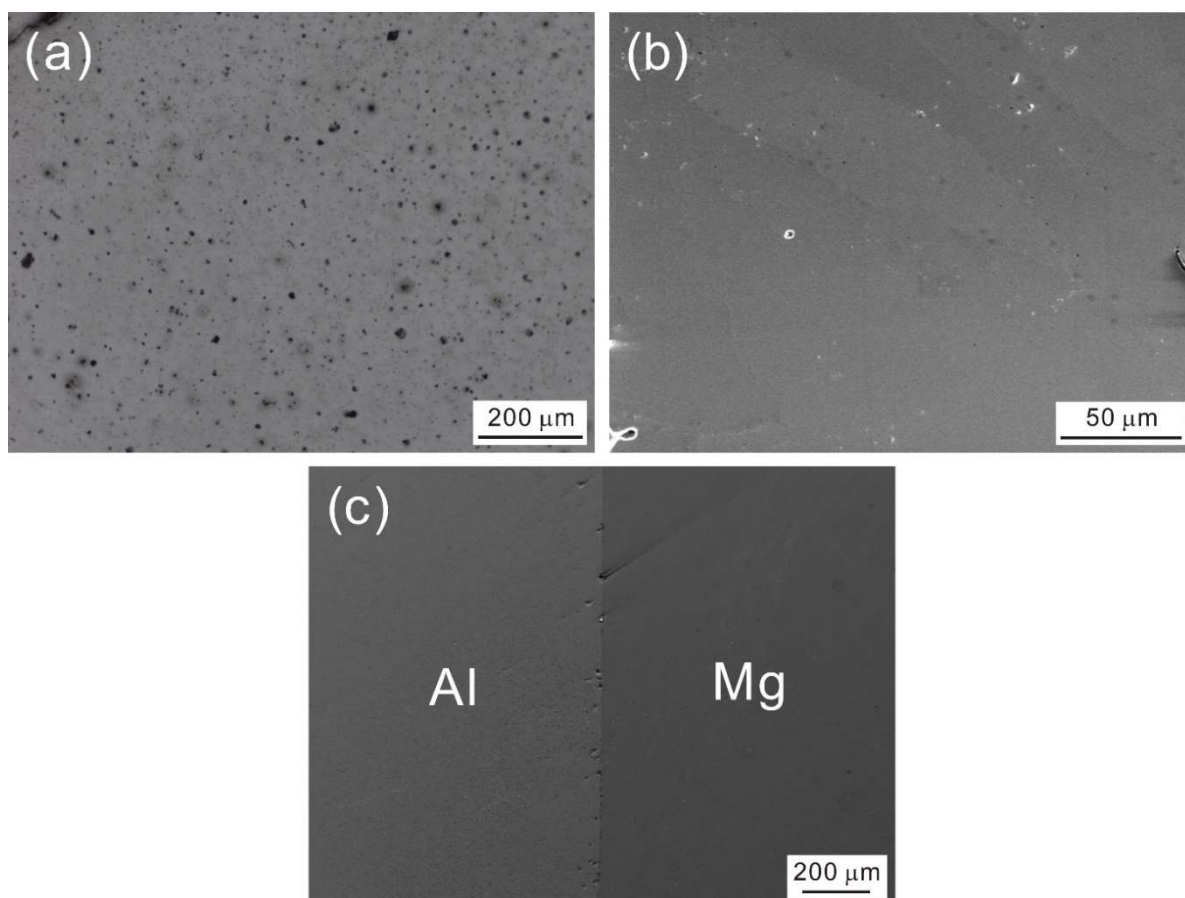


Fig. 4 SEM images of the (a) C14-CaMg₂ Laves phase synthesized by induction melting, (b) C15-CaAl₂ Laves phase synthesized by arc-melting, and (c) the Mg-Al diffusion couple after heat treatment at 400 °C for 1 week. No diffusion layer of the Mg₁₇Al₁₂ intermetallic phases was obtained due to oxidation.

It has been reported that the Mg-Al-Ca intermetallic phases can be synthesized by combinatorial sputtering [33]. However, desorption of volatile film-forming species during sputtering at elevated temperatures makes the sputtering of C36-Ca(Mg,Al)₂ Laves phase challenging. In the present work, different methods were tried to synthesize bulk materials of the C36-Ca(Mg,Al)₂ Laves phase. A graphite crucible with boron nitride spray and a sintered boron nitride crucible can be utilized during induction melting to avoid reaction between the melt and the crucible. Besides, a diffusion multiple consisting of pure Mg, Al and Ca and a Mg-CaAl₂ liquid-solid diffusion couple were prepared to synthesize the C36-Ca(Mg,Al)₂ Laves phase. In addition, the flux growth method [34] and the Bridgman method were also used to synthesize the C36-Ca(Mg,Al)₂ Laves phase.

In order to synthesize the C36-Ca(Mg,Al)₂ Laves phase, Mg-30Al-44Ca (wt.%) alloys were prepared by induction melting using a graphite crucible with boron nitride spray under Ar protection. The graphite crucible was dissolved during melting, and thus it was replaced by a sintered boron nitride crucible. However, the sintered boron nitride crucible is so brittle that it fractured during synthesis. Since no suitable crucible can be used, manual induction melting in a quartz tube was performed to synthesize the C36-Ca(Mg,Al)₂ Laves phase instead. Pure Mg, Al, Ca were mixed and placed in a quartz tube. The quartz tube was evacuated and back-filled with Ar. The alloys were re-melted three times to ensure homogeneity. In addition, a Mg-Al-Ca diffusion multiple was prepared from two blocks of pure Mg and Al with a thin Ca foil in between. The Ca foil was produced by melting and cold rolling. However, due to the oxidation of Ca the diffusion multiple failed. A Mg-CaAl₂ liquid-solid was prepared to synthesize the C36-Ca(Mg,Al)₂ Laves phase instead. A block of Mg was placed on top of a C15-CaAl₂ Laves phase alloy and melt inside an arc-melting furnace under protective Ar atmosphere. While Mg melted first due to the lower melting point, the C15-CaAl₂ Laves phase alloy remained solid and therefore formed a liquid-solid diffusion couple with the molten Mg. The composition of the Mg-30Al-44Ca (wt.%) alloy prepared by manual induction melting significantly deviates from the nominal composition, presumably due to a Mg loss during induction melting. As shown in Fig. 5(a), the Mg-30Al-44Ca (wt.%) alloy mainly contains Mg and C15-CaAl₂ Laves phase. Fig. 5(b) shows that the diffusion zone of the Mg-CaAl₂ liquid-solid diffusion couple

mainly contains dendrites of C15-CaAl₂ and a eutectic mixture of Mg and C15-CaAl₂. Thus, the synthesis of the C36-Ca(Mg,Al)₂ Laves phase by manual induction melting and liquid-solid diffusion couple methods was not successful.

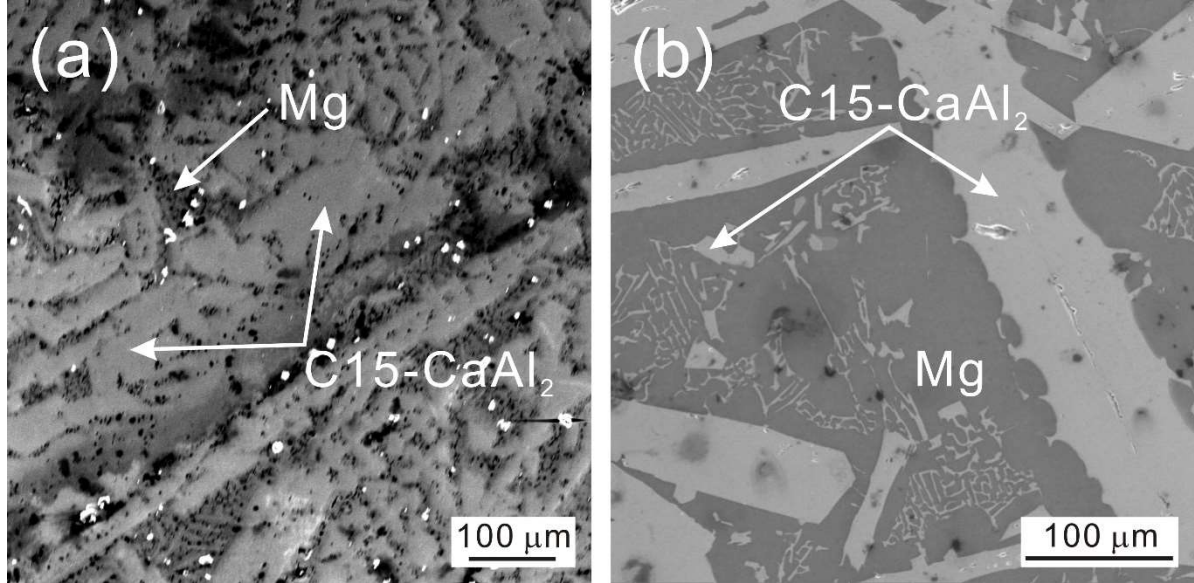


Fig. 5 SEM images of the (a) Mg-30Al-44Ca (wt.%) alloy synthesized by manual induction melting, and (b) Mg-CaAl₂ liquid-solid diffusion couple.

The flux growth method [34] was then used to synthesize the C36-Ca(Mg,Al)₂ Laves phase. Figs. 6(a) and 6(b) shows a schematic illustration of the setup. The starting materials of a Mg-30Al-44Ca (wt.%) alloy were mixed and placed in an alumina crucible with a mesh fixed at a position above the alloy for decanting the melt at the end of crystal growth. The entire crucible was encapsulated using a Quartz tube filled with Ar (Fig. 6(c)). The quartz tube was heated up to 870 °C and annealed for 2 h to melt the starting materials. After melting, the quartz tube was cooled down to 850 °C at 10 °C/h and then slowly cooled down to 750 °C at 1 °C/h, followed by centrifugation to spin off the remaining liquid phase. According to the phase diagram [24,28,35], at the composition of Mg-30Al-44Ca (wt.%) the C36-Ca(Mg,Al)₂ Laves phase is in equilibrium with the liquid phase at 750 °C. Therefore, after removing liquid phase, the crystal of the C36-Ca(Mg,Al)₂ Laves phase can be obtained. However, as shown in Fig. 6(d), after cooling the quartz tube was blackened on the inside and showed radial cracking at the position where the crucibles met. After cracking the tube we found one ingot (Fig. 6(e)) in the crucible and no materials on the grid. It suggests that the whole melt solidified above 750°C and there was no liquid left to be centrifuged into the upper crucible. The fact that there was no liquid phase present at 750°C could either be due to an error in the phase diagram, a significant change

in melt composition due to evaporation losses, or a temperature offset between our thermocouple and the actual temperature in the crucible.

Finally, we tried to synthesize the C36-Ca(Mg,Al)_2 Laves phase by the Bridgman method. Pure elements at composition Mg-28Al-46Ca (wt.%) were placed in a cylindrical tantalum crucible of 14 mm in diameter and 70 mm in length. The crucible was sealed with 0.6 bar Argon and placed on a water-cooled cold finger in a Bridgman apparatus, the chamber of which was then heated to 900 °C. After temperature equilibration the actual growth was carried out by lowering the crucible out of the hot zone at a velocity of 5 mm/h.

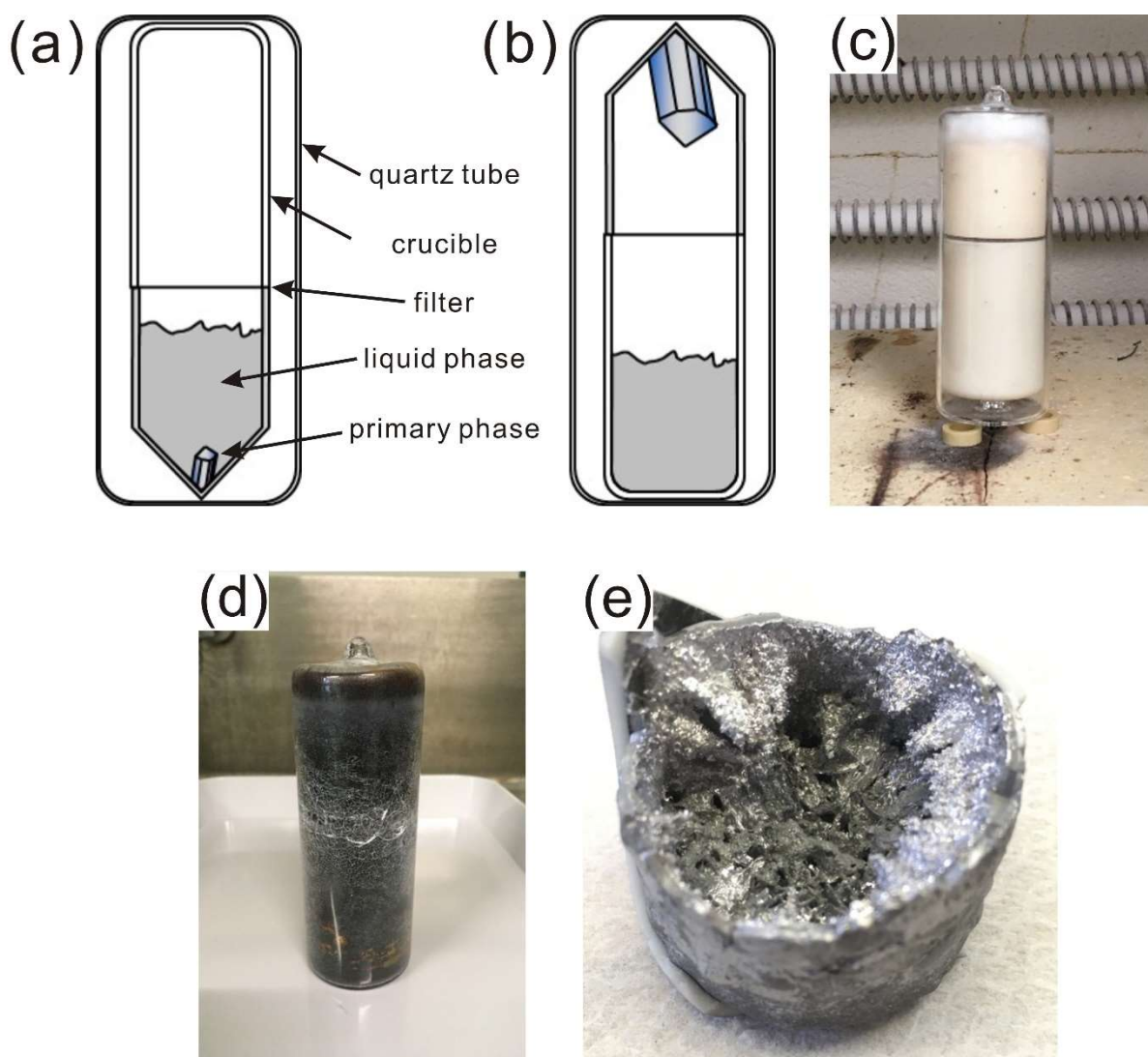


Fig. 6 (a) A schematic illustration of the set-up of the solution growth method. (b) After heat treatment, the primary phase was separated from the remaining liquid phase by centrifugation. (c) An alumina crucible encapsulated in a quartz tube filled with Ar. (d) After cooling the quartz tube was blackened on the inside and showed radial cracks. (e) Only one ingot was obtained in the crucible and no materials were left on the grid.

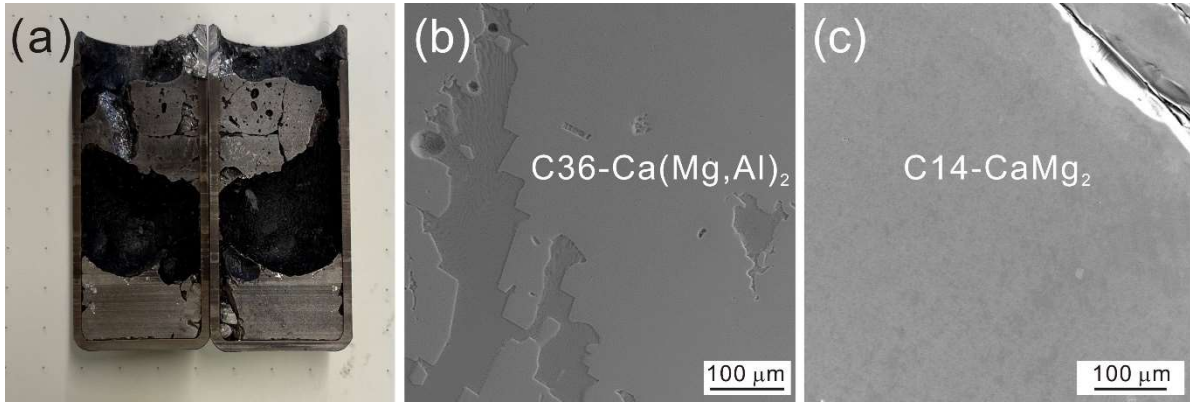


Fig. 7 (a) The Mg-28Al-46Ca (wt.%) alloy synthesized by the Bridgman method to obtain the C36-Ca(Mg,Al)₂ Laves phase. SEM images of the (b) top and (c) bottom parts of the sample.

As shown in Fig. 7(a), the Mg-28Al-46Ca (wt.%) alloy synthesized by the Bridgman method contains two parts and a large void in the middle. The reason why and how the large void occurs are not clear yet. The microstructures of the top and the bottom parts of the sample obtained by the Bridgman method are shown in Figs. 7(b) and 7(c), respectively. Their average compositions measured by EDS are Mg-45.37Al-38.63Ca (at.%) and Mg-2.27Al-39.40Ca (at.%), respectively. The EBSD measurements indicate that the top and the bottom parts of the sample are the C36-Ca(Mg,Al)₂ and C14-CaMg₂, respectively. Therefore, it is possible to obtain the C36-Ca(Mg,Al)₂ Laves phase after a time-consuming process of trial and error but the synthesis of flawless single-phase bulk materials of the C36-Ca(Mg,Al)₂ Laves phase is very difficult.

4 Conclusions

Due to the high reactivity and high vapor pressures of Mg and Ca and high affinity of Al with Fe, the synthesis of bulk materials of Mg-Al-Ca solid solutions, composites and intermetallic phases for specific scientific purposes is rather challenging. Different methods were investigated in the present work to show the challenges and pitfalls in the synthesis of the Mg-Al-Ca bulk materials. The following conclusions are drawn:

(1) To reduce the evaporation of Mg and Ca, the Mg-Al-Ca solid solutions can be synthesized by induction melting using a steel crucible under Ar atmosphere with high pressure. During melting and casting, the high pressure Ar atmosphere can reduce casting defects and improve mechanical properties of the as-cast Mg-Al-Ca alloys. The precipitation along grain boundaries

and the intragranular segregation in the Mg-Al-Ca solid solutions can be significantly reduced by hot rolling and homogenization annealing.

(2) The Mg-Al-Ca composites comprising a Mg matrix and a network of the Mg-based Laves phase can be synthesized by induction melting under Ar atmosphere. When the Al content is low (≤ 6 wt.%), the Fe contamination in the Mg-Al-Ca composites is negligible, and thus steel crucible can still be used during melting. The phases and microstructures of the Mg-Al-Ca composites can be adjusted the alloy composition and heat treatment.

(3) While the C14- CaMg_2 Laves phase can be synthesized by induction melting using a steel crucible under Ar protection, the C15- CaAl_2 Laves phase can be prepared by arc melting. However, the synthesis of $\text{Mg}_{17}\text{Al}_{12}$ intermetallic phase by the diffusion couple technique was not successful due to the oxidation of the contact surfaces during heat treatment. The synthesis of the C36- $\text{Ca}(\text{Mg},\text{Al})_2$ Laves phase by manual induction melting failed, due to a high loss of Mg during melting. No C36- $\text{Ca}(\text{Mg},\text{Al})_2$ Laves phase can be obtained from the liquid-solid Mg- CaAl_2 diffusion couples, either. It is possible to synthesize the C36- $\text{Ca}(\text{Mg},\text{Al})_2$ Laves phase by the Bridgman method but it is challenging to produce flawless single-phase bulk materials of the C36- $\text{Ca}(\text{Mg},\text{Al})_2$ Laves phase.

Acknowledgements:

We thank Mr. Jürgen Wichert and Mr. Michael Kulse for their technical supports in alloy synthesis. This work was supported by the German research foundation (DFG) within the Collaborative Research Centre SFB 1394 “Structural and Chemical Atomic Complexity—From Defect Phase Diagrams to Materials Properties” (Project ID 409476157). H. Springer wishes to acknowledge funding through the Heisenberg-program of the Deutsche Forschungsgemeinschaft (Project ID 416498847).

Author contributions:

L. Tanure and H. Springer conceived and designed the experiments. W. Luo wrote the manuscript. M. Felten, D. Zander and W. Delis analysed the microstructures of Mg-Al-Ca solid solutions. N. Aye performed characterizations of the Mg-Al-Ca composites. M. Freund contributed to the characterizations of the Mg-Al-Ca intermetallics. C. Thomas and M. Feuerbacher contributed to the synthesis of the C36- $\text{Ca}(\text{Mg},\text{Al})_2$ Laves phase. S. Sandlöbes-Haut and S. Korte-Kerzel provided feedback and suggestions to improve the experiments. All authors contributed to discussion of the results and reviewed the manuscript.

Conflicts of Interest: The authors declare no conflict of interest.

References

1. Kulekci, M.K. Magnesium and its alloys applications in automotive industry. *Int. J. Adv. Manuf. Technol.* **2008**, *39*, 851-865.
2. Jayasathyakawin, S.; Ravichandran, M.; Baskar, N.; Anand Chairman, C.; Balasundaram, R. Mechanical properties and applications of Magnesium alloy – Review. *Mater. Today: Proc.* **2020**, *27*, 909-913.
3. Sandlöbes, S.; Friák, M.; Korte-Kerzel, S.; Pei, Z.; Neugebauer, J.; Raabe, D. A rare-earth free magnesium alloy with improved intrinsic ductility. *Sci. Rep.* **2017**, *7*, 10458.
4. Suzuki, A.; Saddock, N.D.; Jones, J.W.; Pollock, T.M. Solidification paths and eutectic intermetallic phases in Mg–Al–Ca ternary alloys. *Acta Mater.* **2005**, *53*, 2823-2834.
5. Zhang, L.; Deng, K.-k.; Nie, K.-b.; Xu, F.-j.; Su, K.; Liang, W. Microstructures and mechanical properties of Mg–Al–Ca alloys affected by Ca/Al ratio. *Mater. Sci. Eng. A* **2015**, *636*, 279-288.
6. Sanyal, S.; Paliwal, M.; Bandyopadhyay, T.K.; Mandal, S. Evolution of microstructure, phases and mechanical properties in lean as-cast Mg–Al–Ca–Mn alloys under the influence of a wide range of Ca/Al ratio. *Mater. Sci. Eng. A* **2021**, *800*, 140322.
7. Zubair, M.; Sandlöbes, S.; Wollenweber, M.A.; Kusche, C.F.; Hildebrandt, W.; Broeckmann, C.; Korte-Kerzel, S. On the role of Laves phases on the mechanical properties of Mg–Al–Ca alloys. *Mater. Sci. Eng. A* **2019**, *756*, 272-283.
8. Amberger, D.; Eisenlohr, P.; Göken, M. Microstructural evolution during creep of Ca-containing AZ91. *Mater. Sci. Eng. A* **2009**, *510-511*, 398-402.
9. Luo, A.A.; Powell, B.R.; Balogh, M.P. Creep and microstructure of magnesium-aluminum-calcium based alloys. *Mater. Sci. Eng. A* **2002**, *33*, 567-574.
10. Chisholm, M.F.; Kumar, S.; Hazzledine, P. Dislocations in Complex Materials. *Science* **2005**, *307*, 701-703.
11. Hazzledine, P.M.; Pirouz, P. Synchroshear transformation in Laves phases. *Scr. Metall. Mater.* **1993**, *28*, 1277-1282.
12. Paufler, P. Early work on Laves phases in East Germany. *Intermetallics* **2011**, *19*, 599-612.
13. Felten, M.; Nowak, J.; Grünewald, P.; Schäfer, F.; Motz, C.; Zander, D. The Role of Native Oxides on the Corrosion Mechanism of Laves Phases in Mg–Al–Ca Composites. In Proceedings of the Magnesium 2021, Cham, 2021//, 2021; pp. 217-225.
14. Hasegawa, M. Chapter 3.3 - Ellingham Diagram. In *Treatise on Process Metallurgy*, Seetharaman, S., Ed.; Elsevier: Boston, 2014; pp. 507-516.

15. Honig, R.E. Vapor Pressure Data for the More Common Elements. *RCA Review* **1957**, *18*, 195-204.
16. Xiong, N.; Friedrich, S.; Mohamed, S.R.; Kirillov, I.; Ye, X.; Tian, Y.; Friedrich, B. The Separation Behavior of Impurities in the Purification of High-Purity Magnesium via Vacuum Distillation. *J. Sustain. Metall.* **2022**, *8*, 1561-1572.
17. Luo, A.A. Magnesium casting technology for structural applications. *J. Magnes. Alloy.* **2013**, *1*, 2-22.
18. Kumar, A.; Kumar, S.; Mukhopadhyay, N.K. Introduction to magnesium alloy processing technology and development of low-cost stir casting process for magnesium alloy and its composites. *J. Magnes. Alloy.* **2018**, *6*, 245-254.
19. Ikeda, O.; Ohnuma, I.; Kainuma, R.; Ishida, K. Phase equilibria and stability of ordered BCC phases in the Fe-rich portion of the Fe–Al system. *Intermetallics* **2001**, *9*, 755-761.
20. Hradilová, M.; Vojtěch, D.; Kubásek, J.; Čapek, J.; Vlach, M. Structural and mechanical characteristics of Mg–4Zn and Mg–4Zn–0.4Ca alloys after different thermal and mechanical processing routes. *Mater. Sci. Eng. A* **2013**, *586*, 284-291.
21. Okamoto, H. Ca–Mg (calcium–magnesium). *J. Ph. Equilibria Diffus.* **1998**, *19*, 490.
22. Okamoto, H. Al–Mg (aluminum–magnesium). *J. Ph. Equilibria Diffus.* **1998**, *19*, 598.
23. Okamoto, H. Al–Ca (aluminum–calcium). *J. Ph. Equilibria Diffus.* **2003**, *24*, 91-91.
24. Kevorkov, D.; Medraj, M.; Li, J.; Essadiqi, E.; Chartrand, P. The 400°C isothermal section of the Mg–Al–Ca system. *Intermetallics* **2010**, *18*, 1498-1506.
25. Stein, F.; Leineweber, A. Laves phases: a review of their functional and structural applications and an improved fundamental understanding of stability and properties. *J. Mater. Sci.* **2021**, *56*, 5321-5427.
26. Voß, S.; Stein, F.; Palm, M.; Raabe, D. Synthesis of defect-free single-phase bars of high-melting Laves phases through modified cold crucible levitation melting. *Mater. Sci. Eng. A* **2010**, *527*, 7848-7853.
27. Zolriasatein, A.; Shokuhfar, A. Homogenizing annealing heat treatment effects on the microstructure, hardness and thermal behavior of Al12Mg17 complex metallic alloy. *Mater. Des.* **2015**, *75*, 17-23.
28. Cao, H.; Zhang, C.; Zhu, J.; Cao, G.; Kou, S.; Schmid-Fetzer, R.; Chang, Y.A. Experiments coupled with modeling to establish the Mg-rich phase equilibria of Mg–Al–Ca. *Acta Mater.* **2008**, *56*, 5245-5254.

References

- [1] J. F. Nie, K. S. Shin and Z. R. Zeng. ‘Microstructure, Deformation, and Property of Wrought Magnesium Alloys’. In: *Metallurgical and Materials Transactions A* 51.12 (2020), pp. 6045–6109.
- [2] J. Hirsch and T. Al-Samman. ‘Superior light metals by texture engineering: Optimized aluminum and magnesium alloys for automotive applications’. In: *Acta Materialia* 61.3 (2013), pp. 818–843.
- [3] H. Pan, Y. Ren, H. Fu, H. Zhao, L. Wang, X. Meng and G. Qin. ‘Recent developments in rare-earth free wrought magnesium alloys having high strength: A review’. In: *Journal of Alloys and Compounds* 663 (2016), pp. 321–331.
- [4] H. Somekawa. ‘Effect of Alloying Elements on Fracture Toughness and Ductility in Magnesium Binary Alloys; A Review’. In: *Materials Transactions* 61.1 (2020), pp. 1–13.
- [5] J. Bohlen, D. Letzig and K. U. Kainer. ‘New Perspectives for Wrought Magnesium Alloys’. In: *Materials Science Forum* 546-549 (2007), pp. 1–10.
- [6] T. M. Pollock. ‘Weight Loss with Magnesium Alloys’. In: *Science* 328.5981 (2010), pp. 986–987.
- [7] W. J. Joost. ‘Reducing Vehicle Weight and Improving U.S. Energy Efficiency Using Integrated Computational Materials Engineering’. In: *Jom* 64.9 (2012), pp. 1032–1038.
- [8] C. Romanowski. ‘Magnesium Alloy Sheet for Transportation Applications’. In: *Magnesium Technology 2019*. Ed. by V. V. Joshi, J. B. Jordon, D. Orlov and N. R. Neelameggham. Springer International Publishing, pp. 3–12.
- [9] S. R. Agnew and Ö. Duygulu. ‘Plastic anisotropy and the role of non-basal slip in magnesium alloy AZ31B’. In: *International Journal of Plasticity* 21.6 (2005), pp. 1161–1193.
- [10] M. H. Yoo. ‘Slip, twinning, and fracture in hexagonal close-packed metals’. In: *Metallurgical Transactions A* 12.3 (1981), pp. 409–418.
- [11] P. G. Partridge. ‘The crystallography and deformation modes of hexagonal close-packed metals’. In: *Metallurgical Reviews* 12.1 (1967), pp. 169–194.
- [12] R. V. Mises. ‘Mechanik der plastischen Formänderung von Kristallen’. In: *ZAMM - Journal of Applied Mathematics and Mechanics / Zeitschrift für Angewandte Mathematik und Mechanik* 8.3 (1928), pp. 161–185.
- [13] N. Stanford and M. Barnett. ‘Effect of composition on the texture and deformation behaviour of wrought Mg alloys’. In: *Scripta Materialia* 58.3 (2008), pp. 179–182.
- [14] R. Pei, Y. Zou, M. Zubair, D. Wei and T. Al-Samman. ‘Synergistic effect of Y and Ca addition on the texture modification in AZ31B magnesium alloy’. In: *Acta Materialia* 233 (2022).
- [15] Z. R. Zeng, Y. M. Zhu, S. W. Xu, M. Z. Bian, C. H. J. Davies, N. Birbilis and J. F. Nie. ‘Texture evolution during static recrystallization of cold-rolled magnesium alloys’. In: *Acta Materialia* 105 (2016), pp. 479–494.

- [16] Z. R. Zeng, M. Z. Bian, S. W. Xu, C. H. J. Davies, N. Birbilis and J. F. Nie. ‘Texture evolution during cold rolling of dilute Mg alloys’. In: *Scripta Materialia* 108 (2015), pp. 6–10.
- [17] L. Wang et al. ‘Review: Achieving enhanced plasticity of magnesium alloys below recrystallization temperature through various texture control methods’. In: *Journal of Materials Research and Technology* 9.6 (2020), pp. 12604–12625.
- [18] J. Wu, L. Jin, J. Dong, F. Wang and S. Dong. ‘The texture and its optimization in magnesium alloy’. In: *Journal of Materials Science & Technology* 42 (2020), pp. 175–189.
- [19] H.-S. Jang, J.-K. Lee, A. J. S. F. Tapia, N. J. Kim and B.-J. Lee. ‘Activation of non-basal $\langle c + a \rangle$ slip in multicomponent Mg alloys’. In: *Journal of Magnesium and Alloys* (2021).
- [20] Z. Pei et al. ‘Ab initio and atomistic study of generalized stacking fault energies in Mg and Mg–Y alloys’. In: *New Journal of Physics* 15 (2013), p. 043020.
- [21] C. M. Cepeda-Jiménez, J. M. Molina-Aldareguia and M. T. Pérez-Prado. ‘Effect of grain size on slip activity in pure magnesium polycrystals’. In: *Acta Materialia* 84 (2015), pp. 443–456.
- [22] H. Yu, Y. Xin, M. Wang and Q. Liu. ‘Hall-Petch relationship in Mg alloys: A review’. In: *Journal of Materials Science & Technology* 34.2 (2018), pp. 248–256.
- [23] Z.-G. Li, Y. Miao, H.-L. Jia, R. Zheng, M.-H. Wang and H.-Y. Wang. ‘Designing a low-alloyed Mg–Al–Sn–Ca alloy with high strength and extraordinary formability by regulating fine grains and unique texture’. In: *Materials Science and Engineering: A* 852 (2022).
- [24] H. Pan et al. ‘Ultra-fine grain size and exceptionally high strength in dilute Mg–Ca alloys achieved by conventional one-step extrusion’. In: *Materials Letters* 237 (2019), pp. 65–68.
- [25] S. R. Agnew, J. A. Horton, T. M. Lillo and D. W. Brown. ‘Enhanced ductility in strongly textured magnesium produced by equal channel angular processing’. In: *Scripta Materialia* 50.3 (2004), pp. 377–381.
- [26] A. Yamashita, Z. Horita and T. G. Langdon. ‘Improving the mechanical properties of magnesium and a magnesium alloy through severe plastic deformation’. In: *Materials Science and Engineering: A* 300.1 (2001), pp. 142–147.
- [27] B. Beausir, S. Biswas, D. I. Kim, L. S. Tóth and S. Suwas. ‘Analysis of microstructure and texture evolution in pure magnesium during symmetric and asymmetric rolling’. In: *Acta Materialia* 57.17 (2009), pp. 5061–5077.
- [28] B. Q. Shi, Y. Q. Cheng, X. L. Shang, H. Yan, R. S. Chen and W. Ke. ‘Hall-Petch relationship, twinning responses and their dependences on grain size in the rolled Mg–Zn and Mg–Y alloys’. In: *Materials Science and Engineering: A* 743 (2019), pp. 558–566.
- [29] C. Ha, J. Bohlen, S. Yi, X. Zhou, H.-G. Brokmeier, N. Schell, D. Letzig and K. U. Kainer. ‘Influence of Nd or Ca addition on the dislocation activity and texture changes of Mg–Zn alloy sheets under uniaxial tensile loading’. In: *Materials Science and Engineering: A* 761 (2019).
- [30] M. Zecevic, I. J. Beyerlein and M. Knezevic. ‘Activity of pyramidal I and II $\langle c+a \rangle$ slip in Mg alloys as revealed by texture development’. In: *Journal of the Mechanics and Physics of Solids* 111 (2018), pp. 290–307.

- [31] N. Xia et al. ‘Enhanced ductility of Mg–1Zn–0.2Zr alloy with dilute Ca addition achieved by activation of non-basal slip and twinning’. In: *Materials Science and Engineering: A* 813 (2021).
- [32] K. Wei et al. ‘Grain size effect on tensile properties and slip systems of pure magnesium’. In: *Acta Materialia* 206 (2021), p. 116604.
- [33] S. Sandlöbes, M. Friák, J. Neugebauer and D. Raabe. ‘Basal and non-basal dislocation slip in Mg–Y’. In: *Materials Science and Engineering: A* 576 (2013), pp. 61–68.
- [34] K. X. Sun et al. ‘Quantitative study on slip/twinning activity and theoretical critical shear strength of Mg alloy with Y addition’. In: *Materials Science and Engineering: A* 792 (2020).
- [35] N. Stanford. ‘Micro-alloying Mg with Y, Ce, Gd and La for texture modification—A comparative study’. In: *Materials Science and Engineering: A* 527.10-11 (2010), pp. 2669–2677.
- [36] Y. Chino, K. Sassa and M. Mabuchi. ‘Texture and stretch formability of a rolled Mg–Zn alloy containing dilute content of Y’. In: *Materials Science and Engineering: A* 513-514 (2009), pp. 394–400.
- [37] B. L. Wu, Y. H. Zhao, X. H. Du, Y. D. Zhang, F. Wagner and C. Esling. ‘Ductility enhancement of extruded magnesium via yttrium addition’. In: *Materials Science and Engineering: A* 527.16-17 (2010), pp. 4334–4340.
- [38] Y. Chino, K. Sassa and M. Mabuchi. ‘Texture and Stretch Formability of Mg-1.5 mass%Zn-0.2 mass%Ce Alloy Rolled at Different Rolling Temperatures’. In: *MATERIALS TRANSACTIONS* 49.12 (2008), pp. 2916–2918.
- [39] K. Hantzsche, J. Bohlen, J. Wendt, K. U. Kainer, S. B. Yi and D. Letzig. ‘Effect of rare earth additions on microstructure and texture development of magnesium alloy sheets’. In: *Scripta Materialia* 63.7 (2010), pp. 725–730.
- [40] D. Wu, W.-n. Tang, R.-s. Chen and E.-h. Han. ‘Strength enhancement of Mg–3Gd–1Zn alloy by cold rolling’. In: *Transactions of Nonferrous Metals Society of China* 23.2 (2013), pp. 301–306.
- [41] H. Wang, C. J. Boehlert, Q. D. Wang, D. D. Yin and W. J. Ding. ‘In-situ analysis of the tensile deformation modes and anisotropy of extruded Mg-10Gd-3Y-0.5Zr (wt.%) at elevated temperatures’. In: *International Journal of Plasticity* 84 (2016), pp. 255–276.
- [42] T. Liu, Y. Liu, L. Xiao, S. Zhou and B. Song. ‘Role of Al in the Solution Strengthening of Mg–Al Binary Alloys’. In: *Metals* 12.1 (2022).
- [43] Z. T. Li, X. G. Qiao, C. Xu, X. Q. Liu, S. Kamado and M. Y. Zheng. ‘Enhanced strength by precipitate modification in wrought Mg–Al–Ca alloy with trace Mn addition’. In: *Journal of Alloys and Compounds* 836 (2020), p. 154689.
- [44] C. H. Cáceres and D. M. Rovera. ‘Solid solution strengthening in concentrated Mg–Al alloys’. In: *Journal of Light Metals* 1.3 (2001), pp. 151–156.

- [45] H. Cao, C. Zhang, J. Zhu, G. Cao, S. Kou, R. Schmid-Fetzer and Y. A. Chang. ‘Experiments coupled with modeling to establish the Mg-rich phase equilibria of Mg–Al–Ca’. In: *Acta Materialia* 56.18 (2008), pp. 5245–5254.
- [46] S. Sandlöbes, M. Friak, S. Korte-Kerzel, Z. Pei, J. Neugebauer and D. Raabe. ‘A rare-earth free magnesium alloy with improved intrinsic ductility’. In: *Sci Rep* 7.1 (2017), p. 10458.
- [47] N. Stanford and M. R. Barnett. ‘Solute strengthening of prismatic slip, basal slip and twinning in Mg and Mg–Zn binary alloys’. In: *International Journal of Plasticity* 47 (2013), pp. 165–181.
- [48] T. Nakata, T. Mezaki, C. Xu, K. Ohishi, K. Shimizu, S. Hanaki and S. Kamado. ‘Improving tensile properties of dilute Mg-0.27Al-0.13Ca-0.21Mn (at.%) alloy by low temperature high speed extrusion’. In: *Journal of Alloys and Compounds* 648 (2015), pp. 428–437.
- [49] T. Nakata, C. Xu, Y. Matsumoto, K. Shimizu, T. T. Sasaki, K. Hono and S. Kamado. ‘Optimization of Mn content for high strengths in high-speed extruded Mg-0.3Al-0.3Ca (wt%) dilute alloy’. In: *Materials Science and Engineering: A* 673 (2016), pp. 443–449.
- [50] Y. Chino, T. Ueda, M. Kado and M. Mabuchi. ‘Solid Solution Softening Mechanisms in Mg–Ca Alloy’. In: *MATERIALS TRANSACTIONS* 52.9 (2011), pp. 1840–1843.
- [51] Y. Chino, T. Ueda, Y. Otomatsu, K. Sassa, X. Huang, K. Suzuki and M. Mabuchi. ‘Effects of Ca on Tensile Properties and Stretch Formability at Room Temperature in Mg–Zn and Mg–Al Alloys’. In: *MATERIALS TRANSACTIONS* 52.7 (2011), pp. 1477–1482.
- [52] Y. B. Zuo, X. Fu, D. Mou, Q. F. Zhu, L. Li and J. Z. Cui. ‘Study on the role of Ca in the grain refinement of Mg–Ca binary alloys’. In: *Materials Research Innovations* 19.sup1 (2015), S1-94-S1-97.
- [53] Z. R. Zeng, Y. M. Zhu, J. F. Nie, S. W. Xu, C. H. J. Davies and N. Birbilis. ‘Effects of Calcium on Strength and Microstructural Evolution of Extruded Alloys Based on Mg-3Al-1Zn-0.3Mn’. In: *Metallurgical and Materials Transactions A* 50.9 (2019), pp. 4344–4363.
- [54] Z. R. Zeng, M. Z. Bian, S. W. Xu, C. H. J. Davies, N. Birbilis and J. F. Nie. ‘Effects of dilute additions of Zn and Ca on ductility of magnesium alloy sheet’. In: *Materials Science and Engineering: A* 674 (2016), pp. 459–471.
- [55] U. M. Chaudry, T. H. Kim, S. D. Park, Y. S. Kim, K. Hamad and J.-G. Kim. ‘Effects of calcium on the activity of slip systems in AZ31 magnesium alloy’. In: *Materials Science and Engineering: A* 739 (2019), pp. 289–294.
- [56] G. Zhu, L. Wang, J. Wang, J. Wang, J.-S. Park and X. Zeng. ‘Highly deformable Mg–Al–Ca alloy with Al₂Ca precipitates’. In: *Acta Materialia* 200 (2020), pp. 236–245.
- [57] Y. Zhong, J. Liu, R. A. Witt, Y.-h. Sohn and Z.-K. Liu. ‘Al₂(Mg,Ca) phases in Mg–Al–Ca ternary system: First-principles prediction and experimental identification’. In: *Scripta Materialia* 55.6 (2006), pp. 573–576.

- [58] M. Zubair, S. Sandlöbes, M. A. Wollenweber, C. F. Kusche, W. Hildebrandt, C. Broeckmann and S. Korte-Kerzel. ‘On the role of Laves phases on the mechanical properties of Mg-Al-Ca alloys’. In: *Materials Science and Engineering: A* 756 (2019), pp. 272–283.
- [59] M. Zubair et al. ‘Laves phases in Mg-Al-Ca alloys and their effect on mechanical properties’. In: *Materials & Design* 225 (2023).
- [60] M. Freund et al. ‘Plastic deformation of the CaMg₂ C14-Laves phase from 50 - 250°C’. In: *Materialia* 20 (2021).
- [61] K. Ozturk, Y. Zhong, Z.-K. Liu and A. A. Luo. ‘Creep resistant Mg-Al-Ca alloys: Computational thermodynamics and experimental investigation’. In: *JOM* 55.11 (2003), pp. 40–44.
- [62] S. Sandlöbes, S. Zaefferer, I. Schestakow, S. Yi and R. Gonzalez-Martinez. ‘On the role of non-basal deformation mechanisms for the ductility of Mg and Mg–Y alloys’. In: *Acta Materialia* 59.2 (2011), pp. 429–439.
- [63] S. Sandlöbes et al. ‘The relation between ductility and stacking fault energies in Mg and Mg–Y alloys’. In: *Acta Materialia* 60.6-7 (2012), pp. 3011–3021.
- [64] S. Sandlöbes, Z. Pei, M. Friák, L. F. Zhu, F. Wang, S. Zaefferer, D. Raabe and J. Neugebauer. ‘Ductility improvement of Mg alloys by solid solution: Ab initio modeling, synthesis and mechanical properties’. In: *Acta Materialia* 70 (2014), pp. 92–104.
- [65] Z. Wu and W. A. Curtin. ‘Mechanism and energetics of $\langle c + a \rangle$ dislocation cross-slip in hcp metals’. In: *Proc Natl Acad Sci U S A* 113.40 (2016), pp. 11137–11142.
- [66] Z. Wu, R. Ahmad, B. Yin, S. Sandlöbes and W. A. Curtin. ‘Mechanistic origin and prediction of enhanced ductility in magnesium alloys’. In: *Science* 359.6374 (2018), pp. 447–452.
- [67] A. Maldar, L. Wang, B. Liu, W. Liu, Z. Jin, B. Zhou and X. Zeng. ‘Activation of $\langle c \rangle$ dislocations in Mg with solute Y’. In: *Journal of Magnesium and Alloys* (2021).
- [68] Z. Ding, S. Li, W. Liu and Y. Zhao. ‘Modeling of Stacking Fault Energy in Hexagonal-Close-Packed Metals’. In: *Advances in Materials Science and Engineering* 2015 (2015), pp. 1–8.
- [69] F. C. Frank and W. T. Read. ‘Multiplication Processes for Slow Moving Dislocations’. In: *Physical Review* 79.4 (1950), pp. 722–723.
- [70] S. R. Agnew, L. Capolungo and C. A. Calhoun. ‘Connections between the basal I1 “growth” fault and $c+a$ dislocations’. In: *Acta Materialia* 82 (2015), pp. 255–265.
- [71] M. H. Yoo, J. R. Morris, K. M. Ho and S. R. Agnew. ‘Nonbasal deformation modes of HCP metals and alloys: Role of dislocation source and mobility’. In: *Metallurgical and Materials Transactions A* 33.3 (2002), pp. 813–822.
- [72] Z. Pei, M. Friák, S. Sandlöbes, R. Nazarov, B. Svendsen, D. Raabe and J. Neugebauer. ‘Rapid theory-guided prototyping of ductile Mg alloys: from binary to multi-component materials’. In: *New Journal of Physics* 17.9 (2015).
- [73] D. Hull and D. Bacon. *Introduction to Dislocations (Fifth Edition)*. Oxford: Butterworth-Heinemann, 2011, pp. ix–x.

-
- [74] G. Gottstein. *Materialwissenschaft und Werkstofftechnik: Physikalische Grundlagen*. Springer Berlin Heidelberg, 2014.
- [75] J. W. Christian and S. Mahajan. ‘Deformation twinning’. In: *Progress in Materials Science* 39.1 (1995), pp. 1–157.
- [76] S. Mahajan and D. F. Williams. ‘Deformation Twinning in Metals and Alloys’. In: *International Metallurgical Reviews* 18.2 (1973), pp. 43–61.
- [77] I. J. Beyerlein and C. N. Tomé. ‘A dislocation-based constitutive law for pure Zr including temperature effects’. In: *International Journal of Plasticity* 24.5 (2008), pp. 867–895.
- [78] D. W. Brown et al. ‘Development of intergranular thermal residual stresses in beryllium during cooling from processing temperatures’. In: *Acta Materialia* 57.4 (2009), pp. 972–979.
- [79] J.-F. Nie. ‘Precipitation and Hardening in Magnesium Alloys’. In: *Metallurgical and Materials Transactions A* 43.11 (2012), pp. 3891–3939.
- [80] A. Akhtar and E. Teghtsoonian. ‘Solid solution strengthening of magnesium single crystal“ I alloying behaviour in basal slip’. In: *Acta Metallurgica* 17 (1969), pp. 1339–1349.
- [81] R. O. Ritchie. ‘The conflicts between strength and toughness’. In: *Nat Mater* 10.11 (2011), pp. 817–22.
- [82] Y. Wei et al. ‘Evading the strength-ductility trade-off dilemma in steel through gradient hierarchical nanotwins’. In: *Nat Commun* 5 (2014), p. 3580.
- [83] R. Peierls. ‘The size of a dislocation’. In: *Proceedings of the Physical Society* 52.1 (1940), p. 34.
- [84] F. R. N. Nabarro. ‘Dislocations in a simple cubic lattice’. In: *Proceedings of the Physical Society* 59.2 (1947), p. 256.
- [85] E. O. Hall. ‘The Deformation and Ageing of Mild Steel: III Discussion of Results’. In: *Proceedings of the Physical Society. Section B* 64.9 (1951), p. 747.
- [86] N. J. Petch. ‘The Cleavage Strength of Polycrystals’. In: *Journal of the Iron and Steel Institute* 174 (1953), pp. 25–28.
- [87] P. B. Hirsch, R. W. Horne and M. J. Whelan. ‘LXVIII. Direct observations of the arrangement and motion of dislocations in aluminium’. In: *The Philosophical Magazine: A Journal of Theoretical Experimental and Applied Physics* 1.7 (1956), pp. 677–684.
- [88] P. Anderson, J. Hirth and J. Lothe. *Theory of Dislocations*. Cambridge University Press, 2017.
- [89] H. Suzuki. *Dislocations and Mechanical Properties of Crystals* by J. C. Fischer, W. G. Johnston, R. Thomsen and T. Vreeland. John Wiley & Sons, Inc., 1956.
- [90] E. Orowan. ‘Zur Kristallplastizität. III’. In: *Zeitschrift für Physik* 89.9 (1934), pp. 634–659.
- [91] G. I. Taylor. ‘The mechanism of plastic deformation of crystals. Part I.—Theoretical’. In: *Proceedings of the Royal Society of London. Series A, Containing Papers of a Mathematical and Physical Character* 145.855 (1934), pp. 362–387.

- [92] G. I. Taylor. ‘Plastic strain in metals’. In: *J. Inst. Metals* 62 (1938), pp. 307–324.
- [93] J. M. Burgers. ‘Geometrical considerations concerning the structural irregularities to be assumed in a crystal’. In: *Proceedings of the Physical Society* 52.1 (1940), p. 23.
- [94] J. Hirth and J. Lothe. *Theory of Dislocations*. Wiley, 1982.
- [95] J. Friedel and R. Smoluchowski. ‘Les dislocations’. In: *Physics Today* 10.7 (1957), p. 36.
- [96] Z. Wang, M. Saito, K. P. McKenna and Y. Ikumura. ‘Polymorphism of dislocation core structures at the atomic scale’. In: *Nat Commun* 5 (2014), p. 3239.
- [97] D. J. Bacon and M. H. Liang. ‘Computer simulation of dislocation cores in h.c.p. metals I. Interatomic potentials and stacking-fault stability’. In: *Philosophical Magazine A* 53.2 (1986), pp. 163–179.
- [98] E. Schmid. ‘Neuere Untersuchungen an Metallkristallen’. In: *Proceedings of the International Congress on Applied Mechanics* 204.2 (1924), pp. 342–353.
- [99] E. Schmid and W. Boas. ‘Theorien der Kristallplastizität und -festigkeit’. In: *Kristallplastizität: Mit Besonderer Berücksichtigung der Metalle*. Ed. by E. Schmid and W. Boas. Berlin, Heidelberg: Springer Berlin Heidelberg, 1935, pp. 279–301.
- [100] J. F. W. Bishop and R. Hill. ‘XLVI. A theory of the plastic distortion of a polycrystalline aggregate under combined stresses’. In: *Philosophical Magazine Series 1* 42 (1951), pp. 414–427.
- [101] J. Gawad, D. Banabic, A. Van Bael, D. S. Comsa, M. Gologanu, P. Eyckens, P. Van Houtte and D. Roose. ‘An evolving plane stress yield criterion based on crystal plasticity virtual experiments’. In: *International Journal of Plasticity* 75 (2015), pp. 141–169.
- [102] R. D. Jones, F. Di Gioacchino, H. Lim, T. E. J. Edwards, C. Schwalbe, C. C. Battaile and W. J. Clegg. ‘Reduced partitioning of plastic strain for strong and yet ductile precipitate-strengthened alloys’. In: *Scientific Reports* 8.1 (2018), p. 8698.
- [103] K. Farrell and P. R. V. Evans. ‘Some observations on mechanical twinning in polycrystalline niobium’. In: *Journal of the Less Common Metals* 8.4 (1965), pp. 222–234.
- [104] J. Wang, I. J. Beyerlein and C. N. Tomé. ‘An atomic and probabilistic perspective on twin nucleation in Mg’. In: *Scripta Materialia* 63.7 (2010), pp. 741–746.
- [105] A. Ghaderi and M. R. Barnett. ‘Sensitivity of deformation twinning to grain size in titanium and magnesium’. In: *Acta Materialia* 59.20 (2011), pp. 7824–7839.
- [106] R. E. Reed-Hill and W. D. Robertson. ‘Additional modes of deformation twinning in magnesium’. In: *Acta Metallurgica* 5.12 (1957), pp. 717–727.
- [107] M. A. Meyers, O. Vöhringer and V. A. Lubarda. ‘The onset of twinning in metals: a constitutive description’. In: *Acta Materialia* 49.19 (2001), pp. 4025–4039.
- [108] I. J. Beyerlein, L. Capolungo, P. E. Marshall, R. J. McCabe and C. N. Tomé. ‘Statistical analyses of deformation twinning in magnesium’. In: *Philosophical Magazine* 90.16 (2010), pp. 2161–2190.

- [109] P. R. Thornton and T. E. Mitchell. ‘Deformation twinning in alloys at low temperatures’. In: *The Philosophical Magazine: A Journal of Theoretical Experimental and Applied Physics* 7.75 (1962), pp. 361–375.
- [110] G. F. Bolling and R. H. Richman. ‘The Effect of Solute on Slip and Mechanical Twinning in Iron Alloys’. In: *Canadian Journal of Physics* 45.2 (1967), pp. 541–557.
- [111] B. A. Bilby, A. G. Crocker and A. H. Cottrell. ‘The theory of the crystallography of deformation twinning’. In: *Proceedings of the Royal Society of London. Series A. Mathematical and Physical Sciences* 288.1413 (1965), pp. 240–255.
- [112] M. R. Barnett. ‘Twinning and its role in wrought magnesium alloys’. In: *Advances in Wrought Magnesium Alloys*. 2012, pp. 105–143.
- [113] E. Schmid and G. Wassermann. ‘Über die mechanische Zwillingsbildung von Zinkkristallen’. In: *Zeitschrift für Physik* 48.5 (1928), pp. 370–383.
- [114] S. R. Agnew. ‘Deformation mechanisms of magnesium alloys’. In: *Advances in Wrought Magnesium Alloys*. 2012, pp. 63–104.
- [115] M. H. Yoo and C. T. Wei. ‘Slip Modes of Hexagonal-Close-Packed Metals’. In: *Journal of Applied Physics* 38.11 (1967), pp. 4317–4322.
- [116] M. R. Barnett. ‘A taylor model based description of the proof stress of magnesium AZ31 during hot working’. In: *Metallurgical and Materials Transactions A* 34.9 (2003), pp. 1799–1806.
- [117] A. Chapuis and J. H. Driver. ‘Temperature dependency of slip and twinning in plane strain compressed magnesium single crystals’. In: *Acta Materialia* 59.5 (2011), pp. 1986–1994.
- [118] S. R. Agnew, J. A. Horton and M. H. Yoo. ‘Transmission electron microscopy investigation of c+a dislocations in Mg and -solid solution Mg-Li alloys’. In: *Metallurgical and Materials Transactions A* 33.3 (2002), pp. 851–858.
- [119] H. Fan, Q. Wang, X. Tian and J. A. El-Awady. ‘Temperature effects on the mobility of pyramidal $\langle c + a \rangle$ dislocations in magnesium’. In: *Scripta Materialia* 127 (2017), pp. 68–71.
- [120] Z. Wu and W. A. Curtin. ‘The origins of high hardening and low ductility in magnesium’. In: *Nature* 526.7571 (2015), pp. 62–7.
- [121] U. Kocks and D. Westlake. ‘The importance of twinning for the ductility of CPH polycrystals’. In: *AIME Met Soc Trans* 239.7 (1967), pp. 1107–1109.
- [122] K. K. Alaneme and E. A. Okotete. ‘Enhancing plastic deformability of Mg and its alloys—A review of traditional and nascent developments’. In: *Journal of Magnesium and Alloys* 5.4 (2017), pp. 460–475.
- [123] O. Muránsky, D. G. Carr, M. R. Barnett, E. C. Oliver and P. Šittner. ‘Investigation of deformation mechanisms involved in the plasticity of AZ31 Mg alloy: In situ neutron diffraction and EPSC modelling’. In: *Materials Science and Engineering: A* 496.1-2 (2008), pp. 14–24.

- [124] J. Koike, T. Kobayashi, T. Mukai, H. Watanabe, M. Suzuki, K. Maruyama and K. Higashi. ‘The activity of non-basal slip systems and dynamic recovery at room temperature in fine-grained AZ31B magnesium alloys’. In: *Acta Materialia* 51.7 (2003), pp. 2055–2065.
- [125] H.-S. Jang and B.-J. Lee. ‘Effects of Zn on $c + a$ slip and grain boundary segregation of Mg alloys’. In: *Scripta Materialia* 160 (2019), pp. 39–43.
- [126] K.-H. Kim, J. B. Jeon, N. J. Kim and B.-J. Lee. ‘Role of yttrium in activation of $c + a$ slip in magnesium: An atomistic approach’. In: *Scripta Materialia* 108 (2015), pp. 104–108.
- [127] C. M. Cepeda-Jiménez, J. M. Molina-Aldareguia and M. T. Pérez-Prado. ‘EBSD-Assisted Slip Trace Analysis During In Situ SEM Mechanical Testing: Application to Unravel Grain Size Effects on Plasticity of Pure Mg Polycrystals’. In: *Jom* 68.1 (2015), pp. 116–126.
- [128] Z. Wu and W. A. Curtin. ‘Intrinsic structural transitions of the pyramidal $I +$ dislocation in magnesium’. In: *Scripta Materialia* 116 (2016), pp. 104–107.
- [129] K. Y. Xie, Z. Alam, A. Caffee and K. J. Hemker. ‘Pyramidal I slip in c -axis compressed Mg single crystals’. In: *Scripta Materialia* 112 (2016), pp. 75–78.
- [130] B. Zhou et al. ‘Dislocation behavior in a polycrystalline Mg-Y alloy using multi-scale characterization and VPSC simulation’. In: *Journal of Materials Science & Technology* 98 (2022), pp. 87–98.
- [131] J. Wu, S. Si, K. Takagi, T. Li, Y. Mine, K. Takashima and Y. L. Chiu. ‘Study of basal $\langle a \rangle$ and pyramidal $\langle c+a \rangle$ slips in Mg-Y alloys using micro-pillar compression’. In: *Philosophical Magazine* 100.11 (2020), pp. 1454–1475.
- [132] H. L. Kim, J. S. Park and Y. W. Chang. ‘Effects of lattice parameter changes on critical resolved shear stress and mechanical properties of magnesium binary single crystals’. In: *Materials Science and Engineering: A* 540 (2012), pp. 198–206.
- [133] F. Kang, Z. Li, J. T. Wang, P. Cheng and H. Y. Wu. ‘The activation of $c+a$ non-basal slip in Magnesium alloys’. In: *Journal of Materials Science* 47.22 (2012), pp. 7854–7859.
- [134] A. Kula, X. Jia, R. K. Mishra and M. Niewczas. ‘Flow stress and work hardening of Mg-Y alloys’. In: *International Journal of Plasticity* 92 (2017), pp. 96–121.
- [135] D. Utt, A. Stukowski and M. Ghazisaeidi. ‘The effect of solute cloud formation on the second order pyramidal to basal transition of $c+a$ edge dislocations in Mg-Y solid solutions’. In: *Scripta Materialia* 182 (2020), pp. 53–56.
- [136] I. Basu, M. Chen, J. Wheeler, R. E. Schaublin and J. F. Löffler. ‘Stacking-fault mediated plasticity and strengthening in lean, rare-earth free magnesium alloys’. In: *Acta Materialia* 211 (2021), p. 116877.
- [137] D. F. Shi, A. Ma, M. T. Pérez-Prado and C. M. Cepeda-Jiménez. ‘Activation of second-order $\langle c+a \rangle$ pyramidal slip and other secondary mechanisms in solid solution Mg-Zn alloys and their effect on tensile ductility’. In: *Acta Materialia* 244 (2023), p. 118555.
- [138] G. Zhu et al. ‘Improving ductility of a Mg alloy via non-basal $\langle a \rangle$ slip induced by Ca addition’. In: *International Journal of Plasticity* 120 (2019), pp. 164–179.

- [139] H. Somekawa, D. A. Basha, A. Singh, T. Tsuru and M. Yamaguchi. ‘Non-Basal Dislocation Nucleation Site of Solid Solution Magnesium Alloy’. In: *Materials Transactions* 61.6 (2020), pp. 1172–1175.
- [140] L. Wang et al. ‘Study of slip activity in a Mg-Y alloy by in situ high energy X-ray diffraction microscopy and elastic viscoplastic self-consistent modeling’. In: *Acta Materialia* 155 (2018), pp. 138–152.
- [141] D. Buey, L. G. Hector and M. Ghazisaeidi. ‘Core structure and solute strengthening of second-order pyramidal $c+a$ dislocations in Mg-Y alloys’. In: *Acta Materialia* 147 (2018), pp. 1–9.
- [142] A. Tehranchi, B. Yin and W. A. Curtin. ‘Solute strengthening of basal slip in Mg alloys’. In: *Acta Materialia* 151 (2018), pp. 56–66.
- [143] M. R. Fellingner, L. G. Hector and D. R. Trinkle. ‘Solutes that reduce yield strength anisotropies in magnesium from first principles’. In: *Physical Review Materials* 6.1 (2022).
- [144] D. Buey and M. Ghazisaeidi. ‘Atomistic simulation of $<c + a>$ screw dislocation cross-slip in Mg’. In: *Scripta Materialia* 117 (2016), pp. 51–54.
- [145] R. Ahmad, Z. Wu and W. A. Curtin. ‘Analysis of double cross-slip of pyramidal I $c+a$ screw dislocations and implications for ductility in Mg alloys’. In: *Acta Materialia* 183 (2020), pp. 228–241.
- [146] Y. Tang and J. A. El-Awady. ‘Formation and slip of pyramidal dislocations in hexagonal close-packed magnesium single crystals’. In: *Acta Materialia* 71 (2014), pp. 319–332.
- [147] J. A. Yasi, L. G. Hector and D. R. Trinkle. ‘First-principles data for solid-solution strengthening of magnesium: From geometry and chemistry to properties’. In: *Acta Materialia* 58.17 (2010), pp. 5704–5713.
- [148] S. Ganeshan, S. L. Shang, Y. Wang and Z. K. Liu. ‘Effect of alloying elements on the elastic properties of Mg from first-principles calculations’. In: *Acta Materialia* 57.13 (2009), pp. 3876–3884.
- [149] H. Somekawa and C. A. Schuh. ‘Effect of solid solution elements on nanoindentation hardness, rate dependence, and incipient plasticity in fine grained magnesium alloys’. In: *Acta Materialia* 59.20 (2011), pp. 7554–7563.
- [150] Z. Ding, W. Liu, H. Sun, S. Li, D. Zhang, Y. Zhao, E. J. Lavernia and Y. Zhu. ‘Origins and dissociation of pyramidal $<c + a>$ dislocations in magnesium and its alloys’. In: *Acta Materialia* 146 (2018), pp. 265–272.
- [151] H. Pan, H. Fu, B. Song, Y. Ren, C. Zhao and G. Qin. ‘Formation of profuse $<c+a>$ dislocations in deformed calcium-containing magnesium alloys’. In: *Philosophical Magazine Letters* 96.7 (2016), pp. 249–255.
- [152] Y. Tang and J. A. El-Awady. ‘Highly anisotropic slip-behavior of pyramidal I $c+a$ dislocations in hexagonal close-packed magnesium’. In: *Materials Science and Engineering: A* 618 (2014), pp. 424–432.

- [153] T. Tsuru, Y. Udagawa, M. Yamaguchi, M. Itakura, H. Kaburaki and Y. Kaji. ‘Solution softening in magnesium alloys: the effect of solid solutions on the dislocation core structure and nonbasal slip’. In: *J Phys Condens Matter* 25.2 (2013), p. 022202.
- [154] L. Capolungo, I. J. Beyerlein and C. N. Tomé. ‘Slip-assisted twin growth in hexagonal close-packed metals’. In: *Scripta Materialia* 60.1 (2009), pp. 32–35.
- [155] T. Liu, Q. Yang, N. Guo, Y. Lu and B. Song. ‘Stability of twins in Mg alloys – A short review’. In: *Journal of Magnesium and Alloys* 8.1 (2020), pp. 66–77.
- [156] B. Song, R. Xin, Y. Liang, G. Chen and Q. Liu. ‘Twinning characteristic and variant selection in compression of a pre-side-rolled Mg alloy sheet’. In: *Materials Science and Engineering: A* 614 (2014), pp. 106–115.
- [157] J. J. Jonas, S. Mu, T. Al-Samman, G. Gottstein, L. Jiang and É. Martin. ‘The role of strain accommodation during the variant selection of primary twins in magnesium’. In: *Acta Materialia* 59.5 (2011), pp. 2046–2056.
- [158] S. W. Lee, G. Han, T.-S. Jun and S. H. Park. ‘Effects of initial texture on deformation behavior during cold rolling and static recrystallization during subsequent annealing of AZ31 alloy’. In: *Journal of Materials Science & Technology* 66 (2021), pp. 139–149.
- [159] A. Kula, T. Tokarski and M. Niewczas. ‘Strain Localization During Compressive Deformation of Mg-Gd Alloy’. In: *Metallurgical and Materials Transactions A* 51.8 (2020), pp. 3742–3748.
- [160] F. Wang, S. Sandlöbes, M. Diehl, L. Sharma, F. Roters and D. Raabe. ‘In situ observation of collective grain-scale mechanics in Mg and Mg–rare earth alloys’. In: *Acta Materialia* 80 (2014), pp. 77–93.
- [161] K. Atik and M. Efe. ‘Twinning-induced shear banding and its control in rolling of magnesium’. In: *Materials Science and Engineering: A* 725 (2018), pp. 267–273.
- [162] J. Koike. ‘Enhanced deformation mechanisms by anisotropic plasticity in polycrystalline Mg alloys at room temperature’. In: *Metallurgical and Materials Transactions A* 36 (2005), pp. 1689–1696.
- [163] X. Liao, J. Wang, J. Nie, Y. Jiang and P. Wu. ‘Deformation twinning in hexagonal materials’. In: *MRS Bulletin* 41.4 (2016), pp. 314–319.
- [164] D. D. Yin, C. J. Boehlert, L. J. Long, G. H. Huang, H. Zhou, J. Zheng and Q. D. Wang. ‘Tension-compression asymmetry and the underlying slip/twinning activity in extruded Mg–Y sheets’. In: *International Journal of Plasticity* 136 (2021).
- [165] A. E. Davis, J. D. Robson and M. Turski. ‘Reducing yield asymmetry and anisotropy in wrought magnesium alloys – A comparative study’. In: *Materials Science and Engineering: A* 744 (2019), pp. 525–537.
- [166] S. A. Habib, A. S. Khan, T. Gnäupel-Herold, J. T. Lloyd and S. E. Schoenfeld. ‘Anisotropy, tension-compression asymmetry and texture evolution of a rare-earth-containing magnesium alloy sheet, ZEK100, at different strain rates and temperatures: Experiments and modeling’. In: *International Journal of Plasticity* 95 (2017), pp. 163–190.

- [167] E. A. Ball and P. B. Prangnell. ‘Tensile-compressive yield asymmetries in high strength wrought magnesium alloys’. In: *Scripta Metallurgica et Materialia* 31.2 (1994), pp. 111–116.
- [168] J. P. Nobre, U. Noster, M. Kornmeier, A. M. Dias and B. Scholtes. ‘Deformation Asymmetry of AZ31 Wrought Magnesium Alloy’. In: *Key Engineering Materials* 230-232 (2002), pp. 267–270.
- [169] P. Zhou, E. Beeh and H. E. Friedrich. ‘Influence of Tension-Compression Asymmetry on the Mechanical Behavior of AZ31B Magnesium Alloy Sheets in Bending’. In: *Journal of Materials Engineering and Performance* 25.3 (2016), pp. 853–865.
- [170] S.-G. Hong, S. H. Park and C. S. Lee. ‘Role of 10–12 twinning characteristics in the deformation behavior of a polycrystalline magnesium alloy’. In: *Acta Materialia* 58.18 (2010), pp. 5873–5885.
- [171] Y. Xin, X. Zhou and Q. Liu. ‘Suppressing the tension–compression yield asymmetry of Mg alloy by hybrid extension twins structure’. In: *Materials Science and Engineering: A* 567 (2013), pp. 9–13.
- [172] L. Jiang, J. J. Jonas, A. A. Luo, A. K. Sachdev and S. Godet. ‘Twinning-induced softening in polycrystalline AM30 Mg alloy at moderate temperatures’. In: *Scripta Materialia* 54.5 (2006), pp. 771–775.
- [173] M. Lentz, M. Risse, N. Schaefer, W. Reimers and I. J. Beyerlein. ‘Strength and ductility with 1011 - 1012 double twinning in a magnesium alloy’. In: *Nat Commun* 7 (2016), p. 11068.
- [174] M. R. Barnett. ‘A rationale for the strong dependence of mechanical twinning on grain size’. In: *Scripta Materialia* 59.7 (2008), pp. 696–698.
- [175] H. Somekawa and T. Mukai. ‘Hall–Petch relation for deformation twinning in solid solution magnesium alloys’. In: *Materials Science and Engineering: A* 561 (2013), pp. 378–385.
- [176] M. S. Tsai and C. P. Chang. ‘Grain size effect on deformation twinning in Mg–Al–Zn alloy’. In: *Materials Science and Technology* 29.6 (2013), pp. 759–763.
- [177] I. Basu and T. Al-Samman. ‘Competitive twinning behavior in magnesium and its impact on recrystallization and texture formation’. In: *Materials Science and Engineering: A* 707 (2017), pp. 232–244.
- [178] P. Klimanek and A. Pöttsch. ‘Microstructure evolution under compressive plastic deformation of magnesium at different temperatures and strain rates’. In: *Materials Science and Engineering: A* 324.1 (2002), pp. 145–150.
- [179] P. Yang, Y. Yu, L. Chen and W. Mao. ‘Experimental determination and theoretical prediction of twin orientations in magnesium alloy AZ31’. In: *Scripta Materialia* 50.8 (2004), pp. 1163–1168.
- [180] J. Wang, J. M. Molina-Aldareguía and J. Llorca. ‘Effect of Al content on the critical resolved shear stress for twin nucleation and growth in Mg alloys’. In: *Acta Materialia* 188 (2020), pp. 215–227.
- [181] B. C. Suh, J. H. Kim, J. H. Hwang, M. S. Shim and N. J. Kim. ‘Twinning-mediated formability in Mg alloys’. In: *Sci Rep* 6 (2016), p. 22364.

- [182] I. Basu, M. Chen, J. Wheeler, R. E. Schäublin and J. F. Löffler. ‘Segregation-driven exceptional twin-boundary strengthening in lean Mg–Zn–Ca alloys’. In: *Acta Materialia* (2022), p. 117746.
- [183] N. M. Della Ventura, S. Kalácska, D. Casari, T. E. J. Edwards, A. Sharma, J. Michler, R. Logé and X. Maeder. ‘101⁻² twinning mechanism during in situ micro-tensile loading of pure Mg: Role of basal slip and twin-twin interactions’. In: *Materials & Design* 197 (2021).
- [184] B. Li and E. Ma. ‘Zonal dislocations mediating 1011 1012 twinning in magnesium’. In: *Acta Materialia* 57.6 (2009), pp. 1734–1743.
- [185] N. Li, L. Yang, C. Wang, M. A. Monclús, D. Shi and J. M. Molina-Aldareguía. ‘Deformation mechanisms of basal slip, twinning and non-basal slips in Mg–Y alloy by micropillar compression’. In: *Materials Science and Engineering: A* 819 (2021), p. 141408.
- [186] F. Wang and S. Agnew. ‘Dislocation-Twin Interactions in Magnesium Alloy AZ31’. In: *Magnesium Technology 2015*. Ed. by M. V. Manuel, A. Singh, M. Alderman and N. R. Neelameggham. Cham: Springer International Publishing, 2016, pp. 139–144.
- [187] F. Wang and S. R. Agnew. ‘Dislocation transmutation by tension twinning in magnesium alloy AZ31’. In: *International Journal of Plasticity* 81 (2016), pp. 63–86.
- [188] F. Wang, C. D. Barrett, R. J. McCabe, H. El Kadiri, L. Capolungo and S. R. Agnew. ‘Dislocation induced twin growth and formation of basal stacking faults in 101⁻² twins in pure Mg’. In: *Acta Materialia* 165 (2019), pp. 471–485.
- [189] S. Q. Zhu and S. P. Ringer. ‘On the role of twinning and stacking faults on the crystal plasticity and grain refinement in magnesium alloys’. In: *Acta Materialia* 144 (2018), pp. 365–375.
- [190] Z. Keshavarz and M. R. Barnett. ‘EBSD analysis of deformation modes in Mg–3Al–1Zn’. In: *Scripta Materialia* 55.10 (2006), pp. 915–918.
- [191] M. E. Fine. ‘Introduction to Chemical and Structural Defects in Crystalline Solids’. In: *The Chemical Structure of Solids*. Ed. by N. B. Hannay. New York, NY: Springer US, 1973, pp. 283–333.
- [192] J. A. Yasi, L. G. Hector and D. R. Trinkle. ‘Prediction of thermal cross-slip stress in magnesium alloys from a geometric interaction model’. In: *Acta Materialia* 60.5 (2012), pp. 2350–2358.
- [193] B. Wei, W. Wu, M. Gong, S. Yu, S. Ni, M. Song and J. Wang. ‘Influence of lowering basal stacking fault energy on twinning behaviours’. In: *Acta Materialia* 245 (2023), p. 118637.
- [194] J. A. Yasi, T. Nogaret, D. R. Trinkle, Y. Qi, L. G. Hector and W. A. Curtin. ‘Basal and prism dislocation cores in magnesium: comparison of first-principles and embedded-atom-potential methods predictions’. In: *Modelling and Simulation in Materials Science and Engineering* 17.5 (2009).
- [195] X. Wu, R. Wang and S. Wang. ‘Generalized-stacking-fault energy and surface properties for HCP metals: A first-principles study’. In: *Applied Surface Science* 256.11 (2010), pp. 3409–3412.

- [196] A. W. Ruff. ‘Measurement of stacking fault energy from dislocation interactions’. In: *Metallurgical Transactions* 1.9 (1970), pp. 2391–2413.
- [197] A. Seeger, R. Berner and H. Wolf. ‘Die experimentelle Bestimmung von Stapelfehlerenergien kubisch-flächenzentrierter Metalle’. In: *Zeitschrift für Physik* 155.2 (1959), pp. 247–262.
- [198] R. E. Schramm and R. P. Reed. ‘Stacking fault energies of seven commercial austenitic stainless steels’. In: *Metallurgical Transactions A* 6.7 (1975), pp. 1345–1351.
- [199] G. B. Olson and M. Cohen. ‘A general mechanism of martensitic nucleation: Part I. General concepts and the FCC \rightarrow HCP transformation’. In: *Metallurgical Transactions A* 7.12 (1976), pp. 1897–1904.
- [200] A. Reyes-Huamantínco, P. Puschnig, C. Ambrosch-Draxl, O. E. Peil and A. V. Ruban. ‘Stacking-fault energy and anti-Invar effect in Fe-Mn alloy from first principles’. In: *Physical Review B* 86.6 (2012).
- [201] S. Ando, H. Tonda and T. Gotoh. ‘Molecular dynamics simulation of $c+a$ dislocation core structure in hexagonal-close-packed metals’. In: *Metallurgical and Materials Transactions A* 33.3 (2002), pp. 823–829.
- [202] B. Li and E. Ma. ‘Pyramidal slip in magnesium: Dislocations and stacking fault on the 1011 plane’. In: *Philosophical Magazine* 89.14 (2009), pp. 1223–1235.
- [203] J. R. Morris, J. Scharff, K. M. Ho, D. E. Turner, Y. Y. Ye and M. H. Yoo. ‘Prediction of a 1122 hcp stacking fault using a modified generalized stacking-fault calculation’. In: *Philosophical Magazine A* 76.5 (2006), pp. 1065–1077.
- [204] T. Nogaret, W. A. Curtin, J. A. Yasi, L. G. Hector and D. R. Trinkle. ‘Atomistic study of edge and screw $c+a$ dislocations in magnesium’. In: *Acta Materialia* 58.13 (2010), pp. 4332–4343.
- [205] Z. Wu, M. F. Francis and W. A. Curtin. ‘Magnesium interatomic potential for simulating plasticity and fracture phenomena’. In: *Modelling and Simulation in Materials Science and Engineering* 23.1 (2015).
- [206] A. Kumar, B. M. Morrow, R. J. McCabe and I. J. Beyerlein. ‘An atomic-scale modeling and experimental study of $c+a$ dislocations in Mg’. In: *Materials Science and Engineering: A* 695 (2017), pp. 270–278.
- [207] L. Wen, P. Chen, Z. F. Tong, B. Y. Tang, L. M. Peng and W. J. Ding. ‘A systematic investigation of stacking faults in magnesium via first-principles calculation’. In: *The European Physical Journal B* 72.3 (2009), pp. 397–403.
- [208] A. E. Smith. ‘Surface, interface and stacking fault energies of magnesium from first principles calculations’. In: *Surface Science* 601.24 (2007), pp. 5762–5765.
- [209] B. Li, P. F. Yan, M. L. Sui and E. Ma. ‘Transmission electron microscopy study of stacking faults and their interaction with pyramidal dislocations in deformed Mg’. In: *Acta Materialia* 58.1 (2010), pp. 173–179.

- [210] B. Li, P. F. Yan, M. L. Sui and E. Ma. ‘Transmission electron microscopy study of stacking faults and their interaction with pyramidal dislocations in deformed Mg’. In: *Acta Materialia* 58.1 (2010), pp. 173–179.
- [211] N. Chetty and M. Weinert. ‘Stacking faults in magnesium’. In: *Physical Review B* 56.17 (1997), pp. 10844–10851.
- [212] R. L. Fleischer. ‘Rapid Solution Hardening, Dislocation Mobility, and the Flow Stress of Crystals’. In: *Journal of Applied Physics* 33.12 (1962), pp. 3504–3508.
- [213] R. Fleischer. In: *The strengthening of metals*. Ed. by D. Peckner. Vol. 93. New York: Reinhold, 1964, pp. 93–140.
- [214] S. Sandlöbes, I. Schestakow, S. B. Yi, S. Zaefferer, J. Q. Chen, M. Friák, J. Neugebauer and D. Raabe. ‘The Relation between Shear Banding, Microstructure and Mechanical Properties in Mg and Mg-Y Alloys’. In: *Materials Science Forum* 690 (2011), pp. 202–205.
- [215] Y.-J. Hu, V. Menon and L. Qi. ‘Formation of I1 stacking fault by deformation defect evolution from grain boundaries in Mg’. In: *Journal of Magnesium and Alloys* 10.10 (2022), pp. 2717–2729.
- [216] Q. Zhang, T.-W. Fan, L. Fu, B.-Y. Tang, L.-M. Peng and W.-J. Ding. ‘Ab-initio study of the effect of rare-earth elements on the stacking faults of Mg solid solutions’. In: *Intermetallics* 29 (2012), pp. 21–26.
- [217] Y. Dou, H. Luo, J. Zhang and X. Tang. ‘Generalized Stacking Fault Energy of 10-11<11-23> Slip System in Mg-Based Binary Alloys: A First Principles Study’. In: *Materials (Basel)* 12.9 (2019).
- [218] A. Moitra, S.-G. Kim and M. F. Horstemeyer. ‘Solute effect on the a+c dislocation nucleation mechanism in magnesium’. In: *Acta Materialia* 75 (2014), pp. 106–112.
- [219] Z. Pei and J. Yin. ‘The relation between two ductility mechanisms for Mg alloys revealed by high-throughput simulations’. In: *Materials & Design* 186 (2020), p. 108286.
- [220] S. R. Agnew, M. H. Yoo and C. N. Tomé. ‘Application of texture simulation to understanding mechanical behavior of Mg and solid solution alloys containing Li or Y’. In: *Acta Materialia* 49.20 (2001), pp. 4277–4289.
- [221] Y. N. Wang and J. C. Huang. ‘Texture analysis in hexagonal materials’. In: *Materials Chemistry and Physics* 81.1 (2003), pp. 11–26.
- [222] W. Gambin. *Textures and plasticity*. 2001.
- [223] O. Engler and V. Randle. *Introduction to texture analysis: macrotexture, microtexture, and orientation mapping*. CRC press, 2009.
- [224] V. Klosek. ‘Crystallographic textures’. In: *EPJ Web Conf.* 155 (2017), p. 00005.
- [225] H. Pan, Y. He and X. Zhang. ‘Interactions between Dislocations and Boundaries during Deformation’. In: *Materials (Basel)* 14.4 (2021).
- [226] T. R. Bieler, P. Eisenlohr, C. Zhang, H. J. Phukan and M. A. Crimp. ‘Grain boundaries and interfaces in slip transfer’. In: *Current Opinion in Solid State and Materials Science* 18.4 (2014), pp. 212–226.

- [227] U. F. Kocks, C. N. Tomé and H.-R. Wenk. *Texture and anisotropy: preferred orientations in polycrystals and their effect on materials properties*. Cambridge university press, 2000.
- [228] S. Biswas, D.-I. Kim and S. Suwas. ‘Asymmetric and symmetric rolling of magnesium: Evolution of microstructure, texture and mechanical properties’. In: *Materials Science and Engineering: A* 550 (2012), pp. 19–30.
- [229] M. R. Barnett, M. D. Nave and C. J. Bettles. ‘Deformation microstructures and textures of some cold rolled Mg alloys’. In: *Materials Science and Engineering: A* 386.1 (2004), pp. 205–211.
- [230] V. S. Ivaniji and I. A. Moroz. ‘Cold rolling texture development in Zn, Cd and Mg’. In: *Kristall und Technik* 14.4 (1979), pp. 463–469.
- [231] T. Al-Samman and G. Gottstein. ‘Influence of Starting Textures on the Development of Texture and Microstructure during Large Strain Hot Rolling of Pure Magnesium’. In: *Solid State Phenomena* 105 (2005), pp. 201–206.
- [232] T. Al-Samman and G. Gottstein. ‘Room temperature formability of a magnesium AZ31 alloy: Examining the role of texture on the deformation mechanisms’. In: *Materials Science and Engineering: A* 488.1 (2008), pp. 406–414.
- [233] A. Chapuis and Q. Liu. ‘Simulations of texture evolution for HCP metals: Influence of the main slip systems’. In: *Computational Materials Science* 97 (2015), pp. 121–126.
- [234] A. Jäger, P. Lukáč, V. Gärtnerová, J. Haloda and M. Dopita. ‘Influence of annealing on the microstructure of commercial Mg alloy AZ31 after mechanical forming’. In: *Materials Science and Engineering: A* 432.1 (2006), pp. 20–25.
- [235] S. B. Yi, J. Bohlen, S. Sandlöbes, S. Zaefferer, D. Letzig and K. U. Kainer. ‘Microstructural Evolution during Recrystallization of Magnesium Alloys’. In: *Materials Science Forum* 706-709 (2012), pp. 1291–1296.
- [236] S.-H. Kim, B.-S. You, C. Dong Yim and Y.-M. Seo. ‘Texture and microstructure changes in asymmetrically hot rolled AZ31 magnesium alloy sheets’. In: *Materials Letters* 59.29-30 (2005), pp. 3876–3880.
- [237] W. J. Kim, J. B. Lee, W. Y. Kim, H. T. Jeong and H. G. Jeong. ‘Microstructure and mechanical properties of Mg–Al–Zn alloy sheets severely deformed by asymmetrical rolling’. In: *Scripta Materialia* 56.4 (2007), pp. 309–312.
- [238] T. Chen, Z. Chen, L. Yi, J. Xiong and C. Liu. ‘Effects of texture on anisotropy of mechanical properties in annealed Mg–0.6%Zr–1.0%Cd sheets by unidirectional and cross rolling’. In: *Materials Science and Engineering: A* 615 (2014), pp. 324–330.
- [239] Y. Chino, K. Sassa, A. Kamiya and M. Mabuchi. ‘Enhanced formability at elevated temperature of a cross-rolled magnesium alloy sheet’. In: *Materials Science and Engineering: A* 441.1-2 (2006), pp. 349–356.
- [240] T. Motoyama, H. Watanabe, N. Ikeo and T. Mukai. ‘Mechanical and damping properties of equal channel angular extrusion-processed Mg–Ca alloys’. In: *Materials Letters* 201 (2017), pp. 144–147.

- [241] Y. S. Jeong and W. J. Kim. ‘Enhancement of mechanical properties and corrosion resistance of Mg–Ca alloys through microstructural refinement by indirect extrusion’. In: *Corrosion Science* 82 (2014), pp. 392–403.
- [242] M. A. Steiner, J. J. Bhattacharyya and S. R. Agnew. ‘The origin and enhancement of 0001 112⁻⁰ texture during heat treatment of rolled AZ31B magnesium alloys’. In: *Acta Materialia* 95 (2015), pp. 443–455.
- [243] A. Imandoust, C. D. Barrett, T. Al-Samman, K. A. Inal and H. El Kadiri. ‘A review on the effect of rare-earth elements on texture evolution during processing of magnesium alloys’. In: *Journal of Materials Science* 52.1 (2016), pp. 1–29.
- [244] T. Al-Samman and X. Li. ‘Sheet texture modification in magnesium-based alloys by selective rare earth alloying’. In: *Materials Science and Engineering: A* 528.10-11 (2011), pp. 3809–3822.
- [245] J. Bohlen, M. R. Nürnberg, J. W. Senn, D. Letzig and S. R. Agnew. ‘The texture and anisotropy of magnesium–zinc–rare earth alloy sheets’. In: *Acta Materialia* 55.6 (2007), pp. 2101–2112.
- [246] D. Griffiths. ‘Explaining texture weakening and improved formability in magnesium rare earth alloys’. In: *Materials Science and Technology* 31.1 (2015), pp. 10–24.
- [247] J. P. Hadorn, K. Hantzsche, S. Yi, J. Bohlen, D. Letzig, J. A. Wollmershauser and S. R. Agnew. ‘Role of Solute in the Texture Modification During Hot Deformation of Mg-Rare Earth Alloys’. In: *Metallurgical and Materials Transactions A* 43.4 (2011), pp. 1347–1362.
- [248] N. Stanford, D. Atwell and M. R. Barnett. ‘The effect of Gd on the recrystallisation, texture and deformation behaviour of magnesium-based alloys’. In: *Acta Materialia* 58.20 (2010), pp. 6773–6783.
- [249] H. Jiang, Y. Zhang, Q. Kang, Z. Xu, P. Dong and H. Li. ‘The influence of Ca and Gd microalloying on microstructure and mechanical property of hot-rolled Mg-3Al alloy’. In: *Procedia Engineering* 207 (2017), pp. 932–937.
- [250] N. Stanford, G. Sha, J. H. Xia, S. P. Ringer and M. R. Barnett. ‘Solute segregation and texture modification in an extruded magnesium alloy containing gadolinium’. In: *Scripta Materialia* 65.10 (2011), pp. 919–921.
- [251] C. Ha, J. Bohlen, X. Zhou, H. G. Brokmeier, K. U. Kainer, N. Schell, D. Letzig and S. Yi. ‘Texture development and dislocation activities in Mg-Nd and Mg-Ca alloy sheets’. In: *Materials Characterization* 175 (2021).
- [252] J. P. Hadorn, R. P. Mulay, K. Hantzsche, S. Yi, J. Bohlen, D. Letzig and S. R. Agnew. ‘Texture Weakening Effects in Ce-Containing Mg Alloys’. In: *Metallurgical and Materials Transactions A* 44.3 (2013), pp. 1566–1576.
- [253] L. W. F. Mackenzie and M. O. Pekguleryuz. ‘The recrystallization and texture of magnesium–zinc–cerium alloys’. In: *Scripta Materialia* 59.6 (2008), pp. 665–668.
- [254] S. Jo, D. Letzig and S. Yi. ‘Effect of Al Content on Texture Evolution and Recrystallization Behavior of Non-Flammable Magnesium Sheet Alloys’. In: *Metals* 11.3 (2021).

- [255] A. Styczynski, C. Hartig, J. Bohlen and D. Letzig. ‘Cold rolling textures in AZ31 wrought magnesium alloy’. In: *Scripta Materialia* 50.7 (2004), pp. 943–947.
- [256] D. Guan, X. Liu, J. Gao, L. Ma, B. P. Wynne and W. M. Rainforth. ‘Exploring the mechanism of “Rare Earth” texture evolution in a lean Mg-Zn-Ca alloy’. In: *Sci Rep* 9.1 (2019), p. 7152.
- [257] D. W. Kim, B. C. Suh, M. S. Shim, J. H. Bae, D. H. Kim and N. J. Kim. ‘Texture Evolution in Mg-Zn-Ca Alloy Sheets’. In: *Metallurgical and Materials Transactions A* 44.7 (2013), pp. 2950–2961.
- [258] J.-Y. Lee, Y.-S. Yun, W.-T. Kim and D.-H. Kim. ‘Twinning and texture evolution in binary Mg-Ca and Mg-Zn alloys’. In: *Metals and Materials International* 20.5 (2014), pp. 885–891.
- [259] Y. M. Kim, C. Mendis, T. Sasaki, D. Letzig, F. Pyczak, K. Hono and S. Yi. ‘Static recrystallization behaviour of cold rolled Mg-Zn-Y alloy and role of solute segregation in microstructure evolution’. In: *Scripta Materialia* 136 (2017), pp. 41–45.
- [260] S. Nandy, S.-P. Tsai, L. Stephenson, D. Raabe and S. Zaefferer. ‘The role of Ca, Al and Zn on room temperature ductility and grain boundary cohesion of magnesium’. In: *Journal of Magnesium and Alloys* 9.5 (2021), pp. 1521–1536.
- [261] H. Somekawa, A. Singh and T. Inoue. ‘Enhancement of toughness by grain boundary control in magnesium binary alloys’. In: *Materials Science and Engineering: A* 612 (2014), pp. 172–178.
- [262] H. Somekawa, A. Singh, T. Mukai and T. Inoue. ‘Effect of alloying elements on room temperature tensile ductility in magnesium alloys’. In: *Philosophical Magazine* 96.25 (2016), pp. 2671–2685.
- [263] H. Somekawa, A. Kinoshita and A. Kato. ‘Effect of alloying elements on room temperature stretch formability in Mg alloys’. In: *Materials Science and Engineering: A* 732 (2018), pp. 21–28.
- [264] V. Gärtnerová, A. Singh, A. Jäger and T. Mukai. ‘Deformation behavior of ultra-fine-grained Mg-0.3 at% Al alloy in compression’. In: *Journal of Alloys and Compounds* 726 (2017), pp. 651–657.
- [265] H. Somekawa, M. Yamaguchi, Y. Osawa, A. Singh, M. Itakura, T. Tsuru and T. Mukai. ‘Material design for magnesium alloys with high deformability’. In: *Philosophical Magazine* 95.8 (2015), pp. 869–885.
- [266] H. Pan, G. Qin, Y. Ren, L. Wang, S. Sun and X. Meng. ‘Achieving high strength in indirectly-extruded binary Mg–Ca alloy containing Guinier–Preston zones’. In: *Journal of Alloys and Compounds* 630 (2015), pp. 272–276.
- [267] N. Ikeo, M. Nishioka and T. Mukai. ‘Fabrication of biodegradable materials with high strength by grain refinement of Mg–0.3 at.% Ca alloys’. In: *Materials Letters* 223 (2018), pp. 65–68.

- [268] Y. Wang, S. B. Kang and J. Cho. ‘Microstructure and mechanical properties of Mg–Al–Mn–Ca alloy sheet produced by twin roll casting and sequential warm rolling’. In: *Journal of Alloys and Compounds* 509.3 (2011), pp. 704–711.
- [269] M. Cihova, R. Schäublin, L. B. Hauser, S. S. A. Gerstl, C. Simson, P. J. Uggowitzer and J. F. Löffler. ‘Rational design of a lean magnesium-based alloy with high age-hardening response’. In: *Acta Materialia* 158 (2018), pp. 214–229.
- [270] H. Pan et al. ‘Mechanistic investigation of a low-alloy Mg–Ca-based extrusion alloy with high strength–ductility synergy’. In: *Acta Materialia* 186 (2020), pp. 278–290.
- [271] R. Cheng et al. ‘Effects of single-pass large-strain rolling on microstructure and mechanical properties of Mg–Al–Ca alloy sheet’. In: *Materials Science and Engineering: A* 786 (2020), p. 139332.
- [272] Q. Huang, Y. Liu, M. Tong, H. Pan, C. Yang, T. Luo and Y. Yang. ‘Enhancing tensile strength of Mg–Al–Ca wrought alloys by increasing Ca concentration’. In: *Vacuum* 177 (2020), p. 109356.
- [273] D. Kevorkov, M. Medraj, J. Li, E. Essadiqi and P. Chartrand. ‘The 400°C isothermal section of the Mg–Al–Ca system’. In: *Intermetallics* 18.8 (2010), pp. 1498–1506.
- [274] A. Suzuki, N. D. Saddock, J. W. Jones and T. M. Pollock. ‘Solidification paths and eutectic intermetallic phases in Mg–Al–Ca ternary alloys’. In: *Acta Materialia* 53.9 (2005), pp. 2823–2834.
- [275] W.-Y. Yu, N. Wang, X.-B. Xiao, B.-Y. Tang, L.-M. Peng and W.-J. Ding. ‘First-principles investigation of the binary AB₂ type Laves phase in Mg–Al–Ca alloy: Electronic structure and elastic properties’. In: *Solid State Sciences* 11.8 (2009), pp. 1400–1407.
- [276] F. Islam and M. Medraj. ‘THERMODYNAMIC MODELLING OF THE Mg–Al–Ca SYSTEM’. In: *Canadian Metallurgical Quarterly* 44 (2005), pp. 523–536.
- [277] H. Okamoto. ‘Al–Mg (aluminum–magnesium)’. In: *Journal of Phase Equilibria* 19.6 (1998), p. 598.
- [278] H. Okamoto. ‘Ca–Mg (calcium–magnesium)’. In: *Journal of Phase Equilibria* 19.5 (1998), p. 490.
- [279] H. A. Elamami, A. Incesu, K. Korgiopoulos, M. Pekguleryuz and A. Gungor. ‘Phase selection and mechanical properties of permanent-mold cast Mg–Al–Ca–Mn alloys and the role of Ca/Al ratio’. In: *Journal of Alloys and Compounds* 764 (2018), pp. 216–225.
- [280] S. Sanyal, M. Paliwal, T. K. Bandyopadhyay and S. Mandal. ‘Evolution of microstructure, phases and mechanical properties in lean as-cast Mg–Al–Ca–Mn alloys under the influence of a wide range of Ca/Al ratio’. In: *Materials Science and Engineering: A* 800 (2021).
- [281] J. S. Park and Y. W. Chang. ‘The Effect of Alloying Elements on the c/a Ratio of Magnesium Binary Alloys’. In: *Advanced Materials Research* 26–28 (2007), pp. 95–98.
- [282] L. Zhang, K.-k. Deng, K.-b. Nie, F.-j. Xu, K. Su and W. Liang. ‘Microstructures and mechanical properties of Mg–Al–Ca alloys affected by Ca/Al ratio’. In: *Materials Science and Engineering: A* 636 (2015), pp. 279–288.

- [283] S. M. Liang, R. S. Chen, J. J. Blandin, M. Suery and E. H. Han. ‘Thermal analysis and solidification pathways of Mg–Al–Ca system alloys’. In: *Materials Science and Engineering: A* 480.1-2 (2008), pp. 365–372.
- [284] Z. T. Li, X. D. Zhang, M. Y. Zheng, X. G. Qiao, K. Wu, C. Xu and S. Kamado. ‘Effect of Ca/Al ratio on microstructure and mechanical properties of Mg–Al–Ca–Mn alloys’. In: *Materials Science and Engineering: A* 682 (2017), pp. 423–432.
- [285] G. Han, D. Chen, G. Chen and J. Huang. ‘Development of non-flammable high strength extruded Mg–Al–Ca–Mn alloys with high Ca/Al ratio’. In: *Journal of Materials Science & Technology* 34.11 (2018), pp. 2063–2068.
- [286] B. Kondori and R. Mahmudi. ‘Effect of Ca additions on the microstructure and creep properties of a cast Mg–Al–Mn magnesium alloy’. In: *Materials Science and Engineering: A* 700 (2017), pp. 438–447.
- [287] W. J. Delis, P. C. Huckfeldt, B. Hallstedt, P.-L. Sun, D. Raabe, S. Korte-Kerzel and S. Sandlöbes-Haut. ‘Influence of Al and Ca on the Ductility of Mg–Al–Ca Alloys’. In: *Advanced Engineering Materials* 26 (2024), p. 2301071.
- [288] R. L. Doiphode, S. V. S. N. Murty, N. Prabhu and B. P. Kashyap. ‘Grain growth in calibre rolled Mg–3Al–1Zn alloy and its effect on hardness’. In: *Journal of Magnesium and Alloys* 3.4 (2015), pp. 322–329.
- [289] W. Yuan, S. K. Panigrahi, J. Q. Su and R. S. Mishra. ‘Influence of grain size and texture on Hall–Petch relationship for a magnesium alloy’. In: *Scripta Materialia* 65.11 (2011), pp. 994–997.
- [290] S. M. Razavi, D. C. Foley, I. Karaman, K. T. Hartwig, O. Duygulu, L. J. Kecskes, S. N. Mathaudhu and V. H. Hammond. ‘Effect of grain size on prismatic slip in Mg–3Al–1Zn alloy’. In: *Scripta Materialia* 67.5 (2012), pp. 439–442.
- [291] A. Jain, O. Duygulu, D. W. Brown, C. N. Tomé and S. R. Agnew. ‘Grain size effects on the tensile properties and deformation mechanisms of a magnesium alloy, AZ31B, sheet’. In: *Materials Science and Engineering: A* 486.1-2 (2008), pp. 545–555.
- [292] H. Yu, C. Li, Y. Xin, A. Chapuis, X. Huang and Q. Liu. ‘The mechanism for the high dependence of the Hall-Petch slope for twinning/slip on texture in Mg alloys’. In: *Acta Materialia* 128 (2017), pp. 313–326.
- [293] S. H. Choi, D. H. Kim and B. S. Seong. ‘Simulation of strain-softening behaviors in an AZ31 Mg alloy showing distinct twin-induced reorientation before a peak stress’. In: *Metals and Materials International* 15.2 (2009), pp. 239–248.
- [294] Y. B. Chun and C. H. J. Davies. ‘Texture effects on development of shear bands in rolled AZ31 alloy’. In: *Materials Science and Engineering: A* 556 (2012), pp. 253–259.
- [295] K.-H. Kim, J. H. Hwang, H.-S. Jang, J. B. Jeon, N. J. Kim and B.-J. Lee. ‘Dislocation binding as an origin for the improvement of room temperature ductility in Mg alloys’. In: *Materials Science and Engineering: A* 715 (2018), pp. 266–275.

- [296] J. Wang, Y. Chen, Z. Chen, J. Llorca and X. Zeng. ‘Deformation mechanisms of Mg-Ca-Zn alloys studied by means of micropillar compression tests’. In: *Acta Materialia* 217 (2021), p. 117151.
- [297] W. Hume-Rothery, W. Mabbott Gilbert, K. M. Channel Evans and H. C. H. Carpenter. ‘The freezing points, melting points, and solid solubility limits of the alloys of silver and copper with the elements of the b sub-groups’. In: *Philosophical Transactions of the Royal Society of London. Series A, Containing Papers of a Mathematical or Physical Character* 233.721-730 (1934), pp. 1–97.
- [298] W. J. Delis, L. Berners, S. Korte-Kerzel and S. Sandlöbes-Haut. ‘Effect of Lean Alloyed Al and Ca on the Texture Development of Cold Rolled Mg Sheets’. In: *Metals* 13.4 (2023).
- [299] W. Luo et al. *Metallurgical synthesis methods for Mg-Al-Ca scientific model materials*. 2023. arXiv: 2303.08523 [cond-mat.mtrl-sci].
- [300] D. Andre et al. ‘Metallographic preparation methods for the Mg based system Mg-Al-Ca and its Laves phases’. In: *Materials Characterization* 192 (2022), p. 112187.
- [301] X.-L. Nan, H.-Y. Wang, L. Zhang, J.-B. Li and Q.-C. Jiang. ‘Calculation of Schmid factors in magnesium: Analysis of deformation behaviors’. In: *Scripta Materialia* 67.5 (2012), pp. 443–446.

List of Figures

1.1	Workflow and structure of this thesis including the resulting publications. All alloy compositions stated in wt.-%.	3
2.1	Determination of the Schmid factor (published under a Creative Commons CC BY 4.0 license [102]).	5
2.2	Mechanism of deformation twinning. a) Twinning elements b) Example: Schematic for an extension twin in Mg (adapted from [112]).	6
2.3	Schematic hexagonal lattice structure with the important slip planes.	7
2.4	Basal stacking faults in Mg. a) I1 intrinsic stacking fault, b) I2 intrinsic stacking fault, extrinsic stacking fault and d) twin-like stacking fault.	10
2.5	Ideal pole figures for the {0001} basal texture (adapted from [221]).	12
3.1	Correlation of the elongation with YS and UTS [24, 26, 42, 43, 46, 49, 51, 53, 54, 240, 241, 260–272], including the results of this study [287].	14
3.2	Determination of the Hall-Petch constant by linear correlation of the YS and grain size $d^{-1/2}$ for all considered Mg-Al-Ca-X alloys [24, 26, 42, 43, 46, 49, 51, 53, 54, 240, 241, 260–272], including the results of this study [287].	14
3.3	Correlation of the UTS and tensile elongation with the alloying content of Al to Mg (left) (filled icons from literature [26, 42, 51, 261–264] and open icons from this study [287]) and Ca to Mg (right) (filled icons from literature [24, 54, 240, 241, 260, 261, 263, 265–267] and open icons from this study [287]).	15
3.4	Correlation of the UTS and tensile elongation with the alloying content of Mg-Al-Ca alloys (filled icons from literature [43, 46, 51, 260, 271, 272] and open icons from this study [287]).	16
4.1	Mechanical properties obtained from tensile tests of all investigated compositions [287].	18
4.2	Intensities of the (0002)-peak in dependence of the Ca content and its solubility [287].	18
4.3	Statistic analysis of the activated slip system in each composition [287].	19
4.4	Maximum intensities of the basal (0002) peak for samples with basal normal direction related to the relative height reduction (ϵ_h) during cold rolling, including the absolute mean error (published under a Creative Commons CC BY 4.0 license [298]).	20
4.5	(a) S4 alloy with the transverse direction facing upwards cold rolled to 5% height reduction: Top: Inverse pole figure map. Bottom: Kernel average misorientation map. (b) S9 alloy with the transverse direction facing upwards cold rolled to 5% height reduction: Top: Inverse pole figure map. Bottom: Kernel average misorientation map (published under a Creative Commons CC BY 4.0 license [298]).	21
4.6	Examples of compressed MPs with different off-basal tilt. a) - d) showing basal slip and e) shows twinning indicated with the arrow.	22
4.7	Two examples of TEM lamellae taken from MPs exhibiting GBs. a) S4 alloy with 15.1° off c-axis tilt and b) S2 alloy with 77.7° off c-axis tilt. Blue arrows indicate $\langle c + a \rangle$ slip and pink arrows indicating SFs.	23

4.8	Example of a TEM lamella taken from a MP (S3 alloy with 88.6° off c-axis tilt) deformed with twin formation. Blue arrows indicate $\langle c + a \rangle$ slip and pink arrows indicating SFs	24
4.9	Reconstructed APT specimen taken from a 2 nd order pyramidal slip line detected during the slip line analysis of the S5 alloy showing the distribution of Al and Mg. Courtesy of Deborah Neuss, Materials Chemistry, RWTH Aachen University. . . .	24

List of Tables

2.1	Predominant slip systems in hexagonal Mg [10, 11, 115].	7
2.2	Predominant twinning systems in Mg [74, 112].	9
4.1	Alloys studied with nominal compositions and chemical analysis (ICP-OES) in wt.-%.	17
4.2	Average CRSSs for basal slip in dependency of the composition and the corresponding Al:Ca ratio.	22